INNER SHELL AND VALENCE SHELL ELECTRON EXCITATION OF GASEOUS MOLECULES STUDIED BY ELECTRON ENERGY LOSS SPECTROSCOPY

by

RANA N.S. SODHI

B.Sc. (Hon.), University of Reading, 1975

M.Sc., University of Alberta, 1980

A THESIS SUBMITTED IN PARTIAL FULFILLMENT OF

THE REQUIREMENTS FOR THE DEGREE OF

DOCTOR OF PHILOSOPHY

in

THE FACULTY OF GRADUATE STUDIES

Department of Chemistry

We accept this thesis as conforming

to the required standard

The University of British Columbia

August, 1984

In presenting this thesis in partial fulfilment of the requirements for an advanced degree at the University of British Columbia, I agree that the Library shall make it freely available for reference and study. I further agree that permission for extensive copying of this thesis for scholarly purposes may be granted by the head of my department or by his or her representatives. It is understood that copying or publication of this thesis for financial gain shall not be allowed without my written permission.

Department of CHEMISTRY

The University of British Columbia
1956 Main Mall
Vancouver, Canada
V6T 1Y3

Date 12 OCTOBER 1984

Abstract

Electron energy loss spectroscopy has been used to obtain the inner shell electron excitation spectra of several different series of gaseous molecules. The spectra were all recorded under small momentum transfer conditions (usually 2.5 keV impact energy and small angle (~1°) scattering) and all spectral regions (both central atom and ligand) accessible by the present instrumentation (<1000 eV) have been measured. The series of molecules investigated include nitrogen containing molecules (NF_3, NH_3 and the methyl amines) and several phosphorus compounds (PX_3, X = H, F, Cl and CH_3; PF_5, OPF_3 and $OPCl_3$). In addition the spectra of $Si(CH_3)_4$ have been obtained and compared with published spectra of related Si containing compounds. All of the inner shell spectra show continuum structures which in many cases can be reasonably assigned to σ^* shape-resonances. However, comparison of the inner shell electron excitation spectra of NF_3 with the X-ray photoelectron spectra (also reported here) show that continuum structure can also be ascribed, in some cases, to onsets of "shake-up" continua. The relationship of shape-resonance position and bond length is also examined in the systems studied here.

The valence shell electron energy loss spectra of many of the above molecules are also reported. The assignment of these spectra is shown to be greatly facilitated by a comparison with the inner shell spectra.

Finally, the inner shell and valence shell electron energy loss spectra of trans-1,3-butadiene and allene are also reported and assigned. In particular, the spectral assignment of the inner shell spectrum of allene allows clarification of its complex and controversial valence shell spectrum.

Table of Contents

List of Tables

List of Figures

Acknowledgements

I wish to express my sincere thanks to my research supervisor, Dr. C.E. Brion. It has been a pleasure to have worked with him and his support, direction and assistance will always be greatly appreciated. Thanks are also due to the various members of Dr. Brion's research group for contributing to an enjoyable working environment. Special thanks go to Dr. Suzannah Daviel for recording the valence shell spectra of NF_3 and $Si(CH_3)_4$ on the new spectrometer and to Tong Leung for some assistance with computing.

Dr. D.P. Chong, Dr. M.C.L. Gerry and Dr. A.J. Merer of this department are thanked for helpful discussions, as are Dr. A.P. Hitchcock (McMaster) and Dr. P.L. Langhoff (Indiana). Dr. R.G. Cavell and Anna-Marie Venezia-Floriano (Alberta) are thanked for supplying a number of ionisation potentials of the molecules presented here.

Much appreciation is due to Tilly Schreinders for the typing of this thesis.

The staff in the departmental workshops must also be thanked for their capable assistance in the maintenance of the spectrometer.

Finally I wish to express my great appreciation to Marilyn Daniels for all her patience and encouragement. This thesis is dedicated to her.

CHAPTER 1

INTRODUCTION

A. General Introduction

In the last twenty years there has been a growing interest in the use of electron impact spectroscopy to probe electronic excitations in atomic and molecular systems. Electron energy loss spectroscopy (EELS) [1-3] is a well established technique for the study of electronic transitions in the valence region. More recently [4] the technique has been extended to the study of inner shell (core) electron transitions. In the past decade inner shell electron energy loss spectroscopy (ISEELS) has produced much new and interesting spectroscopic data [5-9] at resolutions comparable to, or in some cases better than, that achievable with photoabsorption techniques in the soft X-ray range. Much of the work performed on inner shell electron excitation (both ISEELS and photoabsorption) up to 1982 has been summarised in a recently published bibliography [10].

In EELS, a monoenergetic beam of electrons is used to excite various electronic transitions in the sample. The energy required for such a transition can be found by measuring the energy loss of the scattered electrons (i.e. the electrons which caused the transitions). The system may be described as:-

$$e(E_o) + M \longrightarrow M^* + e(E_o - E')$$

where E_o is the energy of the incident beam and $(E_o - E')$ is the energy of the scattered electron. Thus E', the energy loss (analogous to photon energy), is the energy required for the sample to go from the M ground state to the M^* excited state.

It can be seen that information akin to photoabsorption is obtained, however, the use of electrons has some differences which in some cases lead to distinct advantages.

1) Photoabsorption is a resonant process, the photon energy must exactly match the transition energy, whereas with electron impact the process is non-resonant since the excess energy is carried off by the scattered electron.
2) Different sources and hence techniques are required in photoabsorption in order to cover a wide range of energies. Electron impact, however, allows coverage of a range extending from zero energy loss to the X-ray region with a single spectrometer.
3) In the soft X-ray region (~200 eV - 1000 eV), the resolution of electron impact excitation is comparable or better than that achieved so far with photoabsorption [8].
4) With low momentum transfer (high incident energy and small scattering angle) a fast electron beam provides a dipole excitation mechanism which is an effective alternative to the use of a tuneable photon source. A virtual photon field is induced in the

target by the passing electron. The target sees the electric field associated with the beam as a sharp impulse in time, which, with high enough energy, approaches a delta function. Fourier transforming this into a frequency domain yields a continuous range of frequencies (assuming an ideal delta function) of uniform intensity. Thus spectra obtained in this manner will closely resemble optical spectra and in essence the optical (dipole) selection rules will apply. On lowering the impact energy and/or increasing the scattering angle, the momentum transfer is increased and optically forbidden transitions become more important. In this way the use of electrons not only compliments the information obtained by photoabsorption but is also able to extend it.

The primary concern of the work described in this thesis is the study of dipole allowed transitions in a variety of molecular systems as obtained by using high energy electron impact and small scattering angle. The major focus will be on inner shell electron excitation, however, valence shell electron excitation for many of the systems will also be presented. The inner shell excitation spectrum is often simpler and less ambiguous to assign than the valence shell excitation spectrum since the originating orbital is usually well separated from the other orbitals and can be positively identified. Thus knowledge of the term values (difference of the excitation feature from the ionisation limit) from the inner shell spectrum can aid in the interpretation of the valence shell spectrum. Before discussing some of

the theoretical considerations relevant to electron impact, the relationship with photoabsorption and the features observed in electron excitation spectra in more detail, it is useful to briefly review some of the aspects of electron spectroscopy in general and how they relate to electron excitation.

B. Description of various processes in electron spectroscopy

The various types of processes which can occur are illustrated in Figure 1.1. Note that both X-ray (K, L, M, ...) and orbital (1s, 2s, 2p, 3s, 3p, ...) notation for electron energy levels will be used interchangeably throughout this thesis.

I) Electron Excitation.

As this is the main topic of this work, this is introduced first, however, only a brief description is presented here. A more detailed and complete description follows in the subsequent sections. The process is is illustrated in Figures 1.1B and 1.1C in terms of a one electron picture. Interaction of the initial ground state of a molecule or atom with either a photon or electron can cause one of the electrons of the target species to be promoted to an unoccupied level. Use of a photon requires the transition energy (E') to be exactly equal to the photon energy whereas an incoming electron can impart whatever energy is required. Figure 1.1B shows the promotion of an inner shell electron while Figure 1.1C shows that of a valence electron. The transition energies for the former (1.1B) lie

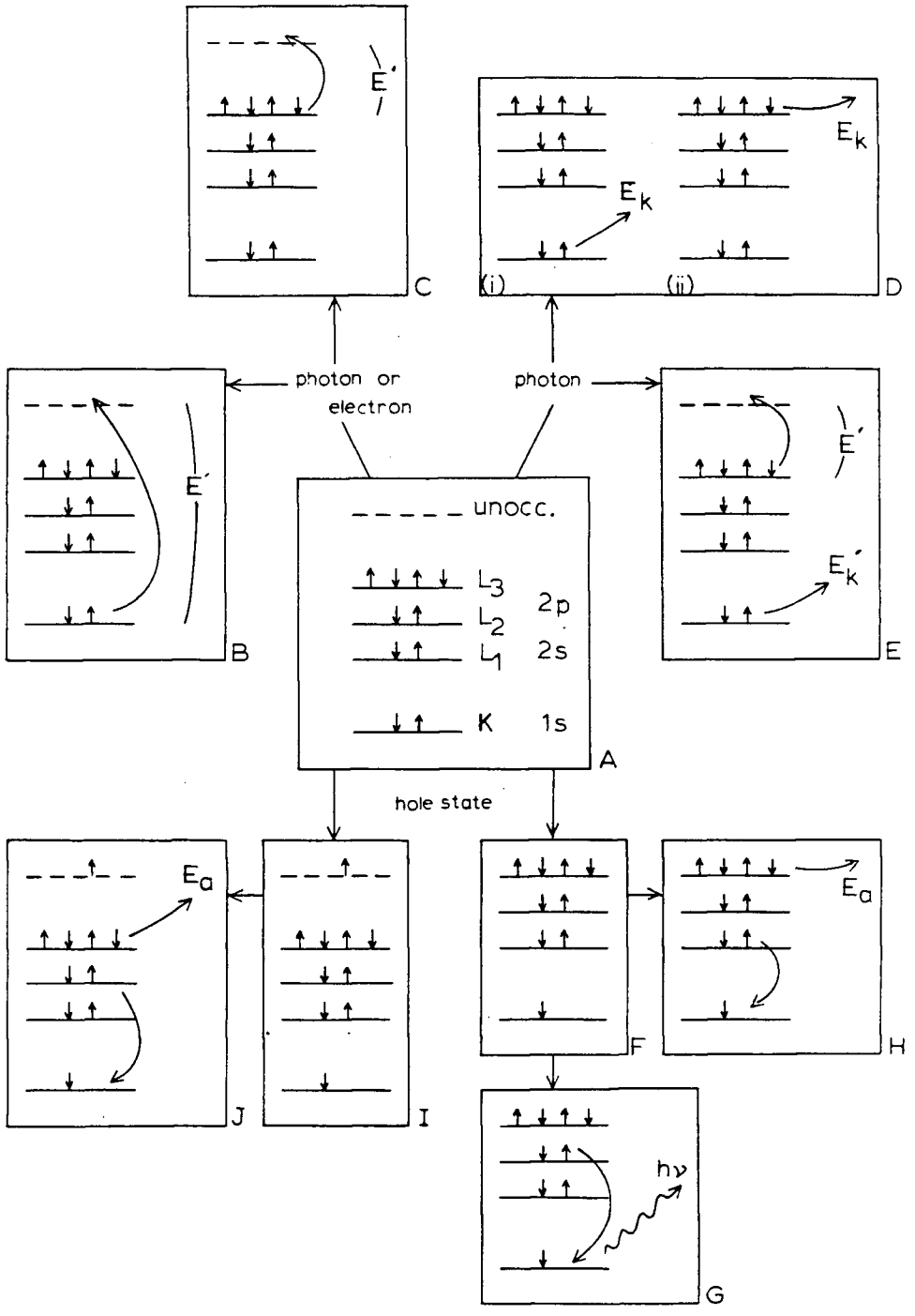

Figure 1.1 Processes involved in electron spectroscopy.

A. Initial state
B,C. Electron excitation by electron impact or photoabsorption (section B.I)
D. Photoionisation (i) XPS (ii) UPS (section B.II)
E. Photoionisation resulting in excited ion states - "shake-up" - "shake-off" (section B.III)
F. Core vacancy resulting from ion formation allows G and H (section B.IV)
G. X-ray fluorescence
H. Auger process
I. Core vacancy resulting from formation of an excited neutral species allows J (section B.IV)
J. Autoionisation.

(typically) in the XUV or soft X-ray regions of the electromagnetic spectrum while for the latter (1.1C) the transition energies are in the vacuum or far UV. Thus in photoabsorption several different monochromators are usually needed to cover the UV and X-ray region.

Transitions to the unoccupied levels from a particular level in atoms will result in an excitation spectrum consisting of a series of lines converging upon the particular ionisation limit. The series fits the following Rydberg formula.

$$T = E_{IP} - E' = \frac{R}{(n^*)^2} = \frac{R}{(n-\delta_\ell)^2} \qquad (1.B.1.)$$

where E' is the transition energy; E_{IP} is the ionisation limit; R is the Rydberg constant (13.605eV); n^* is the effective quantum number and is obtained by correcting the principal quantum number, n, by a quantum defect, δ_ℓ, which is characteristic of the ℓ quantum number (i.e. whether the electron is promoted to an s, p, d etc. type of orbital). For the hydrogen atom $\delta_\ell = 0$, thus the quantum defect can be thought of as a measure of the deviation from simple hydrogen-like behaviour. The term value, T, is the difference of the Rydberg feature from the ionisation limit. In essence it can be thought of as the binding energy of the newly promoted electron occupying the Rydberg orbital. The intensity of transitions to the Rydberg orbitals falls as n^{-3} [11,12], thus it becomes increasingly difficult to observe the higher lying Rydberg states.

The concept of the Rydberg orbital can be extended to molecules. The Rydberg orbitals are large and diffuse and hence will increasingly see the molecule as one large core. However, in addition to Rydberg orbitals, molecules will also have unoccupied virtual valence orbitals which arise out of the MO scheme. These orbitals are usually the antibonding counterparts of the bonding MOs. Thus they are delocalised and of similar size to the occupied outer valence orbitals of the molecule. Depending on the particular molecule, the virtual valence orbitals can be low lying, in which case transitions to them will be seen in the discrete portion of the excitation spectrum, however, they may be high lying and thus occur in the continuum.

The above aspects of Rydberg and valence orbitals will be expanded upon in section E. A good review of the orbital concept in molecular spectroscopy has been given by Wittel and McGlynn [13]. Robin [12] also gives a detailed discussion of Rydberg and valence states.

II) Photoionisation.

This is illustrated in Figure 1.1D. In this the initial state of a molecule or atom is bombarded with photons of a characteristic energy, $h\nu$, a transition occurs in which the final state is an ion plus a free electron. Conservation of energy requires that

$$h\nu = E_K + E_{IP} \qquad (1.B.2)$$

where E_K is the kinetic energy of the ejected electron and E_{IP} is the energy required to form the ion. Since the mass of the ion is several thousand times that of the electron, conservation of momentum dictates that essentially all the kinetic energy is taken up by the ejected electron. Thus by measuring E_K and knowing $h\nu$, E_{IP}, which in the one electron example shown in Fig. 1.1D is the ionisation potential or binding energy of an electron from a particular orbital, can be obtained. The ionisation potential can be equated to the difference in the total energies of the ion state and the ground state of the species:

$$E_{IP}^{s} = E_f{}^{s}(N-1) - E_G(N) \qquad (1.B.3)$$

where E_{IP}^{s} is the ionisation potential of electron s; $E_G(N)$ is the total energy of the ground state and $E_f{}^{s}(N-1)$ is the total energy of the ion which is formed when electron s is removed. Thus the ionisation energies can be obtained theoretically by rigorous calculations of the appropriate total energies.

Quantum mechanically the probability of a transition from the initial ground state (ψ'') to the final state (ψ' $\equiv$ ion + free electron) is proportional to the square of the transition moment integral

$$M = \langle \psi'' | \Sigma p | \psi' \rangle \qquad (1.B.4)$$

where p is the dipole moment operator. Application of the Born-Oppenheimer approximation separates the wave function into a product of electronic (ϕ_e) and nuclear (ϕ_N) functions. Thus equation (1.B.4) can be written as

$$M = \int \phi_v^{*''}(R)\,\phi_v'(R)\,dR \int \phi_e''(r,R)\,|\,\Sigma_i P_e\,|\,\phi_e'(r,R)\,dr \quad (1.B.5)$$

where the nuclear function (ϕ_N) has been further partitioned into vibrational (ϕ_v) and rotational components. In the majority of cases rotational structure cannot be resolved and is ignored (as in (1.B.5)). For a photoelectron transition to be allowed, the integrals in the above equation must be non-zero. Since the final state includes a free electron there is always a non-zero value and as a consequence all one electron transitions are allowed.

The vibrational part of equation (1.B.5) is termed the Franck-Condon factor and gives the intensities and shape of the vibrational envelope. This shape can be indicative of the type of electron being ionised. For example, ionisation of a non-bonding electron would lead to very little change in the nuclear coordinates of the ion from that of the ground state molecule and thus the $v'' = 0 \rightarrow v' = 0$ (where v denotes the vibrational quantum number) transition would have the strongest overlap and there would only be a short progression. In other words the <u>adiabatic</u> and <u>vertical</u> ionisation energies coincide. An adiabatic transition is defined as the least energy required to eject a particular

electron from a molecule in its ground state, i.e. it corresponds to the $v'' = 0 \rightarrow v' = 0$ transition. A vertical transition is defined as the most intense, i.e. a $v'' = 0 \rightarrow v' = n$ transition, where n is the vibrational function with the largest overlap with the ground state.

Traditionally photoelectron spectroscopy has been divided into two sections depending upon the photon source being used. One major branch is Photoelectron Spectroscopy (PES) or Ultraviolet Photoelectron (UPS). In this case ultraviolet radiation, typically He I (21.22 eV) provides the photon source and hence only the valence orbitals are accessible. Use of the He(II) resonance line at 40.81 eV in principle allows the inner valence orbitals to be probed but in practice this is precluded by the He I "shadow". An excellent book by Rabalais [15] covers the various aspects of UPS. The other branch is Electron Spectroscopy for Chemical Analysis (ESCA) or X-ray Photoelectron Spectroscopy (XPS). In this case the photon source is an X-ray. The most common sources used are the Mg Kα (1253.64 eV) and Al Kα (1486.58 eV). Thus the core levels can be accessed. There has been much work on XPS ever since the pioneering work of Siegbahn [16,17]. The primary application arises from the fact that the inner shell electron shows a chemical shift in its binding energy which reflects a change in the molecular environment. A perspective of its impact can be obtained from Siegbahn's Nobel laureate address [18]. The work from this Swedish group has culminated in a new high-resolution multipurpose XPS spectrometer which features X-ray monochromation [19].

Ionisation energies obtained from photoelectron spectroscopy are invaluable to the interpretation of electron excitation spectra in that an accurate and unambiguous value is obtained for the binding energy (or ionisation limit) of a particular electron. In theory, analysis of a Rydberg series should yield the IP (see equation (1.B.1)). However, only a few levels can usually be identified in the valence shell spectrum due to such factors as the n^{-3} drop in intensity, other overlapping transitions as well as deviations of the lower Rydbergs from the series due to possible valence-Rydberg orbital interactions [20]. These factors, the lack of resolution and lifetime considerations make matters even worse for inner shell transitions. Thus it is of far more use to interpret the excitation spectrum knowing the IP accurately from UPS or XPS and hence being able to establish the term values with considerable accuracy. These term values are, in general, characteristic of particular transitions (see section E).

A further aid in interpreting electron excitation spectra can come from the spectral shape of the photoionised band. In ionisation only the nature of the initial orbital has to be considered, however, in excitation both levels must be considered. Thus if the spectral shape (and in particular the vibrational envelope at high resolution) is similar in the ionisation and excitation spectra, the transition is suggestive of one to a Rydberg level. This arises from the large, diffuse and non-bonding nature of the Rydberg orbital and so the upper (Rydberg) state is very similar to the ion state. However, care has

to be exercised since some of the lower Rydberg states may have some anti-bonding character due to Rydberg-valence mixing [20].

III) "Shake-up" and "Shake-off".

Upon photoionisation an excited ion state may be formed in which the photoelectron has been emitted along with the simultaneous excitation of an outer electron either to an excited bound state or into the continuum. The former is termed "shake-up" while the latter is termed "shake-off". The process is illustrated in Fig. 1.1E. Upon ionisation the resultant ion can be in one of a number of states with the ionisation energy of the photoelectron being given by a modified form of equation (1.B.3)

$$E_{IP}^{s,t} = E_f^{s,t} - E_G(N) \qquad (1.B.6)$$

when t = 0, the ion is in its ground state and this gives rise to the major photoionisation peak. The satellite lines are defined by t = 1, 2 etc. and since they denote excited ion states the satellites will appear on the low kinetic energy side of the major peak.

Equation (1.B.6) implies that there is no fundamental difference between the major peak and the satellites and that each state is reached by a one-step, "one-electron" dipole transition [18] (note: photoionisation follows dipole selection rules- see equation (1.B.5)). On a simplistic model, "shake-up" can be thought of as the emission of

a photoelectron with the attendant excitation of a valence electron. Since the allowed, excited ion states must have the same symmetry as the ion in its ground state, the valence electron transition must in essence follow monopole selection rules. Thus it might be thought that there is a direct relationship between XPS satellite structure and valence electron excitation as observed by photoabsorption spectroscopy or EELS. However, care must be taken in any comparison since EELS or photoabsorption spectroscopy leads to an excited neutral state which can essentially be described by a simple one electron description whereas the XPS satellite structure leads to an excited ion state. Martin et al. [21,22] have shown that many electron theory including configuration interaction must be included in both hole and ground state in order to describe the satellite structure accompanying photoionisation adequately. An alternative approach which also accounts for correlation effects is the many-body Green function method used by Cederbaum and co-workers [23,24] to describe inner valence shell ionisation processes.

In addition to providing information on valence electron excitation, knowledge of the XPS satellite spectrum can assist in the interpretation of continuum structure in ISEELS and photoabsorption spectra. The XPS spectrum provides information on the excited ion states and in particular gives the vertical energy for the ionisation processes. The production of these excited ion states would be manifested in ISEELS by (adiabatic) onsets of new continua. Thus it should be possible to identify which features in the ISEELS spectrum

above the ionisation edge (the major ionisation peak) arise from the onsets of excited ion states and by inference which features are due to other types of phenomena such as resonances or double excitations. Continuum structure in ISEELS or photoabsorption spectroscopy will be discussed in section E.

IV. X-ray Fluorescence, Auger Decay and Autoionisation.

Following the creation of a hole state, either as an ion (Fig. 1.1F), or as an excited neutral state (Figure 1.1I), secondary processes can occur which allow the system to achieve a lower energy state. For the ion state in which there is a core vacancy, the two major decay modes are X-ray fluorescence and the Auger process. In the case of X-ray fluorescence the excess energy is released in the form of a photon whereas in the Auger process the excess energy is given to an emitted electron. The two processes are illustrated in Figures 1.1G and 1.1H respectively.

The respective yields for atomic K shell fluorescence and Auger decay are given by

$$W_K = \frac{P_f}{P_f + P_A} \quad \text{and} \quad a_K = \frac{P_A}{P_f + P_A}$$

where W_K is the K shell fluorescence yield, a_K is the Auger yield; P_f and P_A are the transition probabilities for X-ray fluorescence and the Auger process respectively. For the lighter elements the Auger

process dominates [25]. For example, the fluorescent yield for the K shell of the nitrogen atom is 5.2×10^{-3} and its Auger yield is 0.995 [25]. For the L_1 (2s) level of phosphorus, the fluorescent yield is 3.9×10^{-5} and for the $L_{2,3}$ (2p) level it is 6.2×10^{-4} [25].

In spite of the low yield for light elements various X-ray fluorescence studies have been reported utilising high resolution spectrometers [26-28]. X-ray transitions are governed by dipole selection rules and so the $L_{2,3}$ (2p) $\rightarrow$ K (1s) transition (as shown in Fig. 1.1) is allowed but the L_1 (2s) $\rightarrow$ K (1s) transition is forbidden. This factor can aid in the identification of valence states and provide complimentary information to UPS [26]. In other studies, Nordgren et al. [27] have reported the C K-shell X-ray fluorescence spectra of CO_2 and from a Franck-Condon fit of harmonic oscillators have determined the natural width of the C 1s state to be 0.07 $\pm$ 0.02 eV. A further application stems from the combination of X-ray fluorescence energies with UPS ionisation potentials to estimate core-electron binding energies [28].

The Auger process is the dominant decay mode for inner shell vacancies of light atoms. The energy of the Auger electron is given by the difference between the total energy of the initial hole state and that of the two hole state:

$$E_A(XYZ) = E_{M^+(X)} - E_{M^{++}(YZ)} \qquad (1.B.7)$$

where $E_A(XYZ)$ is the kinetic energy of the emitted XYZ Auger electron;

$E_{M^+(X)}$ is the total energy of the initial hole state, a singly ionised species with a hole in level X; $E_{M^{++}(YZ)}$ is the total energy of the final two-hole state, a doubly ionised species with holes in levels Y and Z. Thus in Fig. 1.1H the emitted Auger electron would be designated as the KL_1L_3 Auger transition. Unlike X-ray fluoresence, the Auger process involving an initial K hole state can involve the L_1 shell. Its selection rules are $\Delta L = \Delta S = \Delta J = 0$ and parity unchanged. Thus the Auger process is not a dipole transition followed by ejection of an electron but rather it arises from a coulombic rearrangement of the two electrons involved [29]. Clearly it is the much faster process for light elements (it is $\sim 10^3$ times faster for C and O K-shells than fluorescence [11]). A special type of Auger decay is termed a Coster-Kronig transition. This is a very rapid process and involves an Auger transition in which the primary vacancy is filled by a higher lying electron within the same shell. Thus a $L_1L_{2,3}$ M Coster-Kronig transition would involve the filling of a L_1 hole by an electron from the $L_{2,3}$ sub-shell with the resulting emission of a M-shell electron.

Those Auger spectra which only involve inner shell electrons are atomic-like in nature. As in the case of XPS spectra, inner shell Auger lines also show a chemical shift. Extensive series of KL_2L_3 Auger electron chemical shifts have been reported for Si [30], P [31] and S [32] containing compounds. A combination of Auger and XPS chemical shifts allows an estimate of the extra-atomic relaxation (i.e. attraction of the higher levels towards a hole) upon creation of

a core-hole. With this it is possible to estimate the relative polarisability of the various ligands [31,33]. Auger spectra which involve the valence shell are very complex due to the many overlapping transitions. However, various gas phase studies as well as calculations have been performed on Auger spectra [34-36].

Similar types of decay modes will occur when the hole state arises from electron excitation giving rise to an excited neutral state (Fig. 1.1I). The non-radiative process akin to Auger decay is termed autoionisation (Fig. 1.1J). As in Auger decay, the process involves the filling of the hole with the concomitant ejection of an electron. The emitted electron may be the initially excited electron or some other electron.

These decay modes are important to photoionisation and electron excitation as they govern the lifetime of the hole state and hence the natural line width of the feature. The natural line width (ΔE) is related to the lifetime (Δt) via the Heisenberg uncertainty principle:

$$\Delta E \cdot \Delta T \sim \hbar = 6.582 \times 10^{-16} \text{ eV.sec} \qquad (1.B.8)$$

For example levels which can undergo rapid Coster-Kronig transitions have a short lifetime and hence are wide. For instance the natural linewidth for the L_1 (2s) level in P is 1.26eV whereas it is only 0.033 eV and 0.032 eV for the L_3 ($2p_{3/2}$) and L_2 ($2p_{1/2}$) levels respectively and 0.53 eV for the K (1s) level [37]. In general, the natural linewidth (energy) for a given subshell increases with increase in Z,

along the periodic Table [37].

The above discussions have dealt mainly with inner shell vacancies. Obviously similar processes can occur for valence hole state below the first IP. Another form of mechanism which can occur reducing lifetimes of a particular state is pre-dissociation.

C. Fundamental Concepts in Electron Impact and the Relationship to Photoabsorption

To understand the processes which produce the features in an electron energy loss spectrum and to relate them to the optical (photoabsorption) spectrum, it is necessary to discuss some of the fundamental concepts behind the collision process. This can only come from a quantum mechanical description such as was first given by Bethe in 1930 [38]. A thorough review of Bethe's treatment has been given by Inokuti [39]. Wight [5], using the ideas discussed by Lassettre [40], has also discussed in detail the Bethe theory for electron scattering by the hydrogen atom including a generalisation to more complex species. This approach [5,40] will be followed in the present work. In view of the earlier referenced works, a detailed treatment will not be given and only the pertinent points and definitions will be discussed.

When an incident beam of electrons interacts with a target molecule, the latter may be excited from its initial state to some excited state. The probability of such a transition is known as the

Differential Cross-Section (DCS). This is the number of incident electrons scattered per second through an angle θ into a solid angle $d\Omega$ after exciting the target to its n^{th} excited state, divided by the number of electrons in the incident beam which crossed unit area in one second. If the incident beam is approximated by a plane wave the DCS for inelastic scattering off an H atom is given by [5]:

$$\frac{d\sigma}{d\Omega}(\theta)\, d\Omega = \frac{k_n}{k_o} |f_n(\theta)|^2\, d\Omega \qquad (1.C.1)$$

where k_o and k_n are the wave numbers for the incident and scattered beams respectively and $f_n(\theta)$ is the scattering amplitude. The square of the scattering amplitude, $|f_n(\theta)|^2$, is the number of electrons/unit volume at unit distance and angle θ which have excited the atom to its n^{th} state. Since the wave number is proportional to momentum, $k_n|f_n(\theta)|^2$ is proportional to the number of scattered electrons crossing unit area in one second at angle θ, and k_o is proportional to the total number of electrons in the incident beam crossing unit area per second. Thus the DCS can be experimentally determined by measuring these quantities.

In order to calculate the DCS knowledge of $|f_n(\theta)|$ is required. This will come out of the solution to the Schrödinger equation for the collision, which for the prototype case of electron-H atom scattering, gives an infinite set of coupled differential equations of the

type [41]

$$\left(\nabla_{r_b}^2 + k_n^2 - \frac{2m}{\hbar^2} V_{nn}\right) F_n(\bar{r}_b) = \frac{2m}{\hbar^2} \left[\Sigma + \int\right]_{m \neq n} V_{mn} F_m(\bar{r}_b) \quad (1.C.2)$$

where the matrix element, V_{mn}, is defined as

$$V_{mn} = \int U_n^*(\bar{r}_a) \left(\frac{e^2}{r_{ba}} - \frac{e^2}{r_b}\right) U_m(\bar{r}_a) d\bar{r}_a \quad (1.C.3)$$

and $\bar{r}_a$ and $\bar{r}_b$ are the co-ordinates of the target and incident (projectile) electrons respectively; $F_m(\bar{r}_b)$ represents the wave function of the incident electrons and $U_n(\bar{r}_a)$ are the complete set of eigenfunctions of the unperturbed H atom.

As equation (1.C.2) stands it cannot be solved and various approximations have to be made. One of the most common ones applied in collision theory is the Born approximation [42]. The basic assumption behind this approximation is that there is little interaction between the projectile and the target. Thus the incident wave is undistorted by the interaction and can be represented by an undistorted plane wave; the excitation is due to a direct transition from the ground to the excited state and so all V_{mn} terms are zero except for V_{on}; the potential energy of the interaction between the scattered electron and the atom in its final state is small and so the distortion of the scattered wave can be neglected, therefore $V_{nn} = 0$. The Born approximation is only valid for high incident electron energy

($\gtrsim$ 5-7 times the excitation energy) and hence will be valid in the majority of the cases reported in the present work.

Application of the Born approximation simplifies equation (1.C.2) to

$$(\nabla^2_{r_b} + k_n^2)\, F_n(\bar{r}_b) = \frac{2m}{\hbar^2}\, V_{on}\, e^{i\bar{k}_o \cdot \bar{r}_b} \qquad (1.C.4)$$

which can be solved by the method of Green's functions to yield an expression for $f_n(\theta)$. Thus the DCS can be written as

$$\frac{d\sigma(\theta)}{d\Omega} d\Omega = \frac{m^2}{4\pi^2\hbar^4} \frac{k_n}{k_o} \left| \int e^{i(\bar{k}_o - \bar{k}_n)\cdot \bar{r}}\, V_{on}\, d\bar{r} \right|^2 d\Omega \qquad (1.C.5)$$

(note $\bar{r} = \bar{r}_b$)

Finally by defining a momentum transfer variable, K, where:

$$|\bar{K}|^2 = |\bar{k}_o - \bar{k}_n|^2 = k_o^2 + k_n^2 - 2k_o k_n \cos\theta \qquad (1.C.6)$$

generalising to a N electron system (whose coordinates are given by $\bar{r}_s$) and using the integration formula derived by Bethe [38,39], namely:

$$\int \frac{e^{i\bar{K}.\bar{r}}}{|\bar{r}-\bar{r}_s|} d\bar{r} = \frac{4\pi}{K^2} e^{i\bar{K}.\bar{r}_s} \qquad (1.C.7)$$

the following expression for the DCS is obtained:

$$\frac{d\sigma(\theta)}{d\Omega} = \frac{4m^2e^4}{\hbar^4} \frac{k_n}{k_o} \frac{1}{K^4} \left| \varepsilon_{on}(\bar{K}) \right|^2 \qquad (1.C.8)$$

where the matrix element $\varepsilon_{on}(\bar{K})$ is

$$\varepsilon_{on}(\bar{K}) = \int U^*_n \sum_{s=1}^{N} e^{i\bar{K}.\bar{r}_s} U_o \, d\tau_N \qquad (1.C.9)$$

where $d\tau_N$ indicates integration over all coordinates of the N electron system.

A useful concept which predates quantum mechanics is that of the oscillator strength. The classical picture defined the oscillator strength, f, to be the number of electrons in free oscillation at a particular frequency. The total oscillator strength was the number of electrons in the target. The concept of total oscillator strength has been retained in quantum theory as a useful means of defining transition probability. In effect the transition probabilities are being normalised to the total number of electrons in the system. This is known as the Thomas-Reiche-Kuhn (TRK) sum rule [39].

In the dipole approximation (which covers optical selection rules) the general form for the optical (dipole) oscillator strength is

$$f_{on}(0) = 2E_n \left| \langle \psi_n | \sum_{s=1}^{N} \bar{r}_s | \psi_o \rangle \right|^2 \qquad (1.C.10)$$

Bethe [38,39] has defined a generalised oscillator strength (GOS) for particle collision $f_{on}(K)$ given by

$$f_{on}(K) = \frac{2E_n}{K^2} \left| \langle \psi_n | \sum_{s=1}^{N} e^{i\bar{K}.\bar{r}_s} | \psi_o \rangle \right|^2$$

$$= \frac{2E_n}{K^2} \left| \varepsilon_{on}(K) \right|^2 \qquad (1.C.11)$$

substituting (1.C.11) into (1.C.8) and switching to atomic units the Bethe-Born relationship [38,39] is obtained, namely:

$$f(K) = \frac{E_n}{2} \frac{k_o}{k_n} K^2 \frac{d\sigma(\theta)}{d\Omega} \qquad (1.C.12)$$

This form of oscillator strength is only valid if the Born approximation holds, however, Bethe has also defined the apparent GOS, $f_n'(K,E_o)$, where E_o is the impact energy. This is calculated from the

experimental parameters.

The optical (dipole) oscillator strength is a special case of the GOS. Expanding the exponential function in equation (1.C.11) as a power series in K, i.e.

$$e^{i\bar{K}.\bar{r}} = 1 + iK.r + \frac{(i\bar{K}.\bar{r})^2}{2!} \ldots \frac{(i\bar{K}.\bar{r})^m}{M!}$$

ε_{on} becomes

$$\varepsilon_{on} = 0 + \varepsilon_1(iK) + \varepsilon_2(iK)^2 + \ldots \varepsilon_M(iK)^M \qquad (1.C.13)$$

where $\varepsilon_m = \frac{1}{m!} \langle\psi_n|\Sigma_s \bar{r}_s^m|\psi_o\rangle$ and orthogonality dictates that $\varepsilon_o = \langle\psi_n|\psi_o\rangle = 0$. For m = 1, this matrix element becomes

$$\varepsilon_1 = \langle\psi_n|\Sigma_s \bar{r}_s|\psi_o\rangle \qquad (1.C.14)$$

which is nothing more than the transition moment term in the dipole approximation. Substituting (1.C.13) back into (1.C.11), the expanded form of the GOS is obtained, namely:

$$f(K) = 2\,E_n \{\varepsilon_1^2 + (\varepsilon_2^2 - 2\varepsilon_1\varepsilon_3)K^2 + O(K^4)\}$$
$$= f(0) + f(1)K^2 + f(2)K^4 + \ldots. \qquad (1.C.15)$$

Thus as the momentum transfer, K, approaches zero, the GOS, f(K), approaches f(0) which is the optical oscillator strength (i.e. Limit f(K) = f(0)). The higher terms, f(1), f(2) etc., represent quadrupole, octopole and higher transitions. Lassettre et al. [43] have shown that the GOS approaches the optical limit as K approaches zero regardless of whether the Born approximation applies or not.

From the above discussion it can be seen that if the experimental conditions are selected such that the momentum transfer approaches zero [44] then there exists a direct relationship between the DCS and the optical oscillator strength. This is governed by the Bethe-Born relationship (1.C.12). To achieve low momentum transfer, high incident electron energies (E_o) and small angle (θ) scattering (ideally zero degrees) are required. If the incident energy is very much greater than the energy transfer (i.e. transition energy, E_n) and θ is small, substitution of these quantities into equation (1.C.6) (note: $k_o^2 = 2E_o$ and $k_n^2 = 2(E_o - E_n)$ in atomic units) gives:

$$K^2 = 2E_o \left(\frac{1}{4}\left(\frac{E_n}{E_o}\right)^2 + \theta^2\right) \qquad (1.C.16)$$

thus if $\theta = 0$, the momentum transfer is proportional to the energy transfer and hence equation 1.C.12 indicates that:

$$\frac{d\sigma}{d\Omega} \propto E_n^{-3} f(0) \qquad (1.C.17)$$

Thus dipole spectra produced in this manner by electron impact should be qualitatively similar to their photoabsorption counterparts and only differ by a relative decrease in intensity which is proportional to the inverse of the energy loss cubed. This factor presents little problem for a simple qualitative comparison between optical and electron energy loss spectra, especially over a short range. However, the above correction (1.C.17) has to be applied if a quantitative comparison is required [45]. A review of continuum oscillator strengths as obtained by electron impact spectroscopy has recently been given by Brion and Hamnett [45].

Alternatively dipole oscillator strengths can be obtained by measuring a series of electron energy loss spectra at various momentum transfers and extrapolating back to zero momentum transfer. This can be done in two ways: either by fixing the impact energy and varying the scattering angle, or by fixing the scattering angle (usually at 0°) and varying the impact energy. The former method has been utilised by Lassettre et al. [2] while the latter method has been used by Hertel and Ross [46,47]. One aspect of these methods is that non-dipole transitions can be studied and identified since the oscillator strengths will extrapolate back to zero. However, for the study of optically allowed transitions by electron impact it is far superior and much less tedious to work directly (i.e. as close as possible) to the $K^2 = 0$ limit by appropriate selection of experimental conditions rather than employing the above mentioned extrapolation techniques.

D. The Relative Merits of Electron Energy Loss and Photoabsorption Spectroscopies

In the previous section the relationship between the oscillator strengths obtained by EELS and photoabsorption spectroscopies was established. It was shown that the two techniques could produce the same information with regard to dipole (optical) transitions. In this section the relative merits of using electrons or photons to produce "optical" (i.e. dipole) spectra will be discussed. No further discussion will be given of the ability of electron impact techniques to probe dipole forbidden transitions [1-3].

The obvious question to ask is why would anyone wish to simulate optical spectra using electrons when presumably the spectra could be obtained directly with a photon source? Clearly each technique must have its own advantages and disadvantages. These will arise from the experimental methods required to obtain the spectra and hence the various limitations inherent in these techniques.

To obtain a photoabsorption spectrum a suitable continuum light source is required. Until the advent of synchrotron radiation there was no effective means of obtaining tuneable radiation in the far UV and X-ray regions which would give a continuum source of high flux beyond 20 eV. Conventional light sources utilising hydrogen and noble gas continua have provided a useful, albeit weak, and often structured source extending up to ~20 eV [48] while the X-ray region was limited to the use of weak bremmstrahlung continua sources. However, even

with the availability and use of synchrotron sources there still exist various experimental limitations to the use of photons in certain regions of the electromagnetic spectrum.

In order to use a continuum light source one must select the region of radiation that is required by suitable optical monochromation and then transmit this selected light to the sample. This necessitates the use of windowless (for energies >10 eV) grating vacuum spectrometers. Since this is a dispersive technique and the amount of light absorbed is measured as a function of wavelength (λ), different grating and monochromator designs are required to optimise the running conditions for the various parts of the electromagnetic spectrum. Brown [49] shows illustrations of three types of monochromator in use.

Unlike photoabsorption, EELS is a non-resonant technique. On passing through the sample, some of the primary beam is scattered and the amount of energy required for a particular transition is simply transferred to the system. This amount can easily be obtained by adding an equivalent voltage back to the analyser system thereby allowing the scattered electrons to reach the detector. Thus a single spectrometer is able to cover a wide spectral range (from the IR through to the X-ray). By use of suitable retarding voltages it is possible to run the spectrometer in a "constant analyser pass energy mode" and so the energy resolution can be kept constant throughout the whole spectral range.

It is this final feature which presently gives a major

advantage to EELS over photoabsorption for the 200 - 1000 eV energy loss region. This arises from the inverse relationship of energy and wavelength. The larger the transition energy, the shorter the wavelength and hence the worse the energy resolution. Thus above ~200 eV EELS becomes increasingly advantageous. For example, the "grass-hopper" monochromator shown by Brown [49] is quoted as having a relative bandwidth ($\Delta\lambda/\lambda$) of better than 10^{-3} at 40 Å (i.e. a resolution, $\Delta\lambda$, of 0.04 Å). This corresponds to a FWHM of 0.3 eV for a transition at 310 eV. Recently Shaw et al. [50] have reported the ISEELS spectrum for the C 1s $\rightarrow \pi^*$ transition (287.40 eV) of CO with a resolution of 0.055eV. It should be noted, however, that the same wavelength resolution ($\Delta\lambda$ = 0.04 Å) would be equivalent to 0.03 eV at 100 eV. Perhaps the best example remains the ISEELS N 1s $\rightarrow \pi^*$ transition recorded at 0.075eV resolution [51-53] in which six vibrational levels (centred at 401.10 eV) can be seen (see Fig. 2.5). This structure has not thus far been resolved in any published optical experiment. This spectrum would require a wavelength resolution of 0.006 Å. Figure 1.2 (taken from ref. [6]) shows the equivalent value of $\Delta\lambda$(Å) for fixed EELS resolutions (0.01 eV {state of the art with electron monochromation [50,53]} to 0.5 eV {unmonochromated electron beam from an oxide cathode}) as a function of energy loss. Thus with regard to energy resolution, optical methods are superior below ~200 eV whereas EELS is presently superior above ~200 eV. The resolution criteria is not particularly important above ~1000 eV due to the natural linewidths of the transitions. It becomes advantageous again to use synchrotron

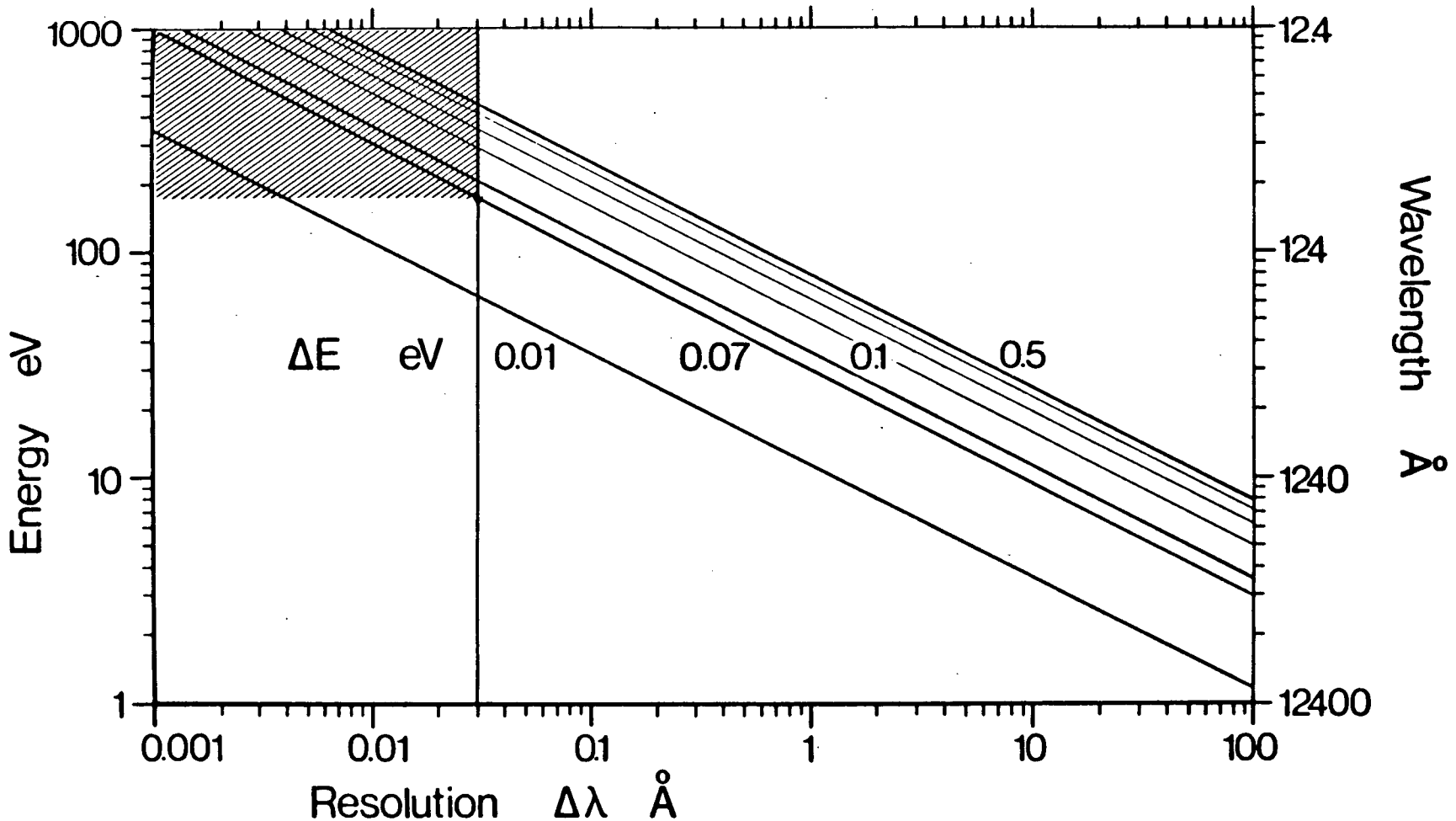

Figure 1.2 Wavelength resolution plotted against excitation energy for fixed values of energy resolution (taken from ref. [6]).

methods, certainly beyond 2.0 - 2.5 keV where optical monochromators are again more efficient. This results from a combination of the high flux capabilities of the synchrotron against the increasing intensity problems experienced with EELS arising from the E_n^{-3} intensity factor (see equation 1.C.17). However, in all optical monochromators the high synchrotron flux is severely attenuated by the low reflectivity of the gratings and mirrors at UV and X-ray energies.

Various problems occur with the utilization of synchrotron radiation and these can often result in additional "spectral features" or incorrect oscillator strengths being observed. These include the possibility of higher energy radiation due to order overlapping, the presence of stray light and contamination of the monochromator mirrors and gratings. This latter problem is particularly serious in the C 1s region since the contamination will arise from carbon deposits formed from the decomposition of diffusion pump oils (for example) and cause a variation in the intensity of the light beam due to absorption. Surface contamination by carbon has even been seen under UHV ($<10^{-9}$ torr) conditions [54]. These same problems do not arise in ISEELS and indeed the true spectral shape (after applying the Bethe-Born correction i.e. E_n^{-3} factor) is obtained. A striking example of incorrect spectral intensity distribution is the valence shell photoabsorption spectrum of N_2 reported by Gürtler et al. [55]. The EELS spectrum, which shows the correct relative intensity, is shown in Fig. 2.4. The difference arises from line saturation effects in the optical work [55] caused by the band width of the light being larger than the

natural line width. Since EELS is a non-resonant process this problem cannot arise in electron impact studies. This aspect has also been discussed by Inokuti [39]. Thus, somewhat ironically, electron impact techniques may provide a more accurate means of obtaining optical oscillator strengths than optical methods! Indeed the experimental method in EELS should be intrinsically more accurate than photoabsorption since the number of electrons which have been scattered is directly measured whereas in photoabsorption a difference is taken between the incident and transmitted light. Methods which use light to excite the sample but use electron yield methods to obtain the "absorption" spectrum [56] avoid the "difference" error, however, they grossly distort the true spectral shape. This arises from secondary processes (Auger or multiple Auger effects) and so more than one electron per photon is produced. The large and variable effect of these secondary processes in the discrete and continuum portions of the inner shell excitation spectra has been clearly demonstrated in dipole coincidence experiments [57-59].

Since the EELS method allows the true spectral shape to be obtained, accurate relative oscillator strengths can be determined. An absolute oscillator strength scale can be obtained either by normalising to a known feature in an absolute intensity optical spectrum or more readily by application of the TRK sum rule (see the previous section). The TRK sum rule normalisation can be applied in a straight forward fashion due to the flat (equal intensity) virtual photon field provided by a fast electron (see above discussion).

A major advantage optical methods have over EELS is the ability to obtain spectra of solids or condensed phases via thin film transmission techniques.

E. Inner Shell Electron Excitation Spectra

In this section the features of inner shell electron excitation spectra originally introduced in section B will be discussed in more detail. They will also be contrasted with their valence shell counterparts. As well as considering the discrete region of the spectrum, features in the continuum spectrum will also be discussed. Since only the dipole transitions will be considered, the following discussion will be appropriate to spectra produced by either optical methods or by fast electron impact in conjunction with small angle scattering.

I. Discrete Portion

In inner shell electron excitation, features in the discrete portion (i.e. below the ionisation limit) can usually be adequately described (semi-quantitatively) in terms of a one-electron picture. In other words, as the promotion of an electron from a core-level to a vacant level (see Fig. 1.1B). Transitions will either be allowed or forbidden on the basis of dipole selection rules. As stated in section B.I, the vacant orbitals are either Rydberg or virtual valence in origin.

The Rydberg orbitals are large, diffuse, atomic-like and extend

well beyond the bounds of the ground state molecule. Thus the details of the molecular structure become less and less important with the Rydberg electron seeing effectively a single charged core [13]. The high lying Rydberg states, which are essentially non-bonding, will therefore be similar in geometry to the ionised state resulting from photoejection of the same electron and hence the respective features in the excitation and ionisation spectra should have a similar spectral shape. The low lying Rydberg orbitals, however, may show some antibonding character due to valence-Rydberg mixing [20,60,61] and thus may exhibit vibrational broadening. As in the atomic case, transitions to molecular Rydberg orbitals will fit a Rydberg series (equation 1.B.1) converging to the ionisation limit. By knowing the term values (i.e. the binding energy of the Rydberg electron), it is possible to estimate the quantum defect (δ_ℓ) which is itself a measure of the deviation from simple hydrogen-like behaviour. The quantum defect is characteristic of the particular ℓ quantum number and reflects the amount of penetration of the particular type of orbital into the core. Since the penetration decreases as s>p>d etc, so does the quantum defect. For second row atoms typical values for s, p and d quantum defects are ~1, 0.6 and 0.1 respectively [12]. However, these values should only be used as a guide and not be applied too strictly. Robin has surveyed many excitation spectra [12] and has estimated empirical limits of 0.7 to 1.3 for s orbitals, 0.5 to 0.7 for p orbitals and -0.2 to 0.2 for d orbitals. On moving to the third row elements, the shielding of the core is not as effective and so the quantum defects of the more penetrating levels

should increase markedly. Typical values suggested for the s, p and d Rydberg levels of the third row are ~2, 1.6 and 0.0 respectively.

Since the transitions studied in the present work are in general governed by dipole selection rules the following transitions: s → s, p → p, d → d and s ↔ d would be formally forbidden in the purely atomic case. However, in the molecule each Rydberg orbital will transform as one of the irreducible representations of the molecular point group and hence one or more of the above transitions may be dipole allowed. Transitions to levels which would be formally dipole forbidden in the atomic case, though, could be expected to exhibit less intensity because of the atomic contribution to the overlap. This has been discussed by Schwarz [60,61] in relation to the 2p absorption spectra of Ar and the iso-electronic third row hydrides. In all cases the 2p → 4p transition, as assigned by Schwarz [60,61] is weaker than the transitions to the 4s and 3d levels.

Thus a combination of the above considerations (i.e. selection rules, term values and intensities) can prove to be most helpful in the interpretation of the Rydberg portion of inner shell excitation spectra.

The virtual valence orbitals arise out of the MO scheme and are usually the antibonding counterparts of the bonding orbitals. Thus they are strongly characteristic of the molecule. Transitions to the virtual valence levels may occur resulting in states which may or may not lie in the discrete region of the excitation spectrum. Transitions to bound virtual states are expected to be relatively strong since the virtual

valence orbitals are delocalised around the molecular framework and have a comparable spatial extent to that of the ground state molecule [13]. These features are also expected to be somewhat broader than those due to Rydberg transitions because of their antibonding nature which can result in a large geometry change in the upper state and hence result in considerable vibrational excitation of the final state.

Depending on the molecule, intense transitions to the virtual valence levels may precede the Rydberg transitions and so have larger term values than those characteristic for Rydberg transitions. For example the 2p ISEELS spectrum of Cl_2 [62] shows two broad transitions to the σ^* level with term values of 9.50 eV from their respective ($2p_{3/2}$ and $2p_{1/2}$) edges. These are well separated from the Rydberg features which are characteristicallay sharp. The term values for the 4s and 3d transitions are 3.56 eV and 1.72 eV giving quantum defects of 2.04 and 0.19 respectively, in good accord with the "expected" values discussed above. The C 1s ISEELS spectra of the methyl halides [63,64] also provide examples where broad features can be ascribed to C 1s $\rightarrow \sigma^*$ transitions preceding the Rydberg transitions. In this case the σ^* orbitals are closer in energy to the lowest Rydberg levels and of the same symmetry. Thus there exists the possibility of Rydberg-valence mixing [20,65]. This is most likely in CH_3F where the features overlap [53,64], however, for the remainder of the molecules the σ^* and ns Rydberg levels (n = 3 for F, 4 for Cl etc) are clearly separated. The term values for the σ^* level vary from 4.65 eV to 5.7 eV while those for the ns level go from 4.05 eV to 3.65 eV for CH_3F through to CH_3I

respectively. In contrast to the methyl halides, methane shows no feature in the discrete portion attributable to a σ^* transition and all the features are ascribed to Rydberg transitions [66,67].

The above examples have all been for systems with σ^* type virtual valence orbitals. Virtual valence orbitals of the π^* type also exist in many molecules. Molecules which contain π-bonds all show strong, low lying features in their electron excitation spectra which can be assigned to transitions to π^* antibonding orbitals. For example, the ISEELS spectrum of C_2H_4 shows an intense C 1s $\rightarrow \pi^*$ transition with a term value of 6.3 eV whereas the spectrum of C_2H_6 only shows Rydberg transitions [68].

The difference between virtual valence and Rydberg orbitals and their extent is really emphasized in molecules in which "inner-well" and "outer-well" states can exist. These "well" states arise from the existence of some sort of potential barrier (see subsequent section) and can lead to the enhancement of "inner-well" (valence) transitions at the expense of transitions to "outer-well" (Rydberg) states. An example is provided by the S 2p spectrum of SF_6 [69,70]. This aspect will be discussed in greater detail in section F. The extent of the Rydberg levels compared to valence levels is also well illustrated by comparing absorption spectra of gaseous and condensed phases [12]. The virtual valence orbitals, being localised around the molecular framework will only be slightly perturbed on going from the gas to a solid state. However, the Rydberg levels will be very much affected and the features in the spectrum will not be visible. Friedrich et al. [65] have used

this method to investigate the valence-Rydberg character of the 2p absorption spectrum of SiH_4 amd PH_3. This technique provides one means of ascertaining Rydberg or valence character in spectra where the features may be overlapped.

II) Continuum Features

In inner shell electron excitation spectra, features can often be seen above the ionisation edge in the continuum. The features can arise from various processes including double excitation, onsets of "shake-up" continua and transitions to quasi-stationary state in the continuum. This final process can give rise to prominent, localised structure(s) which can be observed as much as ~20eV above the ionisation edge and can be described in terms of the out-going electron being trapped in a quasi-stationary state by some form of potential barrier. Such a barrier would isolate the virtual level from the ionisation continua thereby giving the state an increased lifetime. A good example is in the ISEELS [69] or photoabsorption [70] spectrum of the S 2p region in SF_6. This shows two prominent features above the ionisation limit which can be assigned in t_{2g} and e_g σ^* levels or alternatively to t_{2g} and e_g shape-resonances. As this topic is going to be discussed in more detail in section F, no further mention will be made of it here.

Other features in the continuum will result from multi-electron excitation and/or ionisation. Double excitation involves the simultaneous excitation of the core-electron along with a valence electron. In effect it is the ISEELS or photoabsorption analogue of "shake-up" in XPS (see section B.III). These features can be quite prominent and have

been observed, for example, in the inner shell electron excitation spectra of π-bonding systems such as C_2H_4, C_2H_2, C_6H_6 [68], CO [4,45,71] and N_2 [4,71]. Simultaneous excitation and ionisation (ISEELS or photoabsorption analogue of XPS "shake-off") will result in an ion with the same configuration as an XPS "shake-up" state. Thus the (vertical) features appearing in XPS satellite spectra assigned to "shake-up" transitions (i.e. ionisation and excitation) will be manifested in ISEELS/photoabsorption spectra as (adiabatic) onsets of "shake-up" continua.

III) Comparison of Inner Shell Excitation Spectra with Valence Shell Excitation Spectra

Inner shell electron excitation spectra are generally relatively simple to assign due to the energy isolation of the initial core hole which unambiguously defines the initial orbital from which the transition arises. This is in contrast to the much more complex situation that will usually exist in valence shell spectra due to the numerous closely spaced valence orbitals. Thus inner shell spectra can often yield more definite information on the previously unoccupied levels and this in turn can be used to help clarify the assignments in the more complex valence shell spectra.

Obviously there will be differences between the spectra of the two spectral regions (i.e. core and valence) in addition to the overlapping transitions often present in valence electron excitation spectra. First consider the promotion of an electron to a virtual valence orbital. On the promotion of an inner shell electron the final

state will have a localised core hole whereas the promotion of a valence electron will result in a more delocalised valence hole. Therefore the newly promoted electron will see almost a whole extra unit of charge in the inner shell case since the loss of shielding of the nucleus should be greater than that from a delocalised valence hole. Thus the term value (i.e. binding energy) from the inner shell spectrum should be larger than the term value from the valence shell spectrum. In essence one is saying that upon the creation a core hole, the occupied valence levels (including the newly occupied level) will relax more than in the case of the creation of a valence hole. In contrast to the valence orbitals, the Rydberg orbitals are large and diffuse. Therefore a Rydberg electron will see one large core with unit positive charge. It will be less influenced by whether the hole is in the valence shell or at the core. Consequently there will be little increase in term value on going from the valence shell spectrum to the inner shell spectrum for the Rydberg transitions. Wight and Brion [72] have noted differences of upto 0.5 eV only in Rydberg term values whereas differences well in excess of 2 eV can occur with virtual valence levels, as is also clearly seen in the present work. Knowledge of the term values from inner shell spectra will thus provide upper bounds for term values for valence shell spectra and also help identify Rydberg and valence transitions respectively.

Clearly the above discussion assumes that a one electron picture is adequate in both cases to describe the transitions between the levels. While this is probably satisfactory for inner shell excitations

it might not be for valence electron excitations and especially so for valence-valence transitions [13]. A transition from one degenerate level to another level which is also degenerate will result more than one state. For valence-valence transitions the energies may be very different. For instance the first $\pi \rightarrow \pi^*$ transition in benzene, which is $e_{1g} \rightarrow e_{2u}$, results in three state, - $^1B_{2u}$, $^1B_{1u}$ and $^1E_{1u}$ with energies of 4.8, 6.2 and 6.7 eV respectively [13].

F. Potential Barrier and Shape-Resonance Effects.

I) Potential Barriers

For certain molecules an "anomolous" intensity distribution is seen in the discrete and/or continuum region of the inner shell electron excitation spectra. This manifests itself in an enhanced probability of core to valence discrete transitions at the expense of transitions to the Rydberg levels. Furthermore other strong and somewhat broad localised features are often seen <u>above</u> the ionisation edge. These effects were first noted for molecules containing highly electronegative ligands [73]. It was postulated that a strong repulsive force would act on the escaping electron near the electronegative ligands and so an effective (charge) potential barrier would exist in the vicinity of the ligands [73]. The barrier would separate the field into an "inner-well" region and an "outer-well" region.

The effects of such a barrier are well illustrated by the inner shell electron excitation spectra of SF_6 [69,70] which provide, perhaps, the clearest example of such effects. The ISEELS spectra for the

F 1s, S 2s and 2p regions are shown in Fig. 1.3 (taken from ref. [6]). Within a minimal basis set (s and p orbitals) transitions to two virtual valence levels of a_{1g} and t_{1u} symmetries would be expected. Addition of S 3d orbitals would extend these to include two further levels of t_{2g} and e_g symmetry respectively. The S 2p spectrum shows a strong absorption in the discrete region which can be assigned to a transition to the a_{1g} virtual valence level. This is followed by very weak structure assigned to a mixture of overlapping Rydberg transitions and a (dipole forbidden) transition to the t_{1u} level (note that both the F 1s and S 2s spectra show a strong feature corresponding to an allowed transition to this level). Two very prominent features are seen above the edge. These can be ascribed to transitions to the d-like states of t_{2g} and e_g symmetries. It should be noted that the photoabsorption spectrum of the L shell of SF_6 is identical (within experimental error) for both the gas and solid phase [70] thereby providing evidence that the transitions described above are to final state levels within the molecular core i.e. inner-well (valence) states and not Rydberg states.

Thus the effect of the potential barrier is seen to be two-fold. First it can support quasi-stationary states above the ionisation edge which are effectively decoupled from the continuum by the barrier. Secondly, the virtual states within the inner-well will have a strong overlap with the initial state wave-function resulting in spectral features with greatly enhanced intensities. Conversely, the outer-well states (i.e. diffuse Rydberg orbitals), being isolated from the molecular core by the barrier, will have little overlap with the initial state

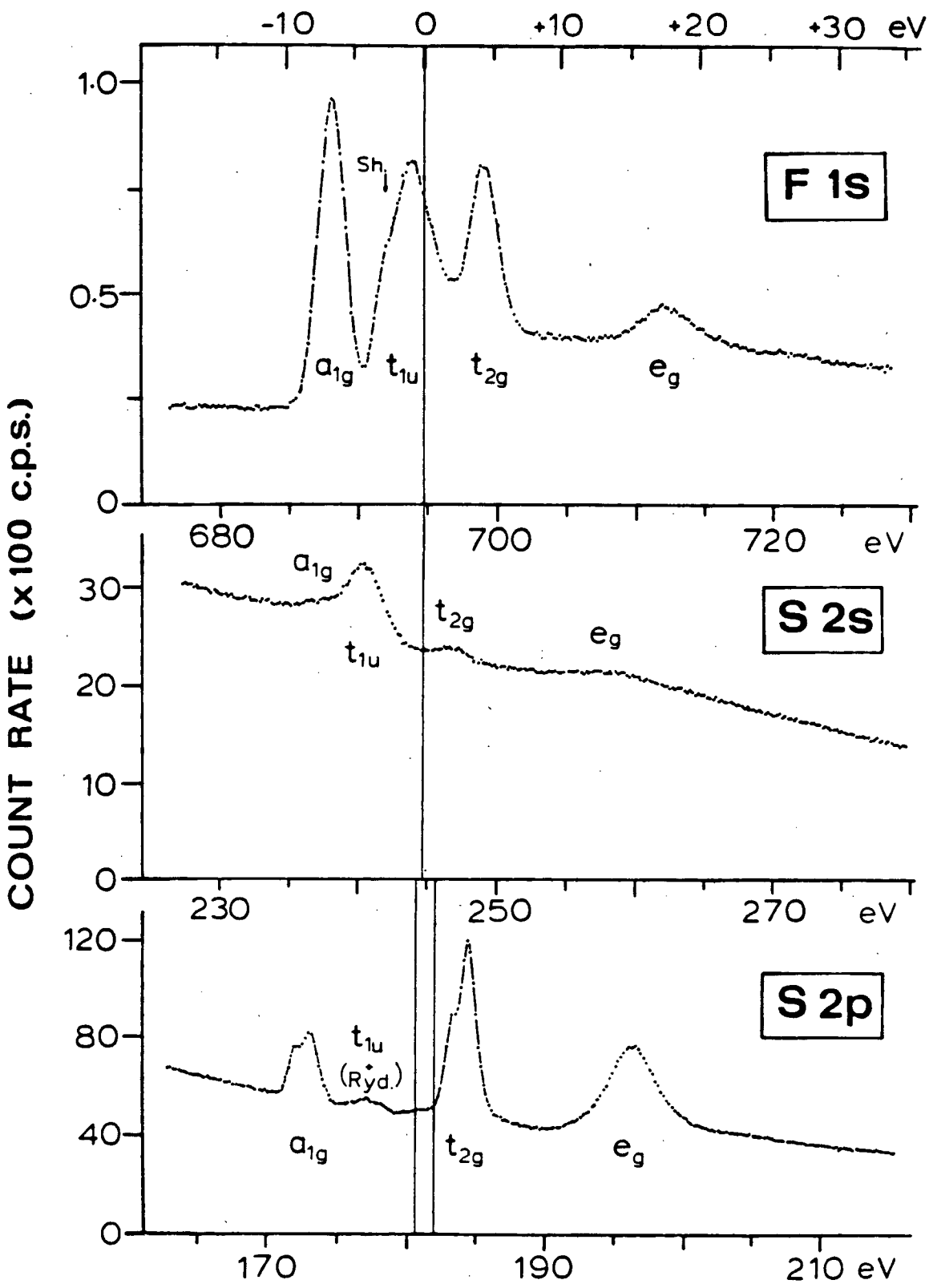

Figure 1.3 Energy loss spectra of SF_6 in the F 1s, S 2s and S 2p excitation regions (taken from ref. [6]).

wave function and this will lead to a drastic reduction in the corresponding transition probabilities.

Features in inner shell electron excitation spectra such as those described above for SF_6 are also present in the spectra of molecules such as N_2 and CO [4,71]. Obviously a barrier formed by a repulsive interaction of the electronegative ligands on the escaping electron (as postulated for SF_6) is not applicable in this case and an alternative model is required. Such a model has been proposed by Dehmer et al. [74-77] involving a shape-resonance description.

II) Shape Resonances

The N 1s ISEELS spectrum of N_2 [4,71] is dominated by a very intense transition at 401.10 eV which has a term value of 8.8 eV with respect to the N 1s ionisation edge (IP = 409.9 eV) and it may be assigned to a $1s \rightarrow \pi^*$ transition. A few, very weak features attributable to Rydberg transitions are also present in the discrete region. At about 9 eV above the edge (i.e. at ~419 eV) a broad relatively intense maximum is seen [4,71]. Thus effects are occurring in the inner shell spectrum of N_2 similar to those observed for SF_6, i.e. enhancement of intensity for transitions to virtual valence levels at the expense of those to the Rydberg levels, and also prominent features in the continuum.

Dehmer and Dill [74,75] have described these observations in terms of a centrifugal barrier which again separates the molecular field into inner-well and outer-well regions. The strong feature at 401.10 eV and the continuum feature are then assigned to shape-resonances caused

by the scattering of the photoelectron (i.e. the excited electron) by the anisotropic molecular field. A shape-resonance is a quasi-stationary state which can be supported in an inner-well potential. The photoelectron (in this case) can be temporarily trapped at a particular resonance energy before tunnelling through the potential (centrifugal) barrier and escaping. Thus a barrier concept is still needed. In this case the barrier is supplied by a competing interaction between the repulsive centrifugal terms ($\sim \ell(\ell+1)/r^2$, where r is measured from the molecular centre) and the attractive coulomb term ($\sim r^{-1}$, where r is measured from outer nucleus) in the total effective potential [77,78]. This balance can result in a centrifugal barrier at the periphery of the molecule. With the correct dimensions this well can support quasi-stationary states which are eigenfunctions of the potential and localised within the molecular core.

Using an X_α multiple scattering approach, Dehmer and Dill [74,75] have calculated the partial cross-sections of the four dipole allowed excitation channels (π_g, π_u, σ_g and σ_u) for the N 1s excitation/ionisation in N_2. On this basis the shape resonances observed at 401.10 eV and 419 eV are assigned to the π_g and σ_u channels respectively. A partial wave expansion of the π_g wave function indicates that it has significant d-wave ($\ell=2$) character while the σ_u channel is seen to have appreciable amounts of p-wave ($\ell=1$) and f-wave ($\ell=3$) character at low kinetic energies (i.e. photoelectron energy above the ionisation energy) [75]. Excitation of the N 1s electron will produce a p-wave which is then scattered by the anisotropic molecular field into the higher ℓ components. These will contribute to the allowed σ and π

ionisation channels thereby making the above transitions possible. The intensity of the transitions can now be explained in terms of resonant trapping of the photoelectron by the appropriate centrifugal barrier.

The intensity of the transition to the π_g state can be attributed to the location of this highly localised state within a centrifugal barrier formed by an ℓ=2 effective potential. Dehmer and Dill [75] have noted that this state is analogous to the π_g shape-resonance observed at ~2.3 eV in e-N_2 scattering experiments [79]. Molecular orbital calculations [80] have shown that the e-N_2 resonance is due to the resonant trapping of an incident d-wave electron which penetrates the ℓ=2 centrifugal barrier and attaches itself to the LUMO (lowest unoccupied molecular orbital) π_g valence orbital. Since a core-hole would exist in the case of inner shell electron excitation the shape-resonance would be shifted to a lower energy and, in this case, appear in the discrete region [81].

The continuum shape-resonance is explained [74,75] by the trapping of the excited electron by an ℓ=3 centrifugal barrier in the σ_u channel. In this case the inner-well potential can support a quasi-stationary state at ~9 eV above the ionisation edge. In other words the partial f-wave (ℓ=3) component of the σ_u wavefunction can overcome its centrifugal barrier and rapidly penetrate the molecular core thereby giving rise to the transition at ~419 eV [74,75].

Thus these resonances are attributed to a high ℓ centrifugal barrier effect. It should be noted that the ℓ=1 component of the σ_u

channel does not show resonant behaviour [82], i.e. the ℓ=1 potential is not sufficient to form an effective barrier. Centrifugal barriers are well known for certain atoms and can lead to prominent features. For example, cerium has a centrifugal barrier for the ℓ=3 effective potential which separates the 4f wavefunction (which is therefore an inner-well state) from the 5f and higher wavefunctions (outer-well states). Thus a strong 3d → 4f transition is seen whereas transitions to the higher f levels are suppressed [11,73]. For lighter atoms (eg. N) the wavefunction for the higher ℓ components are not able to penetrate into the core-region of atoms, however, in the diatomic molecule the added molecular dimension (i.e. making the well wider) allows the potential to support these quasi-stationary states, i.e. it allows penetration of the d- and f-waves into the molecular core. This dimensional aspect is emphasized in that the π_u channel, which acts perpendicular to the molecular axis, has an ℓ=3 component but does not support a resonance [75]. Furthermore, since the ability of a system to support a resonance depends on the dimensions of the anisotropic field, the spectral position of the resonance should provide a sensitive probe of inter-nuclear separation. This aspect will be discussed in more detail later.

Absolute oscillator strength measurements for the K-shell electron excitation and ionisation of N_2 have been made by Kay et al. [71] using ISEELS. An electron impact energy of 8 keV was used to generate the spectrum with the inelastically scattered electrons being samples at zero degree scattering angle. Kay et al. [71] have compared their results with the calculations of Dehmer and Dill [74,75]. Only a semi-quantitative agreement is found between the experiment and the theory. However, all the major features are explained except for those arising from double-excitation processes which are not accounted for in the one-electron scattering model of Dehmer and Dill [74,75]. The calculations overestimate the peak areas of the resonances with the continuum shape-resonance in particular disagreement. The positions are also displaced upwards by ~3 eV in the calculations.

A better agreement is obtained with the techniques employed by Langhoff and co-workers [83-88]. The resonance phenomena is described more in terms of a MO terminology. In this approach, conventional Hartree-Fock calculations utilising gaussian basis sets are performed on the ground state of the molecule. From this calculation a non-local potential for the ionisation channel of interest can be constructed which will be appropriate to describe the motion of the excited electron in the frozen field of the remaining N-1 electrons. The potential has the following form:

$$V_G^{(N-1)} = \sum_{\substack{j=1 \\ (\neq G)}}^{N} (2J_j - K_j) + J_G + K_G \qquad (1.F.1)$$

where J and K are the usual coulomb and exchange operators. The subscript j denotes the doubly-occupied orbitals while G refers to the orbital from which the electron has been excited. This potential, in conjunction with the kinetic energy operator (T) and the nuclear framework potential (V) form the necessary Hamiltonian required to describe the particular excitation channel. Consequently the following one-electron Schrödinger equation

$$((T + V + V_G^{(N-1)}) - \varepsilon)\ \phi_\varepsilon^G = 0 \qquad (1.F.2)$$

can be solved. This results in the so called "improved virtual orbitals" which provide variationally correct approximations for the excited state orbitals within the approximation of a frozen core [84,89]. The bound functions will provide adequate representations of the discrete excitations while the unbound functions provide a pseudo-spectrum of transitions which contains all the necessary physical information to describe the ionisation continuum. Langhoff and co-workers then use Stieltjes-Tchebycheff moment theory [83,88] to convert the pseudo-spectrum into a correct representation of the oscillator strength.

Using this approach, Rescigno and Langhoff [84] have calculated

the partial photoionisation cross-sections for the four accessible dipole-allowed excitation channels in the K-shell electron excitation spectrum of N_2. They assign the discrete shape-resonance at 401.10 eV to a $1\sigma_u \rightarrow 1\pi_g$ core to valence transition. The calculated energy is approximately 4 eV too low and the oscillator strength is overestimated. This is attributed [84] to the neglect of core-relaxation. The transitions to the Rydberg orbitals, which are less sensitive to relaxation effects, agree to within 0.5 eV with experiment. The calculated cross-section for the continuum is in better agreement with experiment than that obtained from the multiple scattering calculation [74,75]. The continuum shape-resonance is ascribed to a $1\sigma_g \rightarrow 3\sigma_u$ core to valence transition. Thus the resonances are both attributed to transitions to virtual valence orbitals which can be equated with the π^* and σ^* anti-bonding orbitals [84]. In this particular case the σ^* orbital is in the continuum.

The MO picture and the scattering model present two complimentary ways of looking at electron excitation and the resonance phenomena. The success of both models in describing the phenomena, at least semi-quantitatively, should not be surprising in that the scattering picture places a localised, quasi-stationary state (resembling a bound state) within the confines of the molecular potential. As such a MO description should also be able to describe the situation. The relationship between the MO calculation and multiple scattering picture for N_2 is further emphasised in that the $1\pi_g$ and $3\sigma_u$ orbitals correlate with the $3d\pi$ and $4f\sigma$ atomic orbitals within the united atom limit [84], consis-

tent with the d-wave and f-wave natures found in the x_α calculation [75].

The above discussion has focussed on N_2. A similar comparison has been made for CO [71,86]. Consideration of other species, such as SF_6 and BF_3 lend support to the parallel interpretation of shape-resonance phenomena using either a MO or multiple scattering perspective. For example, the inner shell excitation spectra of SF_6 have been interpreted with LCAO-MO calculations [90] as have those for BF_3 [91,92]. Multiple scattering calculations have also been performed on the excitation spectra of BF_3 [93] and on the analogous e-SF_6 scattering system [94]. The results of the multiple scattering calculation on BF_3 [93] should be particularly noted with regard to the nature of the trapping mechanism in these molecules. While the angular momenta is found to be large enough ($\ell>2$) in the diatomics to form a centrifugal barrier sufficient to support quasi-stationary states, this is not found in the case of BF_3 [93]. It has been concluded that the barrier in BF_3 results from a combination of centrifugal forces and strong electron repulsion in the neighbourhood of the ligands [93]. Similar conclusion have been suggested for $GeCl_4$ [95]. Regardless of how the potential barrier arises, features associated with shape-resonances can be recognised in many systems, as will be seen in many of molecules studies in the present work. In light of the above discussion these shape-resonances can be often identified with knowledge of the MO scheme of the system.

III) Relationship Between Shape-Resonance Position and Bond Length

As stated earlier, the spectral position of the shape-resonance should provide a probe for inter-nuclear separation. This can be understood in that the barrier, which will define the inner-well potential, is located on the periphery of the molecule and hence reflects the molecular dimensions. If a simplistic "particle in a box" analogy is made, the energies of the stationary states in such a potential should vary with $1/R^2$, where R represents the dimension of the well (i.e. bond length).

A more quantitative way of considering this arises from a multiple scattering treatment. Gustafsson and Levinson [96] have pointed out that within a multiple scattering picture, the wave vector of the photoelectron on resonance (k_r) should be inversely proportional to the distance (R) between the scattering centres, i.e.

$$k_r R = \text{constant} \qquad (1.F.3)$$

Thus if the phase-factors can be neglected, it then follows that the kinetic energy of the photoelectron on resonance should be proportional to $1/R^2$. Gustafsson and Levinson [96] have plotted the difference of resonance energy from threshold (δ) against $1/R^2$ for several diatomics and have obtained a reasonable correlation.

Recently, Natoli [97] has demonstrated theoretically, within a complete multiple scattering picture, that for certain conditions equation (1.F.3) is valid. More specifically, the wave vector (k_r) is given by [97,98]

$$k_r = \sqrt{(\delta - V_o)} \qquad (1.F.4)$$

where V_o is a mean intramolecular potential relative to the vacuum level [98,99] and the constant depends on atomic phase shifts [97-99]. The phase shifts are energy dependent, however, Bianconi et al. [98] have pointed out that if the phase-shift dependence with energy is smooth then (1.F.3) is valid. Bianconi et al. [98] suggest that this should generally be the case for the energy regions where the continuum σ^* shape-resonances are located though not for π^* resonances [97-99].

The term V_o is particular to the system under investigation - bond order as well as atomic pair [98-100]. Thus Hitchcock et al. [100] have simply investigated the relationship of resonance position and bond length empirically. They have shown [100] that for a series of hydrocarbons a simple linear relationship of the type

$$\delta = aR + b \qquad (1.F.5)$$

is adequate to relate the known C-C distance to the σ^* shape-resonance position. Sette et al. [99] have also applied this linear relationship (1.F.5) to investigate σ^* shape-resonance positions and bond lengths in a large variety of molecules. Good linear correlations are seen for classes of molecules characterised by the sum of the atomic numbers of

the atom pair involved in the scattering process the Z dependence arises in the V_o term. As Z increases the attractive part of the potential will increase and this results in the different linear dependence observed for shape-resonance position with bond length for each set [78,99]. The findings of Sette et al. [99] also indicate that the phase-shift dependence can be assumed constant, at least for Z = 12 - 18, for the σ^* resonances.

From the above discussion it is seen that a convincing argument for shape-resonance position and bond lengths can be made. This allows a further means of positively identifying shape-resonance features in the continuum in a series of related molecules. Indeed with careful considerations of the limitations it should be possible to reverse the procedure to obtain bond lengths [98-100].

CHAPTER 2

EXPERIMENTAL

In this chapter the experimental methods used to obtain the electron energy loss spectra presented in this work will be described. During the course of this work, a digital voltmeter (DVM) of high stated accuracy (Datron model 1071 [101]) was obtained. This permitted measurement of a set of accurate reference energies for inner shell electron excitation spectroscopy. This latter work is also presented in this chapter.

A. Experimental Methods

I) The Spectrometer

An existing high resolution ISEELS spectrometer [6,63] was used for all the electron energy loss measurements reported in the present work with the exception of the valence shell spectra of NF_3 and $Si(CH_3)_4$ (see later in this section). The construction and operation of this instrument has already been described in detail and so only a brief description is presented here. For a full description the reader is referred to the Ph.D. thesis of A.P. Hitchcock [6] or the description given in ref. [63].

A schematic of the spectrometer (taken from ref. [6]) is shown in Fig. 2.1. Electrons produced in the gun region (G) by a heated thoriated tungsten ribbon or wire are accelerated to the desired impact energy (typically 2.5 keV) to form a focussed electron beam. The beam

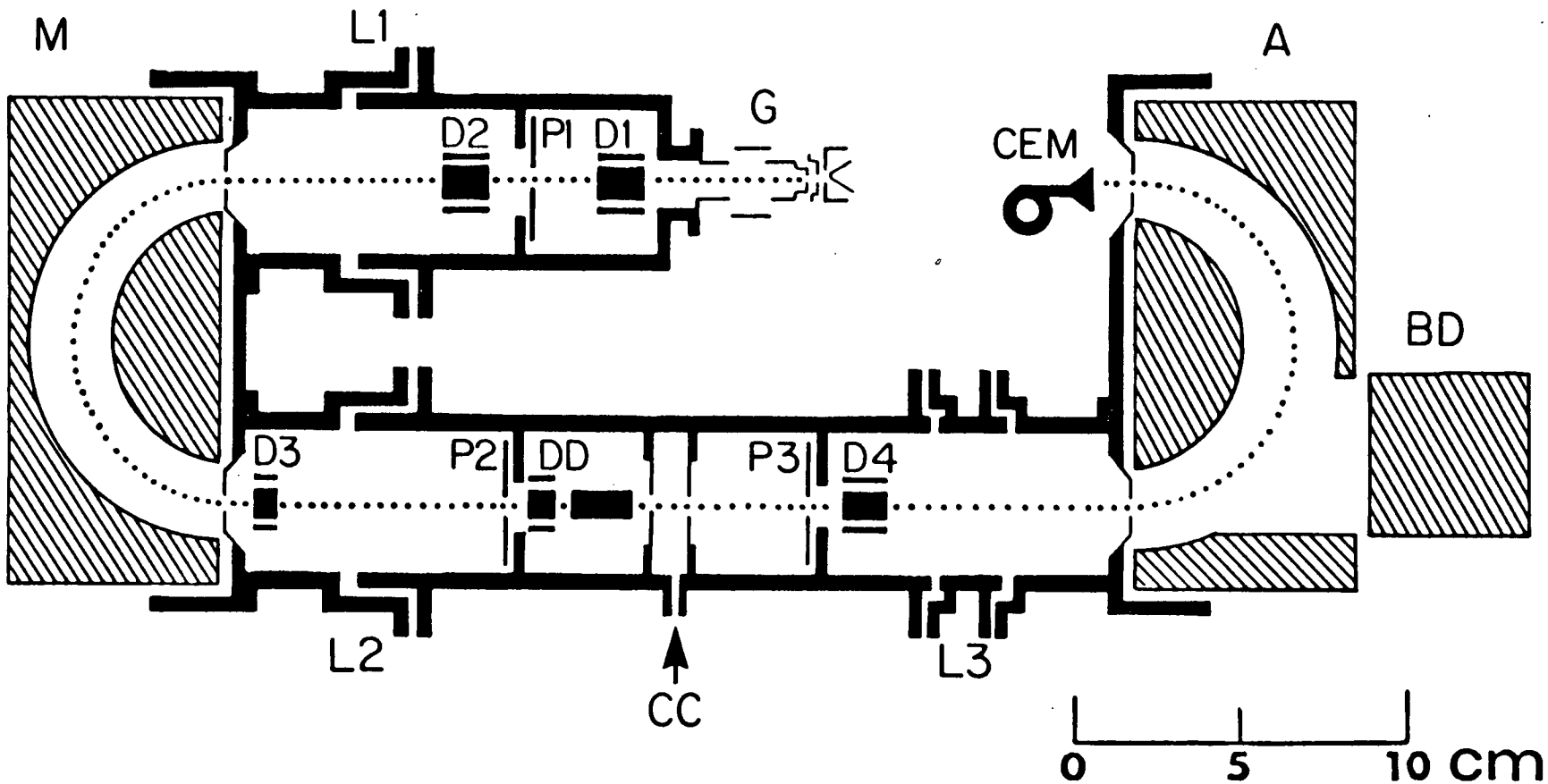

Figure 2.1 Schematic of the Inner Shell Electron Energy Loss Spectrometer (taken from ref. [6]).

is then retarded by a two-element lens (L1) to the required pass-energy of a hemispherical electrostatic analyser which acts as the monochromator (M). Following this the beam is accelerated back to the impact energy by a second two-element lens (L2) to pass through the interaction region (CC) after which it is retarded to the selected pass-energy of a second electrostatic analyser (A) by a three-element lens (L3) and transmitted to the detector (CEM). Various deflection plates (D1-D4) allow minor corrections to the beam path to be made. The beam can be monitored throughout the spectrometer by measuring the current on various apertures (P1-P3) with an electrometer.

Initially the instrument is set up on the primary unscattered beam (zero energy loss) at zero degree scattering angle. This is done by carefully adjusting the deflector plate voltages and monitoring the beam current on plates P1 to P3. The current is maximised and then minimised on each plate in turn and then finally maximised on the detector cone which, in this case, acts as a Faraday cup. The middle element of the three-element lens is set at the voltage which maximises the transmission of the scattered current for the energy loss region about to be studied. Figure 2.2 shows a plot of the experimentally determined optimum focus voltages (with respect to ground) for the middle element of L3 as a function of energy loss for different analyser pass energies at 2.5 keV impact energy. Figure 2.3 shows the focus voltage as a function of analyser pass energy for the energy loss appropriate to the C 1s region (~ 290 eV), the N 1s region (~ 400 eV) and the O 1s region (~ 540 eV).

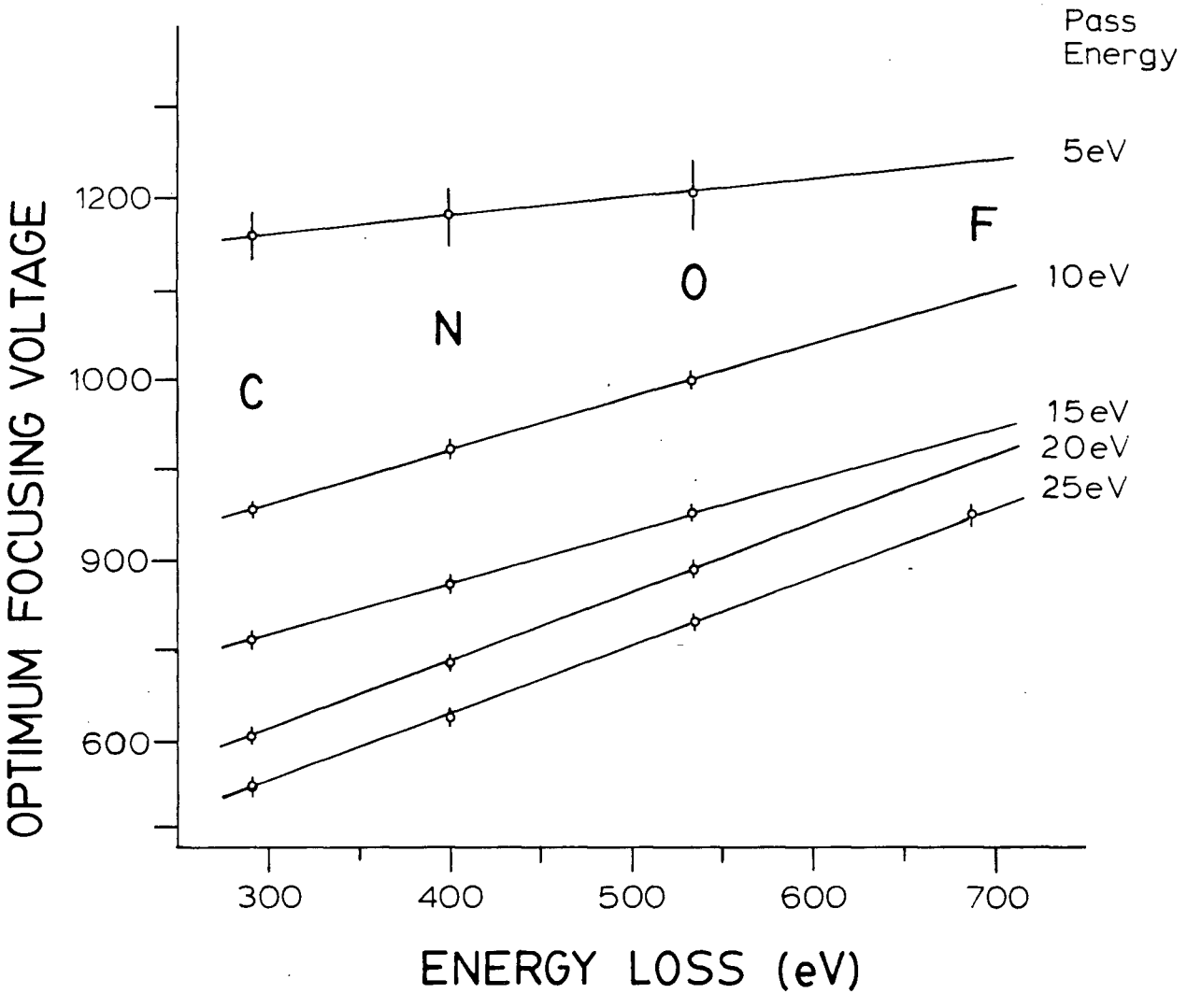

Figure 2.2 Optimum focussing voltages for the middle element of the three-element lens (L3) (see Figure 2.1) as a function of energy loss for different analyser pass energies at 2.5 keV incident energy.

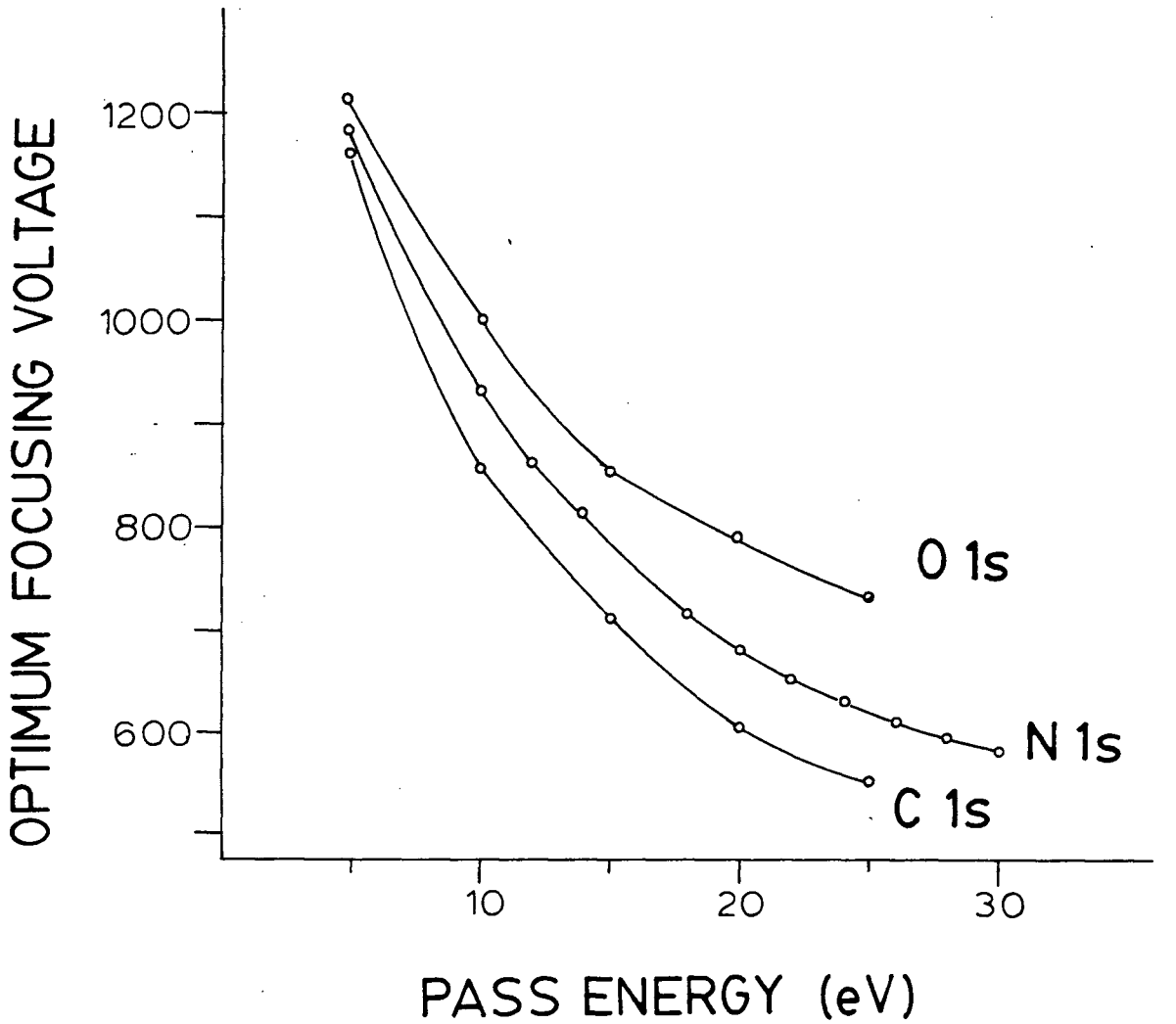

Figure 2.3 Optimum focussing voltages for the middle element of the three-element lens (L3) (see Figure 2.1) as a function of analyser pass energy for selected energy losses at 2.5 keV incident energy.

The resolution of the spectrometer depends on the pass energies of the two analysers. The theoretical resolution of this spectrometer is given by [6]

$$\Delta E_{FWHM} = 0.01 \sqrt{V_M^2 + V_A^2} \qquad (2.A.1)$$

where V_M and V_A are the monochromator and analyser pass energies respectively. The actual resolution can be obtained by measuring the profile of the primary beam.

When running a sample, part of the primary beam is scattered elastically or inelastically by the gas in the interaction region. To obtain a spectrum a voltage, equivalent to the energy loss corresponding to the inelastic scattering, is added on top of the small voltage already applied to the complete analyser system. Thus the scattered electrons can regain their energy loss and be transmitted through the analyser. By using a suitable offset voltage and scanning the energy loss region of interest a full spectrum can be obtained.

A high count rate is attainable with valence shell electron energy loss spectroscopy and so the spectra can be measured at zero degree scattering angle. However, it is not possible to obtain inner shell spectra at zero degree scattering angle on this spectrometer due to the relatively low count rate relative to the small but not insignificant background produced by the backscattering of the intense main beam on the analyser surface. To avoid this, the main beam is passed

through the centre of the gas cell at a small angle by use of a "double-deflection" system (DD). This system consists of two sets of deflecting plates, operating in the energy dispersing planes of the analysers, whose fields act in opposite direction. The plates in the second set are twice the length of the plates in the first set and are placed equidistant from the first set of plates and the centre of the gas cell. The fields are generated by a single voltage source. Thus the beam is deflected by the first set of plates in one direction through angle θ and then deflected back in the opposite direction by the second set of plates through angle 2θ. The net result is that the beam passes through the centre of the gas, where the concentration of gas is the greatest, at an angle θ. Table 2.1 shows the deflection angle (θ) obtained at incident beam energies of 1.5 keV and 2.5 keV for various voltages applied to the "double-deflection" system. Typical operating conditions employed in the present work are 2.5 keV impact energy and a scattering angle of $\sim 1°$. This angle, while small enough to ensure dipole-dominated spectra, allows interception of the main beam by plate P3 before it can reach the analyser. During the set-up procedure and for valence-shell spectra the long plates are grounded out and the short plates (along with their perpendicular counterparts) act in the same manner as the other (x,y) deflector plates.

II) Sample-Handling

A second sample inlet system, completely constructed of stainless steel, was added to the original brass inlet system [6] which was

TABLE 2.1: Deflection angle (θ) for various voltages (V_y) applied to the double-deflection system for impact energies (E_o) of 1.5 keV and 2.5 keV†

Voltage across plates (V_y)	Deflection angle (θ) for impact energies (E_o)	
	1.5 keV	2.5 keV
52	0.90	0.54
106	1.84	1.10
161	2.79	1.68
218	3.78	2.27
277	4.80	2.88

† Deflection angle given by

$$\theta = \tan^{-1} \frac{V_y \cdot x}{2E_o \cdot y}$$

where x = 1.0 cm, length of short plate
y = 1.1 cm, gap between parallel plates

(see any introductory physics text eg. F.W. Sears, M.W. Zemansky and H.D. Young, "University Physics", Addison Wesley (1980) p. 450-451).

retained for the reference gas line. The gas pressure in the new system was controlled by means of a Granville-Phillips series 203 leak valve while that from the reference system was controlled with a Varian leak valve (model 951-5100). The two lines (sample and reference) were connected on the low pressure side of the leak valves prior to being fed into the gas cell. The ambient pressure of the spectrometer, which was monitored by an ionisation gauge, was allowed to rise from a base pressure of 4×10^{-7} torr to 5×10^{-5} torr on sample introduction. Under these conditions only single scattering processes are observed [102].

All the samples were obtained commercially and were of high stated purity. The gas samples were taken directly from the cylinder using the appropriate regulator and all the connections made to the inlet system with 1/4" tubing (copper or stainless steel) and "swagelock" fittings. Liquid samples were transferred from their container to an evacuated glass vial equipped with a teflon valve to which was also attached a short piece of 1/4" diameter glass tubing thereby allowing the sample to be connected directly to the "swagelock" fittings of the inlet system by using teflon ferrules. The liquid samples were degassed by repeated freeze-thaw cycles. Valence-shell spectra were run to check that the samples were free of any obvious volatile impurities and also to ensure that the system was airtight, the latter being an especially important consideration for inner shell spectra in the N and O K-shell regions. A leak could easily be detected by observing the intense N_2 ($X \rightarrow b\,^1\Pi_u$) valence shell feature at 12.93 eV [103]. From its valence-shell spectrum, the sample of PCl_3 was seen

to contain a small amount of HCl impurity which was removed by continuous pumping on the sample cooled down with a dry-ice/methanol mixture. A similar process was also performed with $OPCl_3$ as a precautionary measure, even though no HCl was apparent in the spectrum. No further purification was performed on any of the samples since the spectra indicated that they were essentially free of impurities.

III) Spectral Acquisition, Calibration and Spectrometer Performance

The spectra were obtained in the following manner. The gaseous sample (or sample plus calibrant) was fed into the spectrometer which was set up in the manner described above for the required spectral resolution. It was always necessary to retune the spectrometer upon sample introduction. In practice, it was found that the actual resolution was very close to the theoretical resolution (see equation (2.A.1)) for pass energies $\geq$ 5 eV, however, for high resolution valence shell studies the resolution was best obtained by measuring the He(I) resonance line at 21.218 eV [104]. The spectral region of interest was selected by adding a voltage, corresponding to the required initial energy, on top of the voltage already applied to the analyser system. The region was then successively scanned by voltage programming a power supply (Kepco PX100) which was in series with the energy-loss/analyser power supply (Fluke 410B), using the ramp output from the multichannel analyser (Fabritek 1064). However, for the continuous wide range scan shown in Chapter 4, the ramp voltage was monitored by a Digitec voltmeter and its mechanical readout was connected to the shaft of a potentiometer which

could resistance programme the energy-loss/analyser power supply (see ref. [6] for full details). The voltage applied to the analyser system was measured in the majority of cases with the Datron 1071 DVM, however, for a few of the spectra a Data Precision 3500 DVM was also used.

The pulses from the detector (channeltron) were processed by standard pre-amp/amplifier/discriminator units and the output signal was stored in the multichannel analyser. The signal could also be monitored via a ratemeter. The channel address advances synchronously with the ramp voltage output and so a complete spectrum can be signal averaged. The spectral range was determined by channel step size and the number of points. Any number up to 1000 points could be selected with the aid of a program control unit (Ortec 4610). Spectral acquisition time depended on the number of points, resolution and the energy region studied (due to the E^{-3} drop-off (see equation (1.C.17)). A low resolution (0.35 eV) inner shell spectrum typically took between 6 - 12 hours for the long range spectra in the 100 ~ 350 eV energy loss regions while those for higher energy losses (N 1s, O 1s and F 1s) required collection times between 24 and 48 hours. Acquisition times for the high resolution inner-shell spectra varied between 12 and 48 hours whereas high resolution valence shell spectra could be obtained in a matter of minutes though the spectra were typically run for 1 to 2 hours to optimise the signal/noise ratio.

The data, once obtained, was plotted on a X-Y point plotter (Hewlett Packard 7004B). All measurements were taken from this plot. For data manipulation (background subtraction, scale expansion etc.) the

data was transferred to files on the UBC computer by use of a digitiser.

In principle, once the spectrometer is set-up on the primary beam for zero energy loss, all that is required to put a spectrum on an absolute scale is an accurate reading of the voltage added onto the analyser system (see next section). However, since the spectrometer was set-up using the cone as a Faraday cup and observing the (analogue) current on an electrometer whereas the spectra were run in a pulse count mode, in practice, the spectra obtained in this work were put on absolute scales by comparison with a known feature run under the same operating conditions. The process involved calibrating a feature in the sample spectrum by using an external reference and then using the newly established standard to internally calibrate the rest of the sample spectral features in other energy ranges. To ensure the same operating conditions when using an external reference, reference and sample were run as a mixture. The reference was chosen so that its spectral features and those of the sample did not overlap. The calibrating feature (external or internal) was run both before and after the feature being calibrated to ensure that there was no voltage drift. This procedure was repeated several times. Since the count-rate drops approximately as the inverse-cube of the energy loss, the middle element of the three element lens (L3) was set for the feature with the largest energy loss so as to maximise its count rate. Specific calibration details for the inner shell spectra are presented in the appropriate chapters. The valence shell spectra were all calibrated against the He(I) resonance line (21.218 eV

[104]) except for PCl_3 in which case the HCl impurity was used to calibrate the spectrum before it was pumped away.

Most of the compounds presented in this work quickly degraded the high resolution performance capabilities of the spectrometer. The spectrometer consists of only one chamber pumped by a single diffusion pump with no differential pumping systems to isolate the gas cell from the rest of the spectrometer or the electron gun. Reaction of reactive gases with the gun filament produced a considerable amount of contamination which affected the characteristics of the electron beam and thus frequent cleaning of the spectrometer was necessary to bring it back to optimum performance. The effectiveness of this can be seen in the valence shell and inner shell spectra of N_2 which illustrate the capabilities of the spectrometer. Figure 2.4 shows the N_2 ($X \rightarrow b^1\Pi_u$) valence-valence transiton obtained with a spectral resolution of 0.017 eV which compares very favourably with the spectrum obtained at slightly higher resolution by Geiger et al. [103b]. This feature provides a stringent test for the capabilities of the spectrometer as does the N_2 ($1s \rightarrow \pi^*$) core-valence transition shown in the next section (Fig. 2.5).

IV) Other Measurements

The valence shell spectra of NF_3 and $Si(CH_3)_4$ presented in this work were obtained by Dr. Suzannah Daviel on a new ISEELS spectrometer which has recently come into operation in this laboratory. This new instrument [53], though similar in principle to the ISEELS spectrometer used in the present work employs a number of significant new features including

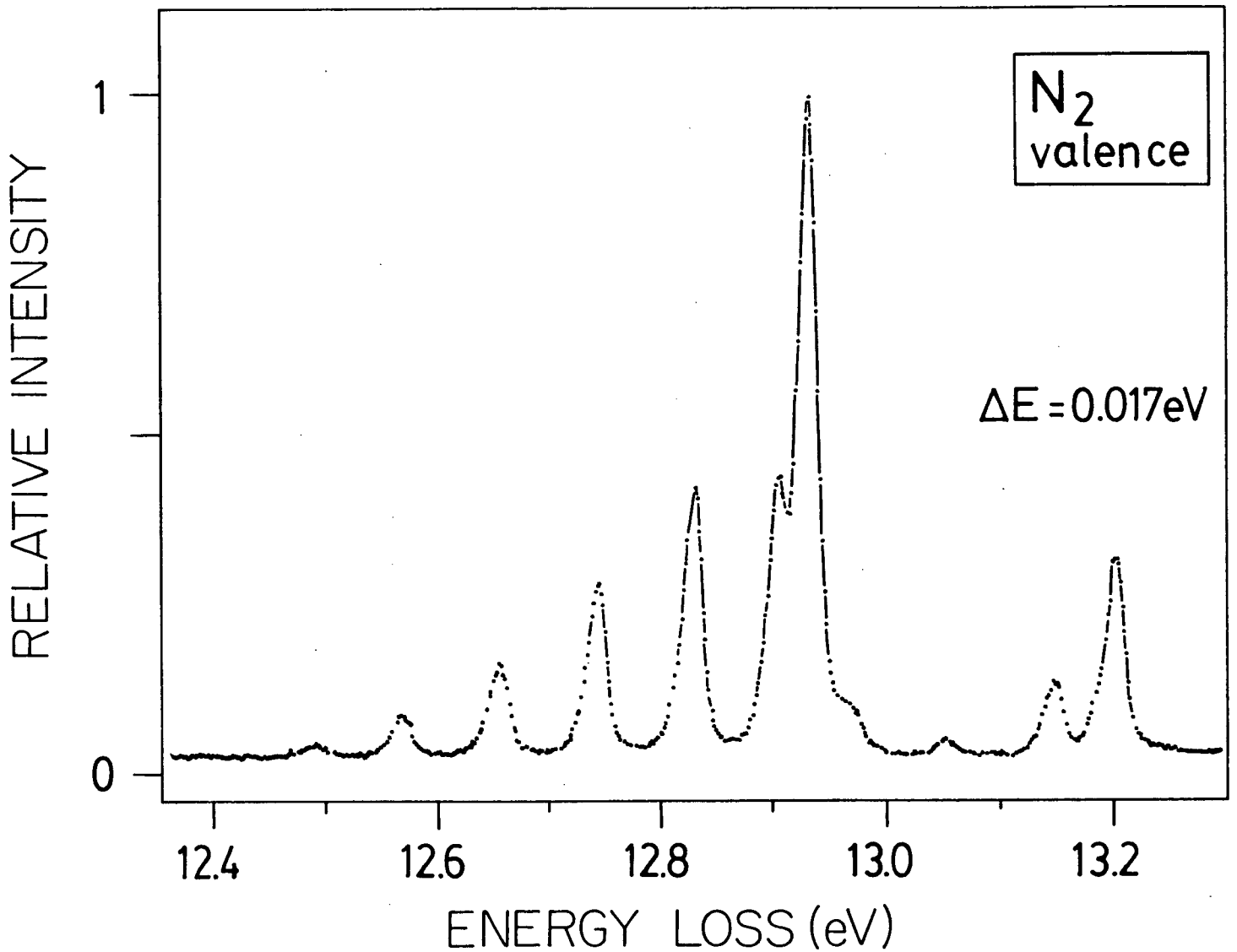

Figure 2.4 High resolution electron energy loss spectrum of N_2 in the region of the $X \rightarrow b^1\Pi_u$ transition.

1) separate differential pumping of the gun, monochromator, interaction and analyser regions

2) large radius (20 cm) hemispherical analysers and

3) carefully designed and highly efficient electron optics. These features have produced significant improvements in resolution, intensity and stability as well as permitting a background free operation at $\theta = 0°$. This latter point is not only significant for inner shell spectra but also for valence shell spectra as it sometimes proved very difficult to tune out "ghosting" effects produced by the back scattering of the main beam in valence shell spectra obtained on the old instrument (see Chapter 7). A full description of the construction and performance of the new instrument is given in ref. [53].

The XPS "shake-up" spectra of NF_3 presented and discussed in Chapter 3 were recorded several years ago by the author on a MacPherson ESCA 36 photoelectron spectrometer situated at the University of Alberta. The experimental details are given in Chapter 3.

B. Reference Energies for Inner Shell Electron Energy Loss Spectroscopy

Spectral measurements of atomic and molecular energy levels generally rely on sufficiently accurately known reference values against which measurements can be calibrated and in this regard ISEELS is no exception. In this section a set of reference energies determined by ISEELS for the energy range 100 - 1000 eV are presented. It should be

noted that electron energy loss spectroscopy (EELS) provides an excellent direct means of measuring the energies of inner shell transitions since, due to the inherent nature of the technique itself, it only involves the direct measurement of a voltage or a voltage difference. This is in contrast to optical methods which are indirect since they rely on a grating equation which is liable to lead to greater energy errors at shorter wavelengths (higher energies). This is well illustrated in the case of the chlorine L-shell excitation spectrum of HCl where two sets of independent ISEELS measurements have recently conclusively shown [105,106] that the energy scales of existing optical absorption spectra are in error by ~ 0.5 eV.

A major source of error in determining higher energy levels in electron spectroscopy particularly EELS is the often limited accuracy of commonly available digital voltmeters (DVM). For example, if a DVM of only 4-1/2 digit capability was used to measure a voltage, up to say 1000 eV, the reading alone could only be determined to ±0.1 eV. With a typical manufacturer's quoted accuracy of ±0.1% the reading at 1000 eV would be no more accurate than ±1 volt! As a result even though somewhat more accurate DVM's are usually used many published excited state and ionisation energies maybe of somewhat limited accuracy. An examination of the literature reveals inconsistencies in some published values particularly in XPS measurements. However, Lee [107] has shown that in the case of XPS non linearities in spectrometer energy response are the principal determining factor. However, in ISEELS spectrometers run at constant pass energies the considerations are different and DVM

accuracy can be a major factor.

In order to make sufficiently accurate measurements, up to 1000 eV, at least 6-1/2 digit capability is desirable with an accuracy of at least ±0.001% or ±0.01 eV. Such instruments are not routinely employed on most electron spectrometers. If highly accurate calibration values are available then new inner shell spectra may be put on accurate energy scales by measuring with reference to these calibrated levels using mixed sample gases. Provided that the calibrant is close by in energy then a DVM of lower accuracy than that used for the original calibration determination will suffice to obtain a sufficiently accurate energy scale. It is the purpose of the work presented in this section to provide such a range of reference calibration values for this purpose. Of the relatively few commercially available DVM which come near to the specifications needed a DATRON model 1071 DVM was selected and the values reported here were measured with this instrument. The DATRON [101] model 1071 6-1/2 digit DVM has a stated accuracy of ±0.001% (90 day) or ±0.002% (1 year) in normal operation. In addition an averaging mode is selectable which yields 7-1/2 digit capability and then the accuracy is claimed to be further increased by a factor of two. The DVM also features auto-recalibration via a built-in microprocessor which compensates for short-term aging. The measurements in the present work were completed within 90 days of a certified factory calibration to the above specifications.

The energy losses corresponding to several known inner shell electronic transitions have been redetermined using the ISEELS spectro-

meter described in the previous section in conjunction with the DATRON model 1071 DVM. Each of the transitions was measured at several different energy resolutions to check for any change in peak envelope or position. This is an effective test since change of resolutiom changes the pass energy of the analyser and the voltages on the three-element lens in the energy loss part of the spectrometer. The fact that peak energies are independent of resolution (Table 2.3) shows that any changes in trajectory in the analyser do not affect the energy scale within the stated uncertainties.

In choosing suitable transitions the following requirements were considered.

(1) Possession of a sufficiently intense, sharp and distinct feature in the energy region of interest. The sharpness of spectral lines is increasingly limited by natural width considerations as the atomic number increases.

(2) Ready availability of the calibrating atom or molecule.

(3) Ease of sample handling and introduction.

(4) Inertness of the substance with respect to decomposition on the hot cathode or on the spectrometer and inlet surfaces.

(5) A range of suitably spaced transitions to span the 100 - 1000 eV region.

It should be noted that in EELS the intensity in a spectrum varies approximately as the inverse cube of the energy loss (see equation 1.C.17) and hence transitions at higher energy losses have an intrinsically lower count rate. This and the fact that higher resolu-

tion is obtained at the expense of decreased count rate means that a compromise between count rate and resolution must often be made. However, for ISEELS a sacrifice in count rate to obtain high resolution is often unnecessary and indeed undesirable since the transitions at higher energy losses are significantly broadened by lifetime considerations ($\Delta E \cdot \Delta t = 7 \times 10^{-16}$ eV sec). Thus nothing is gained in such cases by taking the spectra at unnecessarily high resolution.

Once the sample has been introduced and the spectrometer set up for zero energy loss all that is required for determining the energy scale is a sufficiently accurate reading of the applied voltage to the electron analyser system. In order to ensure that the spectrometer was accurately set up for zero-energy loss the elastically scattered peak was measured in the case of the highest resolution (0.070 eV FWHM). It is possible to do this because the primary unscattered beam does not enter the analyser system. However, at lower resolutions the signal at the channeltron for normal operating conditions was too large to allow direct measurement of the elastic peak and so under these conditions the value obtained for the CO(C 1s $\rightarrow \pi^*(v=0)$) transition by direct measurement at high resolution was used as an alternative reference point. In these measurements CO was introduced simultaneously with the other sample gas. Alternatively, a well known lower energy valence or core transition in the sample itself was used as an internal calibrant. As can be seen from Table 2.3 (see below) the measured transition energy is independent, within experimental error, of the resolution, and whether an elastic or an inelastic reference was used. Thus over the range of

energy resolutions used, which corresponds to normal operations, it can be concluded that energies are independent of any instrumental response function.

Figure 2.5 shows the vibrationally resolved N_2 (N 1s $\rightarrow \pi^*$) transition measured at high resolution. The spectral features are in excellent agreement with earlier published works by Hitchcock and Brion [52] and also by King et al. [51]. This transition provides a very stringent test of the performance of the spectrometer as well as being a most useful calibration point in the median of the energy range up to 1000 eV. Nitrogen K shell excited states have a sufficiently long lifetime that the natural line width ($\sim$ 0.1 eV, see ref. [51] and [52]) merits the use of high resolution and the energy values obtained in this study as well as those from earlier work [51,52] are listed in Table 2.2. The resolution achieved here is comparable to that in the earlier work while the signal to background ratio is somewhat superior. The presently obtained values are seen to be in excellent agreement with those reported by King et al. [51] which were also obtained using a highly accurate voltage measuring system. The present values are consistently higher than the earlier values reported on the same instrument by Hitchcock and Brion [52]. This, as noted below, is due to the limited accuracy of the less sophisticated DVM used in the earlier work.

Carbon monoxide is a very suitable secondary standard since, the C 1s $\rightarrow \pi^*$ transition is dominated by the v=0 transiton [50,52]. Thus there is no reason to expect any significant shift in the energy of the

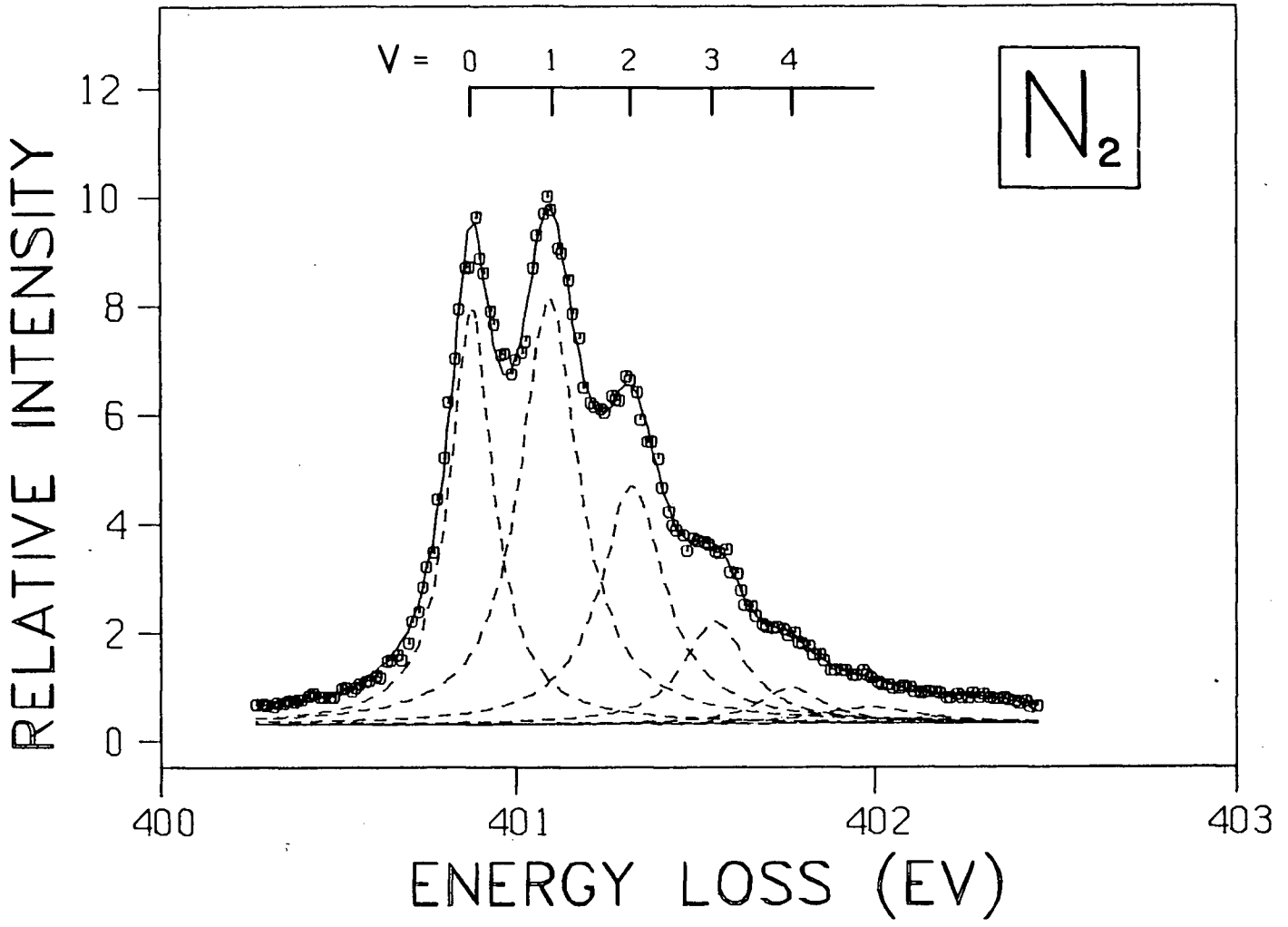

Figure 2.5 High resolution electron energy loss spectrum of N_2 in the region of N 1s → π^* excitation. The solid line through the data points represents the sum of six Lorentzian line shapes.

TABLE 2.2: Transition Energies (eV) in the high resolution N_2 (N 1s $\rightarrow \pi^*$) electron energy loss spectrum

Final State Vibrational Level	Transition energy (eV)†		
	This Work	Hitchcock et al[a]	King et al[b]
0	400.88(2)	400.70(5)	400.86(3)
1	401.10(2)	400.93(1)	401.09(1)
2	401.33(2)	401.16(1)	401.31(1)
3	401.56(5)	401.39(1)	401.54(1)
4	401.77(7)	401.60(2)	401.76(1)
5	401.98(10)	401.82(3)	401.98(2)
6	-	-	401.19(2)

a - reference [52]

b - reference [51]

† - In the present work all estimated errors are absolute whereas the errors for v=1 and above in references [51] and [52] are relative to the energy for the v=0 peak.

peak position with changes in resolution. The peak value for the v=0 transition has been found to be 287.40(2) eV regardless of the resolution used. This was established by running a mixture of He and CO with the He(I) transition (21.218 eV) [104] being used to set the absolute energy scale. The value obtained for the CO(C 1s $\rightarrow \pi^*$(v=0)) transition at both high and low resolutions was found to be the same within experimental error.

Measurements have been made for selected transitions in a series of atoms and molecules whose spectroscopy had previously been studied using ISEELS. Spectral features observed were in all cases identical to those observed in the earlier reported studies of SF_6 [69], Ar [108], CO [50,52], N_2 [51,52] and Ne [109]. Table 2.3 summarises the data obtained for the selected transitions at various energy resolutions. It might be expected that only the SF_6 (S $2p_{1/2} \rightarrow t_{2g}$) and N_2 (1s $\rightarrow \sigma^*$(v=1)) positions would vary with resolution as these alone posses sufficiently intense and resolvable neighbouring transitions (in the case of N_2, the other vibrational components and for SF_6, the S $2p_{3/2}$ spin-orbit component). In fact the separation of the spin-orbit components in SF_6 is large enough that the measured position of the (S $2p_{1/2} \rightarrow t_{2g}$) peak maximum does not vary within experimental error over the range of resolutions employed. For N_2 the curve fitting in Figure 2.5 shows that there is no significant shift of peak maxima for v=0, 1 or 2 at high resolution due to overlap from neighbouring peaks. The small possible shift in peak maximum observed with decrease in resolution (see

TABLE 2.3: Measured energy levels of the reference lines as a function of resolution

Inner-shell Transition	Energy loss (eV) at quoted resolutions (eV) transition[a]				
	0.070[b]	0.105	0.140	0.210	0.350
SF_6 $S2p_{1/2} \rightarrow t_{2g}$	-	184.54(5)	-	-	184.51(5)
Ar $2p_{3/2} \rightarrow 4s$	-	244.37(2)[c]	-	-	-
CO C $1s \rightarrow \pi^*(v=0)$	287.40(2)	-	287.40(2)[d]	-	-
N_2 $1s \rightarrow \pi^*(v=1)$	401.10(2)	-	401.10(4)	401.08(4)	401.05(5)
CO O $1s \rightarrow \pi^*$	534.21(9)	-	534.19(10)	534.20(10)	534.12(10)
SF_6 F $1s \rightarrow a_{1g}$	-	-	-	-	688.27(15)[e]
Ne $1s \rightarrow 3p$	-	-	-	-	867.13(8)

a All values quoted with the energy loss scale established from the CO(C $1s \rightarrow \pi^*(v=0)$) transition except where indicated otherwise. The gases were run as mixtures.

b Zero-energy loss determined from the elastic peak.

c Internal calibration against Ar(I) (11,828(5) eV) - reference [104].

d Measured with respect to He(1) (21.218(1) eV) - reference [104].

e Internally calibrated against SF_6 ($S2p_{1/2} \rightarrow t_{2g}$).

Table 2.3) is consistent with the shape of the intensity distribution in the broad vibrational envelope. However it can be seen that the values quoted for each of the various transitions at the differing resolutions are the same within experimental error. Thus it is possible, with the selected transitions, to use the calibration values for the peak positions in a given spectrum independent of resolution (at least below ~ 0.35 eV FWHM) A summary of the best values obtained here together with literature values from both ISEELS [50-52,69,108,109] and photoabsorption [110-114] are shown in Table 2.4 together with the total estimated uncertainties.

The major possible sources of systematic error in this work include (a) DVM accuracy (b) differences in trajectories for elastic and inelastically scattered electrons due to electron optical effects in the lens system (c) different instrumental response functions for elastic and inelastically scattered electrons (d) spectrometer stability (e) spectral linewidth. The errors due to (a) should be less than 0.01 eV according to the manufacturers' specifications. Resetability was not a problem due to the fact that the DVM had 7-1/2 digits. Errors due to (b) and (c) are considered to be negligible compared to the stated uncertainties in Table 2.4 since the measurements at varying resolution (Table 2.3) show no significant shifts in measured energies. In this regard it should also be noted that peak position shifts were not observed between measurements using elastic and inelastic reference peaks. Change in resolution of the spectrometer involves change of pass energies in the analysers, and thus changes in the decelerating three

TABLE 2.4: Reference energies for inner shell electron energy loss spectroscopy

Inner-shell Transition	Transition energy (eV)[b]				
	ISEELS			Optical	
	This work[a]	Literature	Ref	Literature	Ref
SF_6 S $2p_{1/2} \rightarrow t_{2g}$	184.54(5)	184.27(10)	[69]	184.55	[110]
Ar $2p_{3/2} \rightarrow 4s$	244.37(2)	244.39(1)	[108]		
CO C 1s $\rightarrow \pi^*(v=0)$	287.40(2)	287.31(5) 287.40(2)	[52] [50]		
N_2 1s $\rightarrow \pi^*(v=1)$	401.10(2)	400.93(6) 401.09(4)	[52] [51]		
CO O 1s $\rightarrow \pi^*$	534.21(9)	534.11(8)	[52]	534.2(3)	[111]
SF_6 F 1s $\rightarrow a_{1g}$	688.27(15)	688.0(2)	[69]	687.5 687.8	[112] [113]
Ne 1s $\rightarrow$ 3p	867.13(7)	867.05(8)	[109]	867.13(5)	[114]

a Average values taking into account all the data from the different resolutions (see Table 2.3).

b Errors are shown in brackets e.g. 184.52(6) means 184.52 ± 0.06 eV.

element energy loss lens ratios. This would reveal if any significant energy scale shifts arising from changes in trajectories were occurring. Spectrometer stability (item (d)) is of necessity very high by design since long signal averaged scans are necessary for high resolution operation [52]. Any drift or instability more than ~ 0.01 eV would be immediately apparent as a loss of resolution and a blurring of peak position. Similarly all power supplies were selected with the ripple being less than 0.002 eV peak to peak and the stability corresponding to better than 0.01 eV. The voltage ramp for the energy loss scans was derived from the Fabritek Multichannel Analyser. The linearity of this ramp over the range employed was within the stated uncertainties. This was established by double checking the energy scale by (i) point counting over the number of channels in question and (ii) direct measurement off the spectra. The spectral linewidth (e) for higher energy transitions is often quite large due to natural linewidth (uncertainty principle) considerations. This is reflected in the larger uncertainties for the respective peaks.

While the present values agree well with some of the previously reported data (see Table 2.4) there are some notable discrepancies which lie well outside the boundaries of stated experimental error. The earlier obtained energy values produced using this ISEELS spectrometer [52,69,109] are consistently slightly low compared to the present work. However this is directly attributable to the limited accuracy of the less sophisticated 5-1/2 digit DVM used in the earlier work since the discrepancies are well within the manufacturer's stated error limits for

the instruments used. Agreement of the present work for N_2, CO and Ar with the other published ISEELS data [50,51,108] is excellent. The most serious discrepancy (> 0.5 eV) is with the optical values for the F 1s excitation in SF_6 [112,113]. In this regard it should be noted that the separations between the ISEELS values for SF_6 (S $2p_{1/2} \rightarrow t_{2g}$) and SF_6(F $1s \rightarrow a_{1g}$) are identical in the present and earlier [69] ISEELS work. The electron energy loss measurement is much more direct than the energy calibration of optical instruments particularly at short wavelengths. This together with the generally excellent self-consistency of the other measurements lends confidence to the present ISEELS measurements for SF_6. It is possible that the optical peak shape and therefore peak position could be drastically affected by line saturation effects which can occur in optical spectra due to the resonant nature of the transition [39,115,116].

Thus a consistent set of calibration energies has been obtained in the energy loss range below 900 eV. The set of values (Table 2.4) provides convenient reference points for calibration purposes and these values are used throughout the present work.

CHAPTER 3

INNER SHELL EXCITATION, VALENCE EXCITATION AND CORE IONISATION IN NF_3 STUDIED BY ELECTRON ENERGY LOSS AND X-RAY PHOTOELECTRON SPECTROSCOPIES

In this chapter the ISEELS and XPS spectra of the N 1s and F 1s regions of NF_3 are presented and examined in detail together with the VSEELS spectrum. The information obtained by each technique is different yet complimentary and the interpretation of the results should be facilitated by a joint consideration of all three spectroscopies (VSEELS, ISEELS and XPS) together with previously published photoelectron data [117-119].

The VSEELS spectrum of a molecule is often complex and ambiguous in its assignment because of the possibility of many overlapping transitions arising from the close proximity and number of valence orbitals as well as the numerous manifolds of Rydberg levels. The ISEELS spectra, however, are generally relatively simple and straightforward to assign since the initial core level is usually unambiguous, being well separated in energy from other levels. Thus ISEELS can often give more definite information on the previously unoccupied orbital and this in turn may be useful in clarifying the assignments in the VSEELS spectrum. This depends on the extent to which term values are transferable and an attempt to address this consideration is made in this Chapter. The XPS spectrum provides information on the excited ion

states and and in particular gives the vertical energy for the ionisation processes. The production of these excited ion states would be expected to be manifested in ISEELS by onsets (adiabatic energies) of new continua. Thus the XPS satellite data provides information on which of the features in the ISEELS spectrum above the ionization edge arise from the onsets of excited ion states and by inference which features are due to other types of phenomena such as shape-resonances, or "inner well" states trapped in the continuum [77].

The molecule NF_3 is the fluorinated analogue of NH_3 and is pyramidal with C_{3v} symmetry. Studies of fluorinated compounds are of particular interest due to the highly electronegative nature of the F ligands, since "anomolous" intensity distributions are frequently observed in the electron excitation spectra. In particular for core spectra, a very high relative probability of core to virtual valence transitions has often been observed at the expense of transitions to Rydberg levels. Other distinctive features beyond the ionisation edge are also often observed in such molecules. These effects can be explained in terms of shape-resonances caused by the formation of an effective potential barrier [73,77] either by electron repulsive forces in the neighbourhood of the ligands [73,93] or a centrifugal barrier caused by the anisotropic nature of the molecular field [75,77]. While much work has been done both theoretically and experimentally on the excitation spectra of other fluorinated compounds, such as BF_3 [73,91-93,120-122], CF_4 [66,92,123,124] and SF_6 [69,70,73,77,90] very

little work has been done on NF_3. To date no ISEELS spectra have been reported for either the N or F 1s regions of NF_3. There has, however, been limited discussion of these regions in earlier reported photo-absorption studies [120,121,125] obtained at lower resolution than that used in the present work. Some apparent inconsistencies in this earlier work are investigated in the present more detailed ISEELS measurements. The only VSEELS spectrum is that of unpublished work referred to in the book by Robin [12], while the only UV photoabsorption spectra of the valence shell [126] does not extend beyond 10 eV and is featureless.

To further aid in the assignment of the VSEELS spectrum knowledge of the occupied levels are required. The ionization potentials of these can be obtained from photoelectron spectroscopy. Only the outermost valence shell orbitals (below 21.2 eV) are accessible with He(I) radiation and such spectra hae been reported for NF_3 by Potts et al. [117] as well as Bassett and Lloyd [118] who have also used He(II) radiation. The valence-shell photoelectron spectra utilizing both Zr M_ζ (151.4 eV) and Al Kα (1486.58 eV) have also recently been recorded [119] and these spectra provide the ionization potentials for the inner valence electrons. Some earlier measurements of the 1s core electron ionization potentials of NF_3 have been reported for both F and N [127,128]. A variety of MO calculations have also been reported for NF_3. The only ab-initio calculation so far has been that of Unland et al. [129]. Other less sophisticated calculations have been used including CNDO [118,130,131], MNDO [132] and the Xα method [133,134].

Experimental Details

1) EELS measurements

The inner shell spectra were recorded on the ISEELS spectrometer described in the previous chapter. An impact energy of 2.5 keV was used and the spectra were sampled at ~1° scattering angle. The N 1s spectrum was calibrated against both the CO (C 1s → π^*,v=0) and N_2 (N 1s → π^*v=1) features (see Table 2.4). The newly established N 1s value of NF_3 was used to internally calibrate the F 1s spectrum. The valence shell spectrum was recorded on the new ISEELS spectrometer [53]. An impact energy of 3 keV was used with the scattered electrons sampled at zero degrees. The He(I) line (21.218 eV [104]) was used to calibrate the spectrum.

2) XPS Measurements

The 1s core levels and associated satellite structure were recorded using a McPherson ESCA 36 photoelectron spectrometer situated at the University of Alberta. The spectra were obtained by irradiating the sample with Al Kα ($h\nu$ = 1486.58 eV) X-rays which entered the sample cell through an aluminum foil window of 0.0001" thickness. The sample was fed into the cell via stainless steel feed lines. The pressure was controlled by a Granville- Phillips series 203 variable leak valve and was monitored using a MKS Baratron pressure meter. Typical pressures

used were between 150-200 microns.

The major (1s) line for each region was calibrated separately with the gas and calibrant being mixed on the low pressure side of the inlet system prior to introduction into the sample cell. The pressure of the reference line was also controlled by a Granville Phillips leak valve. Sample and reference gases were of approximate equal pressures with a total pressure somewhere between 150-200 microns. Repeated rapid cycles were run (calibrant-sample-calibrant) to minimize any possible error between reference and sample peaks due to slight pressure drifts. The N 1s line was calibrated against a mixture of Ne and Ar from which the Ne KLL Auger line (804.56(2)eV- kinetic energy) and the Ar 2s core level (326.37(5)eV-binding energy) were used as the reference values [135]. The F 1s line was calibrated against the Ne KLL Auger line and the Ne 1s level (870.31(2)eV-binding energy) [135].

In order to try to distinguish which, if any, of the satellite structures in the N 1s and F 1s XPS spectra are due to inelastic scattering of the outgoing photoelectron, a mixture of Ne and NF_3 at equal pressures was run and the low kinetic energy (i.e., high binding energy) side of the Ne 1s peak was recorded. Since the first "shake-up" feature in the Ne 1s spectrum does not occur until 37.3 eV [17], any feature between this and the major Ne 1s component would be due to energy loss processes involving inelastically scattered photoelectrons. Energy loss contributions from NF_3 would be within 25 eV (see VSEELS spectra, fig. 3.5) of the major 1s component. There would also be a prominent energy loss feature at 16.85 eV [136], due to the intense

2p→3s transition in Ne. The NF_3 valence features will of course be present in the N 1s and F 1s XPS spectra if the corresponding energy loss processes are occurring.

Results and Discussion

NF_3 possess C_{3v} symmetry and its electron configuration is:

$$\underbrace{(1a_1)^2\ (1e)^4}_{\text{F 1s}} \qquad \underbrace{(2a_1)^2}_{\text{N 1s}} \qquad \underbrace{(3a_1)^2\ (2e)^4}_{\text{F 2s}} \qquad \underbrace{(4a_1)^2}_{\text{N 2s}}$$

$$\underbrace{(3e)^4\ (5a_1)^2\ (4e)^4\ (5e)^4\ (1a_2)^2\ (6a_1)^2}_{\text{valence}} \;\vdots\; \underbrace{(7a_1)^0\ (6e)^0}_{\text{virtual valence}}$$

The experimental and calculated ionisation potentials are presented in Table 3.1. The ordering of the occupied levels is that obtained from the X_α calculations [133,134]. However, the ordering of the virtual orbitals is not clear. A MNDO calculation suggests that the $7a_1$ orbital is at the lower energy, whereas HAM/3 and Hartree-Fock [137] calculations give the unoccupied orbitals virtually the same energy with the e orbital being stabilized more relative to the a_1 orbital upon creation of a N 1s hole. Since all of these methods are not expected

Table 3.1

Experimental and calculated ionization potentials for NF_3

Orbital		Expt IP[a] (eV)	Calculated IP (ev)					
			X_α(DV)[b]	X_α(MS)[c]	MNDO	HF[d]	CNDO-MO[e]	CNDO[f]
Unoccupied+	σ_1*	-						
"	σ_2*	-						
Valence[a]	$6a_1$	13.73	13.82	13.97	14.55	14.74	13.95	14.18
"	$1a_2$	16.15	15.91	15.45	16.77*	18.23*	16.94*	18.05*
"	5e	16.55	16.08	15.63	16.61*	17.96*	16.18*	16.34*
"	4e	17.52	17.19	16.71	17.16	19.63	17.84	18.89
"	$5a_1$	19.71	19.45	18.74	19.43	22.63*	21.14	22.71*
"	3e	21.14	21.30	20.62	21.17	22.57*	22.47	22.42*
N 2s	$4a_1$	26.49	25.87	25.89	27.86	30.42	27.47	
F 2s	2e	39.62			43.69	45.49	41.76	
"	$3a_1$	43.06			49.71	49.45	48.63	
N 1s	$2a_1$	414.36						
F 1s	1e	693.24						
	$1a_1$							

(a) Experimental values from ref. 118, HeI, HeII UPS (valence); ref. 119, Zr M_ζ XPS ($4a_1$); ref. 119, Al Kα XPS (2e, $3a_1$); this work (N 1s and F 1s) see Table 3.3.
(b) ref. 133.
(c) ref. 134.
(d) ref. 129.
(e) ref. 131.
(f) ref. 118.
* order different from listed.

+ order is uncertain; MNDO suggests σ_1* is $7a_1$, and σ_2* is 6e, but this is not considered conclusive--see discussion in text.

to give a reliable or meaningful value to the unoccupied levels, no conclusion about their ordering will be drawn and they will be designated as σ_1^* and σ_2^*. All spectra will be discussed with respect to this designation and to the experimental IP's and transitions shown in Tables 3.1, 3.2 and 3.3.

1. Inner Shell Ionization by XPS

Figures 3.1 and 3.2 show the XPS spectra obtained for the N 1s and F 1s regions respectively. The results are summarized in Tables 3.3a and 3.3b. The N 1s IP (414.36 eV) is in fair agreement with the value (414.2 eV) previously reported by Finn et al. [127]. However, there is serious disagreement between the value reported in the present work for F 1s (693.24 eV) and that given by Davis (694.45 eV) [128]. In the present work calibration was achieved by sandwiching the peak in question between the two calibration values (as outlined in the previous section). This calibration procedure gives a check on the linearity of the spectrometer.† It should also be noted that the kinetic energy of the F 1s electron produced by Al Kα X-rays is 793.34 eV which is only

---

† The kinetic energy of the photoelectron is determined by K.E. = $k\Delta V+C$ where ΔV is the potential difference between the analyser plates, k is an experimentally determined machine constant and C accounts for contact potentials. Use of two calibration values allows an experimental determination of k for each run.

Table 3.2

Transitions for C_{3v} Symmetry

Transition	Final State	Dipole Allowed*
$a_1 \leftrightarrow a_1$	A_1	yes
$a_1 \leftrightarrow e$	E	yes
$a_1 \leftrightarrow a_2$	A_2	no
$a_2 \leftrightarrow e$	E	yes
$e \leftrightarrow e$	$A_1 + A_2 + E$	yes

* Transitions from ground state (A_1) to final states of A_1 and E symmetry are allowed

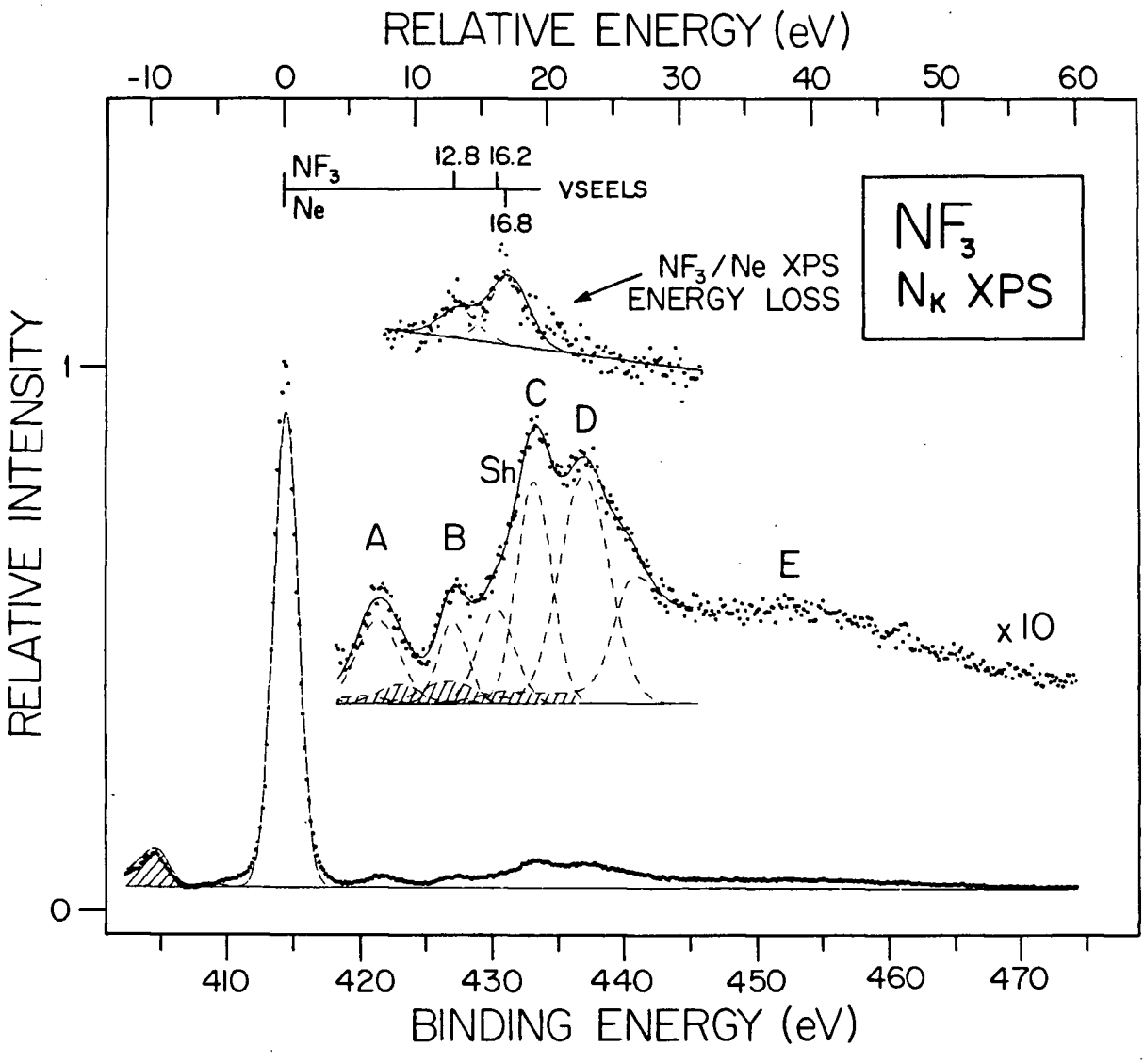

Figure 3.1:
The X-ray photoelectron spectrum for the nitrogen 1s level and associated satellite structure of NF_3 obtained with Aℓ $K\alpha_{1,2}$ (1486.58 eV) radiation. The features have been fitted using a gaussian line shape. The shaded parts are the contributions from higher X-ray ($K\alpha_3$ and $K\alpha_4$) components. Also shown is the spectrum obtained of the low (kinetic) energy side of the neon 1s spectrum from a mixture of Ne and NF_3 (see text for details). The position of the prominent VSEELS transitions are also indicated for Ne and NF_3.

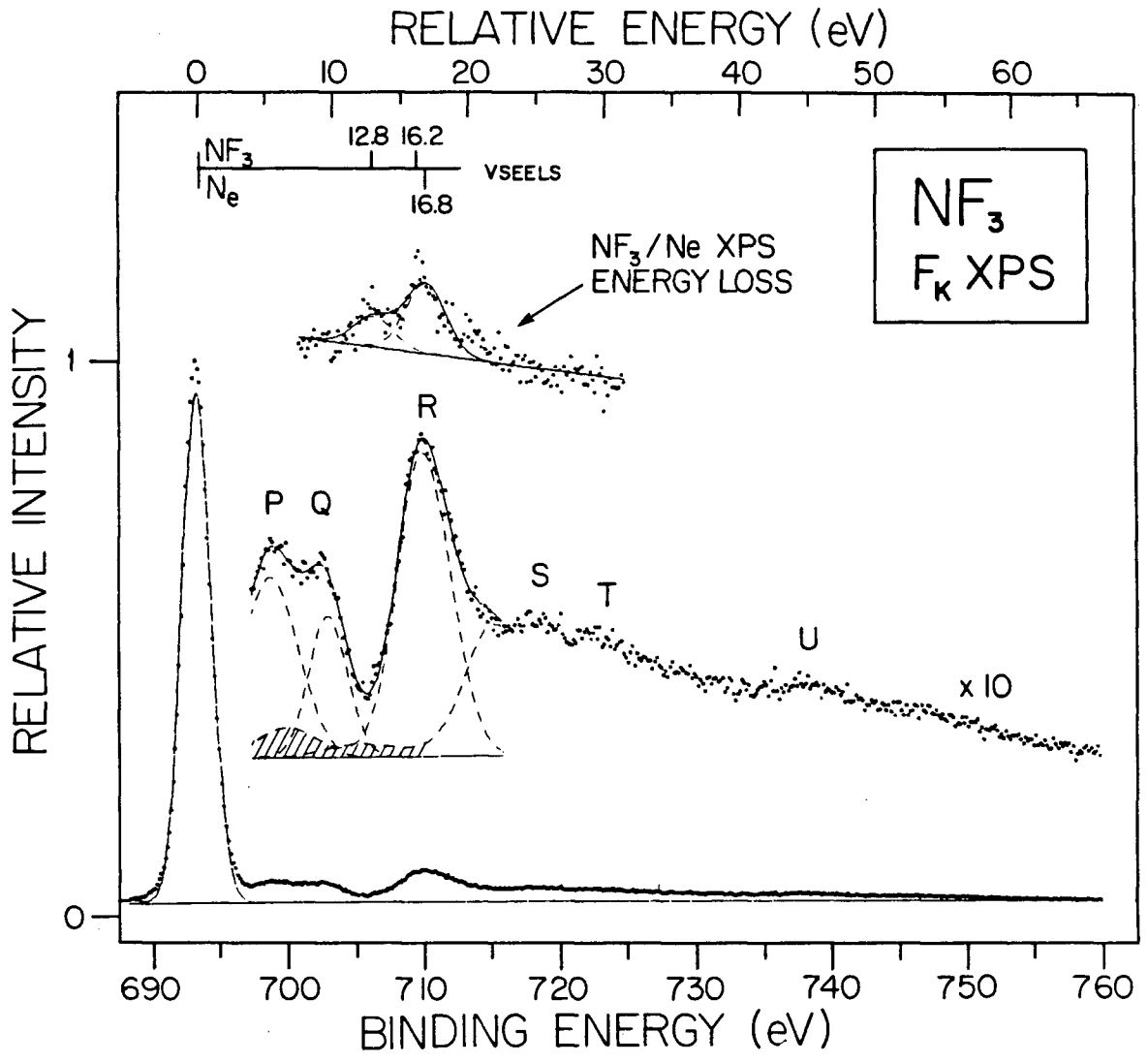

Figure 3.2:
The X-ray photoelectron spectrum for the fluorine 1s level and associated satellite structure of NF_3 obtained with Al $K\alpha_{1,2}$ (1486.58 eV) radiation. The features have been fitted using a gaussian line shape. The shaded parts are the contributions from higher X-ray ($K\alpha_3$ and $K\alpha_4$) components. Also shown is the spectrum obtained of the low (kinetic) energy side of the neon 1s spectrum from a mixture of Ne and NF_3 (see text for details). The position of the prominent VSEELS transitions are also indicated for Ne and NF_3.

Table 3.3(a)

Peak Energies in the N 1s XPS Spectrum of NF_3

Feature	Energy (eV)		Difference energy (eV)	Assignment
	Literature	This work	from main line	
X	414.2[a]	414.36	0	1s hole
A		421.47	7.11	
B		427.13	12.77	
sh		430.39	~16.03	
C		433.26	18.90	
D		437.20	22.66	
BAND E		445-475		shake up & shake off

[a] Ref. 127.

Table 3.3(b)

Peak Energies in the F 1s XPS Spectrum of NF_3

Feature	Energy (eV)		Difference energy (eV)	Assignment
	Literature	This work	from main line	
Y	694.45[a]	693.24	0	1s hole
P		698.45	5.21	
Q		702.64	9.40	
R		709.77	16.53	
S		~719.7	~24.5	
T		~722.3	~29.1	
U		~737.2	~44.0	

[a] Ref. 128.

11.22 eV below the Ne KLL Auger peak used for calibration. Thus the present value is thought correct.

Both the N 1s and F 1s regions exhibit rich satellite structure extending to binding energies at least 60 eV above (i.e., at lower kinetic energies than) the major 1s component. The peaks are broad and this in part reflects the use of unmonochromated Al Kα X-rays (FWHM of the Ne 1s under the conditions used here was ~ 1 eV). This X-ray source contains a variety of lower intensity lines as well as the main $K\alpha_{1,2}$ (unresolved) components. Contributions from the higher X-ray components (mainly $K\alpha_3$ and $K\alpha_4$) have been largely accounted for in the fitting procedure that used a modified version of SUNDERE [138]. The $K\alpha_3$ and $K\alpha_4$ X-ray contributions are shown shaded in Figs. 3.1 and 3.2. Only the most prominent satellite structure has been fitted with no attempt made to fit the extensive lower intensity, unresolved structure extending to higher binding energies (lower kinetic energies). Also shown in each of Figs. 3.1 and 3.2 (uppermost trace) is the spectrum of the high binding energy (low kinetic energy) side of the Ne 1s peak obtained form the Ne/NF_3 mixture. The features are indicative of inelastic scattering (energy-loss) of the emitted photoelectron caused by NF_3 and Ne. It was assumed that the energy loss features would be quite similar in the Ne, N, and F 1s regions since the impact energies of the photoelectrons (616, 1072, and 793 eV respectively) are all well above the excitation energies. The experiment should give an estimate of the extent of energy-loss contributions to the XPS spectra. The major energy loss components in the (low resolution) Ne/NF_3 spectrum in the Ne 1s region

were found to be at 13.4 eV and 16.8 eV (see Figs. 3.1 and 3.2, inserts, which of course are the same spectrum). The former peak is solely due to energy loss contributions from NF_3 and agrees well with features directly observed in the high resolution valence shell spectrum of NF_3 obtained on the EELS spectrometer (see peaks 5-6 (12.81-13.75 eV) of Fig. 3.5). A second NF_3 valence feature of approximately equal intensity would be expected at ~ 16.2 eV (corresponding to peak 8 of Fig. 3.5). However, what is observed is a peak at 16.8 eV of approximately double the expected intensity from NF_3, alone. This is attributed to equal contributions arising from both NF_3 and Ne energy loss features (the Ne 2p→3s energy loss feature occurs at 16.85 eV [136]. Structure at ~ 16.0 eV appears in both the N 1s (shoulder (sh) in Fig. 3.1) and the F 1s (peak R in Fig. 3.2) XPS spectra. The energy loss peak at 13.4 eV is essentially absent in the F 1s XPS spectrum, while some contribution is probably occurring in the N 1s spectrum. However, a comparison of the relative intensities of the spectra in each of figures 1 and 2 leads to the conclusion that a large percentage of the XPS "satellite structure" is due to "shake-up" processes rather than from inelastic scattering.

It can be seen that the satellite structures in the N 1s and F 1s regions are quite different. The N 1s region has a peak A at 7.11 eV above the major 1s component. This is followed by a peak B at 12.77 eV above the main line. This along with a partially resolved shoulder (sh) at 16.0 eV is thought to be at least partially due to the energy-loss features. However the relative intensity of the 12.77 eV feature

suggests that some contribution from genuine satellite structure may be present. The most intense features (C,D) in the N 1s satellite spectra lie in the 18-25 eV region. This is then followed by largely unresolved bands extending out to ~ 60 eV binding energy above the main 1s line.

The F 1s region shows a doublet (P,Q) in the region 5-10 eV above the major 1s component. This is followed by a large peak (R) at 16.6 eV which coincides with the second energy-loss feature. The essential absence in the XPS spectrum of any intense feature at ~ 13 eV (the lower energy-loss feature) leads to the conclusion that the peak at 16.6 eV is largely due to "shake-up" rather than energy-loss processes. At higher kinetic energies there follows a broad region of largely unresolved structure stretching out to ~ 65 eV above the main 1s line. Other structures at S, T, and U are also apparent. The various features of the XPS spectra will be further considered in the interpretation of the electron energy loss spectra (ie: the ISEELS and VSEELS measurements) in the following sections.

Inner shell excitation by ISEELS

The electron energy-loss spectra for the N 1s and F 1s regions of NF_3 are shown respectively in figures 3.3 and 3.4. Figures 3.3a and 3.3b show details of major N 1s transitions recorded at resolutions of 0.14-0.28 eV FWHM while Fig. 3.3c shows a long range scan recorded at resolutions of 0.36 eV FWHM. In a similar way Fig. 3.4a shows the long range spectrum of the F 1s spectrum and Fig. 3.4b the detail. Both spectra in Fig. 3.4 were recorded at a resolution of 0.36 eV FWHM.

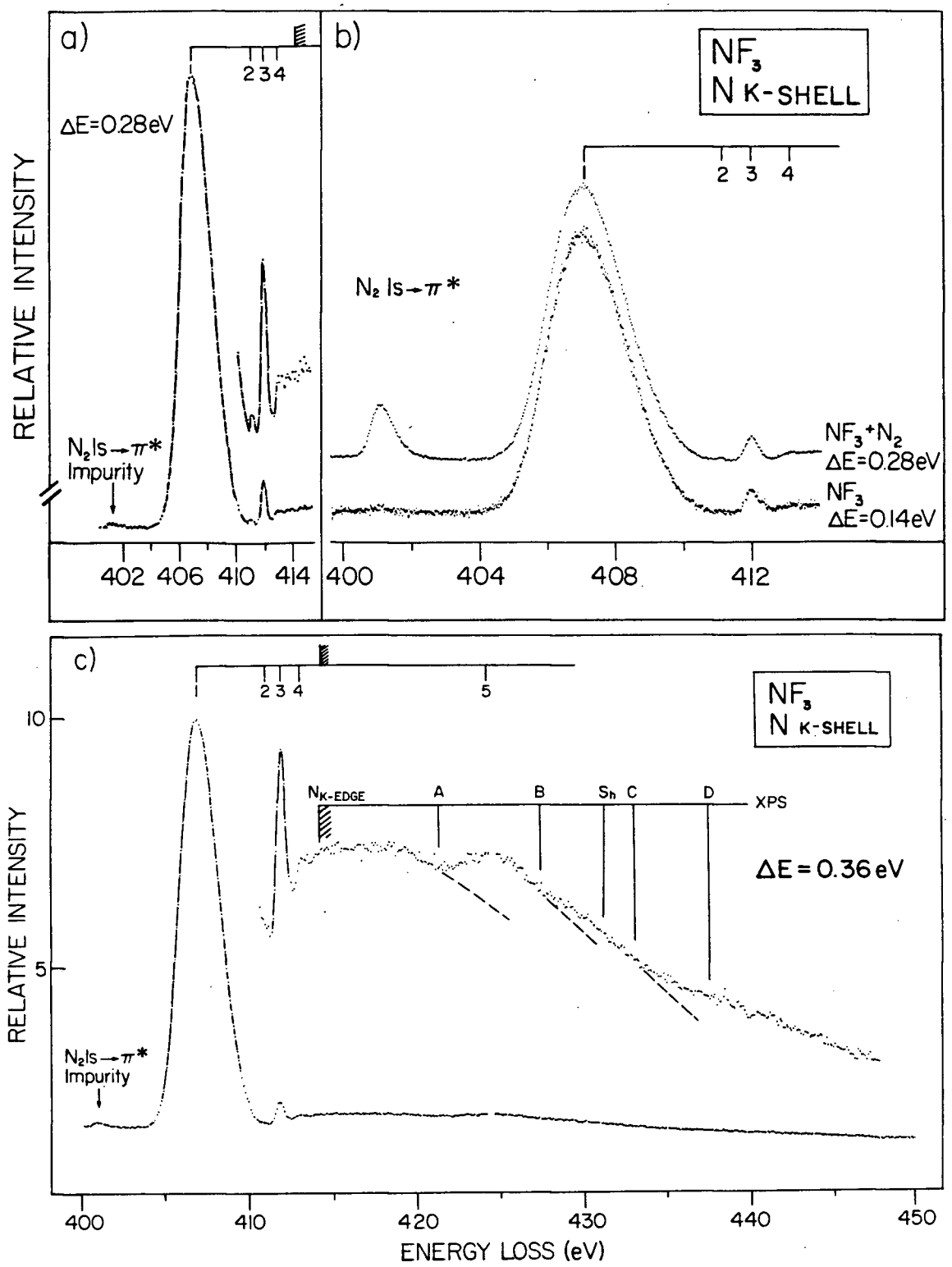

Figure 3.3:

Nitrogen 1s electron energy loss spectra of NF_3. 3.3b) also shows the spectrum of a N_2/NF_3 mixture. The positions of the nitrogen K-edge and the XPS structure in Figure 3.3c) are taken from Figure 3.1 and Table 3.3(a).

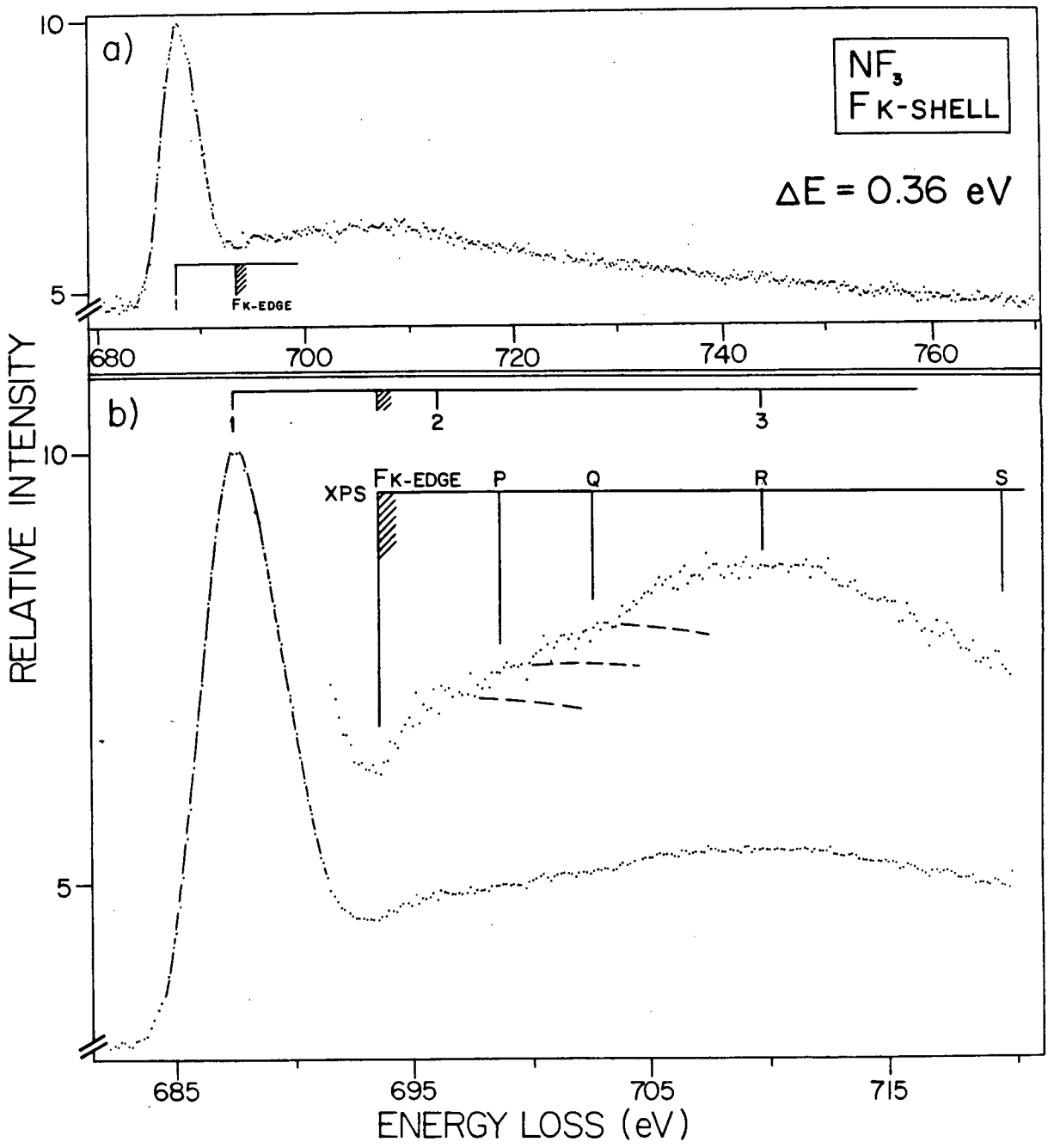

Figure 3.4:
Fluorine 1s electron energy loss spectra of NF_3. The positions of the fluorine K-edge and the XPS satellite structure are taken from Figure 3.2 and Table 3(b).

The energies of the spectral features and possible assignments for the spectra shown in Figs. 3.3 and 3.4 are given in Tables 3.4 and 3.5 respectively.

Both excitation spectra have been studied earlier by Vinogradov et al [125] using soft X-ray photoabsorption. While the present ISEELS work is in generally good agreement with the F 1s spectrum reported in the photoabsorption work [125] there is a serious discrepancy in the case of the N 1s spectrum. In particular Vinogradov et al. [125] report a prominent unassigned feature at 400.9 eV which is essentially absent in the ISEELS spectra of NF_3 reported here. The energy of this peak corresponds closely to that of the N 1s $\rightarrow \pi^*$ transition in molecular N_2 ([4] and Table 2.4) and is thus almost certainly due to an N_2 impurity. This view is confirmed by the ISEELS spectrum we have obtained for a mixture of N_2 and NF_3 which is shown in figure 3.3b (upper trace). It should be noted that there does appear to be a very slight trace of N_2 impurity in all the N 1s spectra of NF_3; however the magnitude of the dominant N_2 ($1s \rightarrow \pi^*$) transition [4] is at most very small. In this regard it should be noted that there is no sharp feature at 12.93 eV in the valence shell spectrum (Fig. 3.5), and this is indicative of the absence of N_2, which has its most intense valence shell transition at 12.93 eV [103]. Thus it is reasonable to conclude that the present NF_3 N 1s spectrum is effectively free from any contributions above 402 eV arising from nitrogen impurities.

The N 1s ISEELS spectrum of NF_3 (Figure 3.3) is dominated by an intense 1s $\rightarrow \sigma^*$ transition at 407.10 eV (peak 1). This can be inter-

Table 3.4

Energies, term values and possible assignments
in the N K-shell energy loss spectrum of NF_3

Feature	Energy Loss (eV)	Term Value	Possible Assignment	Photoabsorption(eV)[a]
				400.9[b]
1	407.10	7.26	1s → σ*	406.6
2	411.02	3.34	1s → 3s	
3	411.99[c]	2.37	1s → 3p	411.9
4	413.24	1.12	1s → 4p	413.0
				413.4
K-edge	414.36[d]	0	1s → ∞	414.1
5	425			

(a) Ref. 125.

(b) This feature was not explained. It is thought to be due to impurity N_2 (1s → π*). See text.

(c) This feature calibrated against CO (C1s → π*) 287.40 eV and N_2 (N1s → π*) 401.10 eV.

(d) XPS this work, see Table 3.3.

Table 3.5

Energies, term values and possible assignments

in the F K-shell spectrum of NF_3 electron energy loss

Feature	Energy Loss(eV)	Term Value	Possible Assignment	Photoabsorption(eV)[a]
1	687.42[b]	5.82	$1s \rightarrow (\sigma^*)$	686.4
K-edge	693.24[c]	0	$1s \rightarrow \infty$	
2	697			
3	~709			

(a) Ref. 125.

(b) Internally calibrated against feature 3 of NF_3 (N 1s) energy loss spectrum.

(c) XPS - see Table 3.3.

preted as an enhanced inner-well final (valence) state trapped by the potential barrier created by the highly electronegative F ligands. This potential barrier model concept has been discussed by Dehmer et al. [73,77]. On the basis of this model the probability of transitions to unoccupied σ^* type valence orbitals (inner-well) would be enhanced at the expense of excitations to Rydberg orbitals (outer-well). In accord with this view the spectrum does show some Rydberg strucure (peaks 2, 3 and 4) of much lower relative intensity leading up to the K-edge. Significant, lower intensity, structure also appears in the continuum. The pre-edge spectrum is qualitatively similar to that observed earlier for the S 2p spectrum of SF_6 [69] which was also attributed to intense inner well valence excitations and weak outer well Rydberg structure.

It is of interest to compare the N 1s energy loss spectrum of NF_3 with that of the isoelectronic molecule $N(CH_3)_3$ (see Figs. 8.3 and 8.4). The spectra are very different and this is attributable to the behaviour of the electronegative F ligand as compared to the electron donating CH_3 ligand. This aspect is discussed in Chapter 8. Finally, in the N 1s ISEELS spectrum of NF_3, a broad maximum is observed in the continuum at ~425 eV.

The F 1s ISEELS spectrum of NF_3 (Fig. 3.4) also shows a strong $1s \rightarrow \sigma^*$ band located at 687.42 eV. There appears to be no Rydberg structure, but this may be masked by the expected large natural width of the σ^* band and its proximity to the F 1s edge. As in the case of the N 1s energy loss spectrum, there exists definite structure in the conti-

nuum with maxima (peaks 2 and 3) at ~ 697 and ~ 709 eV respectively. However, in the case of the F 1s spectrum this structure is on a relatively more intense background compared to the situation in the N 1s region. This is to be expected, however, since the vacancy is on an F atom which is on the periphery of the molecule. The electrons originating from here would likely have much less of a potential barrier to overcome, and thus would have significant probability of going to outerwell states as well. Thus there would likely be less enhancement of the σ^* band relative to the continuum.

The term value for the N 1s → σ^* transition is 7.26 eV, whereas that for the F 1s → σ^* transition is 5.82 eV (Tables 3.4 and 3.5). Thus it would appear that the term values are not transferable between the two core-hole centres. This raises two questions; (a) what is the make up of the σ^* envelope in each case, and (b) what is the effect of the core-hole being on the periphery of the molecule as opposed to being at the centre?

In NF_3 the unoccupied σ^* orbitals are of a_1 and e symmetry, and since the N 1s and F 1s orbitals transform as a_1 and a_1,e respectively, transitions to both σ^* levels are dipole allowed from each centre (see Table 3.2). Both peaks are broad and could be composed of various unresolved components. In an attempt to see what contributions might be expected, MO calculations using HAM/3 [139] were performed. Since HAM/3 is primarily parametrised for π- systems it is not expected to necessarily give good results for σ type systems. However, whereas the eigenvalues obtained might not be satisfactory, the eigenvectors should give

a reasonable indication [140] of the make up of the valence orbitals. Calculations were performed on the molecule with respective core electron vacancies and with half an electron (Transition State Formalism [141]) diffusely added to the virtual orbitals. The eigenvectors of the virtual orbitals in the molecule with an N 1s hole indicate the contribution from the N atom to the 6e orbital to be predominantly $2p_x$ and $2p_y$ (implying a strong s → p dipole allowed transition) while the $7a_1$ orbital is comprised of approximately equal 2s and $2p_z$ character. On this basis the σ^* envelope in the N 1s spectrum would have contributions from both $7a_1$ and 6e orbitals but with a larger contribution from the 6e. On creating an F 1s hole the symmetry of the molecule is reduced from C_{3v} to C_s since the vacancy will be localised on the one F centre. In this case the virtual e and a_1 orbitals become a', a", and a' respectively. The eigenvectors of these orbitals for the F atom with the vacancy show virtually no p orbital contribution to one of the a' and the a" orbitals, leaving the only s → p contribution coming from the remaining a' orbital. Thus the difference in term values may simply reflect the difference in the contribution from the various possible transitions to the broad envelope.

As well as possible effects on symmetry the removal of core electrons (i.e., N 1s or F 1s) will determine the potential in which the electron in the newly occupied orbital finds itself. The σ^* orbitals in the potential barrier model are expected to be mainly within the inner well are hence localised around the (central) N atom. The removal of an N 1s electron increases the core charge by one and so the σ^* orbital

energies will be determined by a Z + 1 (i.e., an O atom) central core. The effect of creating a peripheral hole would not have as much effect since the virtual orbitals are localised around the central atom. Hence an electron in a virtual orbital would be harder to remove (i.e., it would have an increased binding energy (term value)) when there is a central atom vacancy as opposed to a ligand vacancy. This effect was earlier noted in ISEELS core spectra SF_6 [69], in which the virtual orbitals are well separated, thereby removing any ambiguity with regard to the final states. The difference in term values between the species with a S 2p hole and that with an F 1s hole was ~ 1.8 eV. Therefore no definite conclusions can be drawn about the relative separation of the $7a_1$ and 6e orbitals in NF_3 except that they are probably within 1 - 1.5 eV (i.e., the difference in the two term values) of one another.

The N 1s spectrum clearly shows sharp Rydberg structure. Features 3 and 4 (411.99 eV and 413.24 eV) have term values of 2.37 eV and 1.12 eV respectively. This is in excellent agreement with the calculated term values (2.36 eV and 1.18 eV) obtained for n = 3 and 4 respectively when using the approximate quantum defect (δ = 0.6) expected for a p series. Accordingly features 3 and 4 have been assigned as transitions to the 3p and 4p levels. Feature 2 has been assigned as the N 1s $\rightarrow$ 3s (a_1) Rydberg transition. It has a term value of 3.34 eV which gives an estimated quantum defect of 0.98, in agreement with the expected magnitude of the quantum defect (δ = 1.0) associated with an s series.

The positions of the most dominant satellite structures from the

XPS data (Figures 3.1 and 3.2) have also been indicated on the ISEELS spectra (Figure 3.3, A-D and figure 3.4, P-S). Features attributable to ionization and excitation ("shake-up") in XPS should appear as new continua beyond the ionization edge in ISEELS. It should be noted that (a) the values reported from the XPS data are the vertical positions of the broad envelopes whereas the new continua in ISEELS will appear from the onset (ie: adiabatic); (b) the resolution obtained in the ISEELS spectra is about 3 times better than that of the XPS data, thus more onsets might be apparent in ISEELS; (c) no definite inference can be drawn from comparison of the observed cross-section in the one process compared with the other since XPS deals with a photoelectron with kinetic energy several hundreds of eV above the threshold whereas ISEELS will reflect threshold behaviour. Even with the foregoing considerations it should be noted that a comparison of the data from XPS and ISEELS spectra suggests that much of the ISEELS continuum structure can likely be interpreted as being due to the onset of "shake-up" continua (ie: 1s ionization and valence shell excitation). Possible general forms of such continua, starting at apparent discontinuities are indicated by dashed lines on Figs. 3.3 and 3.4. Between the N 1s edge and position A in Figure 3.3 there is an indication of considerable complex structure. This can be attributed to various electron excitations (simultaneous 1s and valence shell excitation). Similar type of structure is also present in the F 1s spectrum. In the N 1s ISEELS spectrum (Fig. 3.3) there is a broad maximum in the continuum (feature 5) at ~ 425 eV. Since no continuum resonances are expected for NF_3 this struc-

ture is presumably due to ionization plus excitation on top of the direct ionization continuum. This feature is associated with a continuum due to "shake-up" A in the XPS spectrum (Fig. 3.1). Similarly, feature 3 (Fig. 3.4) is likely the apparent maximum of a "shake-up" continuum corresponding to the broad peak R (see Fig. 3.2).

Valence Shell Excitation by VSEELS

The valence shell electron energy-loss spectrum for NF_3 is shown in Figure 3.5 and summarized, along with tentative assignments, in table 3.6. The spectrum is qualitatively similar to that reported by Robin [12], however there are some variations in relative intensity. For instance features 7 and 8 are much less intense than in the spectrum reported in the present work. This difference is consistent with the different impact energies used. The spectrum shown by Robin [12] was excited by 100 eV electrons whereas the impact energy used here was 3000 eV. Both spectra were obtained at 0° scattering angle. The spectrum shown by Robin also has an unfortunate break in the data just where feature 9 appears in figure 3.5.

Robin [12] has made a limited assignment in which most transitions are attributed to Rydberg final levels. However it would be expected that the valence orbitals would have a stronger interaction with the virtual valence orbitals than with the more diffuse Rydberg levels especially given the possible existence of a potential barrier which may also affect the valence shell spectrum. In this regard the broadness of some of the observed bands e.g., 1, 2, and 8) is more

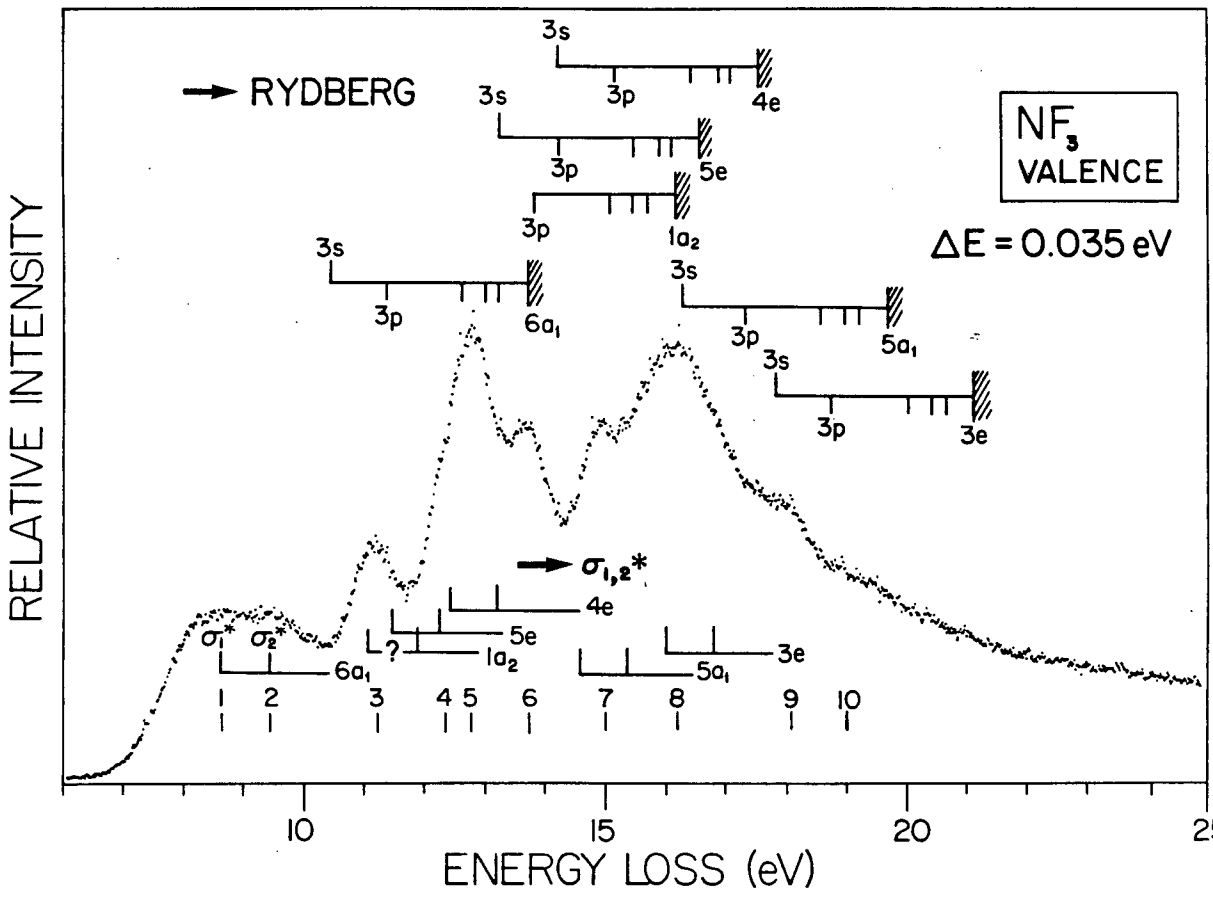

Figure 3.5:

NF_3 valence shell electron energy loss spectrum. The top manifold shows the positions of Rydberg series estimated from term values and the Rydberg formula. The ionization limits are taken from photoelectron spectroscopy. The bottom manifold shows the estimated positions for valence-valence transitions (see text for details).

Table 3.6

Possible Assignments in the Valence Shell Spectrum of NF_3

Major Feature	Observed Energy (eV)	Valence-Valence Assignment	Rydberg Transitions (eV)					
			$6a_1$	$1a_2$	5e	4e	$5a_1$	3e
1	8.64	$6a_1 \rightarrow \sigma_1^*$						
2	9.45	$6a_1 \rightarrow \sigma_2^*$	10.39(3s)					
3	11.21	$1a_2 \rightarrow \sigma_1^*$ †	11.36(3p)					
		$5e \rightarrow \sigma_1^*$						
		$1a_2 \rightarrow \sigma_2^*$ †						
4	12.37	$5e \rightarrow \sigma_2^*$						
		$4e \rightarrow \sigma_1^*$	12.61(4p)					
5	12.81	$4e \rightarrow \sigma_2^*$	13.03(5p)					
			13.26(6p)		13.21(3s)			
6	13.75			13.78(3p)	14.18(3p)	14.13(3s)		
7	15.01	$5a_1 \rightarrow \sigma_1^*$		15.03(4p)		15.15(3p)		
		$5a_1 \rightarrow \sigma_2^*$		15.45(5p)	15.43(4p)			
				15.68(6p)	15.85(5p)			
8	16.20	$3e \rightarrow \sigma_1^*$			16.08(6p)	16.40(4p)	16.37(3s)	
		$3e \rightarrow \sigma_2^*$				16.85(5p)		
						17.05(6p)	17.34(3p)	17.80(3s)
9	18.12	$4a_1 \rightarrow \sigma_1^*$					18.59(4p)	18.77(3p)
10	~19	$4a_1 \rightarrow \sigma_2^*$					19.01(5p)	
							19.24(6p)	20.02(4p)
								20.44(5p)
								20.67(6p)

† $1a_2 \rightarrow 7a_1$, is dipole forbidden. Since it is not known which of σ_1^* or σ_2^* is the $7a_1$, both are given.

suggestive of valence-valence rather than Rydberg transitions. For this reason the spectrum has been assigned as being composed of valence-valence transitions with some Rydberg transitions superimposed.

The spectrum can be divided into three sections; (i) transitions arising from the N lone-pair orbital ($6a_1$); (ii) transitions arising from the F lone-pairs ($1a_2$, 5e and 4e) and transitions arising from the predominantly N-F bonding orbitals ($5a_1$, 3e). Since all the MO schemes (see Table 3.1) give the $6a_1$ as the highest occupied molecular orbital the most likely assignment of features 1 and 2 is to the $6a_1 \rightarrow \sigma_1^*$ and σ_2^* valence-valence transitions since transitions to both the 6e and $7a_1$ orbitals are allowed. It should be noted that the band comprising features 1 and 2 is broad. A further contribution to the width could possibly come from the $6a_1 \rightarrow 3s(a_1)$ Rydberg transition. However, using the 3s term value (3.34 eV) from the ISEELS data discussed above, the predicted position of this feature ($3sa_1$) would be at 10.4 eV in the region between peaks 2 and 3.

In order to predict the positions of other possible valence-valence transitions the experimental separations of the remaining orbittals from the $6a_1$, as derived from photoelectron spectroscopy [118], have been added to the assigned positions of the suggested $6a_1 \rightarrow \sigma_1^*$ and σ_2^* valence-valence transitions. The positions are shown in the lower part of Fig. 3.5. It should be recalled that the $1a_2 \rightarrow 7a_1$ transition is forbidden (see Table 3.2); however, since there is doubt as to the exact ordering of the unoccupied σ^* orbitals, both transitions are

indicated. The ordering of the occupied orbitals is that given by the X_α calculations [133,134]. Other calculations (see Table 3.1) have reversed the order of the $1a_2$ and 5e orbitals. The X_α calculations use transition state formalism and therefore take into account relaxation accompanying ionisation. This ordering also agrees with that obtained by Kellerer et al. [130] in which they calculate a Koopman's theorem defect and combine it with values predicted by CNDO/2 formalisation. With the exception of the X_α calculation all calculations presented in Table 3.1 apply Koopman's theorem.

The agreement obtained between the above predictions of the energies of additional valence-valence transitions and major features in the spectrum shown in Fig. 3.5 is quite good. The $1a_2$, 5e and 4e orbitals are virtually non-bonding and localised on the F atoms [134]. Features 4 and 5 along with much of the intensity under feature 6, which comprise the second section, are attributed mainly to transitions from these orbitals to the σ^* orbitals. The relative narrowness of the bands comprising features 4-6 is consistent with transitions coming from non-bonding orbitals. This is in contrast to the higher energy section comprising features 7-9. The width of this section is quite broad and the bulk of the intensity is assigned to transitions to the σ^* orbitals arising from the $5a_1$ and 3e orbitals, which are predominantly N-F bonding. The structure to higher energy (>18 eV) probably arises from transitions from the $4a_1$ orbital.

The valence shell spectrum shown in Fig. 3.5 is thus likely to contain contributions from a number of valence-valence transitions.

However, transitions to Rydberg levels will also be present. In this regard close examination of the spectrum (Fig. 3.5) shows evidence for fine structure on top of the broader levels attributed to valence-valence transitions. These partially resolved shoulders were repeatedly seen on different scans of the same spectrum. In addition the somewhat narrower bands (3, 6, and 7) have energies corresponding to expected Rydberg transitions (see below). In order to assign possible Rydberg structure it is assumed that the term values for Rydberg levels are transferable between the ISEELS and the VSEELS spectra. Before doing this, however, it is appropriate to consider why Rydberg term values might be transferable whereas virtual valence orbital term values are not necessarily so. From the VSEELS data the term value for the LUMO orbital (σ_1^* - Fig. 3.5, feature 1) is 5.09 eV, whereas the term value corresponding to the peak of the broad envelope encompassing the N 1s $\rightarrow$ σ^* transitions in the N ISEELS data (Fig. 3.3, feature 1) is 7.26 eV. Therefore the σ_1^* term value is likely to be even higher. In essence the term value gives the "binding energy" of the excited electron in the previously unoccupied orbital. Thus in the former case the term value gives the binding energy of the electron in the σ_1^* orbital when the hole exists in the valence shell and in the latter case the binding energy of the electron when an N 1s core hole exists. The loss of shielding by the removal of the valence electron to the virtual valence orbital should be very much less than that caused by the removal of the localised core electron. Hence, in the ISEELS case, the electron in the σ^* orbital should see almost a whole extra unit of charge and so it

should be harder to remove. It will therefore have an increased binding energy (term value). In contrast to the valence orbitals the Rydberg orbitals are large and diffuse and hence will see the molecule as one large core. Thus they should be less affected by where the vacancy occurred and so have transferable term values, whereas the valence orbitals, being much more localised, will be more susceptible to local variations in shielding.

The expected positions of the valence-Rydberg transitions were calculated for n = 3 and 4 using the term values obtained for these levels from the N ISEELS spectrum (i.e., 3.34, 2.37, and 1.12 eV for the 3s, 3p, and 4p orbitals respectively). The positions of the 5p and 6p Rydbergs were estimated using a quantum defect of 0.6 (which applies also to the 3p and 4p levels). These assignments and energies are shown in Table 3.6 and Fig. 3.5 (upper portion). The predicted values of the $6a_1$, $1a_2$, and 4e → 3p transitions (11.36, 13.78, and 15.15 eV respectively) are in agreement with the narrow features 3, 6, and 7, which are at 11.21, 13.75, and 15.01 eV respectively, and these have been assigned accordingly. The transitions to the higher Rydberg levels will not be as intense and weak features in the spectrum can be attributed to these. The spectrum as a whole is consistent with the interpretation given as that of predominantly valence-valence transitions with valence-Rydberg transitions on top.

The assignment of feature 9 is not clear since its width and position is not consistent with an assignment to a Rydberg level. It may also arise, along with the intensity at ~ 19 eV, from transitions to

the σ^* levels originating from the $4a_1$ orbital. This would give it a higher term value than the other valence-valence transitions but one that is more consistent with that from the N 1s ISEELS spectrum. This is not unexpected in view of ideas discussed earlier since the $4a_1$ orbital is essentially due to the N 2s orbital and is thus more localised than the outer valence levels.

Comparison of VSEELS and ISEELS Spectra with the XPS Satellite Structure

The process that occurs in VSEELS is the excitation of an outer (i.e., valence shell) electron to an excited bound state (virtual valence or Rydberg level). The satellite structure in XPS is due to the formation of excited ion states in which the process, at least in a simple model, can be thought of as the emission of a photoelectron with the attendant excitation of an outer electron to either an excited bound state ("shake-up") or to the continuum ("shake-off"). A comparison of the results of the two spectroscopies may yield information on the valence manifold and the types of processes that may occur upon photoionisation. Care has to be taken in any such comparison since VSEELS can essentially be described in terms of one electron process, whereas "shake-up/shake-off" is at least a two electron process. Martin et al. [21] have shown that many-electron theory including configuration interaction has to be included in both the hole and ground states in order to describe adequately the satellite structure accompanying photoionisation. Using this approach they have successfully analysed the satellite structure of HF [22]. An inspection of the data, however, reveals (as

they have noted) that the four most intense peaks can be interpreted, at least to a first approximation in terms of one-electron excitations. Thus an attempt has been made to analyse the NF_3 XPS spectra in terms of one-electron excitations in order to see whether any meaningful information can be obtained without resorting to complex calculations. This is aided by comparison with the VSEELS and ISEELS spectra along with a consideration of the potential barrier phenomenon.

The N 1s XPS satellite spectrum has been assigned (see Table 3.3) as being dominated by transitions to Rydberg levels (peaks C and D, Fig. 3.1) with the lower intensity structure (A, B, E, F, etc.) arising primarily from transitions to the unoccupied valence levels and energy loss features. These tentative assignments have been made on the basis of two considerations.

Firstly, Creber et al. [142] in a study of the XPS satellite spectra of the second row hydrides (CH_4, NH_3, H_2O, HF) isoelectronic with Ne have suggested that Rydberg-like orbitals relax less than valence-type orbitals when a core hole is created in XPS (this incidentally is consistent with the previous assertion that term values are transferable from ISEELS to VSEELS for Rydberg transitions, but not necessarily for transitions to unoccupied valence levels). The energies of peaks A, B, and sh relative to the main 1s line (Fig. 3.1, Table 3.3) are close to the valence shell excitation energies in the VSEELS spectrum (Fig. 3.5, Table 3.6). Further peaks E and F (of Fig. 3.1) would correspond to valence transitions from the $3a_1$ and 2e inner valence orbitals to the σ^* levels. However, peaks C and D are at

relative energies of 18.87 eV and 23.36 eV respectively, which are much greater than the estimated energies of any transitions arising from outer valence orbitals to the virtual valence levels. In view of these observations, and taking into account the conclusions of Creber et al. [142], peaks C and D are assigned as being primarily due to transitions to Rydberg levels from occupied valence levels (i.e., this assumes that both occupied and unoccupied valence orbitals relax to similar extents, but both relax more than Rydberg levels).

Secondly, assuming the above assignment of Rydberg and valence transitions in the XPS spectrum (Fig. 3.1, Table 3.3) is correct, a comparison of intensities between XPS (Fig. 3.1), ISEELS (Fig. 3.3), and also apparently VSEELS (Fig. 3.5) shows an interesting reversal in the relative intensities of transitions to Rydberg and valence levels. In ISEELS, transitions to valence levels predominate over those to Rydberg levels, whereas the reverse situation seems to occur in XPS. This behaviour is not entirely unexpected considering the potential barrier attributed to the three F ligands in NF_3.

In NF_3 the potential barrier (as can be seen from the ISEELS spectra and to some extent the VSEELS spectra here) separates the Rydberg and valence orbitals, causing the ISEELS (and possibly the VSEELS) to be valence dominated. However, in the XPS of NF_3 there is an additional hole (compared to the ISEELS and VSEELS), i.e., one electron less, and this would surely extensively reduce the potential barrier by siphoning of electronic charge from the surrounding F atoms. In these circumstances we might expect to see a relative increase in the ratio of

Rydberg to valence excitation in the XPS "shake-up" spectrum.

The F 1s "shake-up" spectrum of NF_3 is rather different from that of the N 1s. This difference can be immediately attributed to the reduction of symmetry from C_{3v} to C_s upon removal of one of the F 1s electrons. In this case the a_1 orbitals become a", a_2 becomes a", and the e symmetry orbitals reduce to a' and a". Thus a large number of a' → a' and a" → a" valence transitions become possible. In keeping with the arguments used in the case of N 1s, features P, Q, S, and T are probably due to transitions to valence levels, whereas R is due to transitions to Rydberg levels.

Finally, a consideration of the various types of spectra and their relative energies for NH_3 and NF_3 lends some support to the preceeding conclusions. In particular the N 1s ISEELS spectrum of NH_3 ([51] and Chapter 8) is dominated by transitions to Rydberg-type levels since there is no barrier in NH_3. Similarly, the XPS shake-up spectrum of NH_3 [142] appears to be Rydberg-like, with the major features being at similar relative energies to the main 1s line as in the case of NF_3. In the light of the present work it would be of interest to study the various spectra of the molecules NHF_2 and NH_2F in comparison with those of NH_3 and NF_3.

Conclusions

It has been shown in this chapter that while each spectroscopy (ISEELS, VSEELS, and XPS) yields separate information on the electronic structure of molecules, a consideration of all three in conjunction with

each other can lead to a further understanding of each process and the molecular electronic structure. All three spectroscopies give information on valence-valence and valence-Rydberg level electronic transitions.

The ISEELS spectra were found to be typical examples of molecules with highly electronegative ligands in that they showed a strongly enhanced transition to σ^* levels, low-intensity Rydberg structure and features in the continuum. A comparison with the XPS satellite structure indicates that the continuum structure can be associated with "shake-up" phenomena. The VSEELS spectrum show much structure that has been attributed to both valence-valence and valence-Rydberg transitions. Comparing the term values obtained from the ISEELS and VSEELS spectra indicates that those associated with Rydberg levels are transferable, whereas those associated with the virtual valence levels are generally not transferable.

While more specific conclusions must await a detailed and sophisticated theoretical treatment of NF_3, the present studies have clearly indicated that the combined use of various electron spectroscopies provide more detailed insight into fundamental ionisation and excitation processes. In addition, further insights have been gained into the potential barrier model.

CHAPTER 4

ELECTRON ENERGY LOSS SPECTRA OF THE SILICON 2p,2s, CARBON 1s and VALENCE SHELLS OF TETRAMETHYLSILANE

In the previous chapter the ISEELS and VSEELS spectra of a compound with highly electronegative ligands were presented and discussed. It would be instructive to now consider the spectra of a compound which does not have electronegative ligands. In this chapter the ISEELS spectra of tetramethyl silane (TMS), $(CH_3)_4Si$, in the C 1s, Si 2s and 2p regions as well as the VSEELS spectrum are presented. The Si 2p spectra are compared and contrasted with published photoabsorption spectra of SiF_4, SiH_4 and other related Si containing molecules with varying ligands to further examine the effects of the ligand on intensity distribution within the spectra.

TMS is a substance of fundamental and practical importance and is used as a calibrant in NMR spectroscopy. TMS is very stable, however, to date only very limited studies have been made of electronic excitation processes of TMS in the gas phase. For example Roberge et al. [143] have measured the valence shell photoabsorption of TMS and some related molecules up to 85,000 cm^{-1} (i.e. up to an energy of 10.5 eV) which is close to the upper limit of light transmission by windows and lenses in conventional optical spectrometers. Above ~10 eV there are few sources of continuum radiation sufficiently intense for obtain

ing detailed photoabsorption spectra, particularly in the carbon and silicon core excitation region (>100 eV). Synchrotron radiation provides a suitable light source, but to date no such study of TMS has been made, although similar studies of the isoelectronic molecule, SiF_4 [144,145] and also silane, SiH_4 [65,146] have been reported. Dehmer [73] has further discussed the Si 2p absorption spectrum of SiF_4 with reference to the effective potential barrier model. The Si 2p (i.e. $L_{II,III}$) electronic excitation of TMS and its chloro derivatives has been studied by Fomichev et al. [147] using filtered brehmsstrahlung radiation from a tungsten anode in the limited energy range from 102 - 109 eV. No photoabsorption spectrum of either the carbon 1s or the silicon 1s regions of TMS has been published to date.

In contrast to the limited studies made of electron excitation in TMS much work has been reported on the photoelectron spectra of both valence and core regions. These will greatly assist in the interpretation of the electron excitation spectra. He(I) photoelectron spectra of TMS have been reported by several groups [148-150]. The valence shell PES spectrum of the isoelectronic molecule, SiF_4, has also been published [149]. Si 2p binding energies of TMS have been measured in several laboratories [30,151-154].

Experimental Details

The inner shell spectra were recorded using an impact energy of 2.5 keV with the scattered electrons sampled at ~1° scattering angle. The energy scales were established for both regions (Si L-shell and C

K-shell) with respect to the Ar ($2p \rightarrow 4s$) transition at 244.37 eV. The valence shell spectrum was obtained on the new spectrometer [53]. An impact energy of 3 keV was used with the scattered electrons sampled at zero degree scattering angle. The spectrum was calibrated with the He(I) resonance line at 21.218 eV [104].

Results and Discussion

The TMS molecule, $Si(CH_3)_4$ is of T_d symmetry and the electron configuration and unoccupied valence orbitals may be written as [73, 148],

$$(1a_1)^2(2a_1)^2(1t_2)^6(3a_1)^2(2t_2)^6(4a_1)^2(3t_2)^6(5a_1)^2(4t_2)^6(1e)^4(1t_1)^6(5t_2)^6$$

Si1s — C1s — Si2s Si2p — valence

$$(6a_1)^0(6t_2)^0(2e)^0(7t_2)^0$$

unoccupied

The various spectra are usefully discussed with respect to this configuration.

1. Inner Shell Spectra

Figure 4.1 shows a continuous wide range scan of the Si 2p,2s and C 1s regions of the electronic excitation spectrum of TMS between 40 and 380 eV. This survey spectrum was obtained at a resolution of 0.36 eV FWHM. The more prominent features are numbered on the figure consistent with the designations on the more detailed spectra shown in Figures

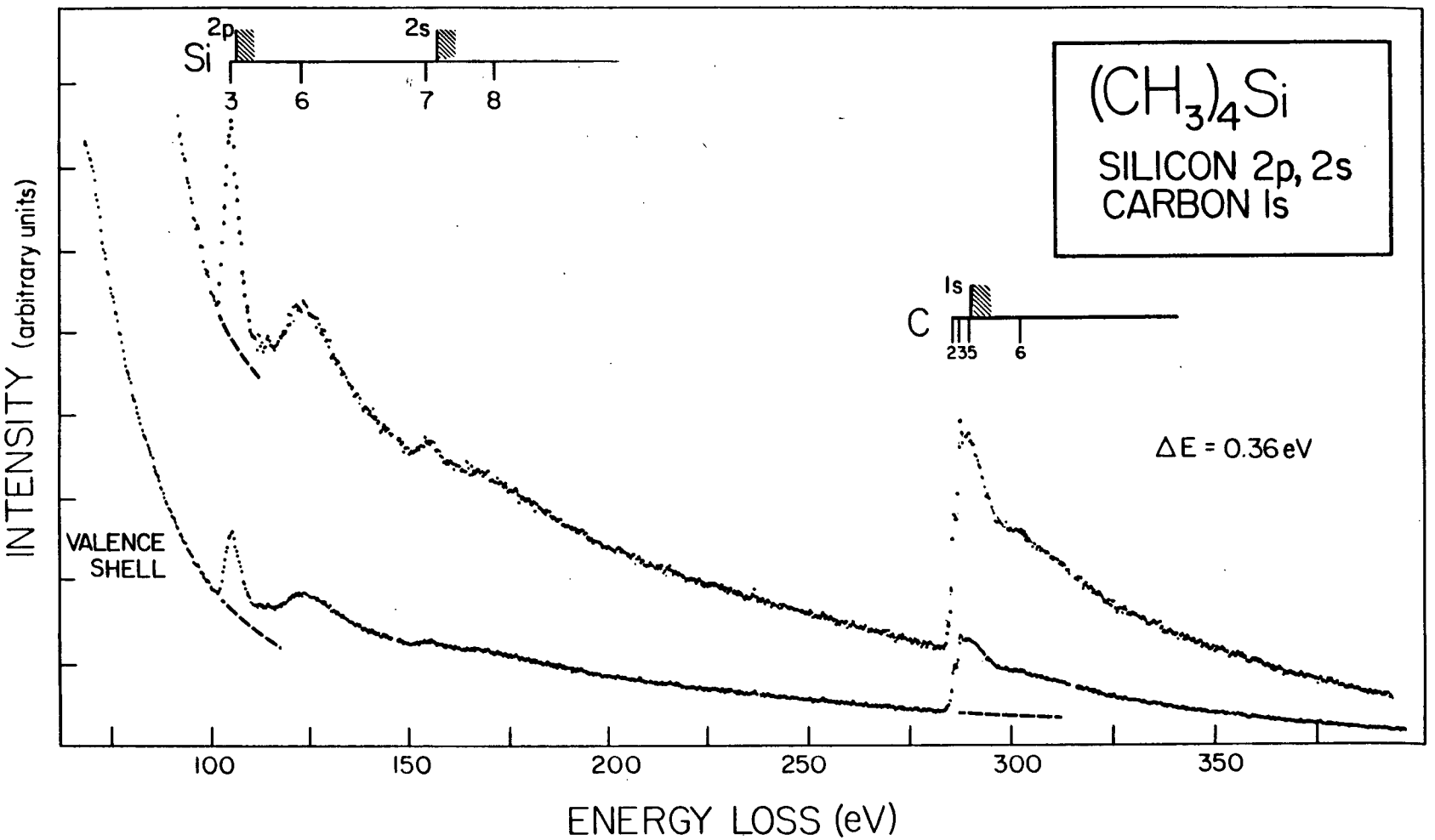

Figure 4.1:
Wide range inner shell electron energy loss spectrum of tetramethylsilane.

4.2 and 4.5. The assignments of the various ionization edges are also discussed later. In the region up to ~100 eV the steeply falling "tail" of the valence shell ionization continuum is clearly visible. The Si 2p spectrum is dominated by two large peaks, one (feature 3) below and one (feature 6) above the ionization limit. Similar but less intense structures (features 7,8) are seen below and above the 2s ionization limit. A sharp increase in cross section is seen at ~285 eV, consistent with the onset of carbon 1s (i.e. K-shell) excitation. A number of discrete states and continuum structures are apparently present and these are discussed in detail below in the section on C 1s excitation.

The overall spectrum (Figure 4.1) displays clear evidence of the separate subshells of Si and C at the expected positions. Since no large shifts in oscillator strength or significant delayed onsets are observed, it is apparent that no strong inter-shell electron correlation effects are occurring. Likewise we may expect that the Si 1s spectrum is even more atomic like due to its comparative "energy isolation" at ~1844 eV [155].

The silicon (2p,2s) and carbon (1s) spectra have been further examined separately at high resolution. Figure 4.2 (lower section) shows the Si 2p and 2s excitation between 100 and 170 eV in greater detail at an energy resolution of 0.36 eV FWHM. The detailed structure in the large peak in the region of ~105 eV is shown at higher resolutions (0.18 eV and 0.10 eV FWHM respectively) in the two upper spectra of Figure 4.2. At least five features (numbered 1-5) are clearly present in this part of the spectrum. The $2p_{3/2}$ ionization edge (105.94

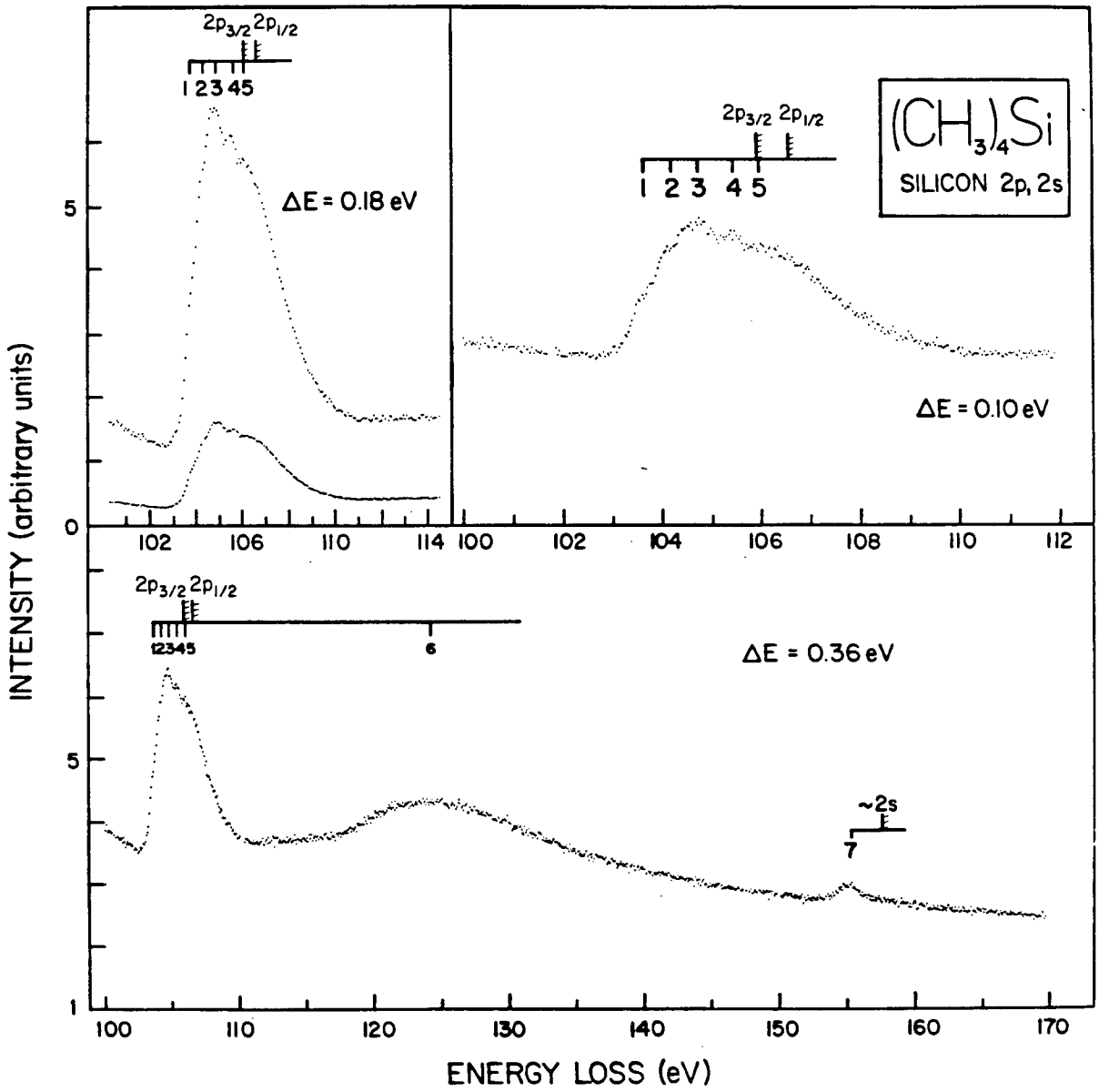

Figure 4.2:
Silicon 2p electron energy loss spectra of tetramethylsilane. Details are given in Table 4.1.

ev) has been assigned using the XPS value for TMS reported by Kelfve et al. [30]. Very similar values have been recorded by Perry and Jolly [151] and also by Drake et al. [152,153]. A value of 100.7 eV reported by Gray et al. [154] is clearly grossly in error. This is not surprising in view of the fact that an arbitrary (and incorrect) value of 285.0 eV was assigned to the carbon 1s binding energy of TMS and this was used [154] to calibrate the scale (the correct value [152,153] should be 289.78 eV, as is discussed below). A value of 0.61 eV for the $2p_{3/2,1/2}$ spin orbit splitting has been used in assigning the $2p_{1/2}$ ionization edge in accord with the findings of Kelfve et al. [30] from their XPS work on a variety of silicon-containing compounds as well as photoabsorption studies on SiH_4 and SiF_4 [65,144,146] and crystalline silicon [156]. It is to be expected that the magnitude of this splitting is largely independent of the molecular type. The Si 2s ionization edge (157.31 eV) has been assigned using the XPS value obtained by Venezia-Floriano and Cavell [157]. This gives a 2p-2s splitting of ~51.2 eV , in close agreement with the estimated splitting of 51.4 eV suggested by Fomichev et al. [147] for Si. A value of 41.5 eV for the 2p-2s splitting in SiH_4 reported by Hayes and Brown [146] is almost certainly incorrect.

The energies, term values and possible assignments of the Si(2p, 2s) spectrum are shown in Table 4.1. The energy values of features 1-5 obtained by Fomichev et al. [147] using soft X-ray absorption are also shown and are consistently lower than the present ISEELS values by approximately 0.5 eV. The shapes and relative intensities of both the present ISEELS and soft X-ray spectra [147] are almost identical in the

Table 4.1

Energies and term values of features in the $Si(2p,2s)$ spectrum of $Si(CH_3)_4$

Feature	Energy[#] (eV)	Term Value		Possible Assignment		Photoabsorption[d] (eV)
		$2p_{3/2}$	$2p_{1/2}$	$2p_{3/2}$	$2p_{1/2}$	
1	103.60	2.34	2.94	$2p \rightarrow a_1$, $t_2/4p$	-	103.15
2	104.19	1.75	2.35	$2p \rightarrow 5s$, 3d	$2p \rightarrow a_1$, $t_2/4p$	103.65
3	104.73	1.21	1.81	$2p \rightarrow 5p$	$2p \rightarrow 5s$, 3d	104.15
4	105.45	0.49	1.09	$2p \rightarrow 4d$	$2p \rightarrow 5p$	104.80
5	105.97	—	0.57	-	$2p \rightarrow 4d$	105.7
$2p_{3/2}$ limit	105.94[a]	0	—	$2p \rightarrow \infty$	-	105.7
$2p_{1/2}$ limit	106.55[b]	—	0	-	$2p \rightarrow \infty$	
6	124.1	-		Resonance ($\sigma^*(7t_2)$)		
7	155.07	2.24[†]		$2s \rightarrow t_2$		
2s limit	~157.31[c] ~157.6[d]	0		∞		
8	~173			Resonance ($\sigma^*(7t_2)$)		

a. XPS values from Reference [30]. References [151-153] give values of 105.83 eV and 106.02 eV respectively.

b. The spin orbit splitting of 0.61 eV has been assigned following data in reference [30]. Similar splittings are reported elsewhere [65,144,146,156].

c. A. Venezia-Floriano and R.G. Cavell, reference [157].

d. Fomichev et al. [147] suggest a Si 2p-2s splitting of 51.4 eV.

† With respect to the 2s limit (157.31 eV, reference [157]).

Estimated uncertainty ±0.05 eV.

energy range 102-108 eV. An examination of the term values for peaks 1-5 with respect to both $2p_{3/2}$ and $2p_{1/2}$ edges shows that the peak spacing is approximately the same as the spin-orbit splitting at the ionization limits (~0.6 eV — see preceeding discussion). It might therefore be possible that a double overlapping Rydberg series converging to the respective $2p_{3/2}$ and $2p_{1/2}$ ionization limits could be contributing to the overall 2p excitation band shown in Figure 4.2. However application of the Rydberg formula and the 2p ionization limits indicates that no simple consistent assignment can be made on the basis of term values and quantum defects. Since only one broad structured band is observed below the ionization edge it is highly likely that this encompasses (mixed) valence and Rydberg states. In particular from consideration of the expected term value it is evident that the 4s Rydberg is missing in the Si(2p,2s) spectra.

It is instructive at ths point to compare the Si 2p spectrum of TMS (i.e. $Si(CH_3)_4$) with the soft X-ray absorption spectrum [144-146] of the isoelectronic molecule SiF_4 and also with the spectra of the species SiH_4, $SiCl_4$ and (solid) SiO_2. The soft X-ray spectra of some of these species are conveniently shown on one diagram in the publication by Dehmer [73]. These, as well as the spectrum of SiH_4 [65] and the presently obtained Si 2p spectrum of TMS have been reproduced on the same energy scale and are shown in Figure 4.3. Four peaks (labelled A, B, C, and D as in reference [73]) occur in each of the Si 2p spectra of SiF_4, $SiCl_4$ and SiO_2 whereas it would seem (Figures 4.1 and 4.2) that only two prominent bands exist in the Si 2p spectrum of TMS. The

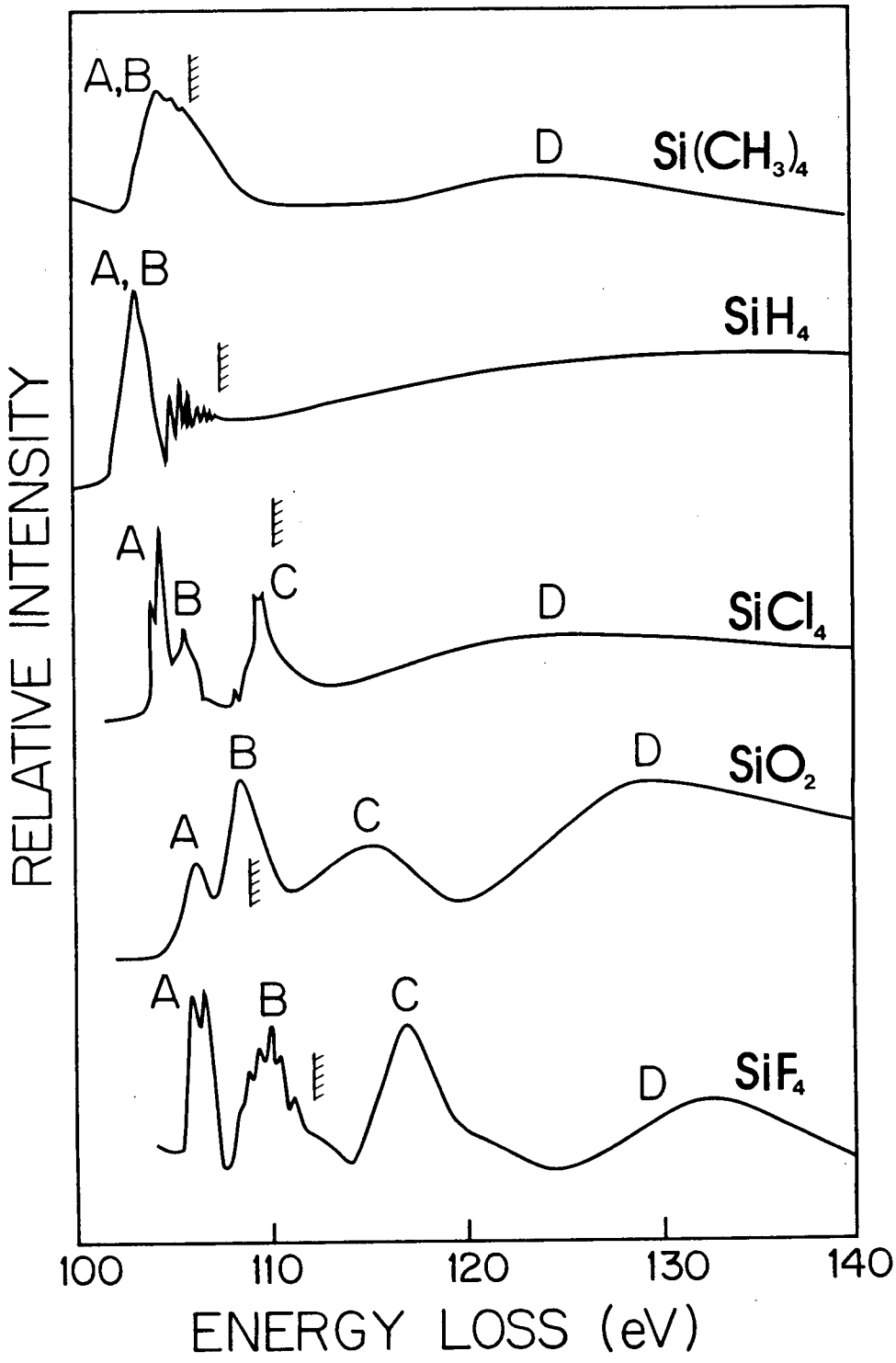

Figure 4.3:
Silicon 2p excitation spectra of various Si containing compounds with Si in a tetrahedral environment; $Si(CH_3)_4$ this work, $SiCl_4$, SiO_2 and SiF_4 as shown in ref. [73]. Details are given in Table 4.2.

difference in behaviour between TMS and SiF_4 can be attributed to the high electronegativity of the F ligand whereas the CH_3 ligand is likely to be electron donating [31,33]. Thus potential (charge) barrier effects [73] are likely to be much greater in SiF_4 than in TMS, and indeed there may be no effective barrier in $Si(CH_3)_4$. If this is the case, then in SiF_4 the band C above the Si 2p edge can be attributed to be an inner-well state trapped by the potential barrier due to the surrounding fluorine ligands. Peaks of type C are also seen [73] in $SiCl_4$ and SiO_2 presumably because these species also have highly electronegative ligands. Very big differences were observed earlier in the carbon K-shell spectra of CF_4 [66,92,133] and CH_4 [66,72], there being an obvious potential barrier effect in CF_4 while CH_4 has a more normal Rydberg type of spectrum. In this regard it is of interest to compare the wide range Si(2p) spectra of TMS with those of SiH_4 [65,146] and elemental Si [146,156] as well as with those of SiF_4 and the other related silicon containing species discussed above. The observed spectrum of $Si(CH_3)_4$ is very similar to those of SiH_4 [65,146] and Si [146,156] and this lends further credence to the suggestion that potential barrier effects in $Si(CH_3)_4$ are effectively absent. Considering now details of the pre-edge structure in the Si 2p spectrum of TMS (Figure 4.2) the large structure (103-110 eV) contains at least five fairly evenly spaced bands at a separation of approximately 0.5 eV. As has been discussed earlier, it has not been possible to fit the peaks to any obvious Rydberg states and furthermore the spacing is not compatible with vibrational structure. Similar conclusions were drawn by Dehmer

[73] for the corresponding band (B) in SiF_4, although Hayes and Brown [146] report having fitted Rydberg series to the same band in SiF_4.

Considering further the region of the TMS spectrum below the Si 2p ionization edge only a single broad band (containing maxima 1-5, Figure 4.2) can be seen and this is likely to encompass a mixture of valence and Rydberg states. In contrast for SiF_4 [144-146], SiO_2 and $SiCl_4$ [73] two bands, A and B [73], are clearly present. Similarly in SiH_4 [65,146] two bands are present below the Si 2p edge. However, a detailed theoretical analysis of a high resolution spectrum of SiH_4 [146] shows that the first band is due to the overlapping $\sigma^*(a_1)$ and $\sigma^*(t_2)$ valence states expected for molecules of T_d symmetry (TMS, SiH_4) for which the unoccupied orbitals are, in order of increasing energy;

$$(a_1)(t_2\text{-p like})(e)(t_2\text{-d like})$$

It is also suggested [65] that the $\sigma^*(a_1)$ has some 4s Rydberg character. The second band in SiH_4 is found [65] to consist of several series of (sharp) Rydberg lines. The nature of these assignments in SiH_4 have been confirmed by running the absorption spectra for solid SiH_4 [65], in which case the Rydberg levels are suppressed. In SiF_4 the two virtual orbitals have been found to be well separated [73,144]. Peak A in SiF_4 has been assigned as $2p \rightarrow \sigma^*(a_1)$ and peak B is a composite of $2p \rightarrow \sigma^*(t_2)$ and the various Rydberg levels [144]. Again the valence characteristics have been confirmed [144] by running the spectrum of the

solid. As noted in reference [144] the term value (in effect the "binding energies" of electrons in the virtual orbitals) for the $\sigma^*(a_1)$ level is higher in SiF_4 than in SiH_4 whereas the reverse is true for the t_2 orbital. This is directly attributable to the electronegativity of the F ligand and therefore it can be expected that as the electronegativity of ligands decrease for a series of silicon compounds bands A (a_1) and B (t_2) should converge. This can clearly be seen in going from $SiF_4 \rightarrow SiCl_4 \rightarrow SiH_4$. Since $-CH_3$ is even less electronegative and in fact electron donating [31,33] it is suggested that the a_1 and t_2 levels in TMS overlap and indeed it is possible that the order may even be reversed. A similar trend of the merging of bands A (a_1-like) and B(t_2-like) can be seen in the Si 2p absorption spectra [147] of $(CH_3)_xSiCl_{(4-x)}$ as x goes from 0 to 4. Given all the considerations discussed above, it is considered that feature 1, and the corresponding part of 2 are due mainly to the $2p_{3/2,1/2}$ components of the overlapped a_1 and t_2 valence bands. In view of the term value (2.35 eV) it is also possible that the t_2 is mixed with the 4p Rydberg level.

The Si 2s orbital in TMS is of a_1 symmetry and so only transitions to the t_2 orbital are dipole allowed. The term value for feature 7 with respect to the 2s edge (see Table 4.1) is 2.24 eV. This feature is therefore assigned as the $2s \rightarrow \sigma^*(t_2)$ transition with possibly some contribution from the 4p Rydberg in view of the term value. This is in accord with the term value for feature 1 of the Si 2p spectrum which lends further support to the suggestion that the a_1 and t_2 states are overlapped or even reversed in the Si 2p spectrum as discussed above.

The close proximity of the Si 2p edge would lead to overlap of the transitions to the valence and Rydberg levels, thus precluding any simple Rydberg analysis as has also been suggested in the case of band B (t_2) for SiF_4 [73]. However, using approximate quantum defects of 2.0 (s), 1.6 (p), and 0.0 (d) applicable for third row (Na-Ar) atom containing molecules, the following term values for the 2p → Rydberg transitions would be expected: 4s (3.40 eV), 4p (2.36 eV), 5s and 3d (1.51 eV), 5p (1.18 eV) and 4d (0.85 eV). Clearly the 4s transition is not observed in the Si L-shell spectra (but see discussion on C 1s spectrum). Features 1 and 2 could be identified with a transition to the 4p Rydberg level; however, this involves a p → p transition, which is dipole forbidden in the purely atomic case. Thus a strong transition (especially considering that the 4s transition is seemingly absent) is not expected and features 1 and 2 are better ascribed to the σ^* orbitals as discussed above. This interpretation is supported by those given on other silicon 2p spectra [65,144] where no transitions to p Rydberg levels have been assigned. In any case, the 4p Rydberg level, being of t_2 symmetry, is likely to mix with the $\sigma^*(t_2)$ orbital to form a $\sigma^*(t_2)$/4p mixed valence-Rydberg state [65]. The width and lack of structure clearly indicate the presence of valence character. Tentative assignments based upon all of the above considerations are given in Table 4.1. Moving on to the structure in the region of and beyond the 2p edge it would appear that the feature C in the SiF_4 and $SiCl_4$ spectrum [6] is absent in TMS. As stated earlier peak C is likely to be a σ^*(2e) inner well state, resonance enhanced [73,75,77]. This

interpretation is supported by the absence of such a peak in SiH_4 [65,146] and crystalline Si [146,156]. A recent study [158] of the asymmetry parameter, β, for photoemission from the Si 2p level of SiF_4 and $Si(CH_3)_4$ (i.e. TMS) shows marked differences in β for the two species in the region 5-16 eV above the respective 2p ionization edges - exactly where peak C is situated in SiF_4 [144-146] but apparently absent in $Si(CH_3)_4$ (see Figure 4.2). The state corresponding to peak C in SiF_4 is expected to quantum mechanically interfere with the underlying 2p direct ionization continua thus causing variations in β compared with the simpler continuum processes in this region in the case of TMS.

A broad continuum feature can be seen in the Si 2p spectra shown in Fig. 4.3 (designated as D). This can be assigned to a d-like $\sigma^*(7t_2)$ shape-resonance feature [73,159]. As was discussed in section F of Chapter 2, the position of this feature should be related in some way to the bond distance between the ionised atom and its neighbour(s). Indeed, within a simple kinetic scattering picture the resonance position from the ionisation edge (δ) should vary linearly with R^{-2} where R is the bond distance [96] (see equation (1.F.3)). Natoli [97,98] has placed this relationship on firmer theoretical grounds but has indicated that the kinetic energy of the electron (δ) should be referenced to an intramolecular potential (V_o) - see equation (1.F.4), which depends on the atoms involved. Hitchcock et al. [100] have shown that a simple linear relationship (equation 1.F.5) is adequate to relate bond distance and resonance position in a series of hydrocarbons. In view of these

discussions, the relationship of the resonance position (D - Fig. 4.3) for these Si-containing compounds with bond length has been examined. Table 4.2 summarises the relevant data from Fig. 4.3 and other literature sources. The energies of the features D (i.e. the t_2 component) as a function of Si-ligand bond distance give points that lie close to straight lines (see Fig. 4.4) of the forms

$$\delta = 38.0\ R^{-2} + 6.4 \quad (r = 0.973)$$

$$\delta = -14.7\ R + 45.1 \quad (r = -0.965)$$

It can be seen that at least for tetrahedral type silicon-containing species the intuitively more reasonable [96-98] R^{-2} variation gives at least as good a linear fit as the more empirical R dependence selected by Hitchcock et al. [100] in the case of carbon-carbon site containing molecules.

Also shown in Fig. 4.4 are the corresponding points for R and R^{-2} dependencies for the features C, which are in the continuum (i.e., SiF_4 and SiO_2) and also that for $SiCl_4$, which is a discrete transition below the Si 2p edge (δ = -0.8 eV). It is also of interest that the plots for features C and D are essentially parallel in each representation. From the linear dependencies estimates have been made of the expected positions of type C features in SiH_4 and $Si(CH_3)_4$ the predicted position (δ = +1 eV) is at ~107 eV in the very broad peak (Fig. 2) around the Si 2p edge. The feature C is generally weaker than D and this is probably why it is not apparent in SiH_4 where D is already rather weak. The lack of

Shape-resonance (features C and D, Fig. 4.3) positions, resonance term values (δ) and bond lengths for relationships shown in Fig. 4.4.

Molecule	position of shape-resonance (eV)[a]		Si 2p[b] IP (eV)	Resonance term value δ = E - IP (eV)		Bond length R (Å)[c]	
	D	C		D	C	R^{-2}	R
$Si(CH_3)_4$	124.1(5)	107.1+	106.1(1)	18.0(6)	~1.0+	0.284	1.875(2)
SiH_4	131.9(10)[d]	113.5+	107.3	24.6(10)	8.1+	0.456	1.481(1)
$SiCl_4$	125.8(10)	109.6	110.4(1)	15.4(11)	-0.8	0.245	2.019(4)
SiO_2	129.5(5)	115.0	108.5(10)	21.0(15)	6.5	0.386	1.61
SiF_4	133.0(5)	117.2	111.9(1)	21.1(6)	5.3	0.414	1.554(4)

(a) $Si(CH_3)_4$ this work; SiF_4 - Ref. [144]; SiH_4, $SiCl_4$, SiO_2 - ref. [73].

(b) $Si(CH_3)_4$, SiH_4, $SiCl_4$, SiF_4, - ref. [30]. 0.2 eV has been added to the Si $2p_{3/2}$ values given in ref. [30] to give an 'average' Si 2p value for the IP.
SiO_2 - ref. [160]. 5.0 eV has been added to the values given in ref. [160] to bring the IP to the vacuum level see ref. [161] for a discussion of this correction procedure.

(c) $Si(CH_3)_4$, SiH_4, $SiCl_4$, SiF_4 - ref. [162], SiO_2 - ref. [163].

(d) This position was estimated from the spectrum of SiH_4 given in ref. [146].

\+ Estimated from Fig. 4.4 using the R^{-2} dependence.

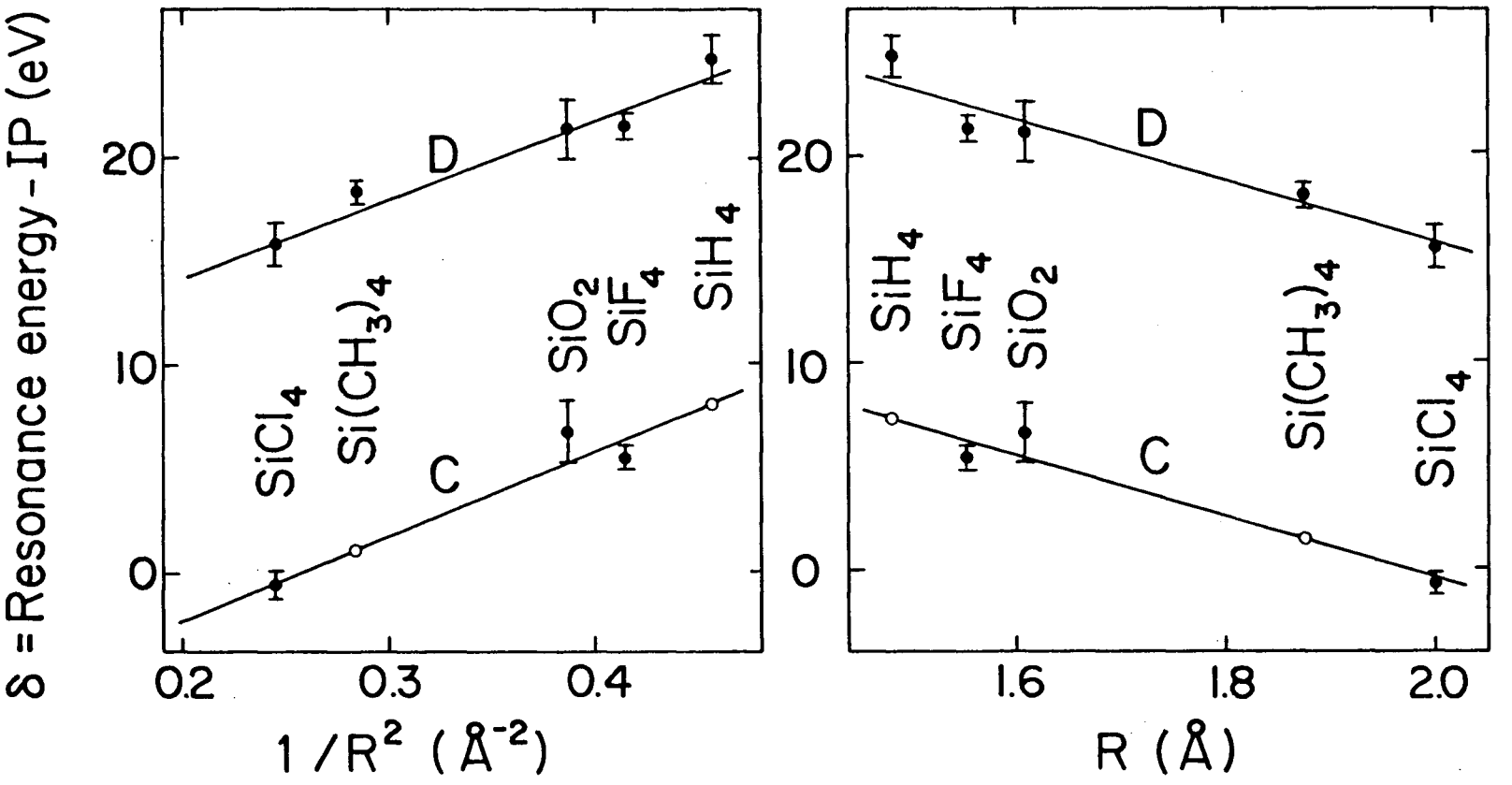

Figure 4.4:
Relationship of bond length to shape resonance (features C and D on Figure 4.3) term value (δ) for silicon containing molecules. Variations are shown of δ with $1/R^2$ (left hand side) and R (right hand side); observed values are shown as solid circles with the open circles being estimated values from the linear plots as shown.

prominent features in the continuum of the SiH_4 spectrum is not surprising due to the low scattering power of the (small) H ligands. This observation lends further general support to the atom-atom scattering viewpoint for understanding resonance features in molecular spectra. The above results for tetrahedral ligand systems surrounding silicon clearly support the existence of a simple relationship between resonance position and the ionized (excited) atom-ligand internuclear separation.

The carbon 1s (K-shell) spectrum of TMS is shown in Figure 4.5 at an energy resolution of 0.36 eV FWHM. The insert shows a more detailed view of the lower energy region at higher resolutionm (0.21 eV FWHM). To date no other carbon 1s spectrum of TMS has been reported. The energies, term values and possible assignments are shown in Table 4.3 together with the carbon 1s binding energy as determined by XPS [152, 153]. The spectrum is strikingly similar in appearance to the C 1s spectrum of CH_4 [67,72] and in this regard the analysis could be considered in terms of a substituted methane. The term values for the first two peaks in TMS (i.e. (1+2) and 3) are 3.40 eV and 2.47 eV whereas those in CH_4 are 3.70 eV and 2.70 eV. The transitions in CH_4 have been assigned as going to the lowest Rydberg levels which are of 3s (a_1) and 3p (t_2) symmetry respectively. The former transition (i.e. to 3s (a_1) is allowed in CH_4 only by vibronic coupling [67]. However in TMS the C 1s orbitals transform as both a_1 and t_2 and so dipole allowed transitions to both a_1 and t_2 orbitals can be expected. Alternatively if the spectrum is analysed in terms of a substituted methane, the local symmetry is C_{3v} and transitions from the 1s (a_1) orbital are dipole

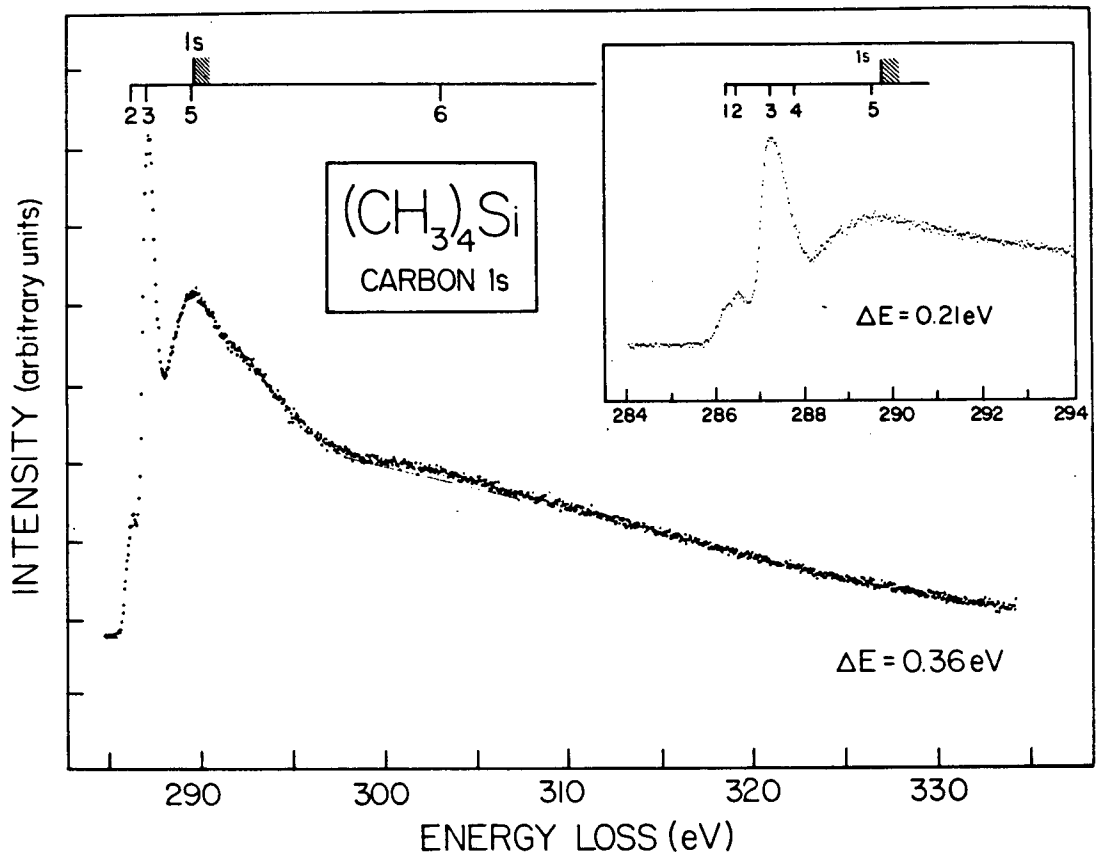

Figure 4.5:
Carbon 1s electron energy loss spectrum of tetramethylsilane. Details are given in Table 4.3.

Table 4.3

Energies, term values and possible assignments of features in the C(1s) spectrum of $Si(CH_3)_4$

Feature	Energy[#] eV	Term Value	Possible Assignment
1	286.26	3.52	1s → 4s (v=0)
2	286.51	3.27	1s → 4s (v=1)
3	287.31	2.47	1s → 4p 1s → $\sigma^*(a_1,t_2)$
5	~289.6		
1s limit	289.78[a]	0	1s → ∞
6	~303		shape resonance ($\sigma^*(7t_2)$)

[a] References [152,153].

[#] Estimated uncertainty ±0.05 eV for peaks 1-3.

allowed to levels of a_1 or e symmetry. Thus peaks (1+2) and 3 can be assigned as transitions from the C 1s to a Rydberg 4s (a_1) orbital and a Rydberg 4p (a_1,3) level†. The increase of intensity for the former transition as compared to that in CH_4 is attributable to it being directly allowed instead of via a vibronic coupling mechanism.

A closer look at the first feature shows that it clearly consists of two components (1+2) separated by ~0.25 eV. This type of phenomenon has also been observed in halogen mono-substituted methanes [63,64] where a separation of 0.30 eV was observed. These were assigned as the v=0 and v=1 components of the corresponding C 1s → ns (a_1) transitions and therefore features 1 and 2 in the C 1s spectrum of TMS have been assigned in a similar manner. Compared to the other substituted methanes feature 3 is broader and lacks the vibrational structure which can be clearly seen in the others [63,64]. It is suggested that feature 3 consists of the 1s → 4p Rydberg transition which lies on top of broader C 1s → σ^* transition (a_1 and t_2). The term value obtained from the Si 2p spectrum (see Table 4.1) agrees with this assignment. The relative intensities and spectral shapes of feature 3 and features (1+2) are consistent with such an interpretation. The large peak marked 5 on Figure 4.5 is mainly due to unresolved higher Rydberg levels converging on the C 1s ionisation edge. A low intensity broad feature (6) in the ionisation continuum may be assigned as a shape resonance (probably $\sigma^*(7t_2)$).

---

† In the case of TMS the lower Rydberg levels are designated as 4s and 4p since the central atom is silicon.

It is of interest to note the complete absence of a Si 2p → 4s (a_1) Rydberg transition since no features appear in the spectrum at the expected term value (~3 eV). This appears to be an example of a case where the first Rydberg level belongs to the ligands as opposed to the molecule as a whole. Examples have been seen [69] where the probabilities of transitions to Rydberg levels are low compared to valence orbitals. This is the case when there exists an effective potential barrier leading to inner well and outer well states. This is not the case for TMS as can be seen from the C 1s spectrum which shows a normal Rydberg type structure unlike the F 1s spectra of SF_6 [69] and SiF_4 [145], both of which exhibit relatively intense inner well type states.

2. Valence Shell Spectrum

The valence shell spectrum of TMS between 6 and 29 eV is shown in Figure 4.6 and summarized, along with tentative assignments, in Table 4.4. The ionization limits shown on Figure 4.6 are taken from measurements made by photoelectron spectroscopy [149,164]. Previously published valence shell excitation spectra, obtained by UV absorption, extend only as far as ~9.2 eV [167], ~10.5 eV [143] and ~11.3 eV [168]. The spectrum reported here shows four distinct bands with partially resolved fine stucture clearly evident in each band. These features arise from transitions to unoccupied virtual valence levels and/or Rydberg levels.

In order to identify which features arise from Rydberg transitions two assumptions have been made. Firstly it has been assumed that

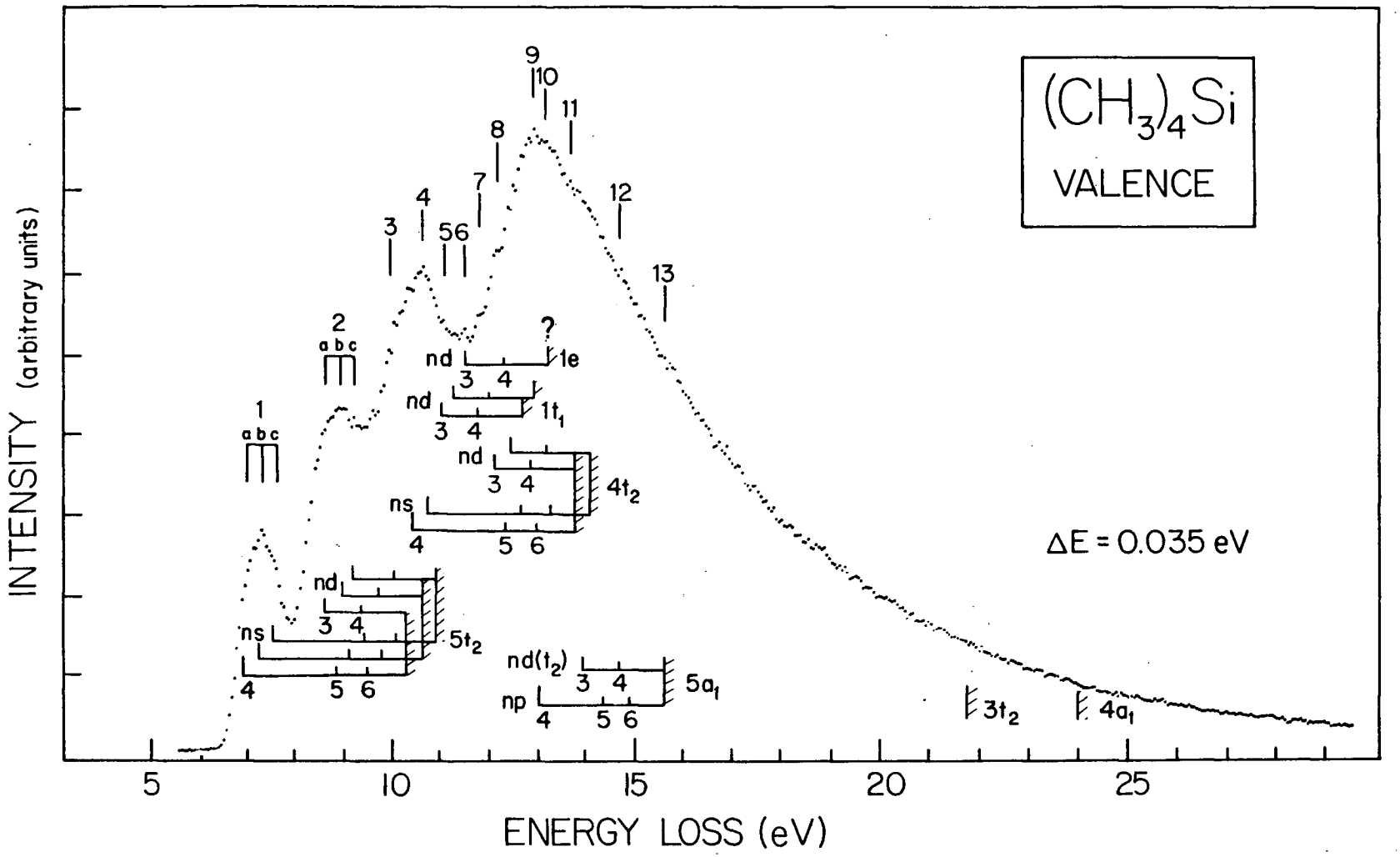

Figure 4.6:
Valence shell electron energy loss spectrum of tetramethylsilane. Estimated positions of the first few members of the Rydberg series are shown below the spectrum. Details are given in Table 4.4.

Table 4.4

Energies and Possible Assignments of Valence Shell Transitions of $Si(CH_3)_4$

Feature	Observed[#] Energy (eV)	Predicted Energies of Rydberg transitions[†] (eV)						IP (ev)[a]
		4s	4P	3d	5s	5p	4d	∞
a	7.04	6.90						
1 b	7.34	7.22 $(5t_2)$						
c	7.64	7.5						
a	8.60			8.62	8.78			
2 b	8.93			8.95 $(5t_2)$	9.11 $(5t_2)$			
c	9.20			9.2	9.4		9.37	
							9.70 $(5t_2)$	
3	10.05						10.0	
		10.4 $(4t_2)$						10.29
4	10.61	10.7						10.62 $(5t_2)$
5	11.00			11.0 $(1t_1)$				10.9
				11.2				
6	11.50			11.5 (1e)				
7	11.81						11.8 $(1t_1)$	
8	12.14			12.1 $(4t_2)$			12.0	
				12.4	12.3 $(4t_2)$		12.3 (1e)	
					12.6			12.7 $(1t_1)$
9	12.86						12.9 $(4t_2)$	12.9
10	13.26		13.1 $(5a_1)$				13.2	13.2 (1e)
11	13.7			13.9 $(5a_1)$				13.8 $(4t_2)$
						14.4 $(5a_1)$		14.1
12	14.7						14.7 $(5s_1)$	
13	15.7							15.6 $(5a_1)$

[†] Originating orbitals are given in parenthesis after the estimated transition energies.

[a] Binding energies from ref. [149] except 1e [164]. Order of orbitals as per ref. [164-165].

[#] Estimated uncertainty ±0.03 eV.

the term values for the Rydberg levels are transferable between the VSEELS and ISEELS spectra. This was discussed in the previous chapter. From the C 1s spectrum of TMS (Figure 4.5, Table 4.3) the mean term value for the (localised - see following discussion of C 1s spectrum) 4s Rydberg level (feature (1+2)) is 3.40 eV and that for the (localised) 4p Rydberg level (feature 3) is 2.47 eV. Using these to calculate the quantum defect by means of the Rydberg formula (equation (1.B.1)) gives rise to term values T of 1.51 eV and 1.21 eV for the 5s and 5p Rydberg levels respectively. The Si 2p spectrum (Figure 4.2) should in principle give the 3d term value. However, the 3d level is not resolved from the 5s and so the value of the 3d term value can only be estimated to have an upper limit of ~1.8 eV. Robin [170] has noted that the term value for the lowest d level is close to 13,500 cm^{-1} (1.67 eV) regardless of the compound's chemical nature and so 1.67 eV and 0.92 eV (obtained from the 3d quantum defect calculated using the Rydberg formula) have been used for the 3d and 4d term values respectively. Secondly, since TMS is of T_d symmetry and the Rydberg orbitals transform as a_1 for the s levels, t_2 for the p levels, and e + t_2 for the d levels, the following valence-Rydberg transitions are dipole allowed on the basis of symmetry considerations:

$$t_2 \rightarrow ns(a_1)$$

$$a_1,\ e,\ t_1,\ t_2 \rightarrow np(t_2)$$

$$t_1,\ t_2 \rightarrow nd(e)$$

$$a_1,\ e,\ t_1,\ t_2 \rightarrow nd(t_2)$$

However, transitions which would be formally dipole forbidden in the case of atomic systems (i.e. s → s, p → p, d → d, s → d) have been assumed to exhibit less intensity than those which are dipole allowed in the atomic case (see Chapter 1, section E). This is most likely to be the case where the MO's are made up of predominantly one (ℓ) type of heavy atom atomic orbital [164].

The HOMO orbital is the $5t_2$ level which is a bonding orbital comprised mainly of C 2p and Si 3p parentage [149,164] and so transitions to the $ns(a_1)$ levels should be seen. The UPS spectrum [149] shows the $5t_2$ level to be Jahn-Teller split into three components with ionization energies of 10.29, 10.62 and 10.90 eV. Thus the $5t_2 \rightarrow ns(a_1)$ transitions could be expected to show three Jahn-Teller components separated by ~0.3 eV with estimated energies of 6.90, 7.22 and 7.50 eV respectively for the first Rydberg level. The first feature in the VSEELS spectrum of TMS does indeed show evidence of three components separated by ~0.3 eV with energies of ~7.0, ~7.3 and ~7.6 eV and therefore these have been assigned accordingly. The centre of the second feature has an energy of 8.93 eV which gives an estimated term value of 1.69 eV (i.e. 10.62 eV - 8.93 eV). Feature 2 is thus assigned as being due predominantly to $5t_2 \rightarrow 3d$ transitions. Again the feature is seen to consist of several components (this is clearer in the UV spectrum reported in ref. [167]). This may be due to Jahn-Teller splitting and/or to transitions to both the 3d(e) and $3d(t_2)$ levels. However, this feature (2) also coincides with transitions from the $5t_2$ level to

the $5s(a_1)$ level. The symmetry allowed $5t_2 \rightarrow 4p(t_2)$ transition would be expected to occur at ~8.1 eV. No sharp structure is observed in this region, consistent with the assumptions that the $5t_2$ orbital is mainly of p character and hence has little probability of transitions to p levels.

The rest of the spectrum has been assigned in a similar manner as indicated in Table 4.4 and Figure 4.6. With the exception of the 1e and $5a_1$ orbitals, the binding energies of the outer valence electrons have been taken from the UPS spectrum reported by Jonas et al. [149]. Their assignment [149], based upon a CNDO/2 calculation, does not agree with the proposed assignment of the X-ray photoelectron spectrum reported by Perry and Jolly [164] based upon intensity considerations and extended Hückel calculations as well as various ab initio calculations [165,166]. The feature at 15.6 eV in the UPS spectrum originally assigned to the 1e orbital [149] has subsequently been attributed to the $5a_1$ orbital, in accord with the other assignments [164-166]. The value of the 1e ionization potential given by Perry and Jolly [164] has been used in the present work. Following the $5t_2$ orbital are the $1t_1$, 1e and $4t_2$ orbitals which have been considered to have mainly C-H bonding character [149,164] and thus to possess a large C 2p component. The $4t_2$ orbital, however, does have some Si 3p character attributed to it [149,164]. The intense feature centred at position 4 is attributable to the $4t_2 \rightarrow 4s(a_1)$ transition. Features 5-8, which are much less intense, can be attributed to transitions from these three orbitals ($1t_1$, 1e and $4t_2$) to the 3d levels. The symmetry allowed transitions to the $np(t_2)$ levels

have been assumed to have little or no intensity since they would involve predominantly p → p transitions. The final outer valence orbital is the $5a_1$ which consists mainly of Si 3s and C 2p atomic orbitals [149,164]. The $5a_1 \rightarrow 4p(t_2)$ transition coincides with the very intense structure around features 9 and 10 which is also where the ionization limits of the $1e$, $1t_1$ and $4t_2$ orbitals occur. Transitions from the $5a_1$ orbital to the $3d(t_2)$ levels may also contribute. It can be seen that the transition energies and structures observed in the spectrum arising from the various orbitals support the assumptions made at the beginning of this section and in Chapter 1, section 5 concerning the relative intensities of allowed and forbidden "atomic-like" transitions in the light of the suggested atomic orbital compositions of the various molecular orbitals [147,164]. Generally the agreement between the observed features and the predicted positions of the valence-Rydberg transitions are quite good. This give more support to the concept of transferability of Rydberg term values between inner shell and valence electron excitations as discussed in Chapter 3. So far nothing has been said about valence-valence transitions. While much of the structure can be attributed to valence-Rydberg transitions the possibility of considerable underlying intensity due to broad valence-valence transitions cannot be ruled out. This conclusion was reached in the assignment of the VSEELS spectrum of NF_3. This interpretation would also be consistent with that for the Si 2p shell spectra of TMS which has been assigned as consisting of overlapping transitions to both valence and Rydberg levels. Thus valence-valence transitions arising from MO's with

Si character (i.e.: $5t_2$, $5a_1$) could be expected. The interpretation of Rydberg transitions on top of valence transitions is also consistent with the spectral intensity distribution. However, no definite conclusions can be made until good quality calculations have been made for the TMS molecule.

CHAPTER 5

ELECTRONIC EXCITATIONS IN PHOSPHORUS CONTAINING MOLECULES. I. INNER SHELL ELECTRON ENERGY LOSS SPECTRA OF PH_3, $P(CH_3)_3$, PF_3 AND PCl_3.

It was seen in the previous chapters that the ligand has a profound effect on the intensity distributions observed in inner shell electron excitation spectra. This was clearly seen when contrasting the Si L-shell spectrum of $Si(CH_3)_4$ with other substituted silanes (see Fig. 4.3). As a continuation of these studies, the energy loss spectra of several phosphorus containing compounds are now reported. To date there have been no electron impact studies on the inner shell excitation spectra of any phosphorus compounds and only limited photoabsorption studies on PCl_3 [171-173], $OPCl_3$ [173,174], $SPCl_3$ [173] and PH_3 [65,146]. However, there have been several theoretical discussions on the P 2p spectrum of PH_3 [60,61,65,170]. In this chapter, the ISEELS spectra of the trivalent phosphorus compounds PX_3 (X = H, F, Cl and CH_3) for the P L-shell regions (F and C K-shell, Cl L-shell) are presented. Following chapters will deal with the ISEELS spectra of the higher coordinate phosphorus compounds PF_5, OPF_3 and $OPCl_3$ and with the VSEELS spectra of some of these compounds.

Experimental Details.

The spectra were all recorded on the ISEELS spectrometer

described in Chapter 2. Unless otherwise stated in the text, all the spectra were obtained using an impact energy of 2.5 keV with the scattered electrons sampled at ~1° scattering angle. All the P 2p spectra were calibrated against the N_2 (N 1s → π^*, v=1) feature at 401.10 eV. The other spectra were internally calibrated against their respective P 2p features.

RESULTS AND DISCUSSION

Phosphorus L-Shell (2p and 2s) Spectra - General Features

The long range spectra of the P 2p,2s (L shell) region are shown in Fig. 5.1. The spectra were recorded at a resolution of 0.36 eV FWHM. The assigned ionisation edges are taken from XPS values [31,175]. Only the P 2p average positions of the $2p_{3/2,1/2}$ doublet were reported [31] due to the limited energy resolution. Therefore an estimated spin-orbit splitting of 0.90 eV has been used [61], along with a statistical weighting of 2:1 to predict the positions of the respective $2p_{3/2}$ (2p - 0.30 eV) and $2p_{1/2}$ (2p + 0.60 eV) edges. Using this procedure the values obtained in the case of PH_3 agree well with those reported by Schwarz [61].

Before examining each spectrum in detail, it is of interest to note the general similarities between the long range spectra presented here (Fig. 5.1) and the spectra of the corresponding silicon compounds (see Fig. 4.3). Each phosphorus L shell spectrum (Fig. 5.1) shows a broad continuum structure (at ~150 - 160 eV in the phosphorus series). The feature was attributed to a d-like shape-resonance [73,77] in the silicon series and presumably an interpretation of a similar structure

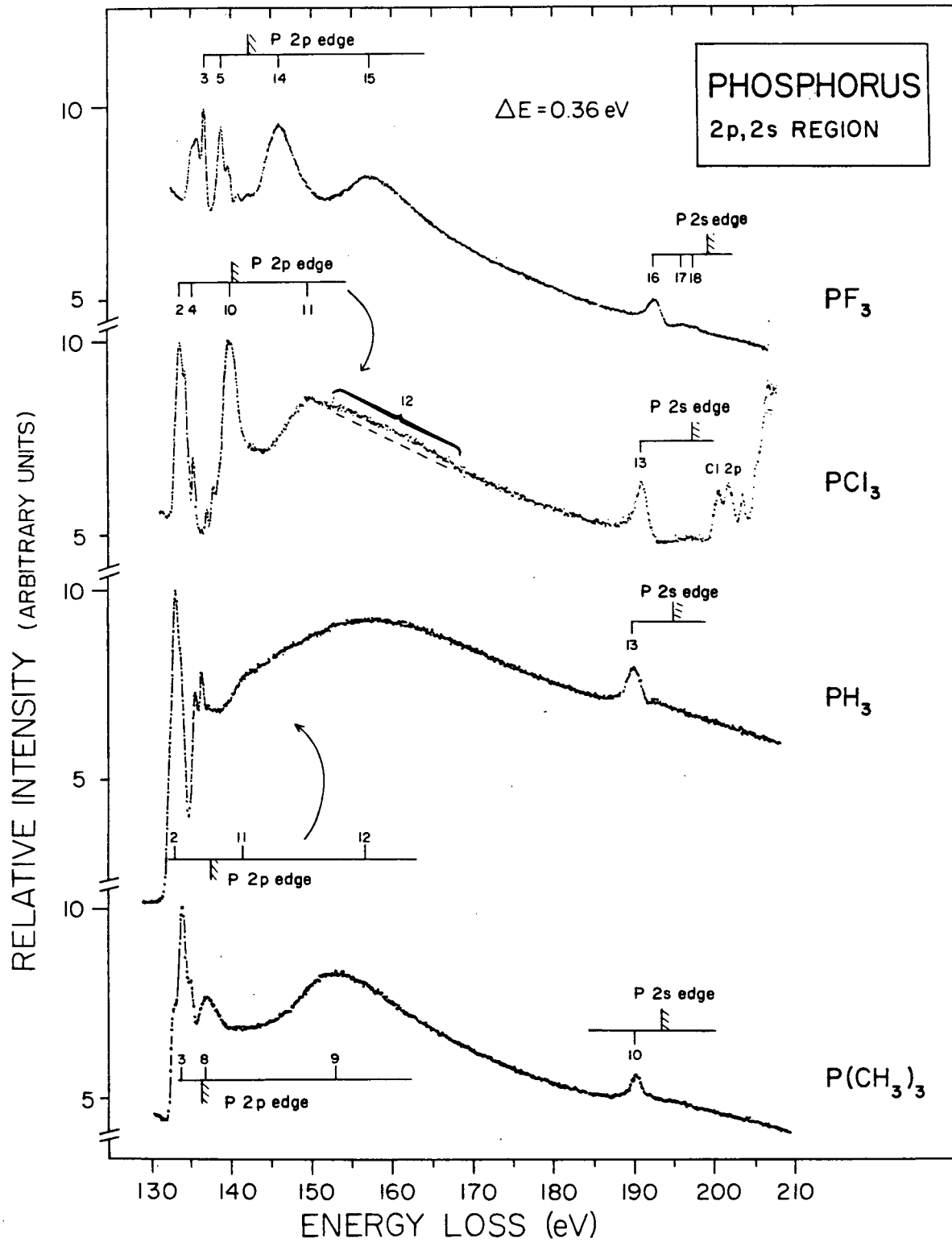

Figure 5.1: Phosphorus 2p,2s wide range electron energy loss spectra of PF_3, PCl_3, PH_3 and $P(CH_3)_3$. All spectra were obtained with an impact energy of 2500 V, a scattering angle ~1°, and a resolution of 0.36 eV FWHM.

can be given here. Similarities between the spectra of respective Si and P containing compounds in the discrete part of the spectrum are:

(i) the hydrides both show a broad feature followed by Rydberg structure leading to the edges

(ii) the fluorides show two well separated major bands, the second with apparent Rydberg structure on top

(iii) the chlorides both show merging bands well below the edge

(iv) all the discrete structures in the methyl compounds are virtually on top of one another and very close to the edge

(v) Both the fluorides and chlorides show a strong inner well trapped [73] or resonance state [77]. In the fluorides this is just above the edge, while in the chlorides it is right at the edge.

It can thus be seen that the ligands have a very similar effect in both series. These ideas will be further discussed in a later section. The assignment of the detailed spectra for each molecule are now considered.

Phosphorus 2p and 2s Spectra - Discrete Regions

The molecules, PX_3, are of C_{3v} symmetry. In a minimum basis set (d orbitals excluded) the empty molecular orbitals are of a_1 and e symmetry (the $-CH_3$ group has been considered as one unit). Table 5.1 lists the dipole allowed transitions to these levels. Since the P 2p orbitals transform as a_1 and e, and the P 2s orbital is of a_1 symmetry, transitions from both these orbitals to both virtual orbitals are allowed. In order to ascertain the positions of the transitions to the

TABLE 5.1

Transitions from the $^1A_1$ Ground State for C_{3v} Symmetry

Final Configuration ‡		Final State	Dipole Allowed from ground state
hole state	occupied σ^* orbital		
a_1	a_1	A_1	Yes
a_1	e	E	Yes
e	a_1	E	Yes
e	e	$A_1 + E$	Yes
e	e	A_2	No

‡ The $(2p_{3/2})^{-1}$, $(2p_{1/2})^{-1}$ and $(2s)^{-1}$ holes are of e, a, and a_1 symmetry respectively. The σ^* orbitals are of a_1 and e symmetry.

virtual orbitals in the P L-shell (i.e., 2p and 2s) spectra two assumptions have been made. Namely:

(i) The major feature in the 2s energy loss is assumed to be 2s → $\sigma^*(e)$ transition

(ii) The term values for features in the P 2s spectrum are assumed to be transferable to the P 2p spectrum.

The first assumption is based upon the make-up of the $\sigma^*(e)$ orbital as compared to the $\sigma^*(a_1)$. The $\sigma^*(e)$ orbital should have a larger proportion of phosphorus 3p orbital character (mainly $3p_x$, $3p_y$) and little phosphorus 3s orbital character in comparison with the $\sigma^*(a_1)$ orbital, which is mainly 3s, $3p_z$[†]. This is supported by CNDO/2 calculations we have performed, as well as by Xα calculations [176]. Thus transitions from an s orbital to the $\sigma^*(a_1)$ level should be weaker than those to the $\sigma^*(e)$ level since the former would have a larger s → s component which is formally dipole forbidden in the case of atomic systems.

The second assumption concerning term value transferability has been discussed earlier (Chapter 1, section E; Chapter 3). The 2s and 2p core-hole vacancies are on the same atom and therefore the electrons should see virtually the same central core potential. However, small differences in term value may occur due to the different shielding

---

[†] Here and in all cases the principal axis of the molecule has been designated as the z axis.

capabilities of the s and p orbitals.

The 2p and 2s regions of the spectra shown in Fig. 5.1 are shown in detail in Figs. 5.2-5.5, which are discussed and presented for each molecule in the following sections. The P 2p regions in Figs. 5.2-5.5 were run at a resolution of 0.18 eV FWH while the 2s regions have been extracted from the long range spectra (Fig. 5.1) which are at a resolution of 0.36 eV. The relative energy scales in Figs. 5.2-5.5 are the same for the respective 2p and 2s spectra and these have been aligned according to their respective ionization edges which were determined from XPS measurements as described above. The 2s spectra as shown were obtained by subtracting a linear ramp background from the total spectrum (Fig. 5.1) so as to more clearly display the spectral features. In all cases (Figs. 5.2-5.5 it can be seen that the spectral features are much broader for the 2s spectra than for the 2p case. This broadening is <u>far</u> beyond that attributable to the differences in energy resolution (0.18 vs. 0.36 eV) which would in any case appear negligible on the energy scale of the figures. Furthermore, there seem to be few if any Rydberg transitions apparent in the 2s spectra. The extremely broad peak (assigned predominantly to the σ^*(e) level) in each of the 2s spectra is attributable to the occurrence of a fast autoionisation process analogous to an $L_1L_{23}M$ Coster-Kronig Auger transition (i.e., an initial vacancy filled from within the <u>same</u> shell plus ejection of a valence electron). In the ISEELS spectra the process would involve an initial excited state with a 2s vacancy being filled by a 2p electron with autoionisation of a valence electron. The relative lifetime broadening

(1.2 eV extra width) observed in the case of argon for the 2s XPS peak relative to that for the 2p peak (see ref. [17], page 4) lends support to this argument. (See also Chapter 1, section B IV).

Phosphine (PH_3)

PH_3 is the simplest molecule presented here and the detailed results for the P 2p and 2s spectra are shown in Fig. 5.2 and Table 5.2. It has been the subject of several earlier studies and discussions [60,61,65,146,170] which have mostly focussed on the 2p region with little or no treatment on the 2s region. The spectrum recorded in the present work is in good agreement with the slightly higher resolution XUV spectra reported by Hayes and Brown [146] and also by Friedrich et al. [65]. Friedrich et al. [65] have compared the various assignments reported in the literature [60,61,146,170]. Their own calculations [65] concur with the conclusions reached by Schwarz [60,61]. Thus peaks 1-3 (Fig. 5.2, Table 5.1) can be assigned as $2p \rightarrow \sigma^*$ transitions followed by the various 2p → Rydberg transitions leading up to the edge. The order of the σ^* levels, according to these studies [60,61,65] is $\sigma^*(a_1)$ followed by $\sigma^*(e)$. This is in agreement with earlier Xα-SW calculations [177] but contrary to the more recent Xα-DV calculation [176]. It is clear in any case that both levels are very close. However, the term value (5.21 eV) for feature 13 which is assigned as $2s \rightarrow \sigma^*(e)$ in the 2s spectrum (Fig. 5.2) is close to that for peak 1 (5.05 eV) and therefore indicates that the recent Xα-DV ordering is likely correct. This

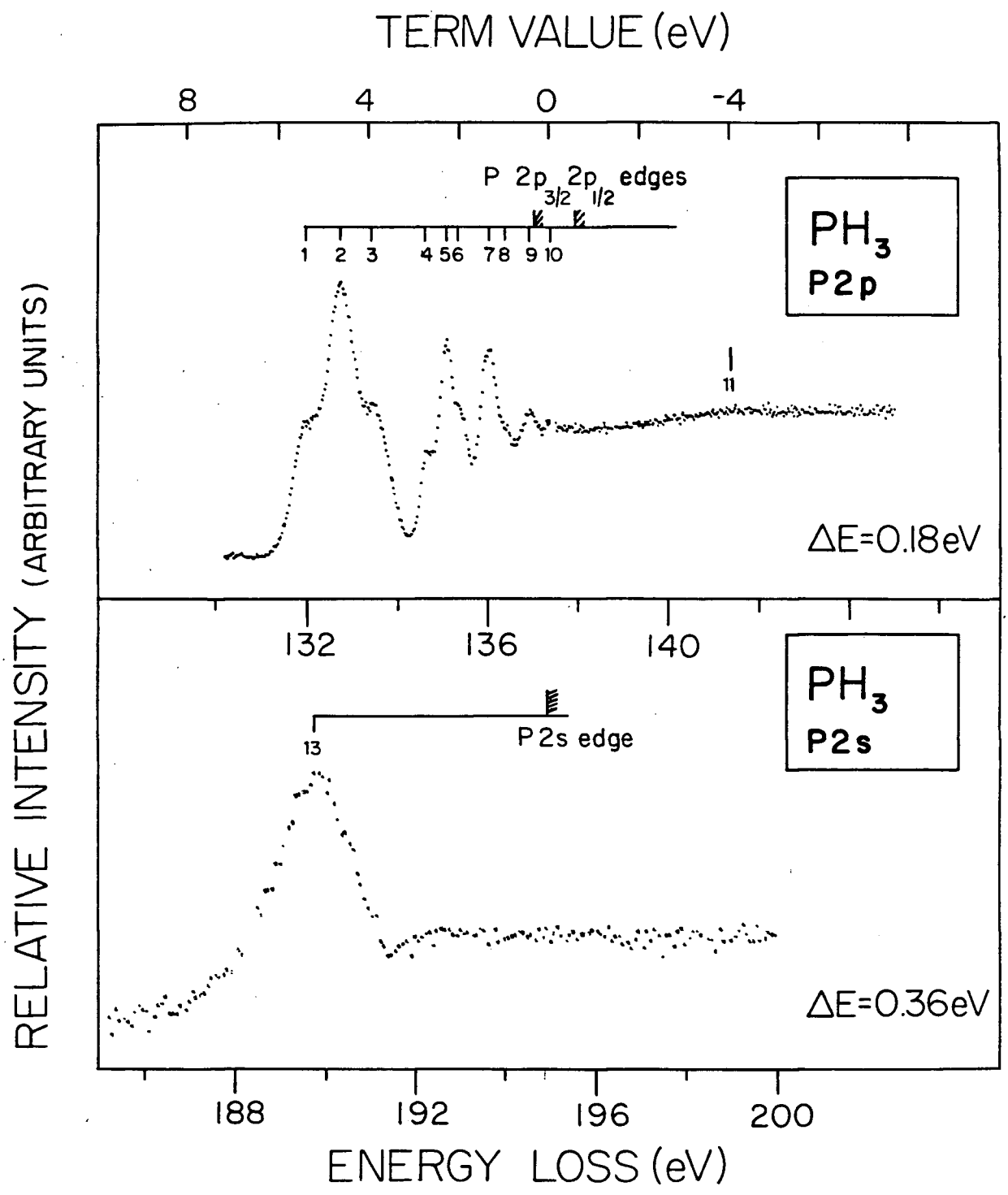

Figure 5.2: Phosphorus 2p and 2s electron energy loss spectra of PH_3. The P 2p spectrum (upper trace) is at high resolution (0.18 eV FWHM). The P 2s spectrum (lower trace) is extracted from Fig. 5.1. The spectra are aligned with respect to the 2p(mean) and 2s ionisation edges.

TABLE 5.2

Energies, Term Values, and Possible Assignments for the P 2p,2s Spectra of PH_3

Feature	Energy Loss[a] (eV)	Term Value (eV)		Possible Assignments[d]	
		$2p_{3/2}$	$2p_{1/2}$	$2p_{3/2}$	$2p_{1/2}$
1	132.00	5.05		$\sigma^*(e)$	
2	132.78	4.27	5.17	$\sigma^*(a_1)$	$\sigma^*(e)$
3	133.46	3.59	4.49		$\sigma^*(a_1)$
4	134.67	2.38	3.28	4s	
5	135.12	1.93	2.83	3d	
6	135.36	1.69	2.59		4s
7	136.06	0.99	1.89	5s,4d	3d
8	136.43(12)	0.62	1.52	6s etc	
9	136.96		0.99		5s,4d
10	137.42(12)		0.53		6s etc
$2p_{3/2}$ limit[b]	137.05	0			
$2p_{1/2}$ limit[b]	137.95		0		
11	141.4(4)	-4.0‡		"shake-up"†	
12	156.7(5)	-19.3‡		"shake-up"	
		2s			
13	189.67(15)	5.21		predominantly 2s → $\sigma^*(e)$	
2s limit[c]	194.88	0			

(a) Estimated uncertainty in energy-loss values is ± 0.08 eV except where stated. Spectra are calibrated against N_2 ($1s \rightarrow \pi^*$, $v = 1$) at 401.10 eV.

(b) The spin-orbit splitting of 0.90 eV [61] has been used to estimate the $2p_{3/2}$ and $2p_{1/2}$ spin-orbit components from the 2p (mean) values [31], see text for details.

(c) Ref. [175].

(d) Final occupied orbital with either $2p_{3/2}$ or $2p_{1/2}$ hole state.

† See Fig. 5.8.

‡ With respect to the 2p (mean) edge [31].

assignment cannot be considered as completely conclusive due to the assumptions discussed above. It should be noted that the feature attributed to the 2s edge by Hayes and Brown in the spectrum of PH_3 [146] is in fact the discrete pre-edge feature (13) observed in the present (Fig. 5.2).

Trimethyl Phosphine ($P(CH3)_3$)

The detailed 2p and 2s spectra of $P(CH_3)_3$ are shown in Fig. 5.3 and the spectral positions and possible assignments summarised in Table 5.3. The 2p spectrum consists of a number of overlapping transitions, all within 3.5 eV of the edge, and is thus difficult to assign unambiguously. There are no obvious Rydberg series, whch may indicate valence-Rydberg mixing [20,65]. The term value for the $2s \rightarrow \sigma^*(e)$ transition (feature 10, Fig. 5.3) is 3.38 eV. This corresponds very closely with that (3.30 eV) for the first feature in the 2p spectrum which has accordingly been assigned as the $2p \rightarrow (2p_{3/2})^{-1}\sigma^*(e)$ transition. Thus the ordering of the virtual orbitals is indicated to be $\sigma^*(e)$ followed by the $\sigma^*(a_1)$ as was found for PH_3 (see preceeding discussion). This is in agreement with the recent Xα calculations [176] which finds the lowest unoccupied orbital with any significant phosphorus contribution to be e in character.

The remainder of the spectrum is difficult to assign. However, in many ways the spectral shape is in keeping with what might be expected if the $2p \rightarrow \sigma^*$ features were superimposed on the Rydberg

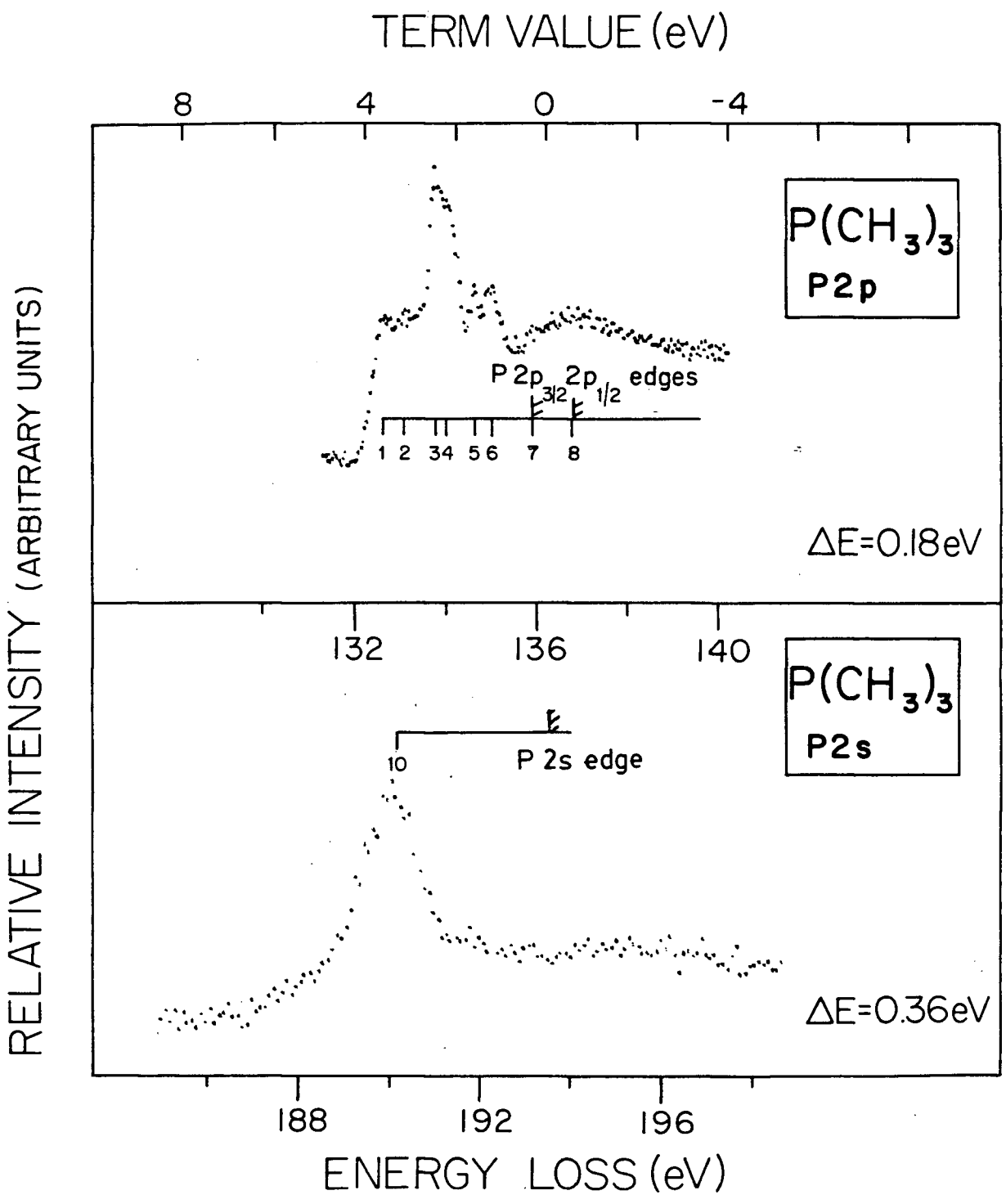

Figure 5.3: Phosphorus 2p and 2s electron energy loss spectra of $P(CH_3)_3$. The P 2p spectrum (upper trace) is at high resolution (0.18 eV FWHM). The P 2s spectrum (lower trace) is extracted from Fig. 5.1. The spectra are aligned with respect to the 2p(mean) and 2s ionisation edges.

TABLE 5.3

Energies, Term Values, and Possible Assignments for the P 2p,2s Spectra of $P(CH_3)_3$

Feature	Energy Loss[a] (eV)	Term Value (eV)		Possible Assignments[d]	
		$2p_{3/2}$	$2p_{1/2}$	$2p_{3/2}$	$2p_{1/2}$
1	132.65	3.30		$\sigma^*(e)$	
2	133.09	2.86	3.76	4s	
3	133.79	2.16	3.06	A	$\sigma^*(e)$
4	134.05 (12)	1.90	2.80	3d, B	4s
5	134.67	1.28	2.18	5s	A
6	135.03	0.92	1.82	4d	3d, B
7	135.9 (2)	0	0.9	edge	4d
8	136.8 (3)		0		edge
$2p_{3/2}$ limit[b]	135.95	0			
$2p_{1/2}$ limit[b]	136.85		0		
9	153.0 (5)	-16.7[†]		Shape-resonance	
		2s			
10	190.23 (15)	3.38		predominantly 2s → $\sigma^*(e)$	
2s limit[c]	193.61	0			

(a) Estimated uncertainty in energy-loss values is ± 0.08 eV except where stated. Spectra are calibrated against N_2 ($1s \rightarrow \pi^*$, $v = 1$) at 401.10 eV.

(b) The spin-orbit splitting of 0.90 eV [61] has been used to estimate the $2p_{3/2}$ and $2p_{1/2}$ spin-orbit components from the 2p (mean) values [31], see text for details.

(c) The 2p(mean)-2s separation was taken to be 57.36 eV based upon the average of other P 2p(mean)-2s separations [175]. This value is within 0.17 eV of all the other separations [175].

(d) Final occupied orbital with either $2p_{3/2}$ or $2p_{1/2}$ hole state. Note that for peaks 3-6 two alternative assignments (A or B) are given (see text) for the two components with $\sigma^*(a_1)$ as the final orbital.

† With respect to 2p (mean) edge [31].

features in the PH_3 spectrum (compare Fig. 5.3 with Fig. 5.2). On this basis features 1, 3-4, and 6 or 1, 3, and 5 in the $P(CH_3)_3$ could be related to features 1, 2, and 3 in the PH_3 spectrum. If this is the case, then features 1 and 3 (Fig. 5.3) can be assigned as the two spin-orbit components of the $2p \rightarrow \sigma^*(e)$ transition and either features 3 and 5 (Scheme A, Table 5.3), or features 4 and 6 (Scheme B, Table 5.3) to the two components of the $2p \rightarrow \sigma^*(a_1)$ transition. The rest of the spectral intensity would then be due to various Rydberg transitions. Feature 2, for instance, would be due in both schemes to the $2p \rightarrow (2p_{3/2})^{-1}4s$ transition with feature 4 having a contribution from the concomitant $2p \rightarrow (2p_{1/2})^{-1}4s$ transition. Based upon the quantum defect calculated from the term value of feature 2, the predicted 5s term value is 1.34 eV, which allows feature 5 to also be assigned as the $2p \rightarrow (2p_{3/2})^{-1}5s$ transition. Transitions to the d Rydberg levels would also be expected. Table 5.2 summarises the possible assignments.

Phosphorus Trifluoride (PF_3)

The 2p spectrum of PF_3 (Fig. 5.4) is rather different from that of the isoelectronic molecule $P(CH_3)_3$ (Fig. 5.3). The data for both the 2p and 2s spectra are shown in Fig. 5.4 and summarised in Table 5.4. There is a clear difference in the 2p spectra which may be ascribed to the effects on the valence-Rydberg separation by the electronegative F ligand as compared to the electron donating $-CH_3$ ligand. Features 1-3 are clearly transitions to virtual valence orbitals, as indicated by the large term values. The second band (features 4-7) is probably comprised

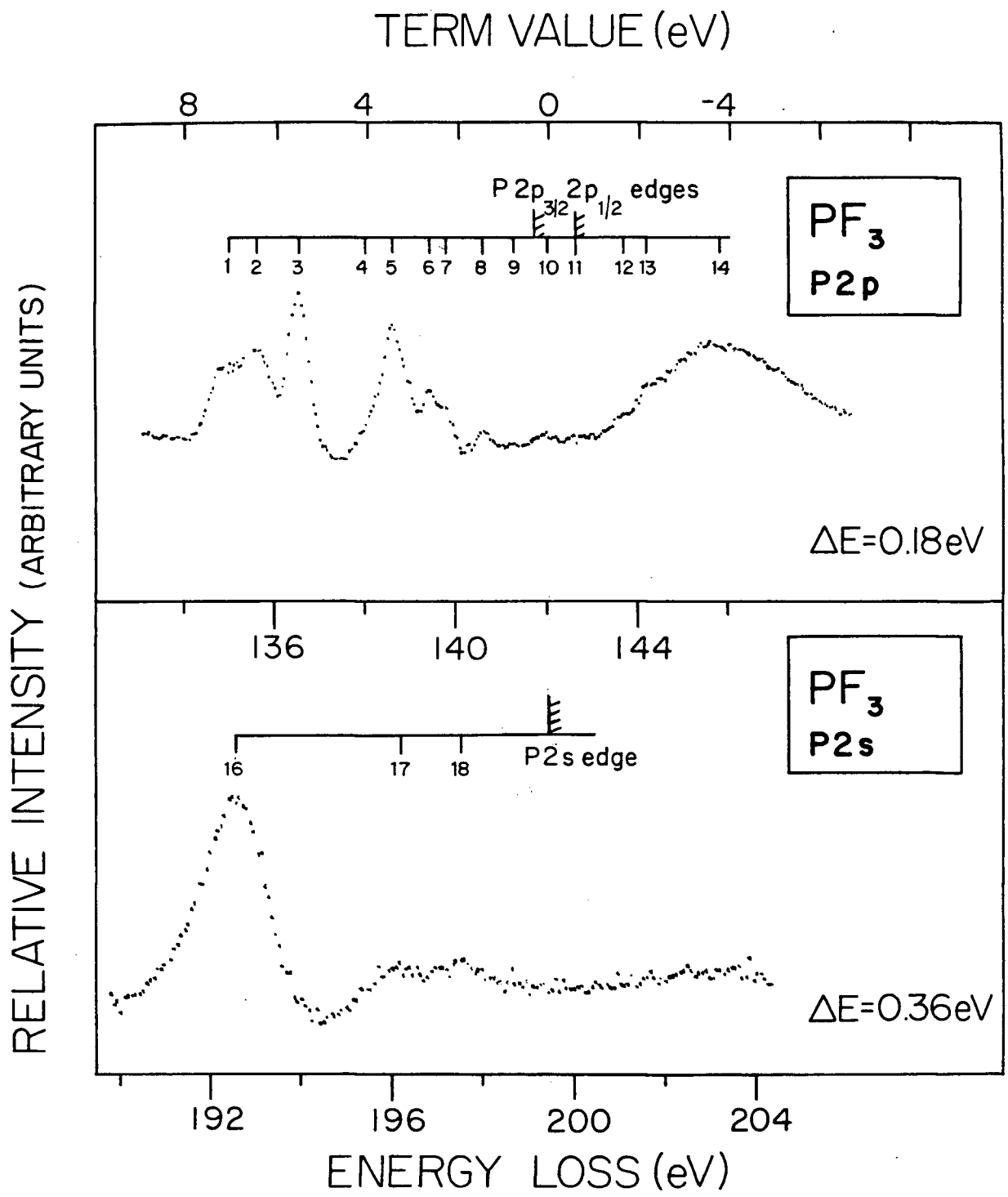

Figure 5.4: Phosphorus 2p and 2s electron energy loss spectra of PF_3. The P 2p spectrum (upper trace) is at high resolution (0.18 eV FWHM). The P 2s spectrum (lower trace) is extracted from Fig. 5.1. The spectra are aligned with respect to the 2p(mean) and 2s ionisation edges.

TABLE 5.4

Energies, Term Values, and Possible Assignments for the P 2p,2s Spectra of PF_3

Feature	Energy Loss[a] (eV)	Term Value (eV)		Possible Assignments[d]	
		$2p_{3/2}$	$2p_{1/2}$	$2p_{3/2}$	$2p_{1/2}$
1	135.00	6.77		$\sigma^*(e)$	
2	135.61	6.16	7.06	$\sigma^*(e)$	
3	136.52	5.25	6.15		$\sigma^*(e)$
4	138.0 (2)	3.77	4.67	$\sigma^*(a_1)$	
5	138.64	3.13	4.03	4s	$\sigma^*(a_1)$
6	139.45	2.32	3.12		4s
7	139.83 (10)	1.94	2.84	3d	
8	140.61	1.16	2.06	5s, 4d	3d
9	141.30 (12)	0.47	1.37		5s, 4d
10	142.03 (15)		0.64	edge	
11	142.7		0		edge
$2p_{3/2}$ limit[b]	141.77	0			
$2p_{1/2}$ limit[b]	142.67		0		
12	143.74 (20)			"Shake-up"	
13	144.25 (20)				
14	145.9 (3)	-3.8†		inner-well state/shape-resonance	
15	157.3 (5)	-15.2†		shape-resonance	
		2s			
16	192.60 (15)	6.89		2s → $\sigma^*(e)$	
17	196.21 (20)	3.28		2s → $\sigma^*(a_1)$	
18	197.53 (20)	1.96		2s → 4p	
2s limit[c]	199.49	0			

(a) Estimated uncertainty in energy-loss values is ± 0.08 eV except where stated. Spectra are calibrated against N_2 ($1s \rightarrow \pi^*$, v = 1) at 401.10 eV.

(b) The spin-orbit splitting of 0.90 eV [61] has been used to estimate the $2p_{3/2}$ and $2p_{1/2}$ spin-orbit components from the 2p (mean) values [31], see text for details.

(c) Ref. [175].

(d) Final occupied orbital with either $2p_{3/2}$ or $2p_{1/2}$ hole state.

† with respect to the 2p (mean edge) [31].

of transitions to the various Rydberg levels. However, the broad shape of the leading edge (feature 4) and also the width of feature 5 suggests that this band may consist of Rydberg transitions superimposed on top of a valence transition. This type of situation was observed for the Si 2p spectrum of SiF_4 [144] and in view of the similar ways in which the ligands seem to affect the central atom in the case of both P and Si, it is thought to be very likely here.

The 2s spectrum shows one intense peak (feature 16) which is assigned as $2s \rightarrow \sigma^*(e)$ (as in the case of PH_3 and also $P(CH_3)_3$) and the term value (6.89 eV) for this corresponds approximately to that for the first band (peaks 1-3) in the 2p spectrum. This feature (16) is followed by further structure (feature 17) which has a term value of 3.28 eV, which corresponds with that for features 4-5 in the 2p spectrum. Since the $2s \rightarrow 4s$ Rydberg transition would be expected to be very weak (it would correspond to a dipole forbidden $s \rightarrow s$ transition in the atomic core), this feature (17) has been assigned as the $2s \rightarrow \sigma^*(a_1)$ transition. Thus on this basis the $\sigma^*(e) - \sigma^*(a_1)$ separation would be quite large (~3.5 eV). This agrees with the Xα calculations of Xiao et al. [176], which predict a ground state separation of 3 eV. Feature 18 is presumably the $2s \rightarrow 4p$ Rydberg transition.

The first band of the 2p spectrum shows three components (peaks 1, 2, and 3). As stated earlier, this has been tentatively assigned to the various components of the $2p \rightarrow \sigma^*(e)$ transition. Peaks 1 and 2 are assigned to the two allowed final states of the $2p \rightarrow (2p_{3/2})^{-1}\sigma^*(e)$

transition (i.e., e <-> e, see Table 5.1) and peak 3 to the $2p \rightarrow (2p_{1/2})^{-1}\sigma^{*}(e)$ transition. The rest of the assignments of the features in the spectrum are summarised in Table 5.4.

Phosphorus Trichloride (PCl_3)

The 2p spectrum of PCl_3 (Fig. 5.5), as in the analogous spectra for PF_3 and PH_3, shows intense structure well below the edge, which must be due to transitions to the virtual valence orbitals because of the large term values (Table 5.5). This is followed by weaker Rydberg structure lying on top of a broad resonance in the region of the 2p edge. The electron impact excited spectrum reported here differs significantly from a previously reported optical (soft X-ray) spectrum [171, 172] in that a prominant extra peak (feature 4, Fig. 5.5) is observed (compare with the optical spectrum as shown in Fig. 5.6). The likelihood of this being due to an impurity seems remote in this spectral region since any phosphorus containing impurity arising from PCl_3 is likely to be extremely involatile and apart from this sharp feature the rest of the spectrum is in agreement with the optical result. However, the spectrum was carefully rechecked using a new sample of PCl_3 from a different source and found to be identical.

Another (non-spectroscopic) possibility is that the extra peak (4) arises from a "ghosting" effect due to the primary electron beam either hitting the anode or some other surface. The possibilities of the peak being due to energy losses caused by scattering from the anode

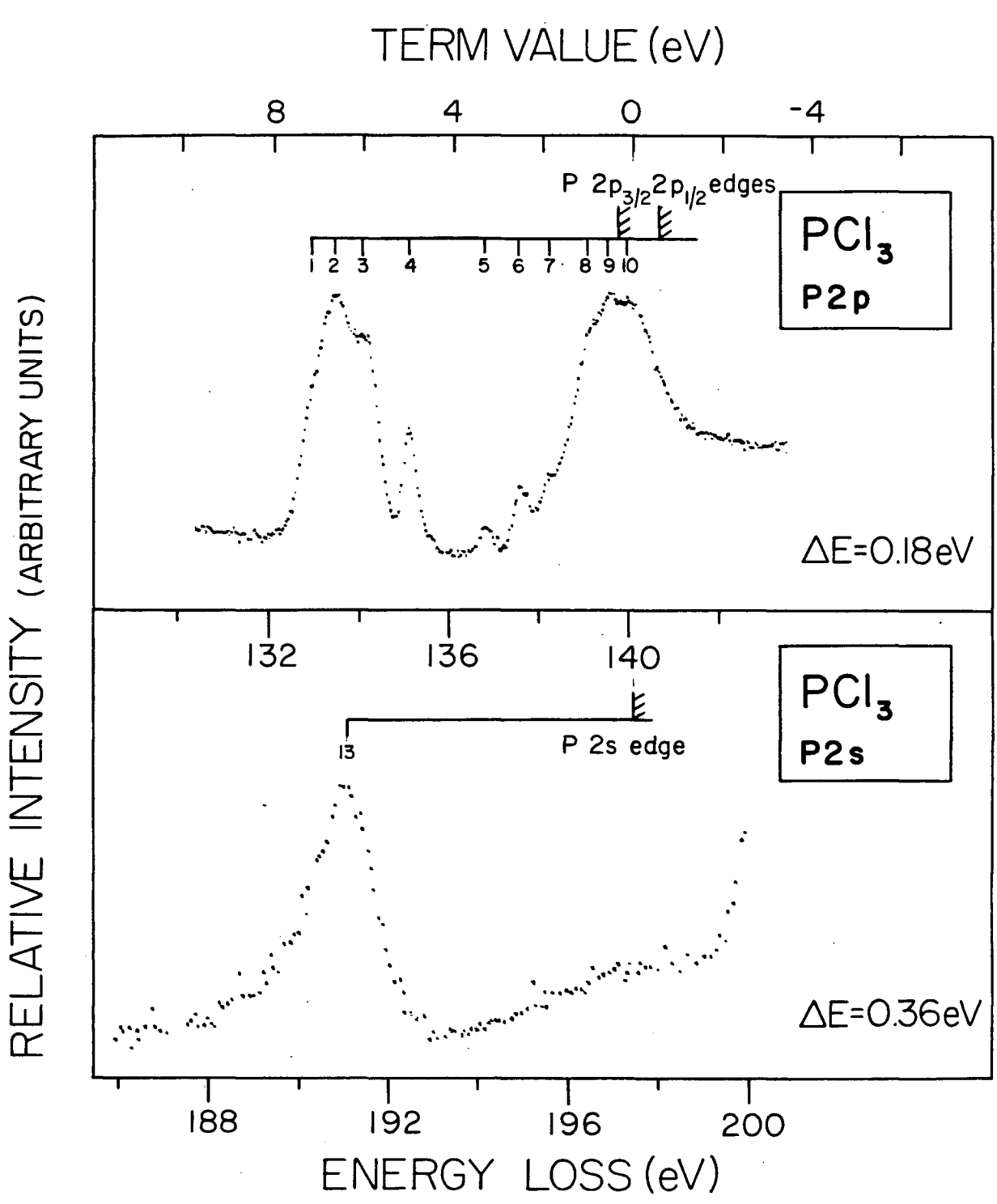

Figure 5.5: Phosphorus 2p and 2s electron energy loss spectra of PCl_3. The P 2p spectrum (upper trace) is at high resolution (0.18 eV FWHM) The P 2s spectrum (lower trace) is extracted from Fig. 5.1. The spectra are aligned with respect to the 2p(mean) and 2s ionisation edges.

TABLE 5.5

Energies, Term Values, and Possible Assignments for the P 2p,2s Spectra of PCl_3

Feature	Energy Loss[a] (eV)	Term Value (eV)		Possible Assignments[d]	
		$2p_{3/2}$	$2p_{1/2}$	$2p_{3/2}$	$2p_{1/2}$
1	132.98 (12)	6.86		$\sigma^*(a_1)$	
2	133.50	6.34	7.24	$\sigma^*(e)$	$\sigma^*(a_1)$
3	134.11 (10)	5.73	6.63		$\sigma^*(e)$
4	135.11	4.73	5.63	Symmetry Forbidden Transition	
5	136.84	3.00	3.93	4s	
6	137.61	2.23	3.13		4s
7	138.25	1.59	2.49	5s, 3d	on top of
8	139.10 (12)	0.74	1.64	6s, 4d	5s, 3d inner-well
9	139.57 (10)	0.27	1.17	etc	state/shape
10	139.98 (12)		0.76		6s, 4d resonance
$2p_{3/2}$ limit[b]	139.84	0			etc.
$2p_{1/2}$ limit[b]	140.74		0		
11	149.5 (5)	9.4†		Shape resonance	
12	152-168			+ "Shake-up"	
		2s			
13	191.07 (15)	6.40		predominantly 2s → $\sigma^*(e)$	
2s limit[c]	197.47	0			

(a) Estimated uncertainty in energy-loss values is ± 0.08 eV except where stated. Spectra are calibrated against N_2 ($1s \rightarrow \pi^*$, v = 1) at 401.10 eV.

(b) The spin-orbit splitting of 0.90 eV [61] has been used to estimate the $2p_{3/2}$ and $2p_{1/2}$ spin-orbit components from the 2p (mean) values [31], see text for details.

(c) Ref. [175]

(d) Final occupied orbital with either $2p_{3/2}$ or $2p_{1/2}$ hole state. Assignment in table for pyramidal excited states. See text for discussion on planar excited states.

†with respect to the 2p (mean) edge [31].

can be eliminated since it would occur at an energy loss equivalent to the anode voltage (~600 V, with respect to the cathode). As a further check the spectrum was also rerun using a lower impact energy of 1500 V instead of the original 2500 V, a procedure that involves complete retuning of the spectrometer. Since the conditions would now be different, any effects of "ghosting", if present, would be expected to change. No change in the number or energy of the spectral features was observed. In view of these observations, feature 4 can be assigned as a dipole-forbidden transition, which is observed in electron impact spectroscopy where the momentum transfer is finite. At the limit of zero momentum transfer the oscillator strength of such a transition should go to zero; i.e., the (dipole) optical oscillator strength vanish at the optical limit [2,8]. Under the conditions used in the present work the momentum transfer is kept as small as possible so as to ensure that dipole processes strongly dominate the spectra. In some earlier spectra weak, non-dipole processes have been observed under these conditions [69,109]. In the case of PCl_3, peak 4 is relatively much more intense than previously observed dipole-forbidden transitions. In order to confirm the optically forbidden nature of this transition the spectrum was run at 1500 V impact energy and several different deflection (scattering) angles up to ~5°, which is the limit of the present beam deflection system. At an impact energy of 1500 V it was possible to tune the spectrometer to operate at an even smaller scattering angle (and hence closer to zero momentum transfer) than at 2500 V due to improved electron optical focussing. Three spectra of PCl_3 and PF_3 obtained at

various momentum transfers (i.e., scattering angles) are shown in Fig. 5.6. The optical absorption spectrum (corresponding to zero momentum transfer) of PCl_3 [171] is also shown for comparison and it clearly indicates the absence of peak 4. In all other respects the ISEELS and optical spectra are equivalent. In the case of the ISEELS spectra a linear function, extrapolated from the leading edge, has been subtracted in order to facilitate the estimation of peak heights. The non-dipole nature of feature 4 in PCl_3 is clearly apparent since its relative intensity to the rest of the spectrum increases markedly with increase in scattering angle. From the dimensions of the deflector plates and the magnitude of the applied voltage it is possible to estimate the deflection angle (θ) for a given electron energy (see Table 2.1). These angles have been estimated for each of the spectra shown in Fig. 6 and used to obtain the momentum transfer, K, in atomic units (a.u.) (see equations 1.C.6 and 1.C.16). It is usual to consider the variation of relative intensities of allowed (or forbidden) transitions with K^2. A plot of the ratios (peak height of feature 4)/(peak height of feature 2) versus K^2 should extrapolate back to zero at zero momentum transfer if feature 4 is dipole forbidden [2,9]. This behaviour is found for feature 4 as indicated in Fig. 5.7, which also shows similar plots for some of the dipole-allowed features of the PCl_3 P 2p spectrum (features 3, 5, and 6 respectively of Fig. 5.6) over the limited range of momentum transfer possible with this instrument. In contrast to the behaviour for feature 4 it can be seen that the ratios for the dipole-allowed transitions remain almost constant. The steep rise in intensity of

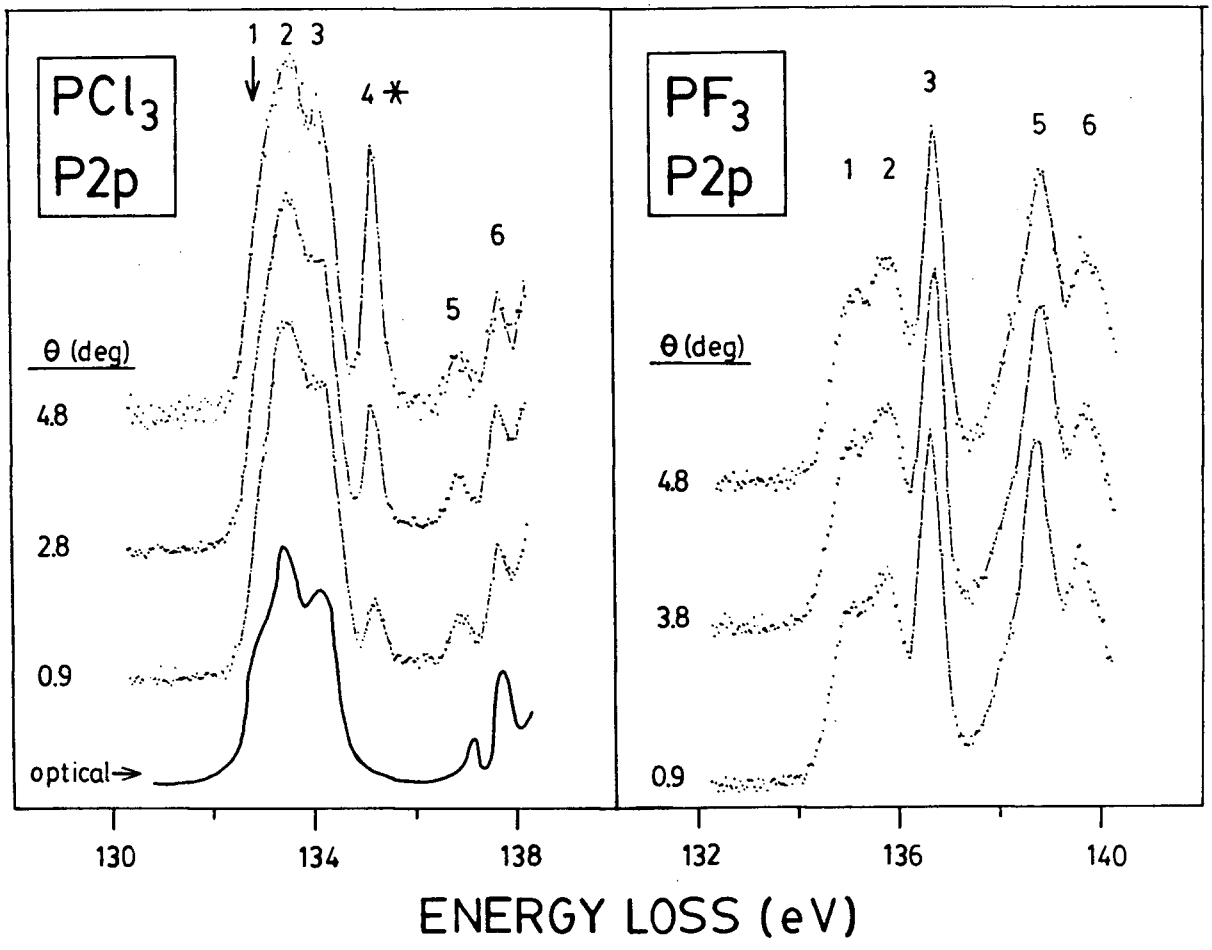

Figure 5.6: Inner shell electron energy loss spectra of (a) PCl_3 and (b) PF_3 at various scattering angles. The spectra were obtained with an impact energy of 1500 V. The dipole-forbidden transition in PCl_3 is marked with an asterisk (*). Also shown with the PCl_3 ISEELS spectrum is the optical spectrum taken from ref. [171].

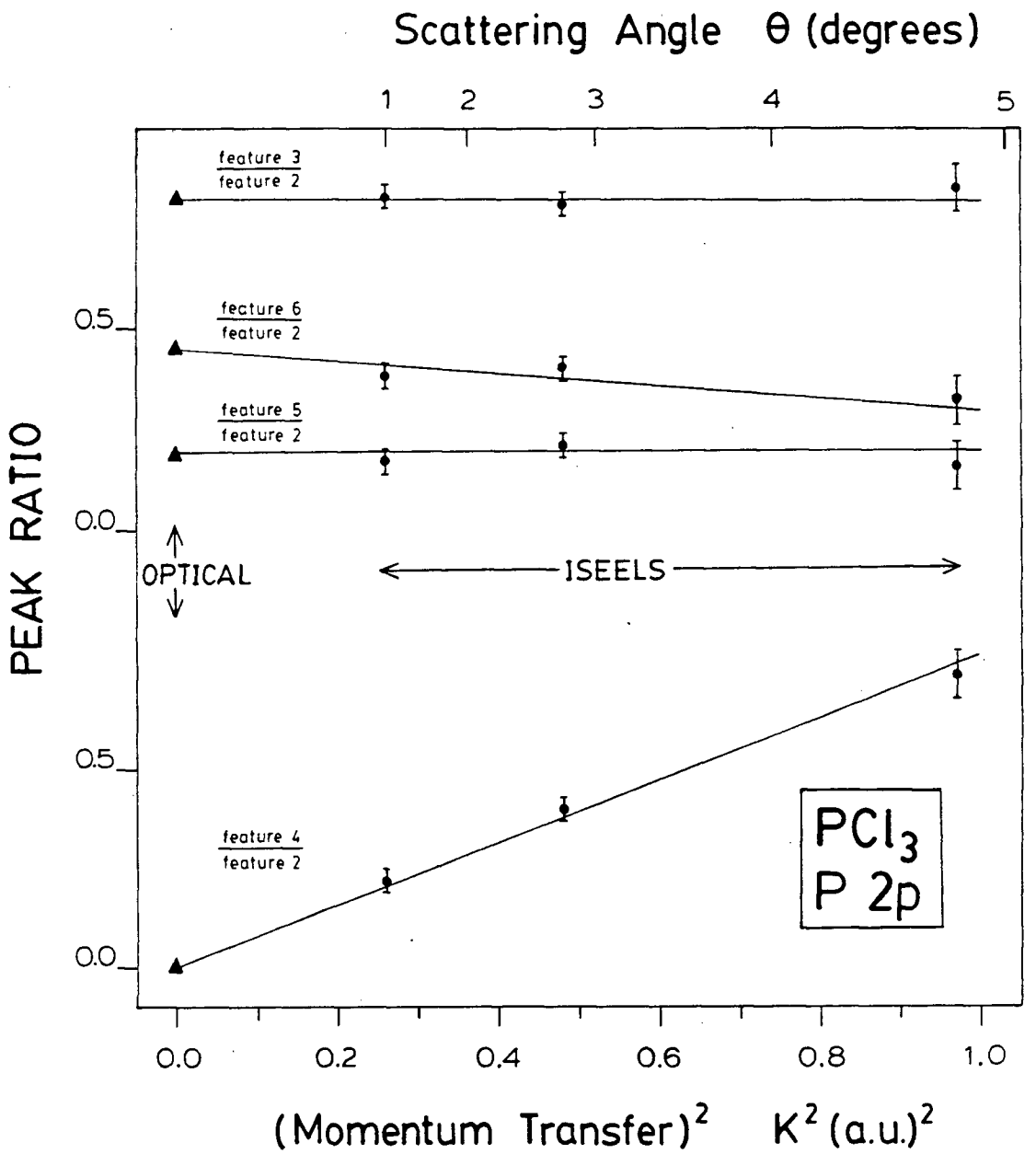

Figure 5.7: Plot of the ratio (peak height of feature X)/(peak height of feature 2) for various transitions (X) in the $_2PCl_3$ spectrum (Fig. 6) as a function of (momentum transfer)^2. Solid circles - ISEELS data; solid triangles - optical data [171].

feature 4 with increase in K^2 is notable in that this is much more rapid than is usually observed for forbidden transitions [2]. The PF_3 spectra (Fig. 5.6, right hand side) show no discernable changes over the same range of momentum transfer. The spectra of PH_3 and $P(CH_3)_3$ were also checked in the same way and again no discernable changes were apparent. The PF_3, $P(CH_3)_3$ and PH_3 were all run under the same conditions as the PCl_3 spectra and provide further evidence that peak 4 is in no way due to "ghosting" or other instrumental effects. The range of momentum transfer is quite small and the sudden and rapid emergence of peak 4 is quite unusual and without precedent in earlier ISEELS studies.

Consider now the assignment of the spectrum P 2p, 2s (Fig. 5.5) of PCl_3. Peaks 1-4 are clearly due to $2p \rightarrow \sigma^*$ levels. The term value for the $\sigma^*(e)$ level from the 2s spectrum (feature 13) is 6.40 eV. The fact that the term value for feature 1 is somewhat larger (6.86 eV) than 6.40 eV suggests this peak arises from the process $2p \rightarrow (2p_{3/2})^{-1}\sigma^*(a_1)$.

If this is the case, the ordering of the virtual levels would be $\sigma^*(a_1)$ followed by $\sigma^*(e)$. This is the reverse of the assignment given by Topol et al. [172] based on an Xα-SW calculation. However, since the calculation only gives a separation of 0.12 eV for the $\sigma^*(a_1)$ and $\sigma^*(e)$ levels the result is inconclusive. Feature 4 is clearly a symmetry-forbidden transition on the basis of the evidence presented above (see also Figs. 5.6 and 5.7). The only dipole-forbidden transition possible, within the C_{3v} point group of the pyramidal molecule, is $2p(e) \rightarrow (2p_{3/2})^{-1}\sigma^*(e)$, with an A_2 final state (see Table 5.1). The only other

possible explanation for feature 4 would arise if there is a geometry change in going to some of the upper states. If this occurs it would most likely be to states of D_{3h} (i.e., planar) symmetry. It is interesting to note that feature 4 is approximately a spin-orbit splitting away from feature 3. This can be explained within the context of a D_{3h} system. Table 5.6 shows the final configurations possible here for D_{3h} symmetry and whether they would be optically accessible from a D_{3h} ground state. It is seen that only the $(2p_{3/2})^{-1}$ $\sigma^*(e')$ (to an E' final state) is accessible under dipole selection rules. Thus feature 3 could be assigned to the dipole allowed $2p \rightarrow (2p_{3/2})^{-1}$ $\sigma^*(e')$ transition with feature 4 as the concomitant (dipole forbidden) $2p \rightarrow (2p_{1/2})^{-1}$ $\sigma^*(e')$ transition. From the spectra (Fig. 5.6) and the angular variation (Fig. 5.7) three dipole allowed features (1-3) are clearly present. Hence the remaining two dipole allowed features (1,2) could be due to $2p \rightarrow (2p_{3/2,1/2})^{-1}$ $\sigma^*(a_1)$ transitions with pyramidal upper and lower states. However, it should be remembered that the initial state is of C_{3v} symmetry and regardless of the final state geometry (i.e., C_{3v} or D_{3h}), the C_{3v} selection rules apply, but with the intensities of transitions being strongest for those which are allowed for both symmetries [178]. Examination of the optical spectrum (Fig. 5.6) shows at most a weak unresolved shoulder at position 4 and more likely no intensity at all in view of the tailing that is apparent on all peaks in the spectrum. The rapid emergence of feature 4 is of interest and clearly theoretical studies, as well as more systematic

TABLE 5.6

Transitions from the $^1A_1'$ Ground State for D_{3h} Symmetry

Final Configuration ‡		Final State	Dipole Allowed from ground state
hole state	occupied σ^* orbital		
e'	e'	$A_1' + A_2'$	No
e'	e'	E'	Yes
e'	a_2''	E"	No
a_2''	e'	E"	No
a_2''	a_2''	A_1'	No

‡ $(2p_{3/2})^{-1}$ and $(2p_{1/2})^{-1}$ holes are of e' and a_2'' symmetry respectively. The σ^* orbitals are of a_2'' and e' symmetry.

variable angle electron impact spectroscopy would be helpful in establishing the identity of this transition.

The remaining features (5-10) can be assigned to the various 2p → Rydberg transitions. The latter few being on top of an inner well trapped state or resonance evident by the large broad underlying peak at ~140 eV in Fig. 5.5 (see following section). The assignments are also summarised in Table 5.5.

Phosphorus 2p, 2s Spectra - Continuum Features

All the phosphorus spectra show considerable intensity at or beyond the 2p edge (Fig. 5.1). In the case of PH_3 this manifests itself as an inflection ~141.4 eV followed by a broad band with a maximum at ~157 eV. This has been attributed to a delayed onset caused by centrifugal barrier effects arising from p → continuum d-like state transitions [49,146]. This effect is seen in atoms (e.g., Si) as well as SiH_4 [146]. A closer examination of the continuum spectrum of PH_3 reveals structure between the edge and the band maximum. This is attributable to ionisation plus excitation ("shake-up"). In ISEELS (or photoabsorption) this would appear as onsets of new continua. An expansion of the PH_3 continuum spectrum is shown in Fig. 5.8 together with the satellite ("shake up") portion of the PH_3 (2p) XPS spectrum measured elsewhere [175]. Both spectra in Fig. 5.8 are plotted on the same horizontal relative energy scale. Much of the intensity in the continuum band of the ISEELS spectrum (upper trace) can be assigned to onsets of "shake-up" continua, evidenced by the peaks in the XPS spectrum (lower trace).

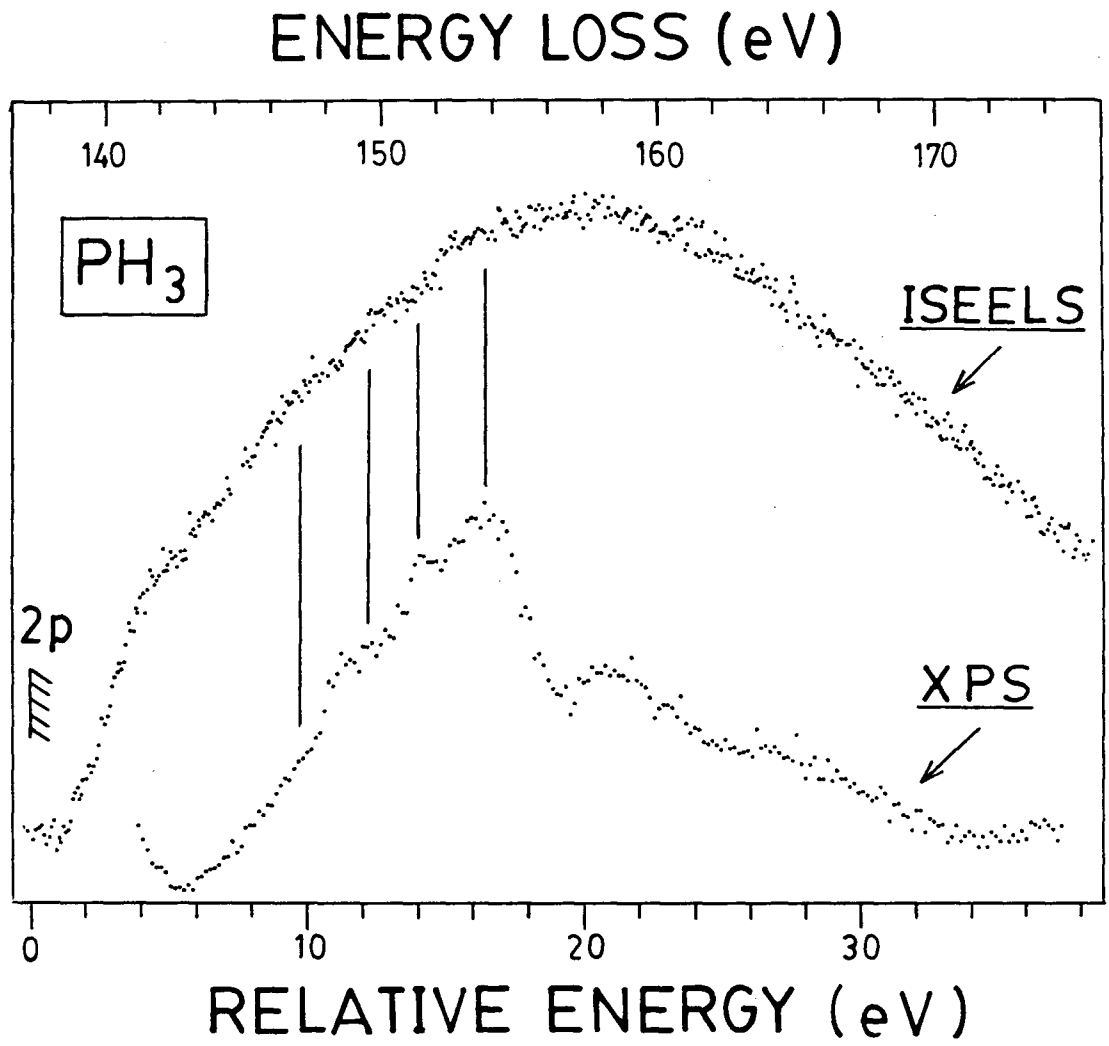

Figure 5.8: Expanded plot of the PH_3 P 2p ISEELS continuum structure. The 2p satellite structure from XPS measurements [175] is shown below plotted on the same relative energy scale, referenced to the 2p (mean) edge.

A similar explanation was used in Chapter 3 to explain continuum structures in ISEELS spectra of NF_3.

Considering now the other molecules whose spectra are shown in Fig. 5.1, it can be seen that the continuum structure is somewhat different to that in PH_3 with the oscillator strength being directed into more localised channels. This is directly attributable to the effects of the bulky, many electron ligands in contrast to the situation in PH_3. Indeed, compared to the other spectra, that for PH_3 is very atomic like in the continuum (compare also Si and SiH_4 [19]). The behaviour of this series of molecules is very similar to those seen in the Si series in Fig. 4.3 and the localised and intense continuum structure (particularly in the case of PF_3 and PCl_3) provide further examples of potential barrier or shape-resonance phenomena [73,77]. Thus both PCl_3 and PF_3 show an intense, sharp feature (Fig. 5.1) at (PCl_3-feature 10) or just beyond (PF_3 - feature 14) the edge which can be described as a resonance enhanced transition to a trapped (probably d-type) state. A small peak is also seen right at the edge in $P(CH_3)_3$, however, it is not as intense as in PF_3 or PCl_3. The methyl ligand is electron-donating [31,33] and so an effective potential barrier would not be expected. The lower intensity is consistent with this. Alternatively, the feature may simply be due to unresolved Rydberg levels converging onto the edge, or a combination of both effects.

All the three molecules show a broader structure between 10 and 20 eV above the edge. These can be attributed to higher d-like shape resonances, although, as has been discussed above, the structure in PH_3 can at least in part be associated with shake-up processes as also observed in XPS [175]. The shape of the PCl_3 structure is interesting in that it shows a sharp rise followed by further largely unresolved structure. It is possible that this shape is due to "shake-up" phenomena on top of the resonance structure as suggested above in the case of PH_3. It would be interesting to compare the ISEELS spectrum with the XPS satellite spectrum, but as yet this has not been reported.

In view of the recent spate of interest between resonance position and bond length [95-100] and the success of the limited series of Si containing compounds shown in the previous chapter, it is of interest to examine whether such a relationship also exists for these compounds. Table 5.7 summarises the relevant data for possible resonances in PF_3, PCl_3, and $P(CH_3)_3$. The lower energy resonance follows the trend observed for silicon, however, the good linear correlation found for the outer resonance in the silicon series is not apparent here. However, a detailed consideration of this phenomenan involves many factors such as different phase shifts of the scattering centre and varying geometries [99]. The reasonable correlation observed in the silicon series may reflect the constant tetrahedral geometry of all the silicon compounds studied. The failure of the correlation in the case of the PX_3 species may be due to their variable geometry. Clearly more

TABLE 5.7

Resonance Term Values δ(eV) and (P-X) Bond Length R(Å)

Molecule	R (Å)[a]	R^{-2} ($Å^{-2}$)	δ (lower) (eV)[b]	δ (higher) (eV)[c]
PF_3	1.563	0.4093	3.8	15.2
$P(CH_3)_3$	1.843	0.2944	0.5	16.7
PCl_3	2.043	0.2396	-0.1	9.4

(a) From Landholdt-Börnstein (New Series) II/7 "Structure Data of Free Polyatomic Molecules" Springer-Verlag, Berlin, 1976.

(b) First resonance position. Data from Tables 5.3-5.5.

δ = Resonance Energy - I.P.

(c) As (b), but for higher resonance.

systematic studies need to be made for a large group of molecules before more definite general conclusions can be drawn.

Ligand Spectra (F 1s, C 1s, and Cl 2p,2s)

The inner shell spectra of the various ligand regions (F 1s, C 1s, and Cl 2p,2s) are each typical of spectra associated with that particular edge. Each ligand spectrum will be discussed in turn and compared with the respective central atom spectra. The virtual valence orbital orderings as discussed in the preceding P 2p,2s spectra have been used in the assignment of the ligand spectra.

The F 1s spectrum of PF_3 is shown in Fig. 5.9 and summarised in Table 5.8. The spectrum consists of a relatively intense peak followed by a broad band with some structure both before and after the edge. The position of the edge is taken from XPS measurements [179]. The F 1s orbitals of PF_3 transform as a_1 and e symmetries and so transitions to all the virtual orbitals (a_1 and e) are possible. Therefore, the first peak is assigned as the F 1s $\rightarrow \sigma^*(e)$ transition using the virtual orbital ordering as assigned in the P 2p,2s spectra. This peak has a term value of 5.2 eV, which is approximately 1.5 eV lower than that for the P 2s or P 2p $\rightarrow \sigma^*(e)$ transition. The difference is of the same order as that found between the N 1s and F 1s $\rightarrow \sigma^*$ transitions in NF_3 (Chapter 3) and that for the S 2p and F 1s $\rightarrow \sigma^*$ transitions in SF_6 [69]. As was previously noted, this difference is directly attributable to the location of the core hole, since the creation of a core hole on the central atom effectively increases the core charge by one, and hence the

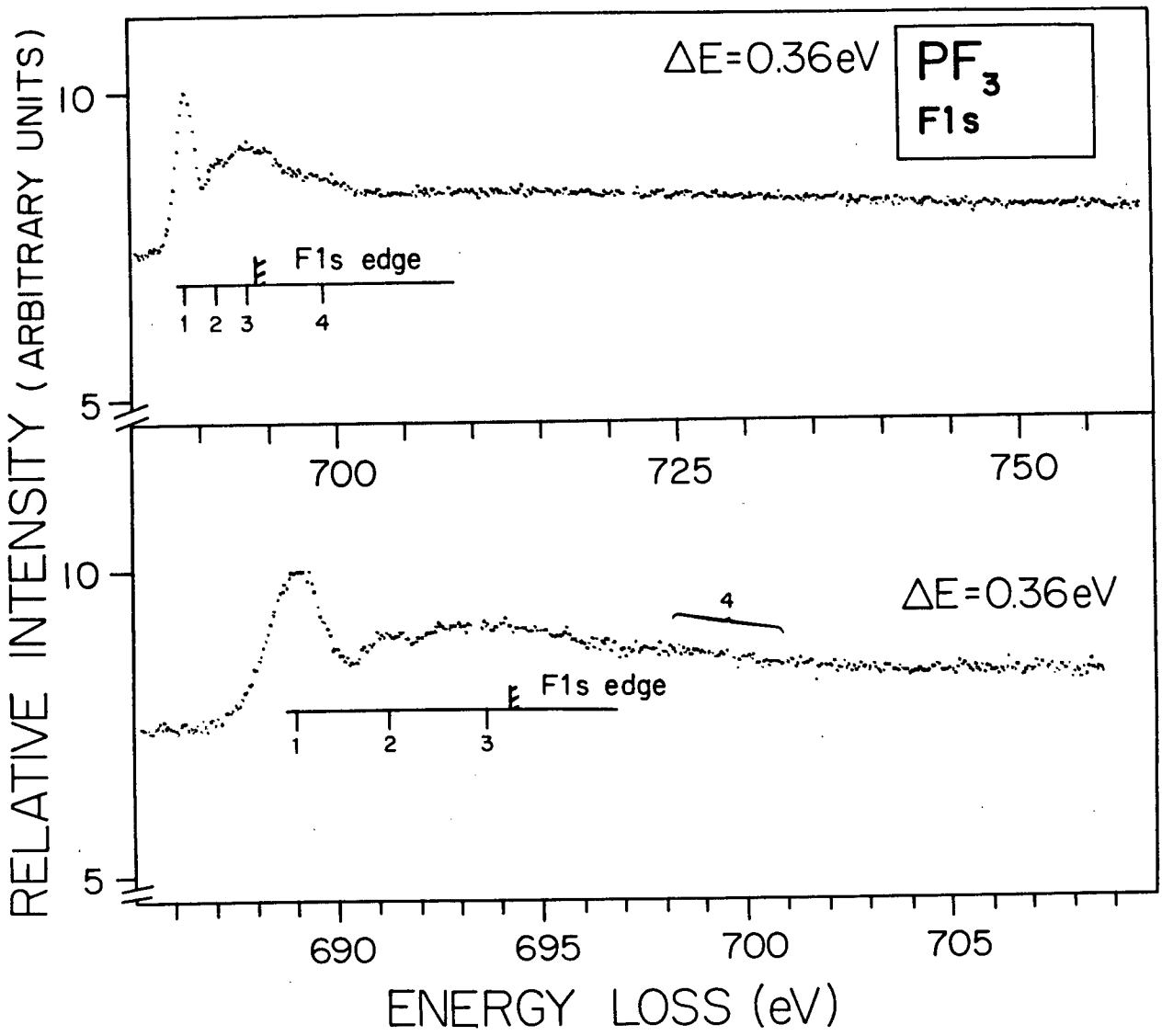

Figure 5.9: Long-range and detailed inner shell electron energy loss spectra of the F 1s region of PF_3.

TABLE 5.8

Energies, Term Values, and Possible Assignments for F 1s Spectrum of PF_3

Feature	Energy Loss[a] (eV)	Term Value (eV)	Possible Assignments
1	688.98 (15)	5.2	$\sigma^*(e)$
2	691.22 (20)	3.0	$\sigma^*(a_1)$/Rydberg
3	693.64 (30)	0.6	Rydberg
F 1s limit[b]	694.2	0	Ionisation edge
4	699.6 (5)	-5.4	d-like shape resonance

(a) Estimated uncertainty given in brackets.

(b) Ref. [179].

σ^* orbital energies are determined by a Z+1 central core, whereas the creation of a peripheral core hole on the F ligand has less effect on the energy of the localised σ^* orbital. Thus the electron in a virtual orbital will have a higher term value when there exists a central hole as opposed to a peripheral hole. The rest of the features can be assigned in a straightforward manner. Feature 2 is assigned, on the basis of its term value, as the F 1s $\rightarrow \sigma^*(a_1)$ transition, but may also include Rydberg transitions. Feature 3 is probably due to Rydberg series converging onto the edge. The weak continuum structure (4) at 699.6 eV is presumably an inner-well state/shape-resonance.

Figure 5.10 shows the C 1s spectrum of $P(CH_3)_3$. The data is summarised in Table 5.9. The C 1s edge is determined from XPS [180]. The spectrum is similar to that of CH_4 [65] and to the C 1s spectrum of $Si(CH_3)_4$ (Fig. 4.5). In assigning the spectrum of $Si(CH_3)_4$ it was useful to compare it with the C 1s spectra of mono substituted methyl halides [64]. A similar process will be used here. Features 1 and 2 are assigned as the C 1s $\rightarrow$ 4s(a_1) and C 1s $\rightarrow$ 4p(e) Rydberg transitions‡. In contrast to the present case for $P(CH_3)_3$, the analogous features in the methyl halide spectra were clearly resolved. It should be noted that the spectrum recorded here for $P(CH_3)_3$ was run at a higher resolution than for the methyl halide spectra [64]. With this in mind, and with the apparent relative closeness of the s and p levels, it is suggested that a C 1s $\rightarrow \sigma^*$ transition is also contained within this

‡ Since the central atom is from the third row (i.e., P), the first Rydberg levels are the 4s and 4p levels.

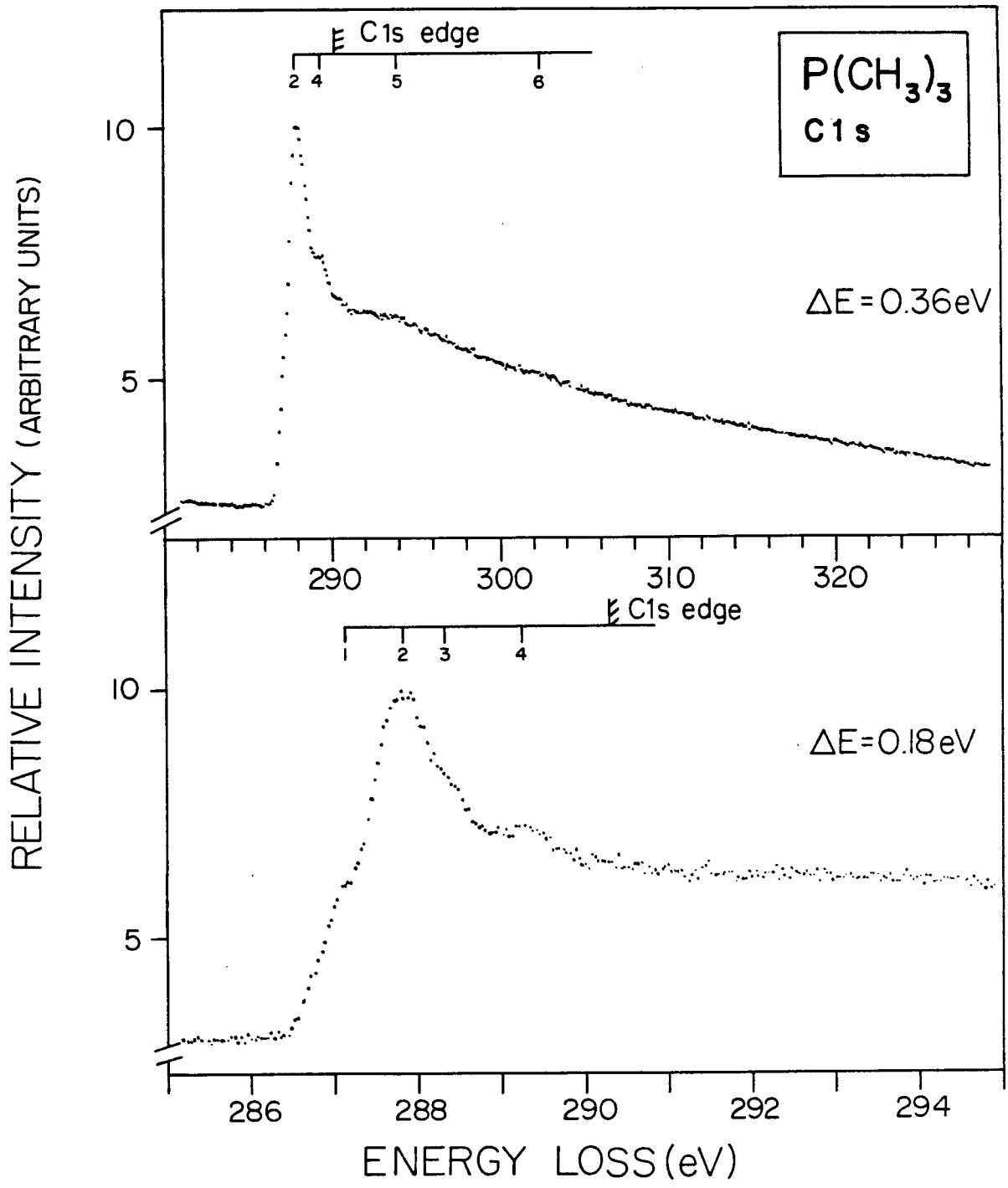

Figure 5.10: Long-range and detailed inner shell electron energy loss spectra of the C 1s region of $P(CH_3)_3$.

TABLE 5.9

Energies, Term Values, and Possible Assignments for C 1s Spectrum of $P(CH_3)_3$

Feature	Energy Loss[a] (eV)	Term Value (eV)	Possible Assignments
1	287.13	3.17	4s on top of σ^*
2	287.83 (8)	2.47	4p(e)
3	288.31	1.99	4p(a_1)
4	289.24	1.06	5p, 3d
C 1s limit[b]	290.30		
5	293.5 (3)	-3.20	"shake-up"
6	302.5 (5)	-12.20	or resonance

(a) Estimated uncertainty ± 0.10 eV except where stated.

(b) Ref [180].

feature. The term values from the P 2p spectrum are consistent with this interpretation. The core hole being localised on the C could very easily lower the term value for the *(e). Indeed, with the close proximity of the *(e) and 4p(e) states the spectrum might be better described in terms of a mixed Rydberg-Valence state [20] as discussed earlier for simpler molecules. Feature 3 is assigned as the C 1s → 4p(a_1) transition and feature 4 to the C 1s → 5p and 3d Rydberg levels. Post-edge structure can also be seen and can be attributed to either "shake-up" or resonances. Structure 6 (~303 eV) is seen in many hydrocarbon spectra and likely to be a σ^{*}(C-H) resonance [100].

Finally the Cl 2p,2s spectrum of PCl_3 is considered. The spectra are shown in Fig. 5.11 and summarised in Table 5.10. The positions of the Cl $2p_{3/2}$ and $2p_{1/2}$ spin-orbit components have been estimated from the reported Cl 2p (mean) XPS value [179] using spin-orbit separation of 1.6 eV [181] along with a 2:1 spectral weighting. The Cl 2s edge was taken from XPS data [179]. The spectrum is in good agreement with the previously published Cl 2p optical absorption spectrum of PCl_3[172,173]. This spectrum is very similar to other Cl L-shell spectra recorded for the various chloromethanes [182].

Features 1 and 2 are attributed to the spin-orbit components of the 2p → σ^{*}(a_1) transitions and features 2 and 3 to the 2p → σ^{*}(e). Since the σ^{*} levels are close, as indicated in the P 2p spectrum, it is possible that 1 and 2 contain all of these transitions. The concept of using the Cl 2s term value to estimate the positions of the σ^{*} components is not as straightforward here since the Cl 2s orbitals

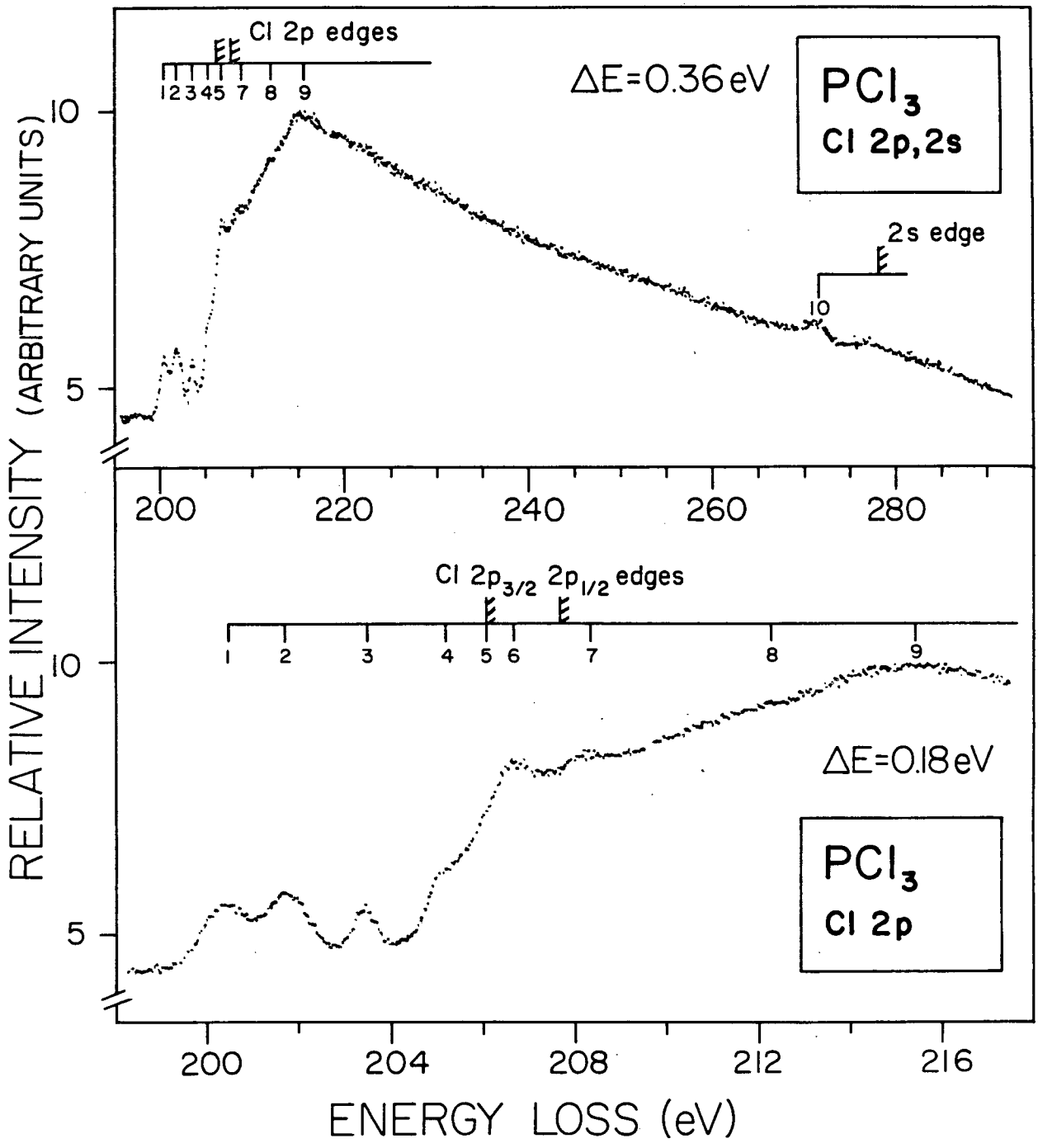

Figure 5.11: Long-range and detailed electron energy loss spectra of the Cl 2p and 2s regions of PCl_3.

TABLE 5.10

Energies, Term Values, and Possible Assignments for the Cl 2p,2s Spectra of PCl_3

Feature	Energy Loss[a] (eV)	Term Value (eV)		Possible Assignments[d]		
		$2p_{3/2}$	$2p_{1/2}$	$2p_{3/2}$	$2p_{1/2}$	
1	200.41	5.7		$\sigma^*(a_1)$		or $2p \rightarrow \sigma^*$
2	201.66	4.4	6.0	$\sigma^*(e)$	$\sigma^*(a_1)$	
3	203.43 (8)	2.6	4.2	4s	$\sigma^*(e)$	or $2p \rightarrow 4s$
4	205.14 (12)	0.9	2.5		4s	
5	206.05	0	1.6	etc.		
6	206.65	-0.6	1.0		etc	on top of
7	208.32		-0.7			resonance
Cl $2p_{3/2}$ limit[b]	206.1					
Cl $2p_{1/2}$ limit[b]	207.7					
8	212.24 (15)	-5.6†		"Shake-up" or resonance		
9	215.43 (30)	-8.8†				
		2s				
10	271.7 (3)	6.5		$2s \rightarrow \sigma^*$		
Cl 2s limit[c]	278.2	0				

(a) Estimated uncertainty in energy-loss values is ± 0.08 eV except where stated.

(b) The spin-orbit splitting of 1.6 eV [181] has been used to estimate the $2p_{3/2}$ and $2p_{1/2}$ spin-orbit components from the 2p (mean) values [179]. Same procedure as for the P 2p has been used.

(c) Ref. [179]

(d) Final occupied orbital with either $2p_{3/2}$ or $2p_{1/2}$ hole state.

† with respect to 2p (mean) edge [179].

transform as both a_1 and e combinations. The term values for the transitions in the Cl 2p spectra are lower than in the P 2p spectra, consistent with the peripheral location of the core hole.

Features 3 and 4 have term values of 2.6 eV and 2.5 eV from the $2p_{3/2}$ and $2p_{1/2}$ edges respectively. This is consistent with a transition to the 4s Rydberg level and they have been assigned accordingly. Thus feature 3 is either solely due to a Rydberg transition or to a combination of valence and Rydberg. The rest of the features can be assigned to various Rydberg transitions. The rapid and intense rise in oscillator strength in the region of the ionisation edge suggests that this may be on top of a broad $2p \rightarrow \sigma^*(a_1)$ resonance - as was found in the P spectrum. The oscillator strength beyond the edge is probably due to various d-like shape-resonances or "shake-up".

CHAPTER 6

ELECTRONIC EXCITATIONS IN PHOSPHORUS CONTAINING MOLECULES. II. INNER SHELL ELECTRON ENERGY LOSS SPECTRA OF PF_5, OPF_3 AND $OPCl_3$

In the preceding chapter, the ISEELS spectra of the trivalent compounds PH_3, PF_3, PCl_3 and $P(CH_3)_3$ were examined and also compared with the spectra of the analogous silicon series. The ligands were seen to have a similar effect on the central atom core spectra for both series, however, unlike the silicon series there did not seem to be a similar linear relationship for shape-resonance position with bond length in the limited pshosphorus series. In the analysis of the P 2p spectra it was found that the term values obtained from the P 2s spectra were very useful. In this chapter, the study of the ISEELS spectra of phosphorus compounds is extended to include PF_5, OPF_3 and $OPCl_3$. The relationship of resonance position with bond length will be further examined as will the assumption that term values from the same core atom centre are transferable. As before, all inner shell regions accessible with the current instrumentation (P L-shell, Cl L-shell, O and F K-shells) are presented.

Experimental Details

The spectra were recorded and calibrated in the same manner as for the trivalent phosphorus compounds.

RESULTS AND DISCUSSION

Phosphorus Spectra

The long-range P 2p,2s spectra are shown in Fig. 6.1. Also shown on the spectra are the positions of the ionisation edges taken from XPS [31,175]. As only the mean 2p values were reported [31] the positions of the $2p_{3/2}$ and $2p_{1/2}$ spin-orbit components were estimated as before, using a spin-orbit splitting of 0.90 eV [61] in conjunction with a spectral weighting of 2:1 (i.e., $2p_{3/2}$ = 2p - 0.30 eV, $2p_{1/2}$ = 2p + 0.60 eV). A comparison of the spectra reported here with the PF_3 and PCl_3 spectra (Fig. 5.1) show a number of similarities which can be associated with the effects of the electronegative ligands. The discrete portions show relatively strong transitions to the virtual valence orbitals at the expense of Rydberg transitions. These are followed by intense transitions which are at the edge in the chloro-compounds, and just beyond the edge in the fluoro-compounds, and these features can be associated with inner-well trapped states/shape-resonances [73,77]. Following this, the spectra show broad continuum features which are also associated with shape-resonances [77]. The nature of the edge and post-edge features will be discussed in more detail later, but first the discrete portions of the spectra will be discussed.

The higher resolution 2p spectra of these compounds have also been obtained and each spectrum is discussed below in turn in comparison with the corresponding 2s region. The 2s spectra are plotted on the same horizontal scale as the 2p spectra. In order to render the features more apparent, a linear ramp, extrapolated from the leading

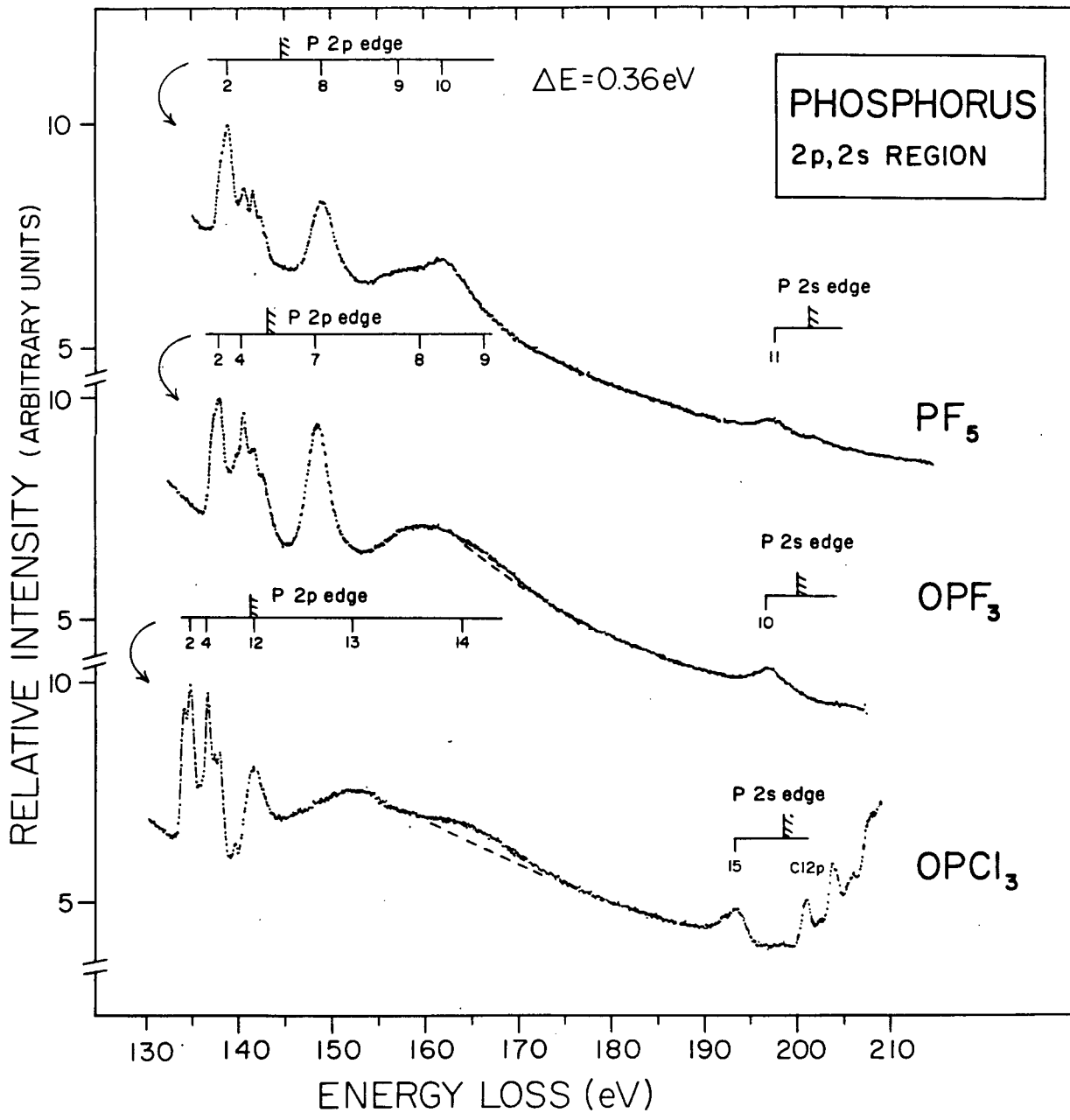

Figure 6.1:

Phosphorus 2p,2s wide range electron energy loss spectra of PF_5, OPF_3, and $OPCl_3$. All spectra were obtained with an impact energy of 2500 V, a scattering angle ~1°, and a resolution of 0.36 eV FWHM.

edge, has been subtracted from the 2s spectra. The OPF_3 and $OPCl_3$ spectra were extracted from the long-range spectra shown in Fig. 6.1, whereas the PF_5 2s spectrum was rerun separately. The P 2p and P 2s spectra are lined up on their respective ionisation edges. In the case of the 2p spectra the mean value of the $2p_{3/2,1/2}$ ionisation edges was used. The 2s spectra are considerably broader than those for the 2p spectra due to fast autoionisation processes of a Coster-Kronig type. Two assumption used in Chapter 5 will also be made here, namely:

(i) the major intensity in the 2s spectrum can be attributed to transitions to orbitals with the largest p orbital content as they will have the largest s → p (atomic) dipole allowed contribution.

(ii) since the core-hole vacancy is situated on the same atom, term values from the 2s spectra are transferable to the 2p region.

Phosphorus Pentafluoride - PF_5

This molecule belongs to the D_{3h} point group. The possible transitions are listed in Table 6.1. Using a minimal basis set, the vacant orbitals are of a_1', e' and a_2'' symmetry. Since in the case of PF_5 the 2s orbital is of a_1' symmetry and the p orbitals transform as e' and a_2'', the following transitions should be dipole allowed in the phosphorus L-shell spectra:

TABLE 6.1

Transitions from the $^1A_1'$ Ground State in D_{3h} Symmetry

Final Configuration ‡		Final State	Dipole Allowed from ground state
hole state	occupied σ^* orbital		
a_1'	a_1'	A_1'	No
a_1'	e'	E'	Yes
a_1'	a_2''	A_2''	Yes
e'	a_1'	E'	Yes
e'	e'	E'	Yes
e'	e'	$A_1' + A_2'$	No
e'	a_2''	E"	No
a_2''	a_1'	A_2''	Yes
a_2''	e'	E"	No
a_2''	a_2''	A_1'	No

‡ $(2s)^{-1}$, $(2p_{3/2})^{-1}$ and $(2p_{1/2})^{-1}$ holes are of a_1', e' and a_2'' symmetry respectively. The σ^* orbitals are of a_1', e' and a_2'' symmetry.

$2s(a_1') \rightarrow \sigma^*(a''_2),\ \sigma^*(e')$

$2p(e') \rightarrow (2p_{3/2})^{-1}\sigma^*(a_1'),\ (2p_{3/2})^{-1}\sigma^*(e')$

$2p(a_2'') \rightarrow (2p_{1/2})^{-1}\sigma^*(a_1')$

The transition $2p(a_2'') \rightarrow (2p_{1/2})^{-1}\sigma^*(e')$ is formally dipole forbidden. From a consideration of the spectrum which is shown in Fig. 6.2, and the spin-orbit splittings of the $2p_{3/2,1/2}$ ionization edges, it seems reasonable to assign features 1 and 2 as the spin-orbit components of the $2p \rightarrow \sigma^*(a_1')$ transition. Feature 3 is the $2p(e') \rightarrow (2p_{3/2})^{-1}\sigma^*(e')$ transition. It has a very similar term value to feature 11, which is assigned as the $2s \rightarrow \sigma^*(e)$ transition. Feature 12, which has no counterpart in the 2p spectrum, is then the $2s \rightarrow \sigma^*(a_2'')$ transition. The rest of the features 4-7, which are relatively sharp, are assigned to various 2p → Rydberg transitions. The assignments are summarised in Table 6.2.

Two points should be emphasised in connection with the above assignments. Firstly, the respective term values for the transitions to the $\sigma^*(e')$ orbital from the 2p(e') and 2s orbitals agree to within 0.1 eV. Secondly, as would be expected, the intensity of the transition assigned to the 2s electron to the doubly degenerate $\sigma^*(e')$ orbital (mainly of P 3p(x,y))[†] is much greater than that to the non-degenerate

---

[†] The principal axis of the molecule in the present work is designated as the z axis.

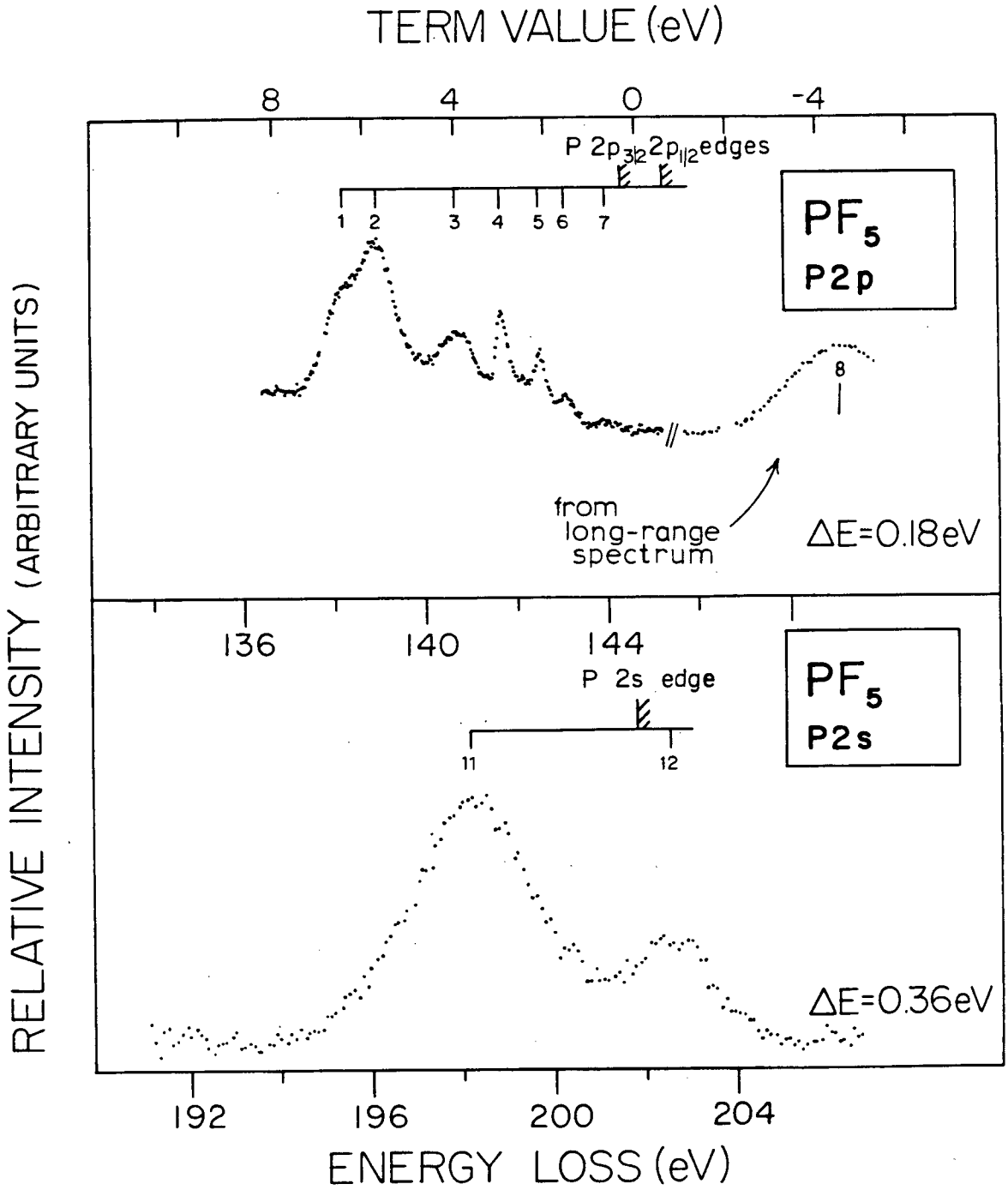

Figure 6.2:

Phosphorus 2p and 2s electron energy loss spectra of PF_5. P 2p spectrum (upper trace) is at high resolution (0.18 eV FWHM). P 2s spectrum (lower trace) is at 0.36 eV FWHM. The spectra are aligned with respect to the 2p (mean) and 2s ionisation edges.

TABLE 6.2

Energies, Term Values, and Possible Assignments for the P 2p,2s Spectra of PF_5

Feature	Energy Loss[a] (eV)	Term Value (eV)		Possible Assignments[d]	
		$2p_{3/2}$	$2p_{1/2}$	$2p_{3/2}$	$2p_{1/2}$
1	138.22 (12)	6.16		$\sigma^*(a_1')$	
2	138.97 (10)	5.41	6.31		$\sigma^*(a_1')$
3	140.73 (10)	3.65	4.55	$\sigma^*(e')$	
4	141.67	2.71	3.61	4s	
5	142.51	1.87	2.77	3d	4s
6	143.10	1.28	2.18	5s, 4d	3d
7	144.00	0.38	1.28		5s, 4d
$2p_{3/2}$ limit[b]	144.38	0			
$2p_{1/2}$ limit[b]	145.28		0		
8	149.1 (3)	-4.4†		inner-well state/shape-resonance	
9	157.5 (5)	-12.8†		$\sigma^*(P\text{-}F_{ax})$ shape resonance	
10	162.2 (5)	-17.5†		$\sigma^*(P\text{-}F_{eq})$ shape resonance	
		2s			
11	198.12 (20)	3.75		$2s \rightarrow \sigma^*(e')$	
2s limit[c]	201.87	0			
12	202.60	-0.73		$2s \rightarrow \sigma^*(a_2'')$	

(a) Estimated uncertainty in energy-loss values is ± 0.08 eV except where stated. Spectra are calibrated against N_2 ($1s \rightarrow \pi^*$, v = 1) at 401.10 eV.

(b) The spin-orbit splitting of 0.90 eV [61] has been used to estimate the $2p_{3/2}$ and $2p_{1/2}$ spin-orbit components from the 2p edge (mean) values [31], see text for details.

(c) Ref. [175].

(d) Final occupied orbital with either $2p_{3/2}$ or $2p_{1/2}$ hole state.

† With respect to the 2p edge (mean) [31].

$\sigma^*(a_2'')$ orbital (mainly of P 3p(z)). This also lends support to the interpretation of the 2s spectra of the trivalent phosphorus compounds where the maximum intensity of the broad envelope was ascribed to the degenerate $\sigma^*(e)$ orbital.

Phosphoryl Trifluoride - OPF_3

The assignment of the P 2p spectrum of OPF_3 (Fig. 6.3) is less clear than that of PF_5 due to the fact that it is a mixture of overlapping transitions. In this regard the situation is similar to that for the central atom ISEELS spectra of PF_3 (Fig. 5.4) and also the optical absorption spectrum of SiF_4 [144]. Thus the spectrum presumably consists of a transition to a virtual orbital, followed by a transition to a higher virtual orbital with superimposed Rydberg transitions. The spectral shape is certainly consistent with such an assignment. The ground state molecule, like its counterpart PF_3, is of C_{3v} symmetry for which the dipole-allowed transitions are listed in Table 5.1.

The vacant orbitals, using a minimal (no d) basis set, are of a_1, e and a_1 symmetry. Transitions to all these levels are possible from the 2s and 2p orbitals. A CNDO/2 calculation indicates that the first a_1 orbital is predominantly P 2s in character and so should show little intensity in the P 2s spectrum. The second a_1 orbital is analogous to the a_2'' orbital in PF_5 with a lot of p(z) character. Thus the 2s spec-

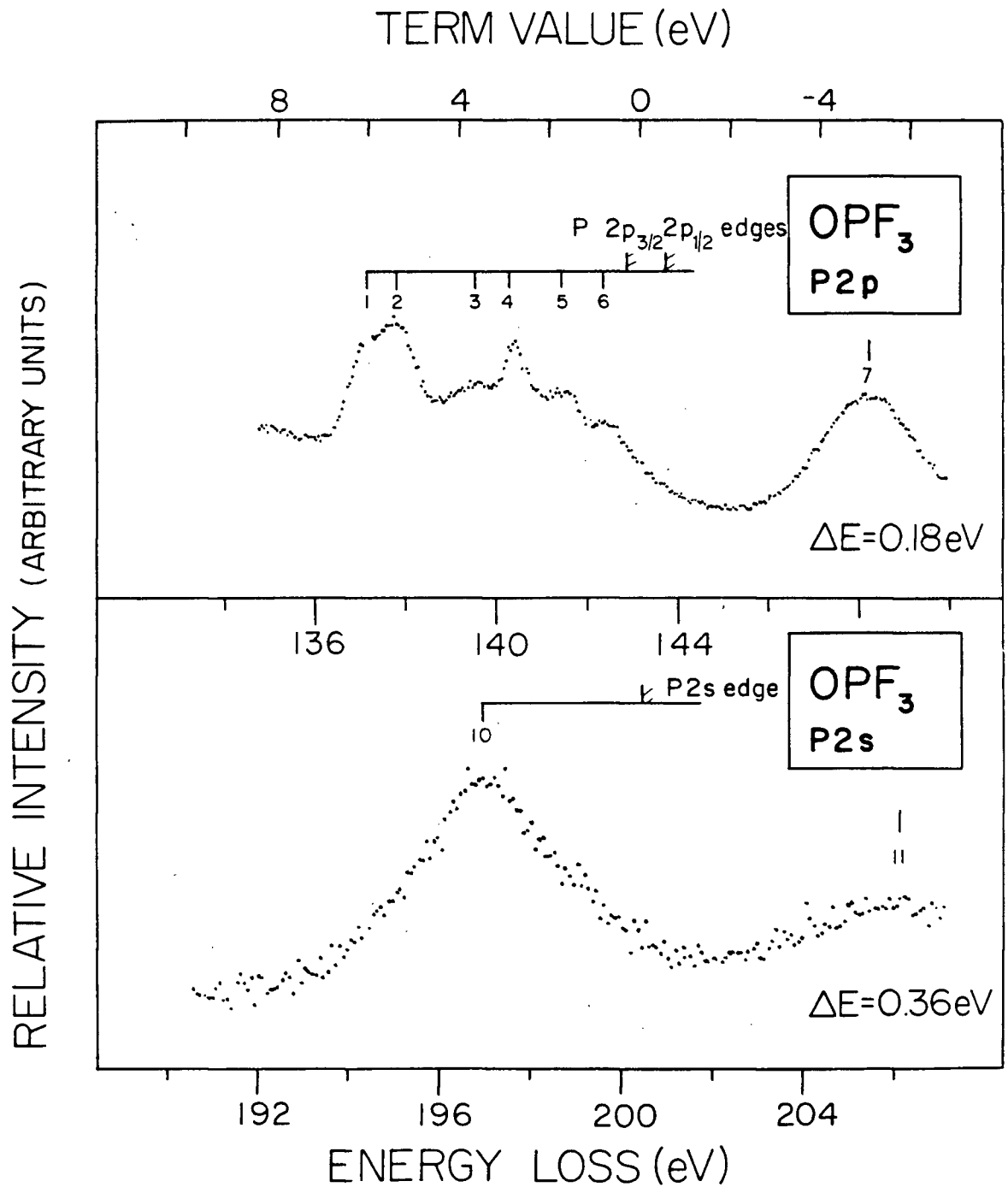

Figure 6.3:
Phosphorus 2p and 2s electron energy loss spectra of OPF_3. P 2p spectrum (upper trace) is at high resolution (0.18 eV FWHM). P 2s spectrum (lower trace) extracted from Figure 6.1. The spectra are aligned with respect to the 2p (mean) and 2s ionisation edges.

trum would be expected to be dominated by a transition to the $\sigma^*(e)$ orbital (as per preceding discussion for PF_5) and feature 10 is assigned as such. The breadth of the peak in the 2s spectrum and the intensity on the high energy side of feature 10 is consistent with there being an additional, less intense $2s \rightarrow \sigma^*(a_1)$ transition underneath, which would be expected in the case of OPF_3 since there are two a_1 type virtual orbitals, as indicated above. The transition to the lower a_1 orbital is likely under the low energy side of peak 10, corresponding to peaks 1 and 2 in the 2p spectrum discussed below. All assignments are summarised in Table 6.3.

Applying these to the 2p spectrum, features 1 and 2 are assigned as the spin-orbit components of the 2p to the first $\sigma^*(a_1)$ orbital. The term values of peaks 3 and 4 with respect to the $2p_{3/2}$ and $2p_{1/2}$ edges are almost the same as the term value of feature 10 (see Table 6.3) thus these transitions are assigned to the spin-orbit components of the $2p \rightarrow \sigma^*(e)$ transitions. However, the intensity, sharpness and term value of feature 4 suggests that it also contains a contribution from the $2p_{3/2}$ spin-orbit component of the $2p \rightarrow 4s$ Rydberg transition. The term value is also in keeping with other phosphorus 4s values (see PF_5). Features 5 and 6 are assigned to higher Rydberg transitions. These are evidently superimposed on top of broad underlying structure that can be assigned to the 2p transition to the second $\sigma^*(a_1)$ orbital. This interpretation is consistent with the proposed assignment of the 2s spectrum discussed above.

TABLE 6.3

Energies, Term Values, and Possible Assignments for the P 2p,2s Spectra of OPF_3

Feature	Energy Loss[a] (eV)	Term Value (eV)		Possible Assignments[d]	
		$2p_{3/2}$	$2p_{1/2}$	$2p_{3/2}$	$2p_{1/2}$
1	137.18	5.78		$\sigma^*(a_1)$	
2	137.86	5.10	6.00		$\sigma^*(a_1)$
3	139.60	3.36	4.26	$\sigma^*(e)$	
4	140.37 (8)	2.59	3.49	4s	$\sigma^*(e)$
5	141.53	1.43	2.33	5s, 3d	4s, 5s, 3d on top of $p \rightarrow \sigma^*(a_1)$
6	142.44	0.52	1.42		
$2p_{3/2}$ limit[b]	142.96	0			
$2p_{1/2}$ limit[b]	143.86		0		
7	148.3 (3)	-5.0†		inner-well state/shape-resonance	
8	159.7 (5)	-16.4†		σ^*(P-F) shape resonance	
9	166.6 (5)	-23.3†		σ^*(P-O) shape resonance	
		2s			
10	196.92 (20)	3.55		2s → σ^*(e)	
2s limit[c]	200.47	0			
11	206.1 (5)	-5.6		inner-well state/shape resonance	

(a) Estimated uncertainty in energy-loss values is ± 0.12 eV except where stated. Spectra are calibrated against N_2 ($1s \rightarrow \pi^*$, $v = 1$) at 401.10 eV.

(b) The spin-orbit splitting of 0.90 eV [61] has been used to estimate the $2p_{3/2}$ and $2p_{1/2}$ spin-orbit components from the 2p edge (mean) values [31], see text for details.

(c) Ref. [175]

(d) Final occupied orbital with either $2p_{3/2}$ or $2p_{1/2}$ hole state.

† With respect to the 2p edge (mean) [31].

Phosphoryl Trichloride - $OPCl_3$

The detailed phosphorus 2p and 2s spectra of $OPCl_3$ are shown in Fig. 6.4 and the spectral information is summarised in Table 6.4. The optical absorption spectrum of $OPCl_3$ in the P 2p region has been previously reported [173,174]. However, it is important to note that the energy scale shown in the preliminary optical work [174] is clearly in error by about 9 eV. However, the spectrum shown in the second paper [173] is consistent with the spectrum reported here. The latter paper [173] also shows the results of an X_α-SW calculation, however, no interpretation is given.

The molecule $OPCl_3$ is of C_{3v} symmetry and so is governed by the same selection rules (Table 5.1) as OPF_3. Proceeding as before, the major feature (15) in the 2s spectrum is assigned to the $2s \rightarrow \sigma^*(e)$ transition. There is evidence of a shoulder on th low energy side of this peak. This is presumably due to a $2s \rightarrow \sigma^*(a_1)$ transition. Applying the 2s term values so obtained (Table 6.4) to the 2p spectrum, features 1 and 2 may be assigned to the spin-orbit components of the $2p \rightarrow \sigma^*(a_1)$ transition and features 3 and 4 to the two components of the $2p \rightarrow \sigma^*(e)$ transition. The term value for feature 5 with respect to the $2p_{3/2}$ edge is 3.57 eV. This is somewhat high for the 4s term value when it is compared to those observed for the peaks assigned to transitions to the 4s level in the other phosphorus spectra. These values lie between ~2.4 and 3.1 eV for the assignments given here and in Chapter 5. Furthermore, the intensity of peak 4 suggests it contains contributions from more than one transition. Since the separation between

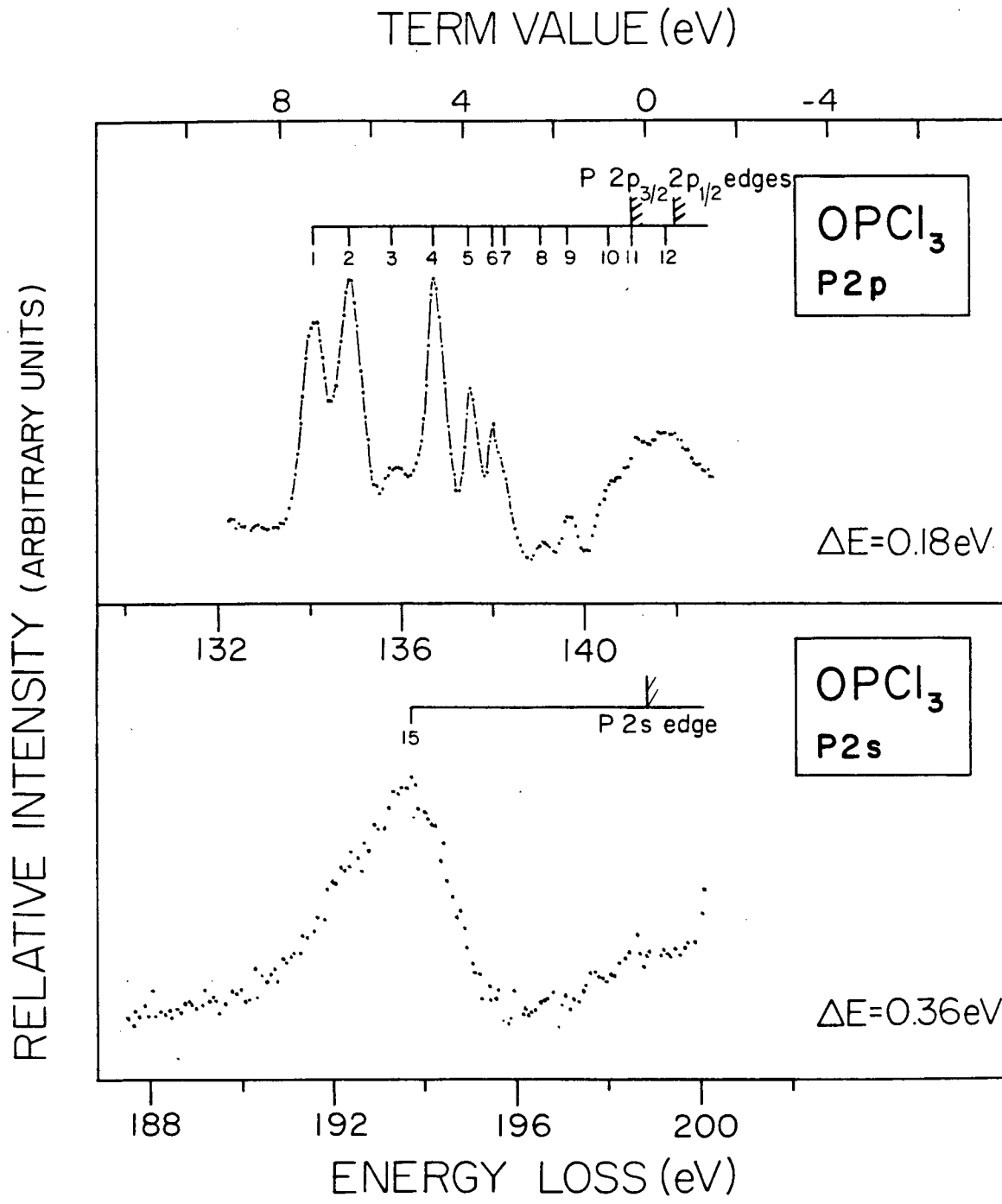

Figure 6.4:

Phosphorus 2p and 2s electron energy loss spectra of $OPCl_3$. P 2p spectrum (upper trace) is at high resolution (0.18 eV FWHM). P 2s spectrum (lower trace) extracted from Figure 6.1. The spectra are aligned with respect to the 2p (mean) and 2s ionisation edges.

TABLE 6.4

Energies, Term Values, and Possible Assignments

for the P 2p,2s Spectra of $OPCl_3$

Feature	Energy Loss[a] (eV)	Term Value (eV)		Possible Assignments[d]	
		$2p_{3/2}$	$2p_{1/2}$	$2p_{3/2}$	$2p_{1/2}$
1	134.06	7.00		$\sigma^*(a_1)$	
2	134.85	6.21	7.11		$\sigma^*(a_1)$
3	135.81 (10)	5.25	6.15	$\sigma^*(e)$	
4	136.67	4.39	5.29	$\sigma^*(a_1)$	$\sigma^*(e)$
5	137.49	3.57	4.47		$\sigma^*(a_1)$
6	138.00	3.08	3.98	4s	
7	138.27 (12)	2.99	3.89	4s + v	
8	139.03	2.03	2.93		4s
9	139.61	1.45	2.35	3d, 5s	
10	140.59 (10)	0.47	1.37	etc	3d, 5s on top of an inner-well state/ shape-resonance
11	141.09 (10)	-0.03	0.87		
12	141.73 (20)		0.23		
$2p_{3/2}$ limit[b]	141.06	0			
$2p_{1/2}$ limit[b]	141.96		0		
13	152.4 (5)	-11.0†		σ^*(P-Cl) shape resonance	
14	164.3 (5)	-22.9†		σ^*(P-O) shape resonance	
		2s			
15	193.67 (20)	5.19		2s → $\sigma^*(e)$	
2s limit[c]	198.86	0			

(a) Estimated uncertainty in energy-loss values is ± 0.08 eV except where stated. Spectra are calibrated against N_2 ($1s \rightarrow \pi^*$, v = 1) at 401.10 eV.

(b) The spin-orbit splitting of 0.90 eV [61] has been used to estimate the $2p_{3/2}$ and $2p_{1/2}$ spin-orbit components from the 2p edge (mean) values [31], see text for details.

(c) Ref. [175]

(d) Final occupied orbital with either $2p_{3/2}$ or $2p_{1/2}$ hole state.

†With respect to P 2p edge (mean) [31].

features 4 and 5 is close to the spin-orbit splitting, they are assigned to the spin-orbit components of the 2p transition to the second (higher energy) $\sigma^*(a_1)$ orbital. The rest of the features are assigned to various Rydberg transitions leading up to the edge. As with PCl_3, the latter transitions are on top of a broad peak that can be assigned to an inner well trapped state or resonance.

Continuum Spectra

A number of broad features are observed in the phosphorus 2p continua in the wide range spectra shown in Fig. 6.1. These features are quite similar to those of PF_3 and PCl_3 and can be attributed to the effects of the electronegative ligands. The intense, relatively sharp features on the edge in $OPCl_3$ (feature 12) and just beyond the edge in OPF_3 (feature 7) and PF_5 (feature 8) are probably best described as inner-well states/shape-resonances trapped by a potential (centrifugal) barrier [73,77]. The higher energy features are broader and can be tentatively assigned to higher d-like shape resonances caused by the scattering of the ionised electron off the neighbouring atoms [77]. As discussed in the previous two chapters and Chapter 1, section F.III, there should be an R^{-2} relationship (R - distance between the scattering centres at a given site) for these features. This did not seem to be the case in the trivalent phosphorus series in Chapter 5, even though the silicon series (Chapter 4) has shown a reasonable correlation with similar ligands. It might be instructive to compare the resonance positions of the molecules here with those in PF_3 and PCl_3 to see

whether the resonance term values for identical pairs of atoms (e.g., P-F, etc.) are of similar magnitude in the different molecules since the respective bond lengths do not vary appreciably (see Table 6.5).

The molecules presented here each have two different types of ligand position (PF_5) or ligand (OPF_3 and $OPCl_3$), unlike those in the previous chapter where all ligands were identical in nature and position. This difference should be reflected in the spectra. Assuming that all the continuum features are due to resonances, $OPCl_3$ and PF_5 clearly show two different resonance contributions ($OPCl_3$ - features 13 and 14, PF_5 - features 9 and 10). The spectrum of OPF_3 shows one resonance (feature 8), but with an indication of a second resonance (feature 9) on the high energy side. The energies (δ) of the resonances above the respective ionisation edges for these molecules, as well as those for PF_3 and PCl_3, are summarised, together with the bond lengths (R), in Table 6.5. Where there are two scattering (interatomic) sites, the lower resonance has been assigned to the site with the longer bond distance [99,100].

As can be seen from Table 6.5, the resonance position (δ) is reasonably constant for a given type of interatomic scattering site in different molecules. The close correspondence between the estimated δ values for the higher energy features in OPF_3 (feature 9) and $OPCl_3$ (feature 14) lends support to their common assignment to σ^*(P-O) type resonances. The lack of a correlation found for PF_3, $P(CH_3)_3$ and PCl_3 can be attributed to different circumstances in the case of $P(CH_3)_3$. Based upon the proposed resonance/bond length relationship, the resonan-

TABLE 6.5

Resonance Positions (δ) Above the Mean Ionisation Edge and Bond Lengths (R)

	Postulated Interatomic Scattering Site					
	P - Cl		P - F		P - O	
Molecule	δ(eV)	R(Å)†	δ(eV)	R(Å)†	δ(eV)	R(Å)†
PCl_3	9.4	2.043				
$OPCl_3$	11.0	1.989			22.1	1.455
OPF_3			16.4	1.524	~23	1.436
PF_3			15.2	1.563		
PF_5			12.8 (Ax) 17.5 (Eq)	1.577 1.534		

†From Landholdt-Börnstein (New Series) II/7, "Structure Data of Free Polyatomic Molecules," Springer-Verlag, (Berlin, 1976).

ce in $P(CH_3)_3$ should have occurred at a smaller value of δ than that in PF_3. The feature in question in $P(CH_3)_3$ (see feature 9 in Fig. 5.1) is quite intense, and in fact more like the broad continuum structure in the case of PH_3. The fact that the $P(CH_3)_3$ spectrum is more like that of PH_3 is not entirely unexpected since the methyl group (like H) is much less electronegative (in fact slightly electron donating) than the highly electronegative ligands of PF_3 and PCl_3. Furthermore, it was seen that much of the continuum intensity in PH_3 could be assigned as "shake-up" rather than resonance-type features. It is possible, therefore, that most of the continuum structure in $P(CH_3)_3$ is also due to "shake-up" and is not in fact due to a resonance and therefore any correlation of R with δ would not be relevant. Obviously care has to be taken in automatically assigning any continuum features to resonances. However, in the case of the present work the close agreement (Table 6.5) between the positions of the features for the same interatomic scattering sites in different molecules lends support to the resonance assignment for the features in question. This conclusion is in keeping with recent suggestions made by Sette et al. [99].

Ligand Spectra

Having assigned the central atom spectra for these molecules, the ligand spectra are now analysed with reference to their respective central atom spectrum.

The spectrum of the F 1s region of PF_5 is shown in Fig. 6.5 and summarised in Table 6.6. There are two types of F ligand, i.e., axial

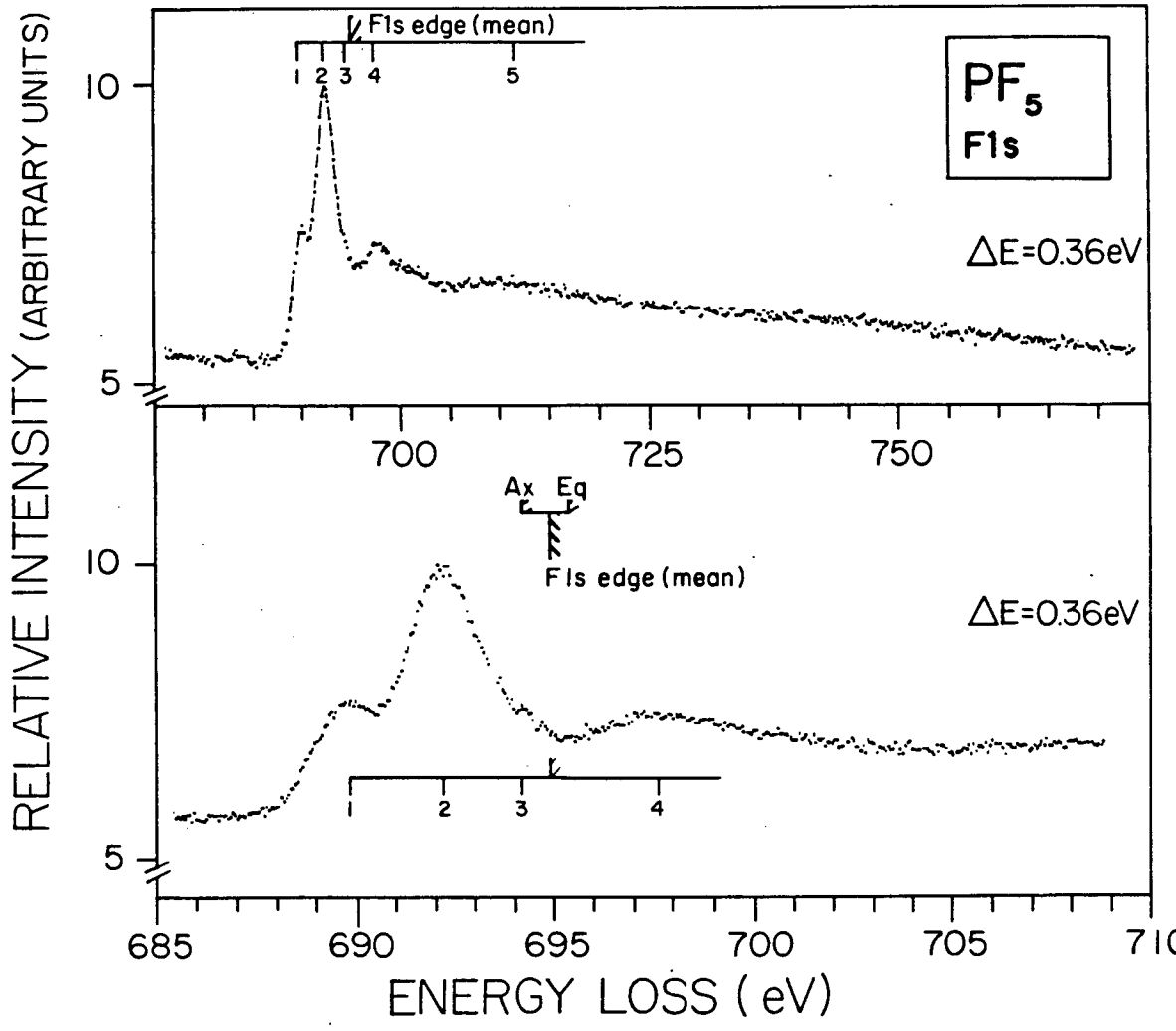

Figure 6.5:

The F 1s Electron Energy Loss spectrum of PF_5; wide range scan (upper trace), detailed spectrum (lower trace).

TABLE 6.6

Energies, Term Values, and Possible Assignments for the F 1s Region of PF_5

Feature	Energy Loss (eV)	Term Value (eV)			Possible Assignment
		Ax.	Eq.	Mean[†]	
1	689.93 (20)	4.3	5.5	5.0	$1s \rightarrow \sigma^*(a_1')$
2	692.22 (20)	2.0	3.2	2.7	$1s \rightarrow \sigma^*(e')$
3	694.2	0	1.2	0.7	Rydberg
F 1s (Ax) limit[a]	694.2				
F 1s (Eq) limit[a]	695.4				
4	697.62 (30)	-3.4	-2.2	-2.7	$1s \rightarrow \sigma^*(a_2'')$
5	~700				inner-well trapped state/shape resonance
6	711.6	-17.4	-16.2	-16.7	shape-resonance

[a] Ref. [179]; Ax. is Axial, Eq. is Equatorial.
Binding energies of 694.1 eV and 695.3 eV have also been reported for the axial and equitorial ligands respectively [183].

[†] With respect to the mean value (694.9 eV) of the F 1s edges.

and equatorial. The F 1s XPS spectrum [179,183] is asymmetric and can be deconvoluted into two components representing the two different environments. Both of the edges as well as the mean position are shown in Fig. 6.5. There is no evidence of individual features leading up to the differing edges, and furthermore, the separation of the features is considerably greater than the reported XPS splitting. It is concluded that the observed features in the ISEELS spectrum are indicative of the final occupied orbitals and not due to a differing originating (i.e., axial or equitorial F) orbital. Thus the term values have been taken with respect to the mean value. As with the molecules in the previous chapter, the term values are lower for the ligand spectrum than those for the central atom spectrum. This difference reflects the different location of the core hole within the molecule, i.e., on the periphery of the molecule for F as opposed to the centre for P. Since the F 1s orbitals transform as $2A_1' + A_2'' + E'$, transitions to all the virtual orbitals are dipole allowed. Thus features 1 and 2 (Fig. 6.5, Table 6.6 are assigned to the F 1s $\rightarrow \sigma^*(a_1')$ and F 1s $\rightarrow \sigma^*(e')$ transitions respectively and feature 4 is assigned to the F 1s $\rightarrow \sigma^*(a_2'')$ transition, consistent with the assigned ordering in the P 2p and 2s spectra discussed above. Feature 3 is thought to be due to various Rydberg transitions. The weak, broad bands, 5 and 6, are assigned to shape resonance transitions similar to those observed in the P 2p spectrum. Their relative lack of intensity can be attributed to the fact that the excited atom is on a ligand; i.e., on the periphery of the molecule.

Figure 6.6 shows the long-range spectra of each of the F and O ligands in OPF_3, while Fig. 6.7 shows the short-range spectra in somewhat more detail. In both figures, the spectra are shown on a common relative energy scale that has been referenced to the respective ionisation edges. The spectra from the two different regions are remarkably similar. The features in the F spectra are somewhat broader due probably to the shorter lifetime of the F core excited state. The spectral data are summarised in Table 6.7. It should be noted that in this case the term values are in most cases quite similar to each other and to those observed in the central atom (P 2p,2s) spectra. Thus features 1, 2, and 3 are assigned to transitions to the $\sigma^*(a_1)$, $\sigma^*(e)$, and $\sigma^*(a_1)$ respectively. Feature 3 cannot be accurately located in the broad shoulder on the high energy side of peak 2 in either the F 1s or O 1s spectra shown in Fig. 6.7. Feature 4 can be assigned to the strong inner-well trapped state/shape-resonance feature seen in the P 2p spectrum. As with PF_5, this feature is weak and this again can be attributed to the peripheral location of the excited atom. The very weak and broad structure signified by the bracket labelled 5 is presumably attributable to a shape-resonance.

Finally the $OPCl_3$ ligand spectra are now considered. The O 1s spectra are shown in Fig. 6.8 and summarised in Table 6.8. The spectrum is very similar in appearance to the O 1s spectrum of OPF_3. There is, however, considerably more background that arises mainly from the tail of the Cl 2p,2s ionisation continua. The term values are significantly lower than those for the P 2p,2s spectra (Table 6.4), consistent with

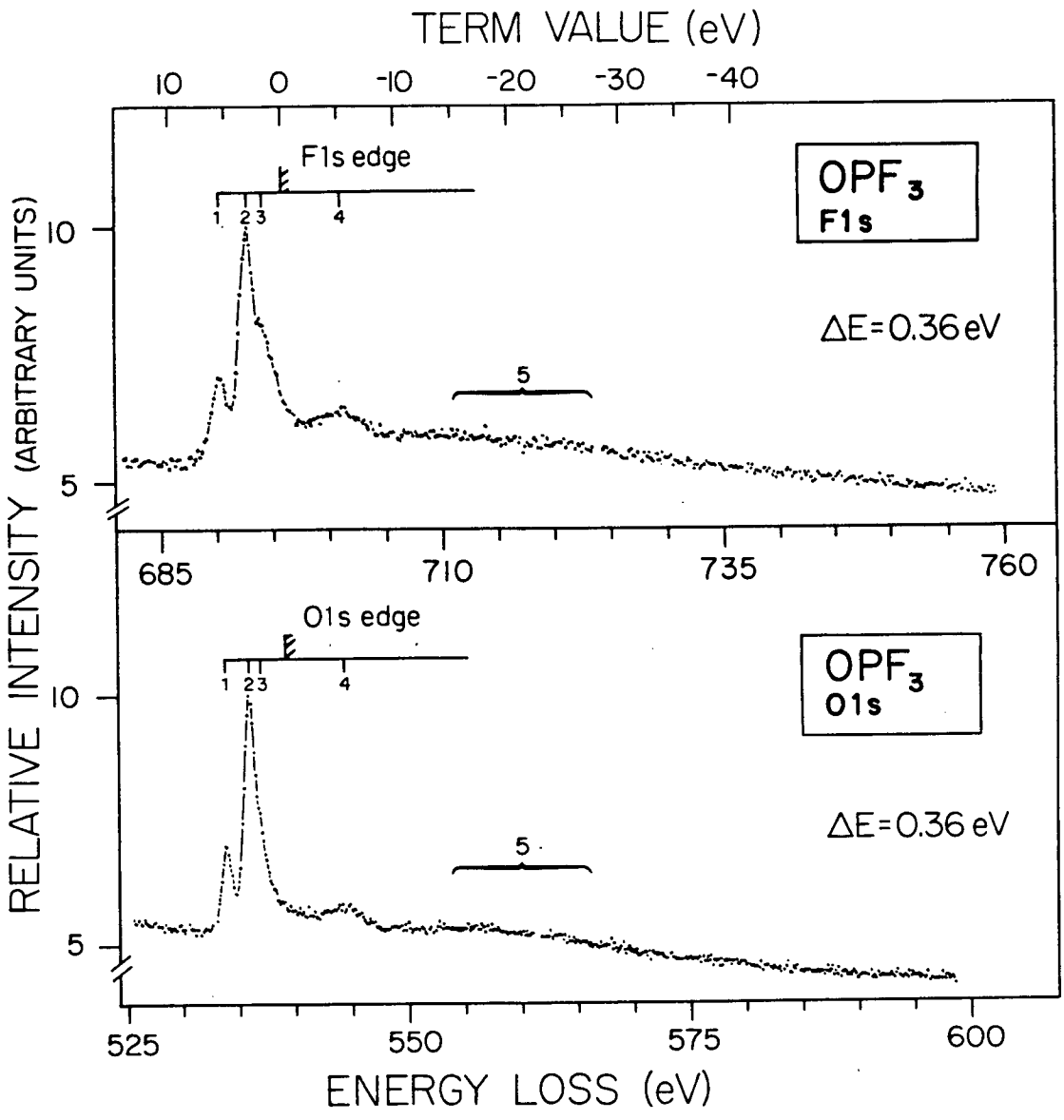

Figure 6.6:

The wide range electron energy loss spectra of the O 1s and F 1s regions of OPF_3. The spectra are aligned with reference to the respective 1s edges.

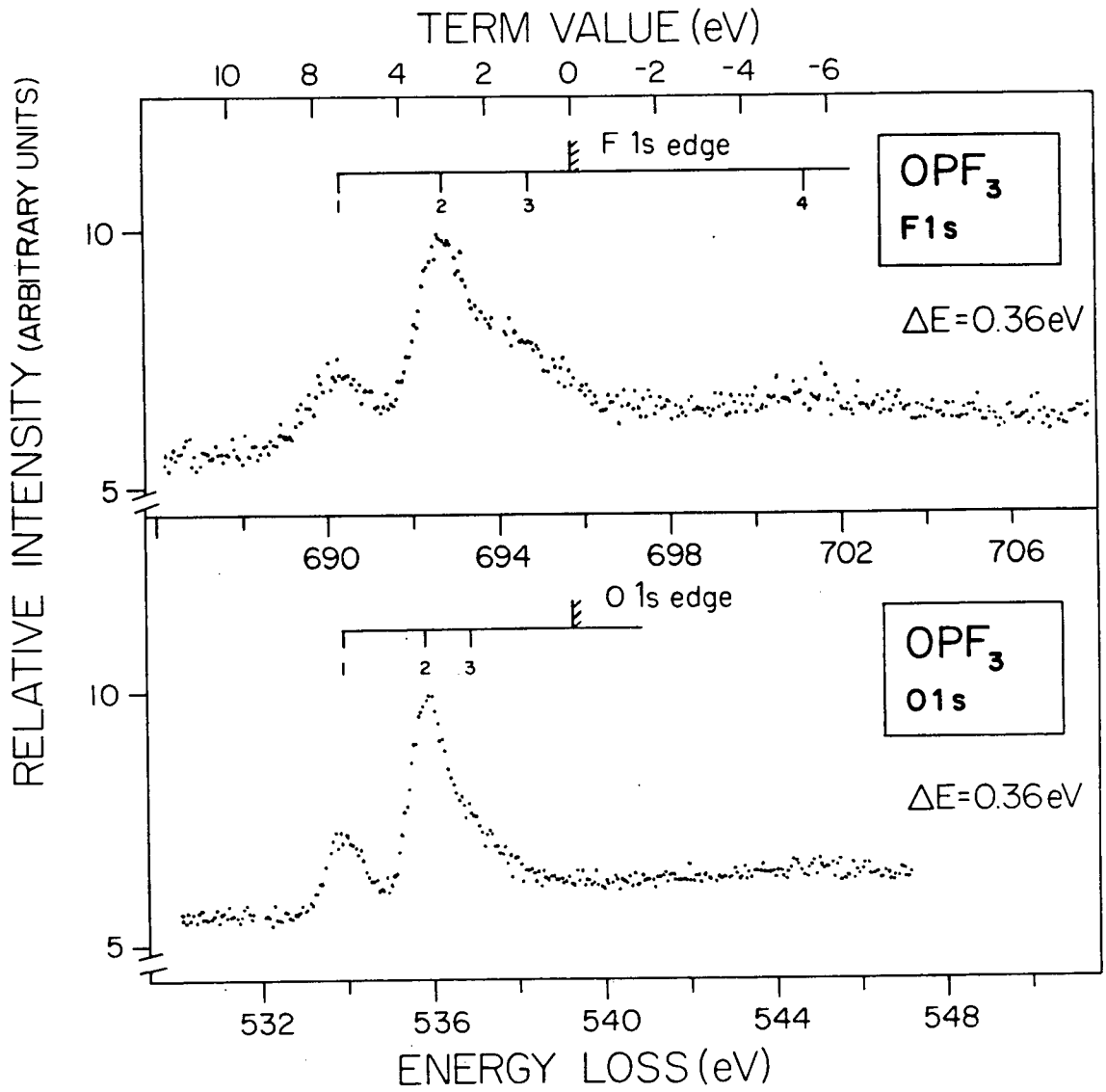

Figure 6.7:

Detailed electron energy loss spectra of the O 1s and F 1s regions of OPF_3. The spectra are aligned with reference to the respective edges.

TABLE 6.7

Energies, Term Values, and Possible Assignments for the O 1s, F 1s Regions of OPF_3

Feature	Oxygen 1s		Fluorine 1s		Possible Assignment
	Energy Loss (eV)	Term Value (eV)	Energy Loss (eV)	Term Value (eV)	
1	533.87 (20)	5.4	690.30 (30)	5.5	$1s \rightarrow \sigma^*(a_1)$
2	535.81 (15)	3.5	692.71 (20)	3.1	$1s \rightarrow \sigma^*(e)$
3	~537		~694		$1s \rightarrow \sigma^*(a_1)$
edge[a]	539.3		695.8		
4	544.3 (5)	-5.0	700.1 (5)	-4.3	inner well trapped state/shape resonance
5	555 - 565		710 - 720		shape-resonance structures

[a]Ref. [179].

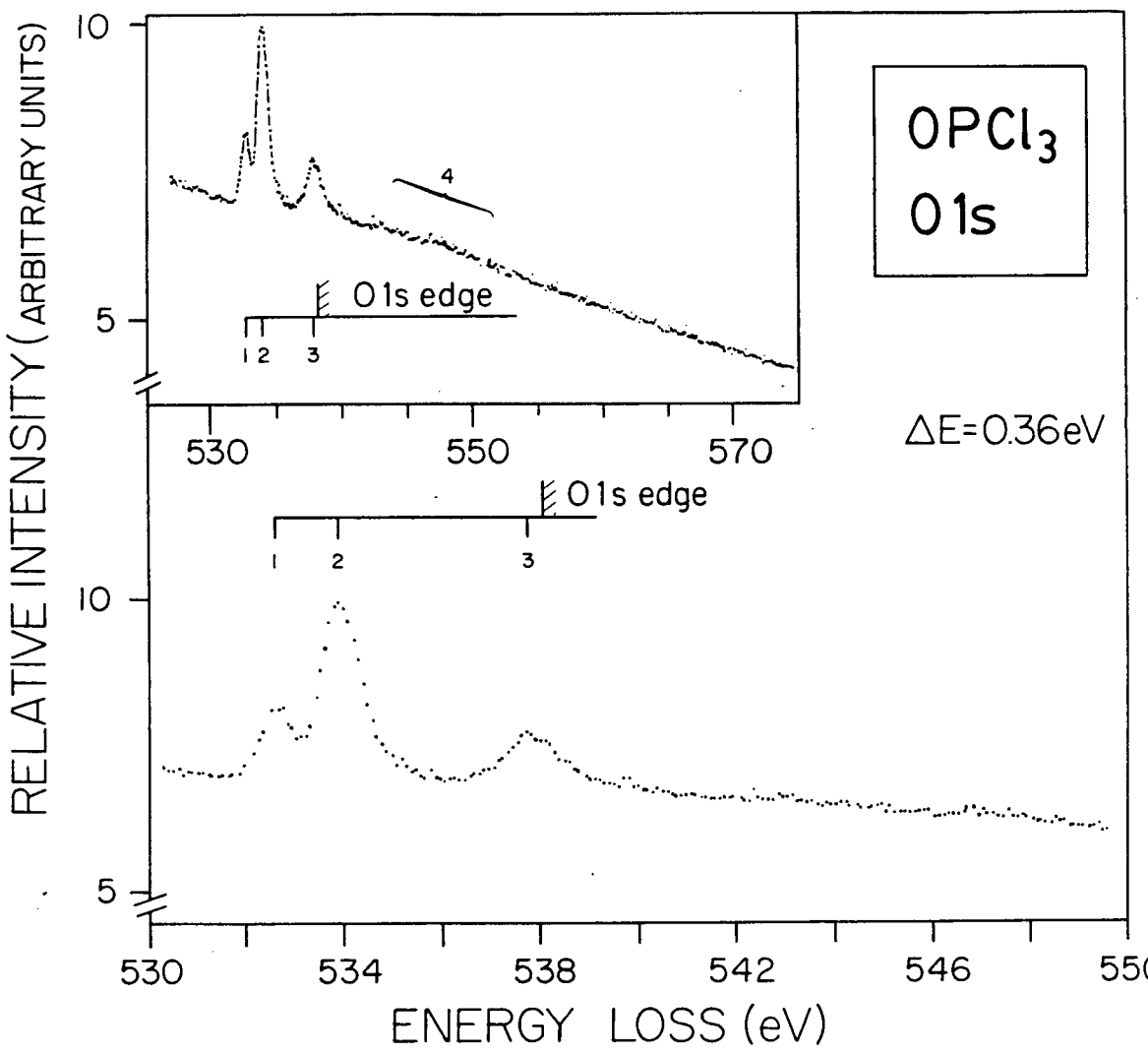

Figure 6.8:

Detailed electron energy loss spectra of the O 1s region of $OPCl_3$. The insert shows a wide range spectrum.

TABLE 6.8

Energies, Term Values, and Possible Assignments for the O 1s Region of $OPCl_3$

Feature	Energy Loss (eV)	Term Value (eV)	Possible Assignment
1	532.60 (15)	5.5	$1s \rightarrow \sigma^*$ (a_1)
2	533.86 (15)	4.2	$1s \rightarrow \sigma^*$ (e)
3	537.72 (20)	0.4	inner well trapped state/ shape-resonance
O 1s limit[a]	538.1	0	
4	542 - 550		shape-resonance

[a]Ref. [179].

the peripheral position of the core hole. This difference is much greater than in the case of OPF_3 (compares Tables 6.3 and 6.7) but more in keeping with that observed for PF_5 and the molecules in Chapter 5. Features 1 and 2 are assigned as transitions to the $\sigma^*(a_1)$ and $\sigma^*(e)$ orbitals respectively. There does not appear to be any significant intensity for a transition to the second $\sigma^*(a_1)$ orbital, however, there is intensity on the high energy side of feature 2 which may be due to such a transition (compare P 2p spectrum, Table 6.4 and Fig. 6.4). Feature 3 is assigned to a transition to an inner-well trapped state/ shape-resonance. The weak structure, labelled 4, is also attributed to a shape-resonance. Figure 6.9 shows the Cl 2p,2s spectra. The spectral data is summarised in Table 6.9. The spectrum is in good agreement with the previously published optical spectrum [173] and is similar to other earlier reported Cl 2p,2s spectra such as those for PCl_3 and the chloromethanes [182]. Overlapping bands complicate the spectral assignment. Features 1 and 2 are assigned to the spin-orbit components of the $2p \rightarrow \sigma^*(a_1)$ transition. Transitions to the other virtual orbitals ($\sigma^*(e)$, $\sigma^*(a_1)$) are also expected. Using the separation of the virtual orbitals from the P 2p spectrum ($\sigma^*(a_1)$-$\sigma^*(e)$ ~ 1.75 eV, $\sigma^*(a_1)$-$\sigma^*(a_1)$ ~2.61 eV) as a guide, features 3 and 5 are assigned to the $2p \rightarrow \sigma^*(a_1)$ transition. The 4s Rydberg transitions are assigned to features 4 and 6. The rest of the Rydberg transitions are on top of the rapid rise in oscillator strength, giving rise to features 7 and 8, which are assigned to a transition to the inner-well trapped state or shape-resonance. Feature 9 is thought due to a σ^*(P-Cl) shape-resonance since δ (the

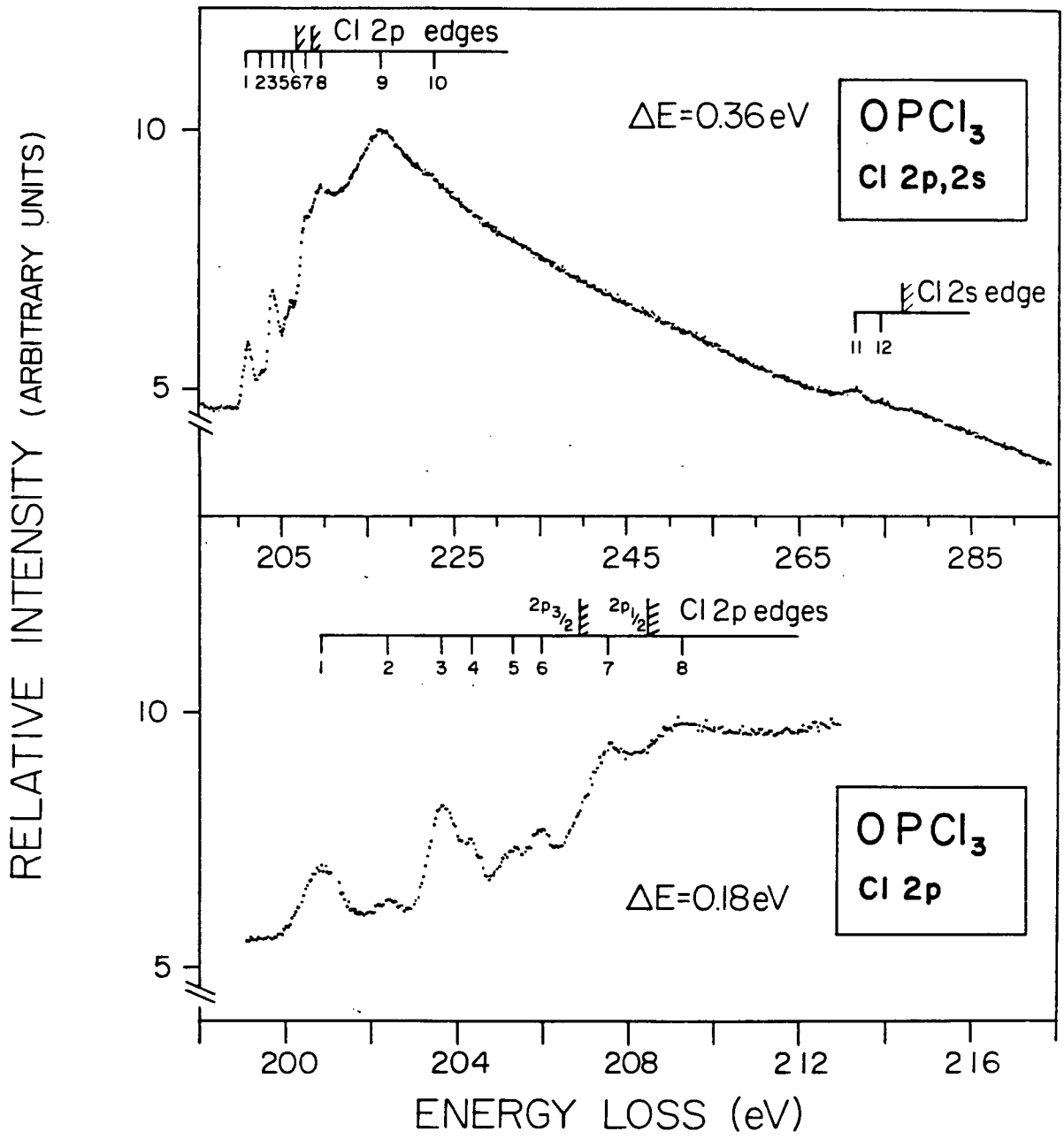

Figure 6.9:

High resolution (0.18 eV FWHM) electron energy loss spectrum of the Cl 2p region of $OPCl_3$ (lower trace). The upper trace shows the combined Cl 2p,2s region recorded with a resolution of 0.36 eV FWHM.

TABLE 6.9

Energies, Term Values, and Possible Assignments

for the Cl 2p,2s Regions of $OPCl_3$

Feature	Energy Loss[a] (eV)	Term Value (eV)		Possible Assignments[d]	
		$2p_{3/2}$	$2p_{1/2}$	$2p_{3/2}$	$2p_{1/2}$
1	200.82	6.0		$\sigma^*(a_1)$	
2	202.35 (10)	4.5	6.1	$\sigma^*(e)$	$\sigma^*(a_1)$
3	203.62	3.2	4.8	$\sigma^*(a_1)$	$\sigma^*(e)$
4	204.28	2.6	4.2	4s	
5	205.27 (10)	1.6	3.2		$\sigma^*(a_1)$
6	205.93 (10)	0.9	2.5	etc.	4s
7	207.52 (10)	-0.7	0.9	inner well state/shape resonance	
8	209.22 (12)		-0.8		inner well state/ shape-resonance
$2p_{3/2}$ limit[b]	206.9	0			
$2p_{1/2}$ limit[b]	208.5		0		
9	216.65	-9.3[†]		σ^*(Cl-P) shape resonance	
10	223	-16[†]		"shake-up"	
		2s			
11	272.6	5.6		$2s \rightarrow \sigma^*$	
12	275.7	2.5		$2s \rightarrow \sigma^*$	
2s limit[c]	278.26	0			

(a) Estimated uncertainty in energy loss ± 0.08 eV unless otherwise stated.

(b) 2p edge Ref. [31]; $2p_{3/2}$ = 2p (mean) - 0.53 eV; $2p_{1/2}$ = 2p (mean) + 1.07 eV; A spin-orbit splitting of 1.6 eV [18] has been assumed.

(c) 2s edge ref. [31].

(d) Final occupied orbital with either $2p_{3/2}$ or $2p_{1/2}$ hole state.

[†]With respect to Cl 2p (mean) edge [31].

negative of the term value) is ~9.3 eV, which is reasonably close to the average value of 10.8 eV observed (see Table 6.5) for σ^*(P-Cl) resonances from the P 2p spectra. A weak feature 10 is possible due to "shake-up".

CONCLUSIONS

The central atom and ligand ISEELS spectra measured for a series of trivalent phosphorus compounds presented in Chapter 5 have been extended to include the higher coordinated phosphorus compounds PF_5, OPF_3, and $OPCl_3$. A number of questions raised in Chapter 5 have been answered. The use of the P 2s term values to assign the P 2p spectra is further supported by the present work. The first two σ^* levels are well separated in the presently studied molecules and hence the assignment of the core to valence transitions is less ambiguous. The respective σ^*(e) (or σ^*(e') for PF_5) term values for the P 2s and 2p spectra were found to be within ~0.1 eV of each other, which lends confidence to the ordering of the σ^* levels as given in the previous chapter, and also indicates that term values are transferable when the core hole is located on the same atom. The continuum structure was similar to that observed for PF_3 and PCl_3 in that there was an intense feature at or just beyond the edge attributable to an inner-well trapped state/shape-resonance followed by broad shape resonances. In addition, each spectrum here showed an extra resonance in comparison with the PX_3 spectra. This is directly attributable to the fact that the molecules here each possess two different kinds of ligands. A comparison of the

resonance positions in the P 2p spectra in PCl_3 and $OPCl_3$ confirmed the σ^*(P-Cl) nature of the resonance in these molecules. A similar conclusion was reached in the assignment of the feature in OPF_3 and PF_3 (i.e., σ^*(P-F)). The resonances in the P 2p PF_5 spectrum were consistent with there being two types of fluorines in PF_5 (i.e., axial and equatorial). A comparison of $OPCl_3$ and OPF_3 confirmed the σ^*(P-O) nature of the second resonance in those molecules. This lends support to the existence of some sort of relationship between resonance position and bond length [96-100]. The absence of such a relationship for the molecules studied in Chapter 5 would appear to be due to a different phenomenon being responsible for the structure in $P(CH_3)_3$. It is possible that the continuum features in $P(CH_3)_3$ are due to "shake-up" processes, as was found for PH_3. Obviously great care must be exercised in the assignment of continuum features which can be ascribed to one or more of several effects including trapped-inner well states, resonances, "shake-up" or double excitation.

CHAPTER 7

ELECTRONIC EXCITATION IN PHOSPHORUS-CONTAINING MOLECULES. III. VALENCE SHELL ELECTRON ENERGY LOSS SPECTRA OF $P(CH_3)_3$, PCl_3, PF_3, $OPCl_3$, and PF_5

Very little information on the valence shell excitation processes exists in the literature on the molecules studied in the previous two chapters. The only reported VSEELS spectrum for any of this series of compounds is that for PH_3 referred to in the book by Robin [12]. However, there have been several photoabsorption studies on some of these molecules, but only over a rather limited energy range (up to ≈10 eV) dictated by the use of conventional optical spectrometers and light sources. These studies included spectra of PF_3 and PCl_3 [184-186], $P(CH_3)_3$, and $OPCl_3$ [185], as well as PH_3 [178,184,185]. In this chapter the VSEELS spectra of $P(CH_3)_3$, PCl_3, $OPCl_3$, PF_3, and PF_5 are presented up to 20 eV and beyond. The spectra are interpreted with the aid of the ISEELS results from Chapters 5 and 6. A comparison of these two techniques was useful in tentatively assigning the VSEELS spectra of, NF_3 and $Si(CH_3)_4$ (see Chapters 3 and 4), since the ISEELS spectra are generally relatively simple to assign due to the energy isolation of the initial core hole, which unambiguously defines the initial orbital of the transition.

EXPERIMENTAL DETAILS

The spectra were all obtained on the spectrometer described in

Chapter 2. An impact energy of 2.5 keV was used to obtain the spectra with the scattered electrons sampled at zero degree scattering angle. The spectra were obtained with a typical energy resolution of 0.035 - 0.050 eV. At zero degree scattering it is not always possible to obtain background-free operation in the valence shell region. This was especially the case for PCl_3 and PF_5. However, removal of the gas indicated that the background signal was smoothly varying and possessed no sharp features due to "ghosting" effects arising from reflection of the primary beam, or secondary emission from electrode surfaces. With the exception of PCl_3 all spectra were calibrated with the He(I) line (21.218 eV). Initially the PCl_3 sample as supplied contained a small HCl impurity that was used to calibrate the spectrum. All traces of HCl were then removed by continuous pumping on a PCl_3 sample that was cooled with a dry-ice/methanol mixture. A similar procedure was used for $OPCl_3$, as a precautionary measure even though no HCl was immediately apparent.

RESULTS AND DISCUSSION

Before discussing the VSEELS spectra it is useful to review some of the pertinent points from the discrete portion of the P 2p spectra reported for these compounds. With the exception of $P(CH_3)_3$ all P 2p spectra show strong core → virtual valence transitions well separated from the core → Rydberg transitions. It is possible to assign these transitions to those going to the final orbitals expected from a minimal basis set. The ordering of the previously unoccupied valence orbitals

was established by comparison of the P 2p spectra with the P 2s spectra. The remaining transitions can be assigned to Rydberg transitions. Since these originate from a 2p level, the dominant Rydberg transitions are assigned as those going to the s and d Rydberg levels. A p → p transition is formally dipole forbidden in the pure atomic case and hence would be expected to have lower intensity, especially in more highly symmetric molecules [61]. Table 7.1 summarizes the term values (T) obtained from Chapters 5 and 6 for transitions to the virtual valence orbitals and also to the assigned 4s Rydberg level. Also shown is the quantum defect (δ) obtained for the s Rydberg series from the 4s term values. These quantum defects all lie between ~1.7-1.9, which is only slightly lower than the "expected" quantum defect of 2 for the s Rydberg series of the third (Na-Ar) row [12].

On moving from the core to the valence region the term values would be expected to be lower for the virtual valence levels. This is easily rationalised in terms of the location of the hole. The loss of shielding caused by the removal of a valence electron should be less than that caused by the removal of a localised core electron from the centre of the molecule and so the electron in the newly occupied σ^* orbital sees something approaching a whole extra unit of charge in the case of a central core hole and hence has a higher term value (i.e., binding energy). This effect has been discussed previously with regard to NF_3 and is similar to the effect which occurs when the core hole is located on a ligand as opposed to the central atom (see the previous chapters). The effect of the initial orbital vacancy location on

TABLE 7.1
Term values (T) for phosphorus L-shell spectra[†] and the calculated s orbital quantum defects (δ)

Molecule	Term Value (eV)[(a)]				Quantum[(f)] Defect δ
	Virtual Orbitals[(b)]			Rydberg 4s	
	$\sigma^*(1)$	$\sigma^*(2)$	$\sigma^*(3)$		
PH_3	5.1	4.5	-	2.48	1.66
PF_3	6.8	~3.5[(c)]	-	3.12	1.91
PCl_3	6.9	6.4	-	3.06	1.89
$P(CH_3)_3$	3.3	~2.0[(d)]	-	2.86	1.82
$OPCl_3$	7.0	6.2	4.4	3.08	1.90
PF_5	6.2	3.6	-0.7[(e)]	2.71	1.76

[†]From Chapters 5 and 6.

(a)Term values are with respect to the P 2p edge except where stated.

(b)Symmetries of the unoccupied virtual orbitals (as assigned in Chapters 5 and 6 are:

	$\sigma^*(1)$	$\sigma^*(2)$	$\sigma^*(3)$
PH_3, $P(CH_3)_3$, PF_3	e	a_1	-
PCl_3	a_1	e	-
$OPCl_3$	a_1	e	a_1
PF_5	a_1'	e'	a_2''

(c)Difficult to locate accurately, mean of $2p_{3/2}$ and 2s term values used.

(d)Mean term value of the two possible assignments given.

(e)This term value is with respect to the P 2s edge.

(f)Calculated from $T = 13.605/(n-\delta)^2$ where n = principal quantum number.

Rydberg term values should be somewhat less because (i) the term values for Rydberg orbitals are smaller than those for the (LUMO) valence orbitals; (ii) the Rydberg orbitals are large and diffuse and will therefore tend to see the molecule as one large core.

In assigning the VSEELS spectra an attempt will first be made to locate the valence → virtual valence transitions. In order to do this it is initially assumed that the term values are independent of the originating valence orbital. All expected term values are calculated from the experimental vertical ionisation potentials as obtained from photoelectron spectroscopy. The vertical ionisation potentials are summarised in Table 7.2. Once the valence → virtual valence transitions are located, the possible valence → Rydberg transitions will be assigned. The term values obtained from Chapters 5 and 6 will be assumed to give upper bounds for those in the valence spectra. Other evidence from the ligand ISEELS spectra will be considered at appropriate junctions in the following discussion of the various VSEELS spectra.

Trimethyl Phosphine ($P(CH_3)_3$)

The VSEELS spectrum of $P(CH_3)_3$ from 4-25 eV is shown in Fig. 7.1. The energies, term values and possible assignments are summarised in Table 7.3. The only previously reported valence shell excitation spectrum is the UV absorption spectrum reported by Halmann [185] which only extends up to ~6.7 eV. This UV spectrum [185] shows a strongly absorbing, broad band centered at ~6.15 eV, in very good agreement with

TABLE 7.2

Molecular orbitals[a] and experimental ionisation potentials[b] (eV) for the valence orbitals of PH_3, PF_3, PCl_3, $P(CH_3)_3$, $OPCl_3$, and PF_5

MO	PH_3	MO[c]	PF_3	PCl_3	$P(CH_3)_3$	MO	$OPCl_3$	MO	PF_5
$5a_1$	10.58	$4a_1$	12.29	10.52	8.65	11e	11.93	2e"	15.54
2e	13.50	$1a_2$	15.89	11.69	11.50	$2a_2$	12.40	6e'	16.46
$4a_1$	21.2	4e	16.31	11.99	11.25	10e	12.94	$5a_2''$	16.75
		3e	17.45	12.94	13.25	$13a_1$	13.48	$8a_1'$	17.13
		$3a_1$	18.57	14.23	13.70	9e	13.86	$1a_2'$	17.79
		2e	19.36	15.19	14.60	$12a_1$	15.35	5e'	18.43
		$2a_1$	22.60	18.81	16.65	8e	16.50	1e"	19.1
						$11a_1$	19.53	$4a_2''$	19.5
								4e'	~21

[a] Order from [176] for PH_3; [133,176,187,188] for PF_3; [188,189] for PCl_3 [189,190] for $OPCl_3$ and [191] for PF_5.

[b] From PES, [192] for PH_3; [118] for PF_3; [193] for PCl_3; [190] for $OPCl_3$; [193,194] for PF_5 and [195] for $P(CH_3)_3$.

[c] Numbering ignoring core-levels.

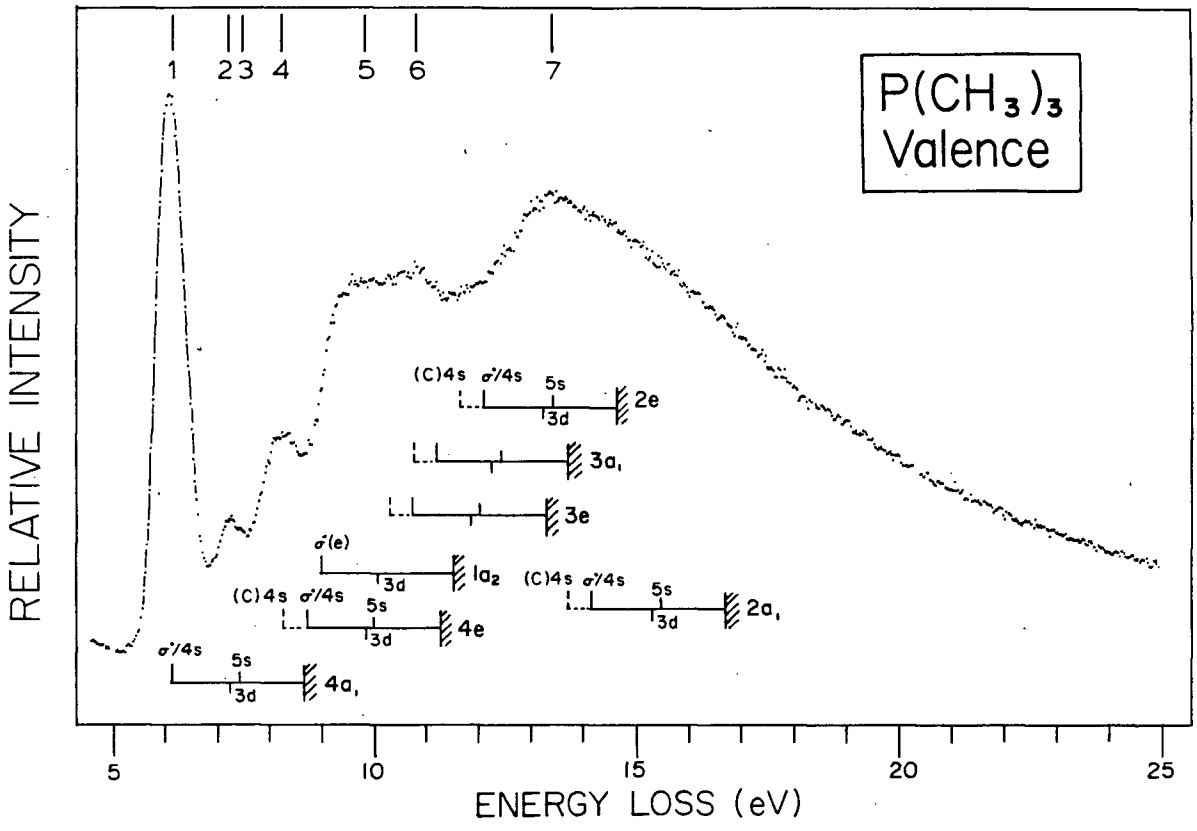

Figure 7.1:

The valence shell electron energy loss spectrum of $P(CH_3)_3$. The ionisation edges are taken from photolectron spectroscopy (see Table 7.2). Positions of valence-valence (tall bars), valence-Rydberg (short bars) transitions as estimated from the term values are shown to each limit (see Table 7.3). The dashed bar indicates term value estimated from the C 1s spectrum.

TABLE 7.3

Energies, term values and possible assignments

for the VSEELS spectrum of $P(CH_3)_3$.

Feature	Energy Loss (eV)	Term Value (eV)[(a)]	Possible Assignments
1	6.11	2.44	$4a_1 \rightarrow \sigma^*(e)$, $\sigma^*(a_1)/4s$
2	7.23	1.42	$4a_1 \rightarrow 3d$
3	7.46	1.19	$4a_1 \rightarrow 5s$
4	8.24	3.01	$4e \rightarrow 4s$
5	9.8		
6	10.6		
7	13.4		

(a) Term values are calculated with respect to the IP of the initial orbital.

These IP's are given in Table 7.2.

feature 1 of the spectrum reported here. Robin has suggested [12] that the intensity of this feature indicates that it has a large HOMO $(4a_1) \rightarrow \sigma(a_1)$ valence component. This feature is also likely to encompass the transition from the HOMO to the 4s Rydberg level; indeed, it is likely that the $\sigma^*(a_1)$ and 4s will form a strongly mixed valence-Rydberg pair as discussed by Friedrich et al. [65]. The term value of feature 1 is 2.44 eV and Robin [12] has indicated that this would be appropriate for a transition to a 4p level. However, ab initio calculations [187] indicate that the $4a_1$ orbital (the phosphorus lone pair) is largely P 3p in character (65% P 3p, 14% p 3s). This result is also borne out be recent X_α calculations [176] (60% P 3p, 11% P 3s). Thus a transition to 4p level should not be very intense [61]. Application of the Rydberg formula to the term value of feature 1 (2.44 eV) indicates that feature 3 could be the $4a_1 \rightarrow 5s$ Rydberg transition. Feature 2 can then be ascribed to the $4a_1 \rightarrow 3d$ Rydberg transition. The term value for this feature is 1.42 eV, which is close to the 1.51 eV expected for a 3d term value calculated using a quantum defect of zero.

The term values obtained for all the above transitions from the outer-most $4a_1$ orbital have been applied with respect to the other IP's in order to predict the positions of the levels leading to the respective limits. These estimated positions are indicated on Fig. 7.1 and it can be seen that the position of transitions leading to the 4e and $1a_2$ limits contributing to feature 4 are over estimated on this basis. The term value for feature 4 from the next (4e) orbital is 3.01 eV. The following orbitals ($4e-3a_1$) have significant C 2p character [176,187]

and the term value of 3.01 eV is much more like that observed for the C 1s → 4s transition. This is similar to the findings for $Si(CH_3)_4$ where it was suggested that the first Rydberg level belonged to the ligand as opposed to the molecule as a whole. Pending a detailed theoretical treatment, nothing much can be said of the rest of the spectrum except that it is built up of a number of overlapping transitions to the σ^* and Rydberg levels.

Phosphorus Trichloride (PCl_3)

Figure 7.2 shows the VSEELS spectrum of PCl_3 from 4-20 eV. The data is summarised in Table 7.4. The spectrum is much more complex than that of $P(CH_3)_3$, having many more clearly resolved transitions. The UV absorption spectrum reported earlier [184,186] at slightly higher resolution shows vibrational structure, but the spectra only extend as far as 10 eV. The term values for features 1 and 2 from the HOMO ($4a_1$) orbital are 4.83 and 4.54 eV respectively. Since these are both much higher than the term value for the 4s Rydberg level (3.06 eV - Table 7.1) from the P 2p ISEELS spectrum, they are assigned as transitions to the $\sigma^*(a_1)$ and $\sigma^*(e)$ virtual valence levels, respectively. The orbital ordering is taken from that given in Chapter 5. However, these levels are close together and the order could easily be in fact reversed.

Applying the term values thus obtained to the other valence levels it can be seen (Fig. 7.2) that much of the spectrum can be reasonably assigned to valence-valence transitions. The features that remain unassigned are therefore attributed to Rydberg transitions. Thus

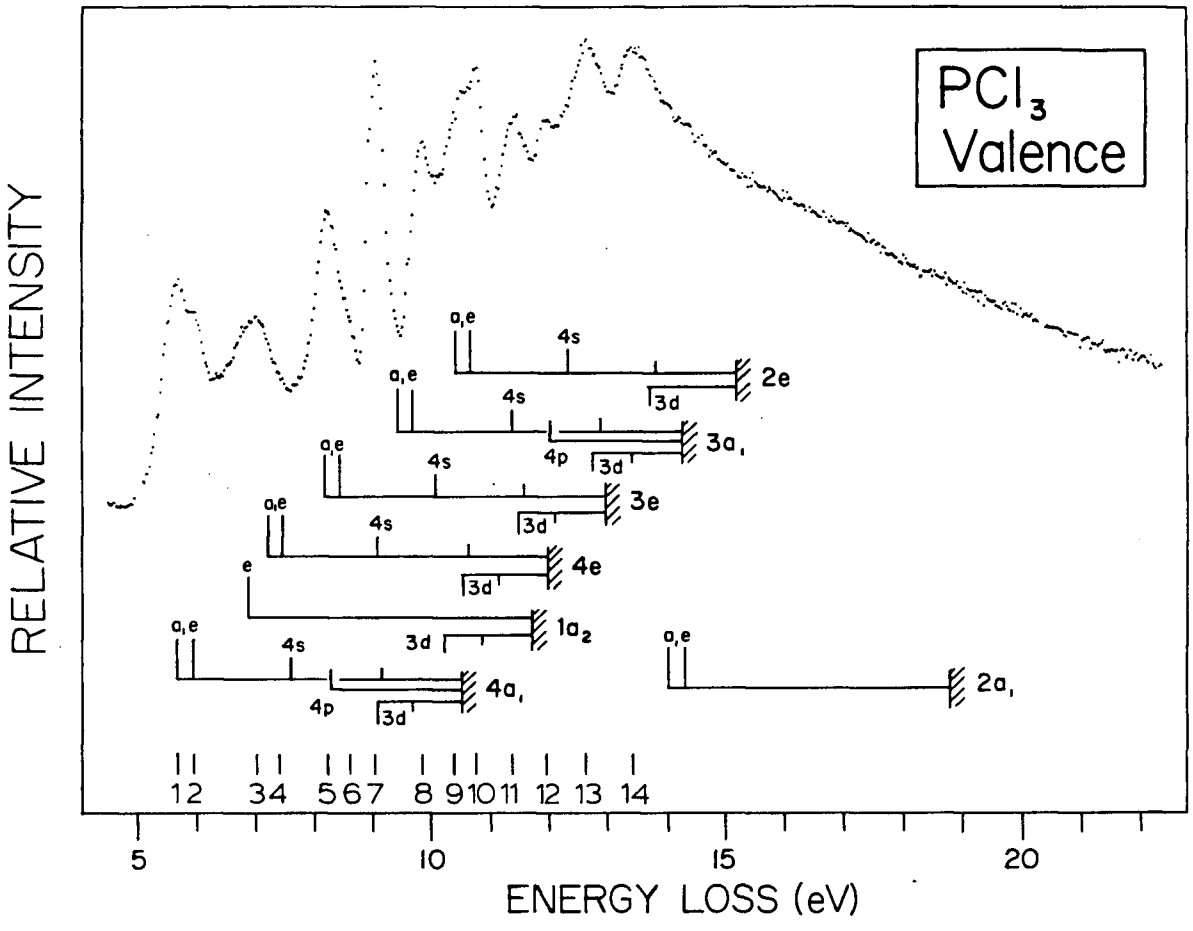

Figure 7.2:

The valence shell electron energy loss spectrum of PCl_3. The ionisation edges are taken from photoelectron spectroscopy (see Table 7.2). Positions of the valence-valence (tall bars), valence-Rydberg (short bars) transitions estimated from the term values are shown leading to each limit (see Table 7.4).

TABLE 7.4

Energies and possible assignments for the VSEELS spectrum of PCl_3

Feature	Energy Loss (eV)	Valence - Valence[(a)] Assignment	Valence - Rydberg[(b)] Assignment
1	5.68	$4a_1 \rightarrow \sigma^*(a_1)$	
2	5.97	$4a_1 \rightarrow \sigma^*(e)$	
3	7.03	$1a_2 \rightarrow \sigma^*(e)$, $4e \rightarrow \sigma^*(a_1)$	
4	7.43	$4e \rightarrow \sigma^*(e)$	$4a_1 \rightarrow 4s$
5	8.25	$3e \rightarrow \sigma^*(a_1)$	$4a_1 \rightarrow 4p$
6	8.63	$3e \rightarrow \sigma^*(e)$	
7	9.05	$3a_1 \rightarrow \sigma^*(a_1)$	$4a_1 \rightarrow 3d$, $4e \rightarrow 4s$
8	9.85	$3a_1 \rightarrow \sigma^*(e)$	$3e \rightarrow 4s$
9	10.48	$2e \rightarrow \sigma^*(a_1)$	$1a_2 \rightarrow 3d$, $4e \rightarrow 3d$
10	10.76	$2e \rightarrow \sigma^*(e)$	
11	11.40		$3e \rightarrow 3d$, $3a_1 \rightarrow 4s$
12	11.96		$3a_1 \rightarrow 4p$
13	12.64		$2e \rightarrow 4s$, $3a_1 \rightarrow 3d$
14	13.42		$2e \rightarrow 3d$

(a) $\sigma^*(a_1)$ term value = 4.83 eV,
$\sigma^*(e)$ term value = 4.54 eV,
IP's: see Table 7.2.

(b)
Only first member of series given:

4s term value = 2.95 eV, 4p term value = 2.26 eV and 3d term value = 1.46 eV.

IP's: see Table 7.2.

the sharp feature 7 is described as a combination of the $4a_1 \rightarrow 3d$ and $4e \rightarrow 4s$ Rydberg transitions, the term values of which are 1.46 eV and 2.95 eV respectively. As with $P(CH_3)_3$, the 3d term value is close to that which is expected (1.51 eV) with a quantum defect of zero. The 4s term value (2.95 eV) is only ~0.1 eV less than that in the ISEELS spectrum. The 4s term value from the Cl 2p spectrum is ~2.6 eV. These term values (as well as those calculated for the 5s and 4d levels) have been applied to the other valence orbital IP's and the positions of the corresponding levels are indicated on the spectrum (Fig. 7.2). It can be seen that all the major features are reasonably accounted for by this tentative assignment process.

Feature 5, which shows a clear vibrational progression in the UV spectrum [186] (with the same vibrational spacing as in the first ionised state in the photoelectron spectrum [117]) has been attributed by Robin [12] to a $4a_1 \rightarrow 4p$ Rydberg transition. The term value (2.26 eV) is in between those of the 4s and 3d levels. The a_1 orbitals should have some P 2s character. According to ab initio calculations [189] the $4a_1$ orbital has 14% P 3s character and 32% P 3p character. Thus a $4a_1 \rightarrow 4p$ transition might be expected. Feature 5 is thought to have this transition on top of the $3e \rightarrow \sigma^*(a_1)$ transition. The calculation also indicates that the $3a_1$ orbital has 3% P 2s character. Applying the term value of 2.26 eV to the $3a_1$ ionisation potential yields a $3a_1 \rightarrow 4p$ transition energy of 11.97 eV, in excellent agreement with feature 12 (11.96 eV). The rest of the outer valence orbitals should have no s character (as also indicated in the calculation [189] and

hence little intensity to the p Rydberg levels.

Phosphorus Trifluoride (PF_3)

The VSEELS spectrum of PF_3 is shown in Fig. 7.3, and the data is summarised in Table 7.5. As in the case of PCl_3, the UV absorption spectrum (up to ~10 eV) has been reported [184,186]. In the UV spectrum [186] feature 3 shows vibrational structure and, like PCl_3, has a similar spacing to that of the first ionised state [192]. The spectrum is quite different to that of PCl_3 with two intense bands (features 1 + 2 and feature 3) followed by overlapping broad features. There are no sharp features that could be obviously assigned to Rydberg transitions, in contrast to the situation in PCl_3. In this regard this spectrum is similar to the inner-shell spectra of PF_3, which are typical of molecules with highly electronegative ligands, in that strong transitions to the valence levels are observed at the expense of Rydberg transitions.

The term values for features 1 and 2 from the $4a_1$ (HOMO) orbital are 4.38 eV and 4.12 eV respectively. Robin [12] has assigned these in turn as due to the transitions $4a_1 \rightarrow 4s$ and $4a_1 \rightarrow \sigma^*$ (P-F). However, the P 2p ISEELS spectrum indicates that the 4s term value is 3.13 eV and therefore the 4s term value in the valence shell spectrum would be expected to be smaller. Therefore, features 1 and 2 have been assigned in the present work to σ^* transitions. The ISEELS assignment gave the $\sigma^*(e)$ level a term value of 6.8 eV and that for the $\sigma^*(a_1)$ of ~3.5 eV. Assuming that this assignment is correct, it is unlikely that the narrowly separated features 1 and 2 are due to the $4a_1 \rightarrow \sigma^*(e)$ and $4a_1 \rightarrow$

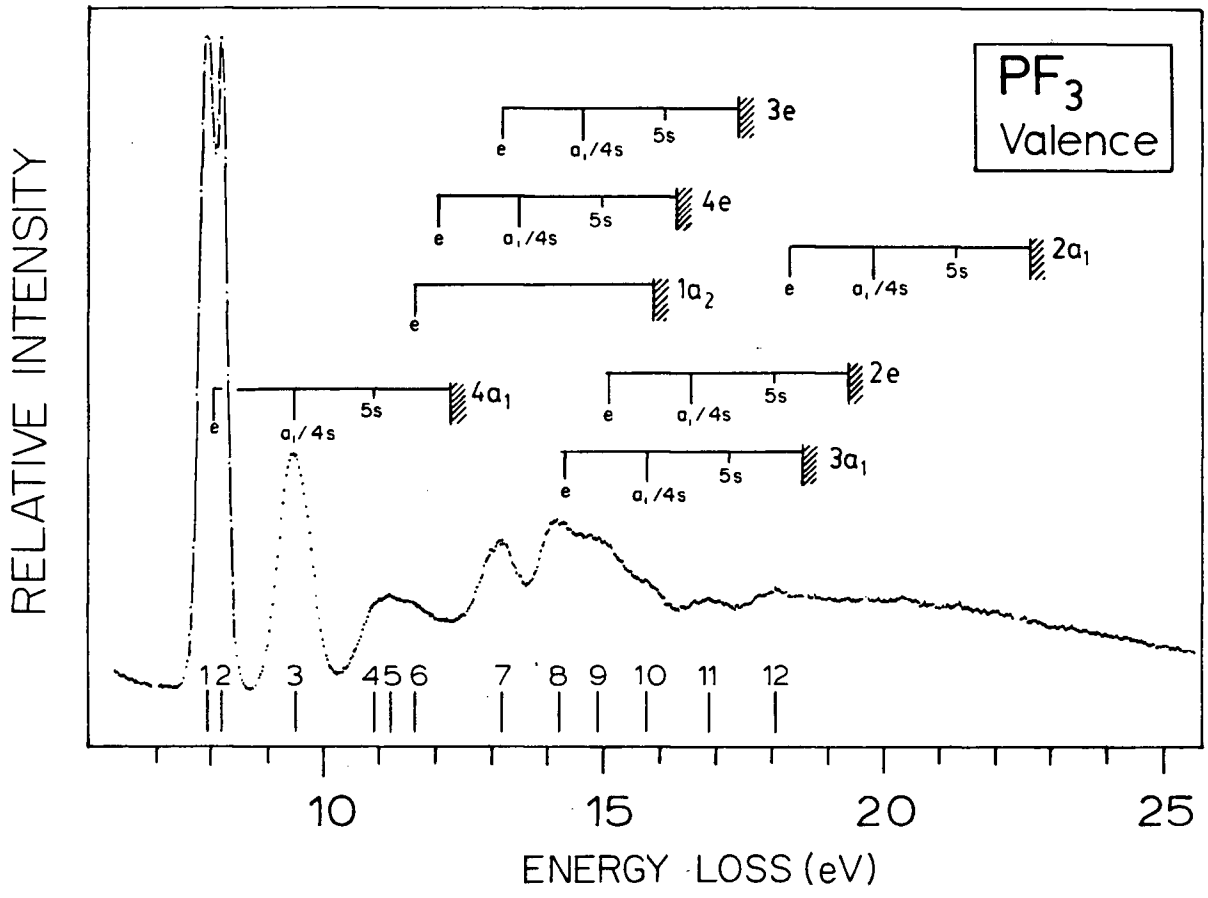

Figure 7.3:

The valence shell electron energy loss spectrum of PF_3. The ionisation edges are taken from photoelectron spectroscopy (see Table 7.2). Positions of transitions from the $4a_1$ orbital have been applied to the other IP's. The spectrum is summarised in Table 7.5.

TABLE 7.5

Energies, term values and possible assignments

for the VSEELS spectrum of PF_3

Feature	Energy Loss (eV)	Term Value (eV)[a]	Possible Assignments
1	7.91	4.38	$4a_1 \rightarrow \sigma^*(e)$
2	8.17	4.12	
3	9.49	2.79	$4a_1 \rightarrow \sigma^*(a_1)/4s$
4	10.89		
5	11.20	4.69	$1a_2 \rightarrow \sigma^*(e)$
6	11.64	4.68	$4e \rightarrow \sigma^*(e)$
7	13.18	4.25	$3e \rightarrow \sigma^*(e)$
	(13.52)†	(2.79)	$4e \rightarrow \sigma^*(a_1)/4s$
8	14.21	4.36	$3a_1 \rightarrow \sigma^*(e)$
	(14.56)†	(2.79)	$3e \rightarrow \sigma^*(a_1)/4s$
9	14.93	4.43	$2e \rightarrow \sigma^*(e)$
10	15.77	2.80	$3a_1 \rightarrow \sigma^*(a_1)/4s$
11	16.88	2.48	$2e \rightarrow \sigma^*(a_1)/4s$ (?)
12	18.09	4.51	$2a_1 \rightarrow \sigma^*(e)$

[a] Term values are calculated with respect to the IP of the initial orbital.
These IP's are given in Table 7.2.

† Position estimated using term value from feature 3.

$\sigma^*(a_1)$ transitions. Therefore, features 1 and 2 are assigned to Jahn-Teller components of the $4a_1 \rightarrow \sigma^*(e)$ transition which would lead to a ^1E degenerate final state. This conclusion concurs with that given previously by McAdams et al. [186] for the valence-shell optical absorption spectrum of PF_3. The difference of ~2.5 eV between the ISEELS and VSEELS term values for the $\sigma^*(e)$ LUMO orbital is in keeping with that found for NF_3 (see Chapter 3) and PCl_3 (compare Tables 7.1 and 7.3). Feature 3 is then assigned as the $4a_1 \rightarrow \sigma^*(a_1)$ (or very likely the $4a_1 \rightarrow \sigma^*(a_1)/4s$) transition. Robin [12] has assigned this feature (3) in the UV spectrum to the $4a_1 \rightarrow 4p$ Rydberg transition. The term value of this feature is 2.79 eV which, as expected, is slightly less than that for the ISEELS 4s (3.13 eV) or $\sigma^*(a_1)$ (~3.5 eV) transitions. Both an ab initio calculation [187] and an X_α calculation [176] indicate roughly equal P 3s and P 3p character to the $4a_1$ orbital. This would imply that transitions to both 4s and 4p Rydberg levels might be seen, but the spectrum does not seem to reflect this situation. Clearly more theoretical work is needed in order to clarify this situation.

The rest of the valence-valence assignments, based upon the term values of features (1 + 2) and 3 with respect to the $4a_1$ limit are shown in Fig. 7.3. On this basis the majority of the remaining features in the spectrum of PF_3 can be reasonably assigned to these valence-valence transitions (Table 7.5). As stated above, there seems to be very little Rydberg structure. Feature 4 has been ascribed to the $4a_1 \rightarrow 3d$ transition by Robin [12]. This feature has a term value of 1.40 eV with respect to the $4a_1$ limit, which is reasonable for such an assignment (a

quantum defect of zero would predict a term value of 1.5 eV).

Phosphoryl Chloride ($OPCl_3$)

The VSEELS spectrum of $OPCl_3$ (Fig. 7.4) is similar to that for PCl_3 in that it shows features that can be ascribed to both valence-valence and valence-Rydberg transitions. The only previously reported spectrum is that by Halmann [185], which extends as far as ~6.7 eV. This spectrum [185] shows a weak plateau at ~6.5 eV that was ascribed to a forbidden $n_o \rightarrow \pi^*$ transition. There is evidence of some very weak structure in this region in the VSEELS spectrum.

The spectrum has been assigned in a similar manner to those for the preceding molecules. Features 1 and 2 are considered to arise from valence-valence transitions since its respective term values (4.36 and 3.74 eV respectively from the 11e orbital) are larger than that ascribed to the 4s Rydberg level (3.08 eV) in the ISEELS spectrum. Thus these features (1 and 2) are assigned to the $11e \rightarrow \sigma^*(a_1)$ and $11e \rightarrow \sigma^*(e)$ transitions respectively. The ordering is that of the P 2p spectrum (term values of 7.0 eV and 6.2 eV) and that of the O 1s spectrum (term values of 5.5 eV and 4.2 eV). The reversal of intensity in contrast to that observed in the O 1s ISEELS spectrum is consistent with the originating orbital in the VSEELS spectrum, being of O 2p character.

The term values with respect to the 11e limit have then been applied to the other IP's (Table 7.2) and the estimated positions of the corresponding transitions are indicated in Fig. 7.4. It should be noted

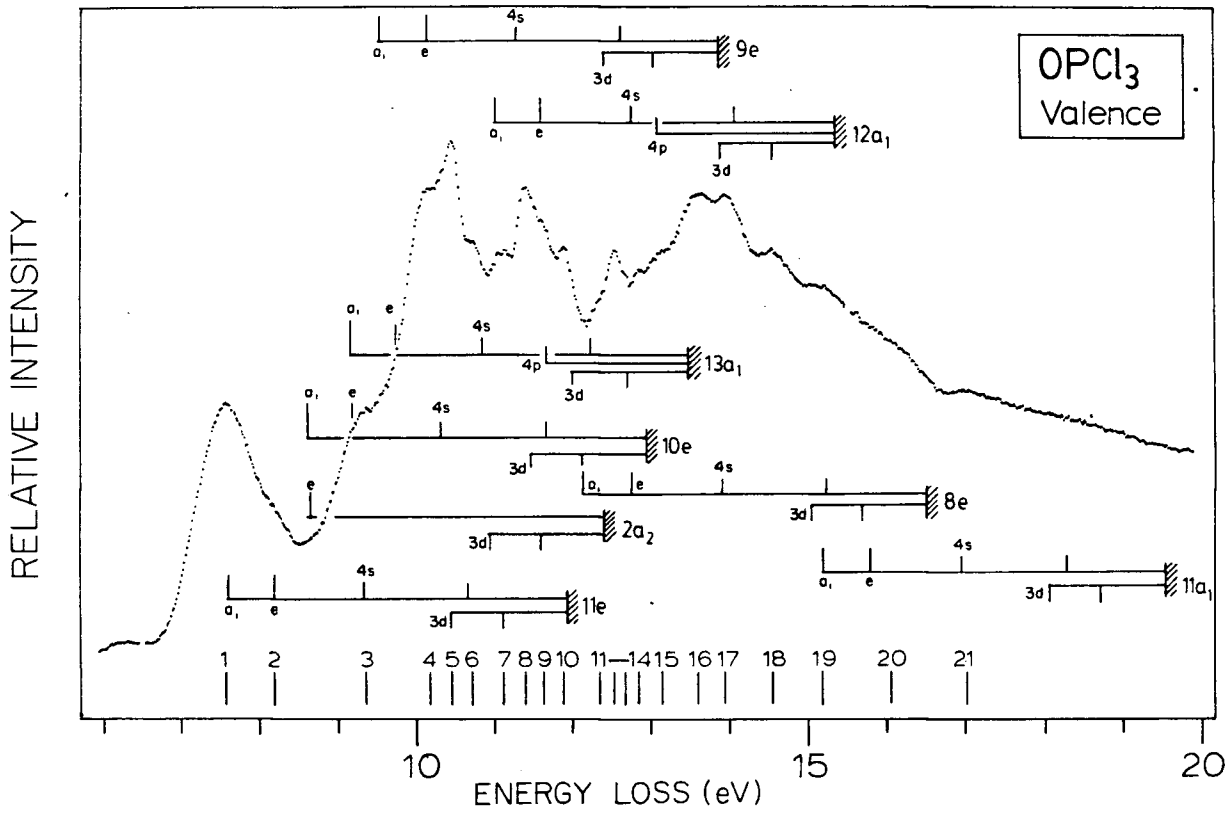

Figure 7.4:

The valence shell electron energy loss spectrum of $OPCl_3$. The ionisation edges are taken from photoelectron spectroscopy (see Table 7.2). Positions of the valence-valence (tall bars), valence-Rydberg (short bars) transitions as estimated from the term values are shown leading to each limit (see Table 7.6).

that feature 2 cannot be assigned to a transition to the LUMO orbital ($\sigma^*(a_1)$) from the $2a_2$ level, as this transition is dipole forbidden under C_{3v} selection rules. Thus the intensity leading up to feature 5 can be reasonably ascribed to the various valence-valence transitions indicated on Fig. 7.4, since the correspondence of the spectral features with the predicted positions is good. The molecule $OPCl_3$ has a second $\sigma^*(a_1)$ virtual orbital (see Table 7.1) that so far has not been considered. From a consideration of this $\sigma^*(a_1)$ ISEELS term value and that of the 4s ISEELS Rydberg level, it is likely to mix with the Rydberg level to give a $\sigma^*(a_1)$/4s conjugate [65] in the valence spectrum.

Feature 5, the first feature not fitted by this proposed valence-valence scheme, has a term value of 1.48 eV with respect to the 11e orbital and can be assigned to the 11e → 3d Rydberg transition. There is also evidence of a shoulder on the low energy side of feature 5. This has a term value ~2.6 eV (similar to the 4s term value in the Cl 2p spectrum) from the 10e orbital, and so is assigned to the 10e → 4s/$\sigma^*(a_1)$ transition. These term values have been applied to the other IP's and the estimated positions of the transitions are indicated on the spectrum. Transitions to the p Rydberg series might also be expeted. The ab-initio calculation [189] indicates that the $12a_1$ orbital has a 10% O 2s component. Thus a $12a_1$ → 4p transition might be expected to have some intensity. Feature 15 has a term value of 2.21 eV with respect to the $12a_1$ ionisation potential. Since this term value is close to that given for the 4p Rydberg level in PCl_3 (2.26 eV). Feature 15 is assigned accordingly. As with PCl_3, this term value is applied

also to the other a_1 symmetry orbital.

Obviously the spectrum is made up of many overlapping transitions, and no clear, unambiguous assignment can be made. The spectral data show evidence of significant contributions from valence-valence transitions. Table 7.6 summarises the positions of the features.

Phosphorus Pentafluoride (PF_5)

Finally, the spectrum of PF_5 will be considered. The spectrum is shown in Fig. 7.5. To date there has been no UV absorption or VSEELS spectrum reported for this molecule. The molecule PF_5 is of D_{3h} symmetry. From a consideration of a minimal basis set, the virtual orbitals are $\sigma^*(a_1')$, $\sigma^*(e')$, and $\sigma^*(a_2'')$. However, only the first two levels will be considered since the $\sigma^*(a_2'')$ level is located right at the ionisation edge in the ISEELS spectra.

The experimental ionisation potentials are taken (Table 7.2) from photoelectron spectroscopy [193,194]. However, there is a considerable lack of agreement between the various calculations as to the orbital ordering. Some of these assignments have been summarised by Goodman et al. [194]. The ordering used in the present work (see Table 7.2) is that of Strich and Veillard [191], who performed an ab-initio LCAO MO SCF calculation with a medium size basis set. Table 7.7 summarises the dipole allowed/forbidden transitions for the outer valence region of this molecule.

From the ISEELS spectrum, the term value of the 4s Rydberg level is 2.75 eV. Since feature 1 has a term value of 3.15 eV with respect to

TABLE 7.6

Energies and term values for the VSEELS

spectrum of $OPCl_3$

Feature	Energy Loss (eV)	Feature	Energy Loss (eV)
1	7.57†	12	12.53
2	8.19†	13	12.66
3	9.35	14	12.83
4	10.18	15	13.14†
5	10.45†	16	13.59
6	10.73	17	13.94
7	11.11	18	14.54
8	11.37	19	15.16
9	11.61	20	16.03
10	11.87	21	17.00
11	12.34		

†Features used to estimate term values - see text.

Term values:

$\sigma^*(a_1)$ = 4.36 eV
$\sigma^*(e)$ = 3.74 eV
$\sigma^*(a_1)/4s$ = 2.6 eV
3d = 1.48 eV
4p = 2.21 eV

These have been applied to the IP's listed in Table 7.2.

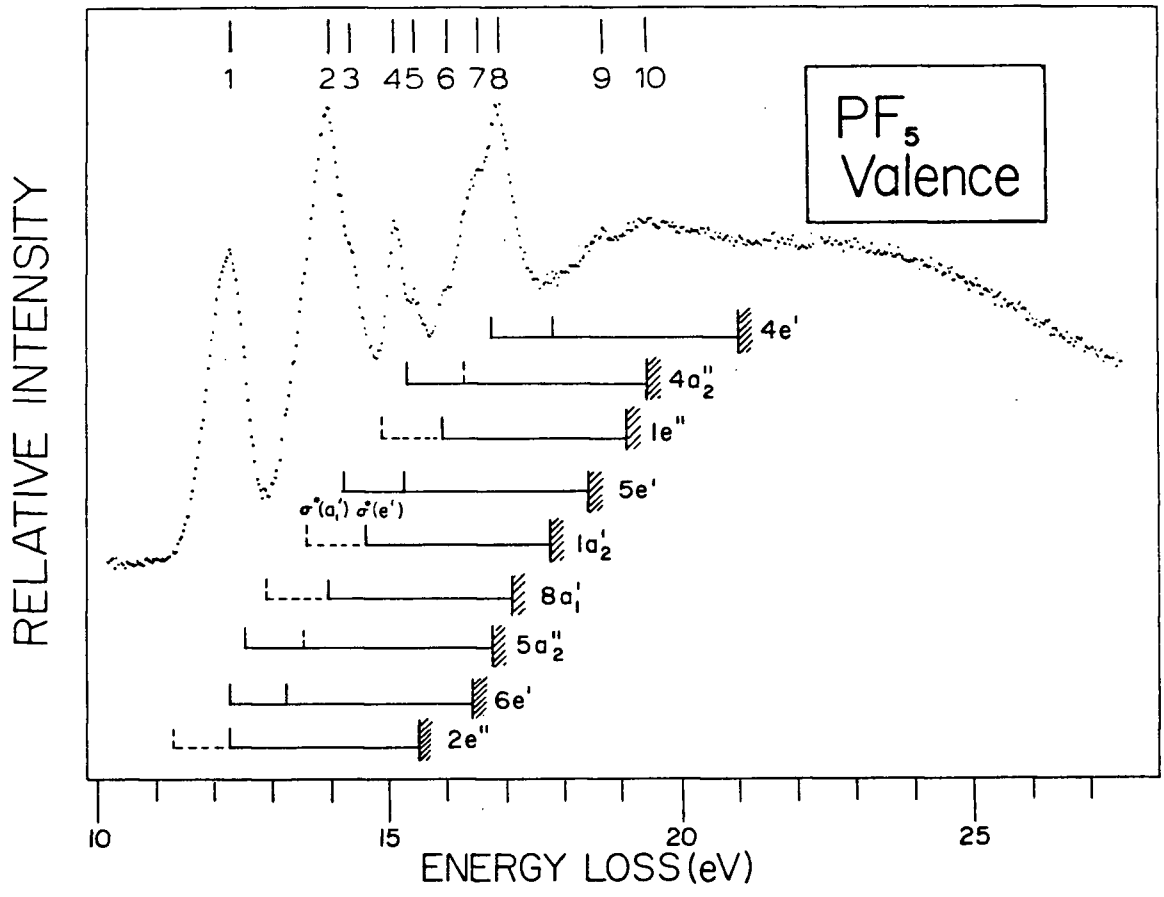

Figure 7.5:

The valence shell electron energy loss spectrum of PF_5. The ionisation edges are taken from photoelectron spectroscopy (see Table 7.2). The ordering is from ref. [191]. Positions of the valence-valence transitions estimated from the term values are shown leading to each limit (see Table 7.8). Dotted bars indicate forbidden transition based on assigned symmetry of ionised orbital.

TABLE 7.7

Dipole allowed/forbidden transitions for PF_5 in D_{3h} symmetry.

Initial Orbital	Transitions to σ^* Levels Dipole Allowed/Forbidden	
	$\sigma^*(a_1)$	$\sigma^*(e')$
$2e''$	No	Yes
$6e'$	Yes	Yes
$5a_2''$	Yes	No
$8a_1'$	No	Yes
$1a_2'$	No	Yes
$5e'$	Yes	Yes
$1e''$	No	Yes
$4a_2''$	Yes	No
$4e'$	Yes	Yes

the HOMO orbital, it is therefore likely due to valence-valence transitions. Given that the two highest occupied MOs are the 2e" and the 6e' orbitals, and considering the selection rules in Table 7.7, feature 1 is ascribed to the $2e'' \rightarrow \sigma^*(e')$ and $6e' \rightarrow \sigma^*(a_1')$ transitions. Thus the term values for the $\sigma^*(e')$ and $\sigma(a_1')$ are ~3.15 eV and 4.17 eV respectively. This compares with 3.6 eV and 6.2 eV for the P 2p spectrum and 2.7 eV and 5.0 eV for the F 1s spectrum shown in Chapter 6. The reduction in term value (~2 eV) for the LUMO orbital in going from ISEELS to VSEELS is in keeping with those observed for other molecules with highly electronegative ligands (eg., NF_3, PF_3, PCl_3, and $OPCl_3$). Thus the assignment of the 2e" to the HOMO orbital is clearly supported by the VSEELS spectrum.

The term values as obtained above for the 2e" and 6e limits are now applied to the other IP's. The positions of all the transitions so derived are indicated in Fig. 7.5, and the assignments summarised in Table 7.8. A dashed vertical line on the spectrum indicates the positions of transitions that are dipole forbidden. The agreement between the spectra and the predicted valence-valence transitions is very good in almost all cases. A better agreement would be obtained if the order (Table 7.2) of the $4a_2''$ and 4e' levels is reversed. The calculation [191] indicates that the separation of these levels is only 0.16 eV, and therefore not reliable for predicting the ordering. The reversal of this ordering is supported by the work of Cox et al. [193], who in the analysis of the He(I) spectrum assigned the 21 eV feature to the $4a_2''$

TABLE 7.8

Energies and possible assignments

for the VSEELS spectrum of PF_5

Feature	Energy Loss (eV)	Possible Assignments[(a)]
1	12.29	$2e'' \rightarrow \sigma^*(e')$, $6e' \rightarrow \sigma^*(a_1')$, $5a_2'' \rightarrow \sigma^*(a_1')$
2	13.96	$6e' \rightarrow \sigma^*(e')$, $8a_1' \rightarrow \sigma^*(e')$
3	14.35	$5e' \rightarrow \sigma^*(a_1')$ $1a_2' \rightarrow \sigma^*(e')$
4	15.13	$5e' \rightarrow \sigma^*(e')$
5	15.43	$4a_2'' \rightarrow \sigma^*(a_1')$ †
6	15.97	$1e'' \rightarrow \sigma^*(e')$
7	16.51	†
8	16.86	$4e' \rightarrow \sigma^*(a_1)$ †
9	18.65	from $7a_1'$ (?)
10	19.4	

†Exchanging $4a_2''$ and 4e' order

5	$4e' \rightarrow \sigma^*(a_1')$
7	$4e' \rightarrow \sigma^*(e')$
8	$4a_2'' \rightarrow \sigma^*(a_1')$

(a)Assignments based on applying following term values to IP's in Table 7.2.

$\sigma^*(e')$	3.15 eV	Feature 1 from 2e"
$\sigma^*(a_1')$	4.17 eV	Feature 1 from 6e'

level. The VSEELS spectrum (Fig. 7.5) can be adequately described by just considering predominantly valence-valence transitions. This is similar to the situation discussed above for PF_3(and also NF_3).

SUMMARY AND CONCLUSIONS

The VSEELS spectra of several phosphorus-containing compounds have been presented in this chapter and compared with their ISEELS spectra. The ISEELS spectra clearly indicate the dominant presence of transitions to σ^* virtual valence levels, specially those with electronegative ligands. Transitions to valence levels also seem to dominate in the valence shell spectra presented here. The term values, as expected, are lower than for the corresponding ISEELS transition (approximately 2-2.6 eV lower for those with highly electronegative ligands, e.g. F). The valence-valence nature of these transitions is evidenced by the term values being even larger than those for the ISEELS 4s Rydberg transitions. The higher term values for the ISEELS spectra are explained by the effect of the localised, central nature of the phosphorus core hole. The ligand ISEELS spectra, where the core hole is situated on the periphery of the molecule, generally have term values that lie in between those of the central atom ISEELS spectra and the VSEELS spectra. Term values for the σ^* levels arising from the three regions of the molecules are summarised in Table 7.9. Also shown are the term values for the 4s Rydberg level. In cases where these are only slightly lower than those for a σ^* orbital of the same symmetry in the P 2p ISEELS spectra, the corresponding feature in the VSEELS spectra cannot be solely assigned to one or the other. In these cases the

TABLE 7.9

Term values from ISEELS and VSEELS for PH_3, $P(CH_3)_3$, PCl_3, PF_3, PF_5, and $OPCl_3$

Molecule	Orbital	ISEELS Term Values (eV)[a]			VSEELS Term Values (eV)
		Phosphorus (2p)	Ligand[b]		
PH_3	$\sigma^*(e)$	5.1			3.76[c]
	$\sigma^*(a_1)$	4.5			
	4s	2.48			
$P(CH_3)_3$	$\sigma^*(e)$	3.3			2.44
	$\sigma^*(a_1)$	~2			
	4s	2.86	3.17		3.01
PCl_3	$\sigma^*(a_1)$	6.9	5.7		4.83
	$\sigma^*(e)$	6.4			4.54
	4s	3.06	2.6		2.95
PF_3	$\sigma^*(e)$	6.8	5.2		~4.4 (4.68)[d]
	$\sigma^*(a_1)$	~3.5	3.0		2.79
	4s	3.12			
PF_5	$\sigma^*(a_1')$	6.2	5.0		4.17
	$\sigma^*(e')$	3.6	2.7		3.15
	4s	2.71			
			Cl	O	
$OPCl_3$	$\sigma^*(a_1)$	7.0	6.0	5.5	4.36
	$\sigma^*(e)$	6.2	4.5	4.2	3.74
	$\sigma^*(a_1)$	4.4	3.2		2.6
	4s	3.08	2.6		

[a] From Chapters 5 and 6.

[b] F 1s, O 1s, C 1s, and Cl 2p as appropiate.

[c] Ref. [12].

[d] With reference to F lone-pair orbital.

feature is probably best ascribed as a mixed valence-Rydberg ($\sigma^*/4s$) level [65]. It should be noted that the difference in term values is much smaller for the Rydberg levels than for the lowest σ^* levels on going from the ISEELS to the VSEELS spectra. Levels assignable to the 3d Rydberg level in the VSEELS spectra were seen to have a constant term value (~1.4-1.5 eV). The quantum defect obtained (~0) is consistent with the assignment to d levels.

It can be seen that, especially in the case of PF_3 and PF_5, the VSEELS spectra are dominated by valence-valence transitions with very little evidence of any Rydberg series. The VSEELS spectra of PF_5 support the assignment of the HOMO orbital of PF_5 as being the 2e" orbital [191,194]. Similarly $OPCl_3$ and PCl_3 show many transitions assignable to valence-valence transitions; however, valence-Rydberg transitions are also apparent. The spectrum of $P(CH_3)_3$ (Fig. 7.1) has a very intense first feature, and in this respect it is quite similar to that observed for PH_3 [12]. The intensity of the first feature in $P(CH_3)_3$ clearly indicates a contribution from valence-valence transition(s). It presumably contains transitions to the $\sigma^*(e)$ and $\sigma^*(a_1)/4s$ levels. The term values for higher energy features, arising from orbitals located on the ligand, are each similar to that for the first transition in the C 1s spectrum (C 1s → 4s transition) and are an indication of a transition to a "localised" Rydberg orbital, as was suggested for $Si(CH_3)_4$ and in the methylamines (see Chapter 8).

In the present work it can be seen that the ISEELS spectra can be used as an aid to the assignment of the more complex VSEELS spectra.

Spectra of condensed phases that result in the suppression of Rydberg transitions would be helpful in clarifying the valence-valence and/or valence-Rydberg nature of the spectra. In this regard the effect of the highly electronegative (F) ligand on the spectra seemingly parallels this effect in that the valence-valence transitions are trapped (and therefore enhanced) by a charge barrier effect of the type more usually involved in the case of inner-shell spectra.

CHAPTER 8

INNER SHELL ELECTRON ENERGY LOSS SPECTRA OF THE METHYL AMINES AND AMMONIA

In Chapters 5 and 6 the ISEELS spectra of several phosphorus compounds were presented and the effects of the ligand on the relative spectral intensities contrasted. A similar comparison was made between the ISEELS spectra of $Si(CH_3)_4$ presented in Chapter 4 and earlier reported photoabsorption spectra of related silicon compounds. The ligand was seen to play an important role in the observed intensity distributions. In contrast to ligands such as H and CH_3, highly electronegative ligands, for example F, enhance the probability of transitions to virtual valence levels at the expense of those to Rydberg levels. This was also seen in the ISEELS spectra of NF_3 presented in Chapter 3. In this chapter, as a continuation of this work, the ISEELS spectra of $(CH_3)_3N$, which is isoelectronic with NF_3, is presented as well as the spectra of the other methyl amines ($(CH_3)_2NH$ and CH_3NH_2) and NH_3. The ISEELS spectra of NF_3, $(CH_3)_3N$ and NH_3 are also compared with the third row phosphorus analogues PF_3, $P(CH_3)_3$ and PH_3.

To date the only previously reported inner shell electron excitation spectra of these molecules have been the ISEELS spectra of NH_3 and CH_3NH_2 reported by Wight and Brion [72] and a recent X-ray absorption spectrum of NH_3 [196]. However, there have been several studies on the valence electron excitation spectra. For example, Tannenbaum et al.

[197] have reported the UV absorption spectra of the methyl amines up to ~8 eV. There have also been numerous studies on NH_3 [198]. The lowest excited states in the valence and inner-shell spectra have been assigned to transitions to levels of mainly 3s and 3p Rydberg character [72,197]. Salahub [199] has performed semi-empirical MO-CI calculations on these molecules and assigned the lowest valence excitations to HOMO (N lone pair) $\rightarrow \sigma^*$ transitions. However, ab initio calculations on NH_3 [200, 201] and $(CH_3)_3N$ [201] support the Rydberg assignment. The spectra presented here provide further evidence for the assignment of the lowest electronic transitions to Rydberg levels.

EXPERIMENTAL DETAILS

The spectra were obtained on the ISEELS spectrometer described in Chapter 2. An impact energy of 2.5 keV was used and the scattered electrons were sampled at ~1° scattering angle. The C 1s spectra of the amines were calibrated against the S $2p_{1/2} \rightarrow t_{2g}$(184.54 eV) feature of SF_6. These C 1s spectra were used, except in the case of $(CH_3)_3N$, to internally calibrate the N 1s regions of the methyl amines. The N 1s spectra of $(CH_3)_3N$ and NH_3 were calibrated against the N_2 (N 1s $\rightarrow \pi^*$ (v = 1), 401.10 eV) and CO (C 1s $\rightarrow \pi^*$ (v = 0), 287.40 eV) features respectively.

RESULTS & DISCUSSION

Carbon 1s spectra

The long-range spectra of the C 1s region of the methyl amines

are shown in Fig. 8.1. These spectra were obtained with a resolution of 0.36 eV FWHM. More detailed short-range spectra, recorded at a higher resolution (0.18 eV FWHM), are shown in Fig. 8.2. The assigned ionization edges for $(CH_3)_3N$ and CH_3NH_2 have been taken from XPS [180,202]. As no value for the C 1s IP of $(CH_3)_2NH$ has been reported, its value was assumed to be the mean of the other two IP's. Table 8.1 summarises the spectral data.

The spectra are similar to that for CH_4 [66,67,72] and the analysis can be considered in terms of that for a mono-substituted methane. The C 1s spectrum of CH_3NH_2 is virtually identical to that for C_2H_6 [68]. Similar observations were made in the C 1s spectra of $P(CH_3)_3$ and $Si(CH_3)_4$.

Hitchcock and Brion have discussed the C 1s spectra of the methyl halides [63,64]. It is instructive to compare the analysis there with the spectra presented here. The methyl halides all possess a feature attributable to low-lying σ^* orbital [64]. However, the rest of the spectrum can be assigned solely to Rydberg transitions. In the amine spectra reported here there is a complete absence of any feature attributable to a low-lying σ^* feature. The discrete portions of the amine C 1s spectra reported here are similar to the remainder of the methyl halide spectra and can be assigned solely to Rydberg features in an analogous manner. The assignments based upon these arguments [64] are shown in Table 8.1

The post-edge behaviour is different in these two sets (i.e., the amines and methyl halides) of molecules. The methyl amines show a broad

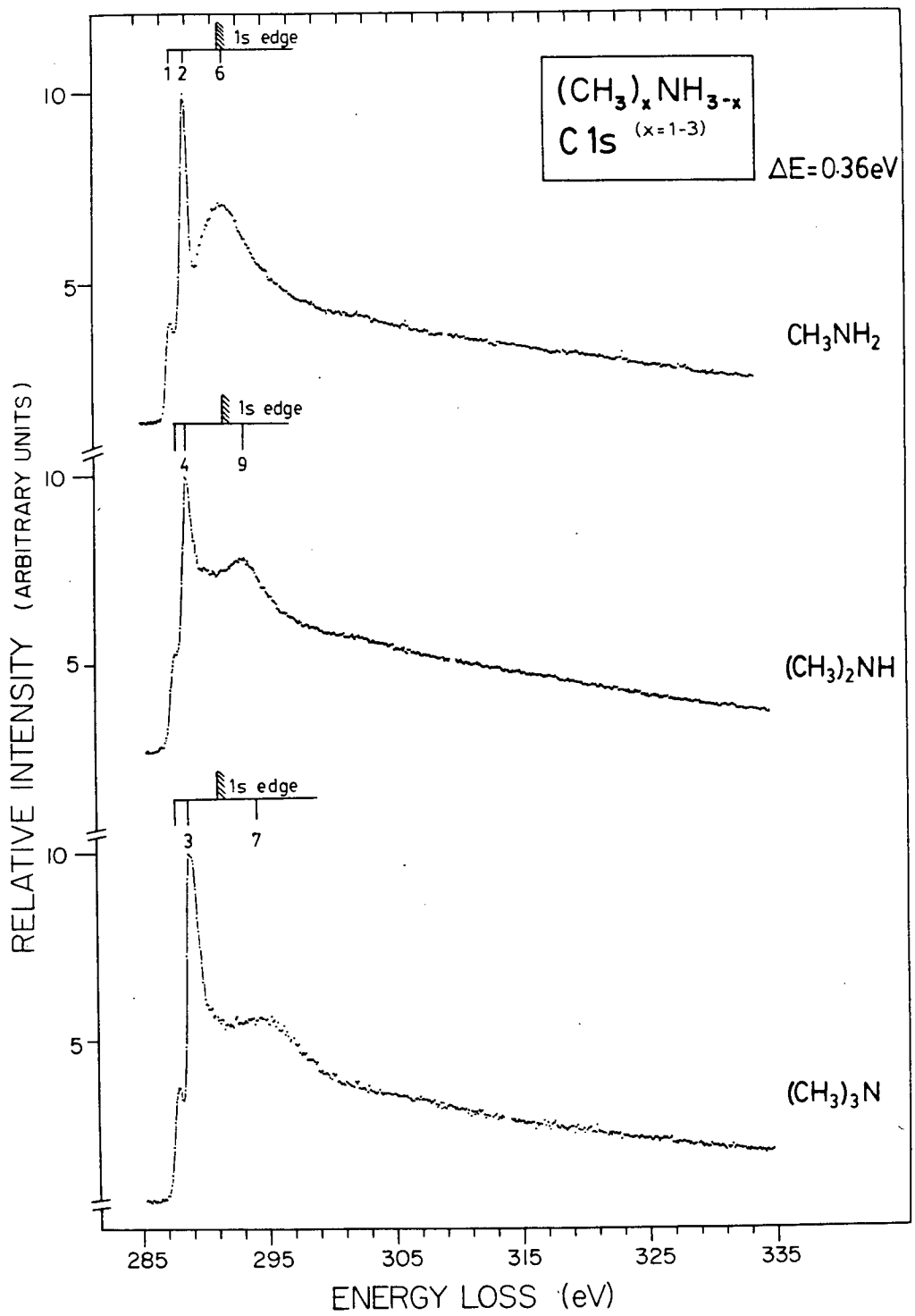

Fig. 8.1:

Long range electron energy loss spectra of the C 1s region of the methyl amines.

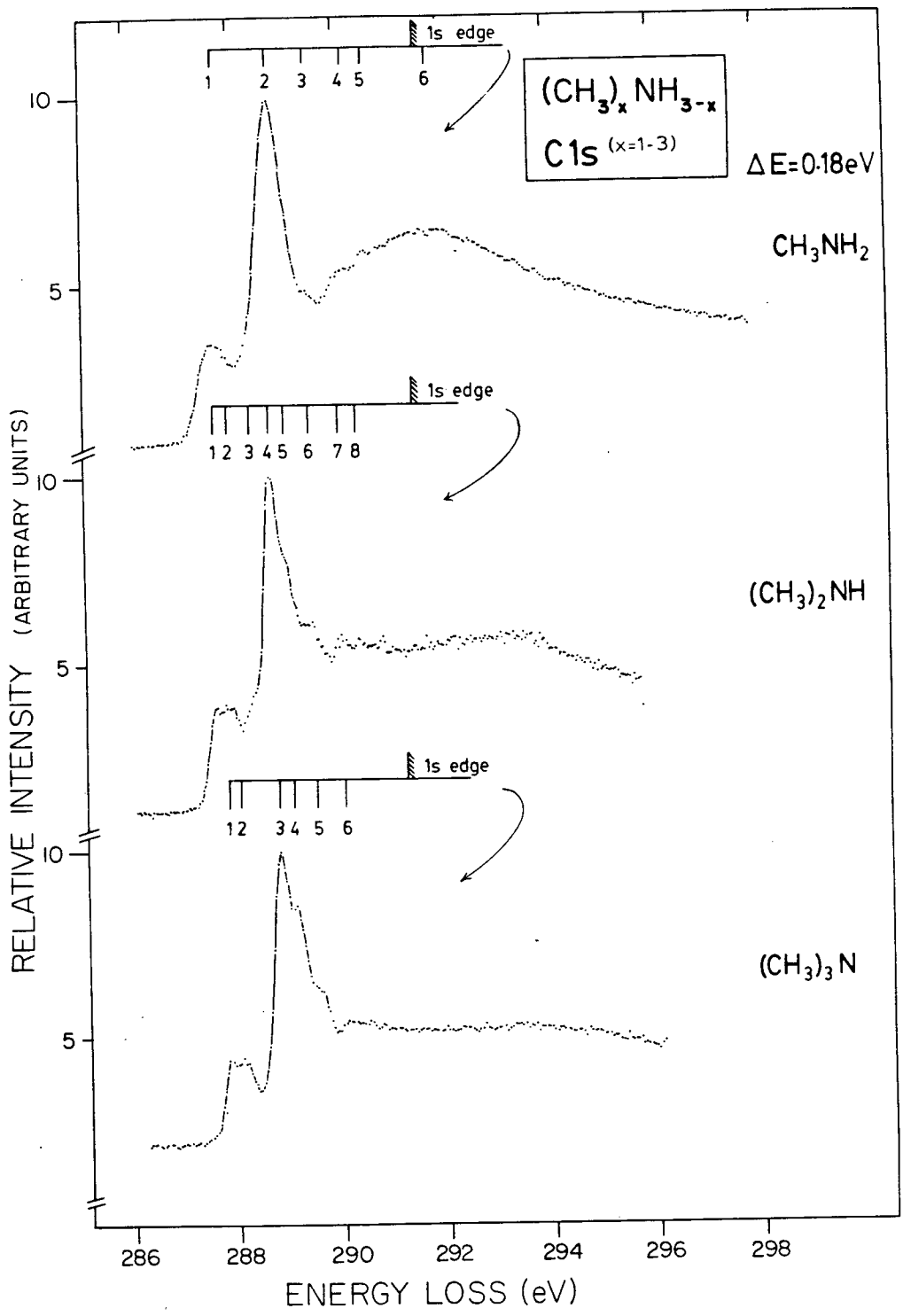

Fig. 8.2:

Short range, high resolution electron energy loss spectra of the C 1s region of the methyl amines.

TABLE 8.1

Energies, Term Values and Possible Assignments

for the C 1s Region of the Methyl Amines

CH_3NH_2			$(CH_3)_2NH$			$(CH_3)_3N$			
Feature	Energy (eV)	T[a] (eV)	Feature	Energy (eV)	T (eV)	Feature	Energy (eV)	T (eV)	Possible[b] Assignment
1	287.70	3.90	1	287.61	3.82	1	287.84	3.42	3s
			2	287.85	3.58	2	288.08	3.18	3s+v
			3	288.3	3.1				
2	288.78+	2.82	4	288.67+	2.76	3	288.80+	2.46	3p(x,y)
			5	288.95	2.48	4	289.07	2.19	3p(x,y)+v
3	289.46	2.14	6	289.46	1.97	5	289.51	1.75	3p(z)
4	290.21	1.39	7	290.03	1.40	6	290.06	1.20	4p(x,y)/3d
5	290.59	1.01	8	290.35	1.08				4p(z)
IP‡	291.60	0	IP‡	291.43	0	IP‡	291.26	0	1s limit
6	291.8	-0.2	9	293.2	-1.8	7	294.3	-3.0	σ^* shape-resonance

+Calibrated feature, estimated uncertainty ± 0.08 eV for CH_3NH_2, $(CH_3)_2NH$; ± 0.15 eV for $(CH_3)_3N$.

‡XPS CH_3NH_2 ref. [202], $(CH_3)_3N$ ref. [180]; $(CH_3)_2NH$ mean of other two values.

(a) T = IP - Energy

(b) $(CH_3)_2NH$ and CH_3NH_2: C_s symmetry p(x,y) ≡ pa', p(z) ≡ pa".

and fairly intense feature just beyond the ionization edge (Fig. 8.1). This is not the case for the methyl halides, nor for that matter methane [67,72]. However, ethane [68] shows similar behaviour to the molecules here. The difference between the C 1s spectra of methane [72] and ethane [68] is nicely illustrated in a recent paper by Hitchcock et al. [100] and clearly indicates a peak just beyond the edge for ethane. The continuum features can be attributed to a σ^* shape resonance [77] associated with the C-C bond in ethane [100] and with the C-N bond in the amines. In MO terms these can be thought of as excitations into a σ^* anti-bonding state [87]. Thus the major difference between the methyl halides and the molecules here is the location of the σ^* orbital. In the former they are low lying and in the discrete portion, whereas in the methyl amines they are in the continuum. The σ^* shape resonances will be discussed further below.

Nitrogen 1s spectra

Figure 8.3 shows the long-range N 1s spectra of the methyl amines. The spectral resolution is 0.36 eV FWHM. More detailed short-range spectra are shown in Fig. 8.4 along with a high-resolution spectrum (0.14 eV FWHM) of NH_3. The 1s ionization edges are taken from XPS measurements [203]. On going from NH_3 to $(CH_3)_3N$ a gradual change in spectral features can be observed. The NH_3 spectrum is characteristic of a dominant (atomic-like) Rydberg spectrum with a largely structureless continuum of low intensity. In contrast, the $(CH_3)_3N$ spectrum shows little Rydberg structure and is dominated by a broad continuum

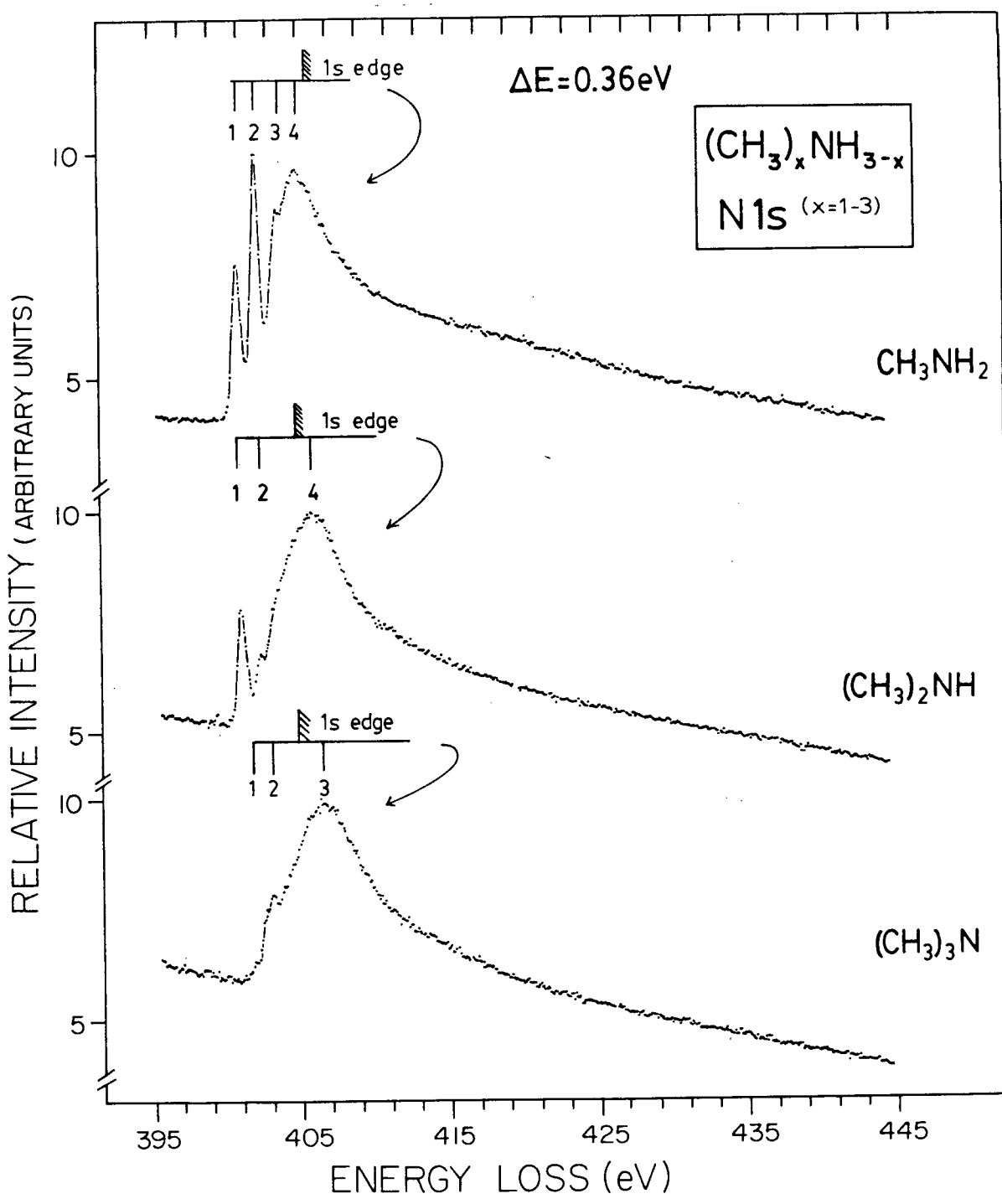

Fig. 8.3:

Long range electron energy loss spectra of the N 1s region of the methyl amines.

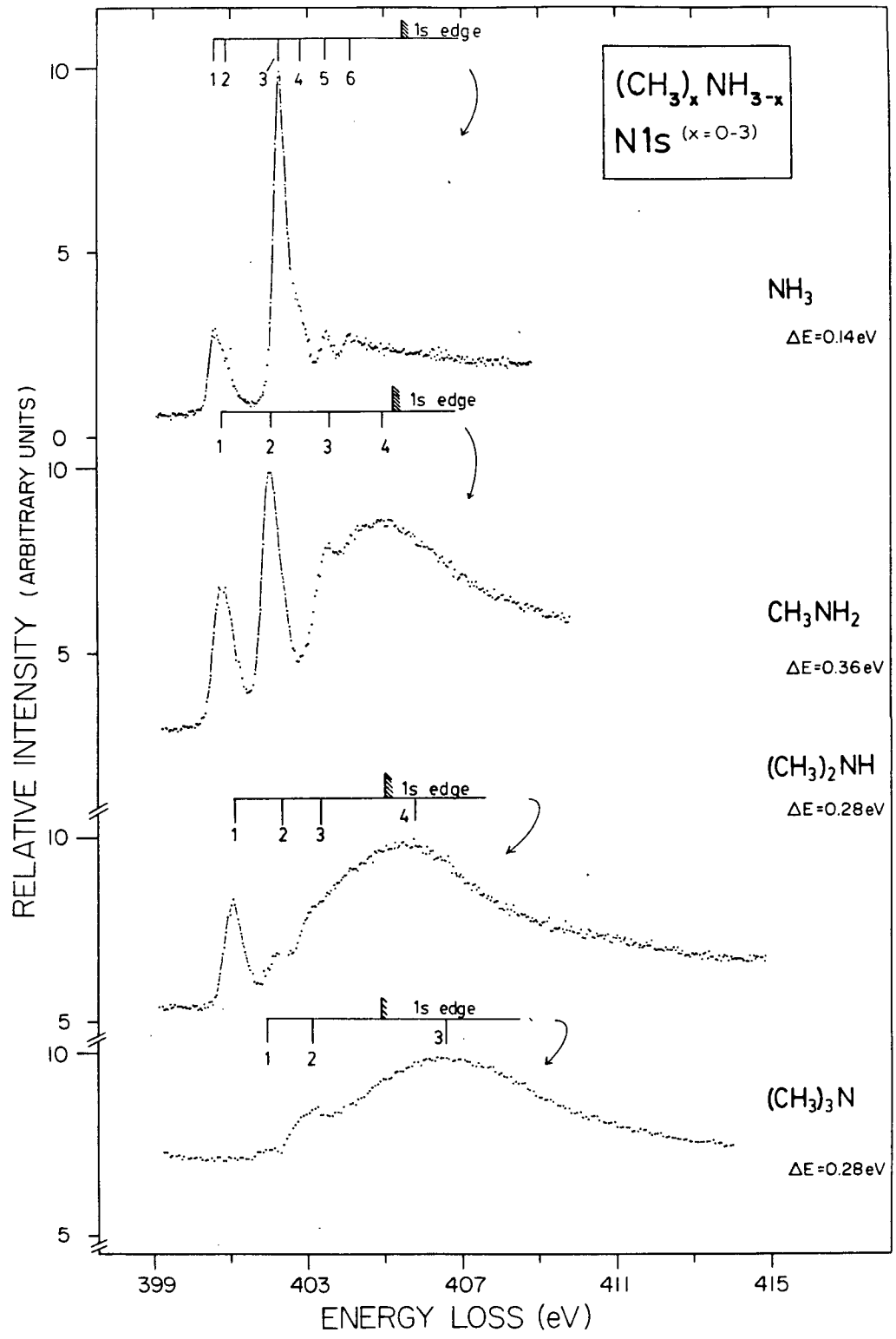

Fig. 8.4:

Short range electron energy loss spectra of the N 1s region of ammonia and the methyl amines. The (differing) spectral resolution is indicated on each spectrum.

feature that can be ascribed to a σ^*(N-C) shape resonance.

As stated above, the NH_3 spectrum can be assigned to transitions to the Rydberg levels and this spectrum has been published earlier [72, 196]. There is no evidence of any distinct σ^* feature in the discrete portion, though Robin [12] has suggested that the HOMO → 3s feature in the valence shell UV spectrum is on top of a continuous valence shell transition, and Schwarz [61] suggests an admixture of valence anti-bonding character for the n = 3 Rydberg levels. Rather weak features in the NH_3 1s continuum (~14 eV above the edge) have been identified with a σ^*(N-H) shape resonance [99]. The NH_3 spectrum presented here is summarized in Table 8.2 along with possible assignments. The results of the earlier ISEELS work [72] and the X-ray absorption spectrum [196] are also shown. The energies of the spectral features in the different ISEELS spectra are in good agreement with each other and with the X-ray absorption spectrum, though in the latter the features are uniformly ~0.1-0.2 eV higher in energy. The assignments in the present work differ only slightly from the earlier ISEELS work [72]. This results from the much higher resolution achieved here. Features 1 and 2 are assigned to the 1s → 3s transition plus vibrational component, thereby concurring with the suggestions of Wight et al. [72]. No vibrational component is discernable at the resolution employed in the X-ray work [196]. Features 3 and 4 are assigned to the 3p(e) and 3p(a_1) Rydberg levels respectively, with a separation of ~0.6 eV, which agrees well with separation observed (< 0.6 eV) in the valence electron excitation spectrum [204]. No feature corresponding to feature 4 was observed

Table 8.2

Energies, Term Values and Assignment for

the N 1s Energy Loss Spectra of NH_3

	ISEELS					X-ray Absorption	
	Present Work			Wight et al.[+]		Akimov et al.[‡]	
Feature	Energy (eV) ± 0.08 eV	Term Value (eV)	Assignment	Energy (eV)	Assignment	Energy (eV)	Assignment
1	400.61	4.91	3s	400.6	3s	400.8	3s
2	400.92	4.60	3s + v	—			
3	402.29	3.23	3p(e)	402.2	3p(e)	402.4	3p(e)
4	402.85	2.67	$3p(a_1)$	—		~403.0	$3p(a_1)$
5	403.52	2.00	4s	403.5	$3p(a_1)$	403.6	4s
6	404.14	1.38	4p/3d	404.1	4s/3d/4p(e)	404.1	4p(e)
IP[*]	405.52	0					

[+]ref. [72]

[‡]ref. [196].

[*]XPS ref. [203]

in the earlier ISEELS work due to poorer resolution [72], however, it is seen in the X-ray spectrum [196]. On this basis feature 5 is now re-assigned to the 1s → 4s transition consistent with the interpretation given by Schwarz [61] and also by Akimov et al. [196].

In comparing the ISEELS spectrum with the valence shell spectrum of the three amines and ammonia, two points can be noted. Firstly, there occurs a reversal in the intensity of the features associated with the 3s and 3p Rydberg levels. This reflects the s-level characteristics of the originating orbital in the core spectra which favour an s → p transition (dipole allowed in the pure atomic case) over the s → s transition (dipole forbidden in the pure atomic case), expecially in a molecule as symmetrical as NH_3 [61]. The second point concerns the term values of the features. The term values are between 0.4 and 0.5 eV larger for the 3s and 3p features in the ISEELS spectra than for the corresponding features in the valence shell spectra [198]. This arises from the localized nature of the core-hole, and thus the newly promoted electron sees a centre approximating a (Z + 1) core. Actually, this difference is quite small and it reflects the Rydberg nature of the final orbital in both spectra. Rydberg orbitals, being large and diffuse, are less sensitive to the location of the hole. In NF_3, where the lowest unoccupied orbital is a σ^* antibonding orbital, the difference in term values between core and valence spectra is 2.17 eV.

Table 8.3 summarizes the spectral features of the N 1s region of the methyl amines. Of these only the spectrum of CH_3NH_2 has been previously reported [72]. As before, the first features of CH_3NH_2 are

TABLE 8.3

Energies, Term Values and Possible Assignments

for the N 1s Region of the Methyl Amines

CH_3NH_2			$(CH_3)_2NH$			$(CH_3)_3N$			
Feature	Energy (eV)	T[(a)] (eV)	Feature	Energy (eV)	T (eV)	Feature	Energy (eV)	T (eV)	Possible Assignment
1	400.78	4.39	1	401.04	3.89	1	(401.8)	(3.0)	3s
2[†]	402.03	3.14	2	402.30	2.63	2	403.0	1.8	3p
3	403.55	1.62	3	403.24	1.69	-	—	--	3d etc.
4	404.8	0.3	4	405.8	-0.9	3	406.5	-1.7	σ^* shape-resonance
IP	405.17		IP	404.93		IP	404.82		

[†]Calibrated feature, estimated uncertainty ± 0.12 eV for CH_3NH_2, $(CH_3)_2NH$; ± 0.2 eV for $(CH_3)_3N$.

[‡]XPS ref. [203]

(a) T = IP - Energy

assigned as transitions to the 3s and 3p levels respectively. The term values are lower than those in NH_3 which would be expected upon replacing an H ligand by an alkyl group [12] and once again the term values are ~0.5 eV higher than for the corresponding valence shell spectra [198]. A further difference between the spectra of CH_3NH_2 and NH_3 is that the relative intensity of the N 1s → 3p transition to that of the N 1s → 3s transition is less in CH_3NH_2. However, the former transition to the 3p is still more intense. The major difference between CH_3NH_2 and NH_3 is the appearance of a broad feature at the edge. This previously unassigned feature [72] parallels that observed in the C 1s spectrum and can be assigned to a σ^*(N-C) shape resonance [99]. The spectrum shows no evidence of any low-lying σ^* orbital below the ionization edge.

The spectrum of $(CH_3)_2NH$ (Figs. 8.3 and 8.4, Table 8.3) also shows transitions that can be assigned to the Rydberg levels. However, the intensity of the N 1s → 3s transition is now larger than that of the N 1s → 3p transition. However, the relative reduction in the 3p intensity is consistent with that observed on going from NH_3 to CH_3NH_2. The first feature in the spectrum is at 401.04 eV, which is very close to the N 1s → π^* feature of N_2 (401.10 eV). The possibility of this feature arising from an N_2 impurity, however, can be discounted since the valence spectrum was run and no trace was found of the very intense N_2 ($X \rightarrow b^1\Pi_u$) feature at 12.93 eV [103]. The term values for the 3s and 3p levels are about ~0.3 eV larger than in the valence spectra [198]. As with CH_3NH_2, the spectrum has a broad, intense feature that is

assigned to a σ^*(N-C) resonance. In this case the feature is centered just above the edge. Once again the spectrum shows no evidence for any low-lying σ^* feature below the edge.

The spectra of $N(CH_3)_3$ (Figs. 8.3 and 8.4, Table 8.3) shows very little Rydberg character. There is an indication of a weak feature, 1, with a term value of 3.0 eV, which is assigned to a transition to the 3s Rydberg level. The term value compares with one of 3.03 eV from the valence shell spectra. The broad feature 2 presumably encompasses transitions to the 3p Rydberg levels and higher. The lack of intensity for the 3s transitions consistent with the arguments made above in the case of NH_3. The spectrum is totally dominated by a σ^*(N-C) shape resonance, centred just above the edge.

GENERAL DISCUSSION

The spectra presented here all support the contention that there are no low-lying σ^* virtual orbitals, and that the lowest levels are Rydberg in nature. This agrees with the assignment of the valence shell spectra (below the first IP) as transitions to levels of predominantly Rydberg character [12,200,201]. In the ISEELS spectra the σ^* levels have been found to be at or only just above the ionisation edges in the amines (Tables 8.1 and 8.3) and seemingly absent in NH_3. For the valence spectra transitions to the σ^* levels would be higher in the continuum than for the core spectra since there would be no core hole to cause a large relaxation. The C 1s spectra are very similar and show an essentially constant 3s/3p intensity ratio. On the other hand, the

Rydberg characteristics of the N 1s spectra change dramatically and certainly do not parallel the C 1s spectra. Indeed, the C 1s spectra could be solely interpreted in terms of a localized Rydberg structure based upon a CH_3X model compound. This phenomenon has also been noted in $Si(CH_3)_4$ and $P(CH_3)_3$.

A broad feature at or just above the edge is present in all of the methyl amine C 1s and N 1s spectra and is associated with the σ^* antibonding orbital formed by the C-N bond. In a multiple scattering picture it is also termed as a σ^* shape-resonance [77]. There has been much discussion recently (see Chapter 1, section F.III) on the relationship between bond length and the shape-resonance position (E_R) from the edge ($\delta = E_R - IP$). Hitchcock et al. [100] have demonstrated that a linear relationship is sufficient to describe the C-C bond length variation and shape-resonance position in a series of hydrocarbons. Sette et al. [99] have made a systematic study on a larger variety of systems. A study on some phosphorus compounds in Chapter 6 also indicated that there is a relationship between bond length/type and resonance position. Table 8.4 lists the C-N bond lengths and resonance positions from the edge (δ). It is seen that as the bond length decreases the relative position of the resonance with respect to the edge moves to higher energy, as has been noted before [99,100]. The lack of data points and the error limits, however, does not allow the exact relationship to be examined.

Finally, it is of value to compare the spectra of NF_3, $(CH_3)_3N$ and NH_3 with their third row analogues PF_3, $P(CH_3)_3$ and PH_3. In

TABLE 8.4

Resonance Energy Positions (δ) From Edge and C-N Bond Lengths (R) for the Methyl Amines

Molecule	R(Å)[a]	δ (eV)[b]	
		C 1s	N 1s
$(CH_3)_3N$	1.451 (3)	3.0	1.7
$(CH_3)_2NH$	1.462 (7)	1.8	0.9
$(CH_3)NH_2$	1.4714 (20)	0.2	-0.3

[a] From microwave spectroscopy. Landholt - Börnstein (New Series) II/7 "Structure Data of Free Polyatomic Molecules," Springer-Verlag, Berlin (1976)

[b] δ = Resonance Energy - IP = -Term Value

previous chapters the effects of the ligand on the P 2p spectra of some phosphorus compounds were compared to the effects on the Si 2p spectra of silicon compounds. The ligand identity had a similar effect in both series. Briefly, the more highly electronegative ligands (e.g., F) enhance the probability of transitions to the σ^* virtual levels at the expense of transitions to the higher-lying Rydberg levels. The term values of the lowest σ^* orbitals were much larger in these compounds than those of compounds with less electronegative ligands such as H. The σ^* levels in the third row hydrides still precede the Rydberg levels. However, the spectrum is much less dominated by the σ^* levels and relatively strong Rydberg transitions are observed. The effect of the electron donating CH_3 ligand leads to possible overlapping or mixed Rydberg-valence transitions. It is of interest to note, however, the complete absence of a 2p → 4s Rydberg transition in the Si 2p spectrum of $Si(CH_3)_4$, implying that this spectrum consists essentially of transitions to valence orbitals. By contrast the C 1s → 4s transition is clearly seen in the C 1s ligand spectrum of $Si(CH_3)_4$. Features in the continuum spectra of $Si(CH_3)_4$ and phosphorus compounds are also present and can be identified in part with d-like σ^* shape resonances.

On comparing the ISEELS spectra of the phosphorus compounds with the spectra of the nitrogen compounds it should be remembered that in the former the 2p spectral region is being considered whereas the 1s region is being considered for the latter. However, important differences (or similarities) can still be noted. The effects of the ligands would appear to be very similar in both series. The major difference

arises with the position of the σ^* antibonding orbitals which are high lying and in the continuum for the N compounds except when it is associated with an electronegative ligand. Thus the N 1s spectrum of NF_3 has a very intense, low-lying N 1s → σ^* transition and only weak transitions to the Rydberg levels. The NH_3 spectrum can be mostly ascribed to Rydberg transitions with the high-lying and weak σ^*(N-H) shape resonance approximately 14 eV into continuum [99], whereas in PH_3 the σ^* transitions precede the relatively intense Rydberg transitions. The N 1s spectrum of $(CH_3)_3N$ is dominated by a N 1s → σ^* shape resonance occurring just beyond the edge and shows little Rydberg character. As in $Si(CH_3)_4$ and $P(CH_3)_3$, the ligand spectrum of $(CH_3)_3N$ shows the typical C 1s → Rydberg transitions. Thus the N spectrum lends further support for the assignments previously given for $P(CH_3)_3$ and $Si(CH_3)_4$, which indicate that the lowest Rydberg levels belong very much to the methyl group and have much C character. The assignment of the $(CH_3)_3N$ valence shell spectrum to Rydberg transitions [12,200,201] is consistent with the above discussion since the σ^* level is in the continuum (and at a higher energy since there would be no core hole). It is interesting to contrast the lack of intensity of transitions to Rydberg orbitals in the N 1s spectra of NF_3 and $(CH_3)_3N$. In the former molecule, NF_3, this can be explained by the formation of a potential barrier resulting in enhanced (inner-well) virtual valence occupied states, and depleted (outer-well) Rydberg states [73,77,92,93]. However, such a barrier should not exist in $(CH_3)_3N$, where the ligands are in fact slightly electron donating in contrast to the highly electronegative F ligands in

NF_3. Thus the lack of Rydberg transition in $(CH_3)_3N$ arises not from the formation of a barrier, but rather from the "localized" nature of the lowest Rydberg members, which appear to be highly concentrated around the methyl groups. This is consistent with the progressive reduction in Rydberg intensity for the N 1s spectra progressing along the series: $NH_3 \rightarrow CH_3NH_2 \rightarrow (CH_3)_2NH \rightarrow (CH_3)_3N$. No features attributable to d-like shape-resonances were noted in the N spectra, and this is in keeping with the fact that N is a row 2 (Li → Ne) atom.

CHAPTER 9

HIGH RESOLUTION C 1s AND VALENCE SHELL ELECTRONIC EXCITATION SPECTRA OF ALLENE AND TRANS-1,3-BUTADIENE STUDIED BY ELECTRON ENERGY LOSS SPECTROSCOPY

In the previous chapters, the effects of electronegative ligands on the intensity distributions observed in inner shell electron excitation spectra have been examined. The intensity distributions can be understood in terms of shape-resonance which result from the trapping of the photoelectron by some type of potential barrier [73,77]. Initially a coulomb-repulsive type of barrier was advocated [73], however, observations of similar phenomena in molecules which do not possess electronegative ligands (eg. N_2 and CO[4,71]) led to the postulation of some form of centrifugal barrier caused by the anisotropic nature of the molecular field [74,75]. In the final study of this work, the spectra of two molecules which fall into this latter category are presented.

Butadiene and allene are the simplest hydrocarbons possessing two carbon-carbon double bonds. Trans-1,3-butadiene (CH_2=CH-CH=CH_2), henceforth referred to as butadiene, is the simplest conjugated system while allene (CH_2=C=CH_2) is the simplest cumulene. Much attention has been focussed upon the lowest valence electronic excited states of these two molecules, both experimentally and theoretically. Valence shell work on butadiene includes UV absorption studies [205 and references

within], variable angle electron energy loss spectroscopy (EELS) at low impact energies [206-211], multiphoton ionisation [212-214] and various theoretical studies [215-218]. Likewise, the valence shell spectrum of allene has also been studied extensively, including UV absorption spectra [219-222], electron impact spectroscopy [223] and theoretical studies [215,224-226]. The only work on the carbon 1s inner shell electron excited states is the low resolution (~1eV FWHM) inner shell electron energy loss spectrum (ISEELS) of butadiene reported recently by Hitchcock et al. [100]. No inner shell electron excitation spectra of allene have so far been published. In this chapter work high resolution ISEELS spectra are presented for butadiene (0.07 - 0.21 eV FWHM) and allene (0.11 - 0.35 eV FWHM). Also shown are the extended valence shell electron energy loss spectra (up to 25 eV) recorded at a resolution of ~0.03 eV FWHM. The previously reported valence shell EELS spectra have only extended as far as ~11.5 eV [207,223].

There has been a great variety of interpretations presented on the valence shell spectra of these molecules, especially for allene. In the previous chapters, different relaxation effects were noted on the Rydberg and virtual valence levels upon creation of a core hole as compared to a hole in the valence shell. Differences in excess of 2 eV have been observed for term values between the two spectral regions for the virtual valence levels (see Chapters 3 and 7) whereas Rydberg term values are largely unaffected by the location of the hole. Increases in term values on going to the inner shell regions have been observed for the Rydberg levels, however, these increases tend to be small (<0.5 eV)

- (see Chapter 8 and ref. [72]). Thus a clear separation of transitions to the Rydberg and virtual valence levels is often seen in inner shell spectra. Hence, from a consideration of the ISEELS spectra presented in this work, it should be possible to obtain an unambiguous assignment and to distinguish clearly between the valence and Rydberg final states. Application of the term values thus obtained to the valence shell spectra is expected to give upper bounds to the term values for the various transitions and so help clarify the assignment of the valence shell spectra.

Experimental Details

All the spectra were obtained on the ISEELS spectrometer described in Chapter 2. The inner shell spectra were calibrated using the N_2 (N 1s $\rightarrow \pi^*$, v=1) transition at 401.10 eV while the valence shell spectra were calibrated against the He I resonance line at 21.218 eV [104].

Results and Discussion

1. Inner shell Spectra

(a) Butadiene (CH_2=CH-CH=CH_2)

The carbon 1s inner shell spectra of butadiene at various energy resolutions are shown in Fig. 9.1. The long range spectrum (Fig. 9.1, lower section) agrees well with the previously published low resolution spectrum by Hitchcock et al. [100]. However, more features can now be observed due to the higher resolution achieved in the present work. The

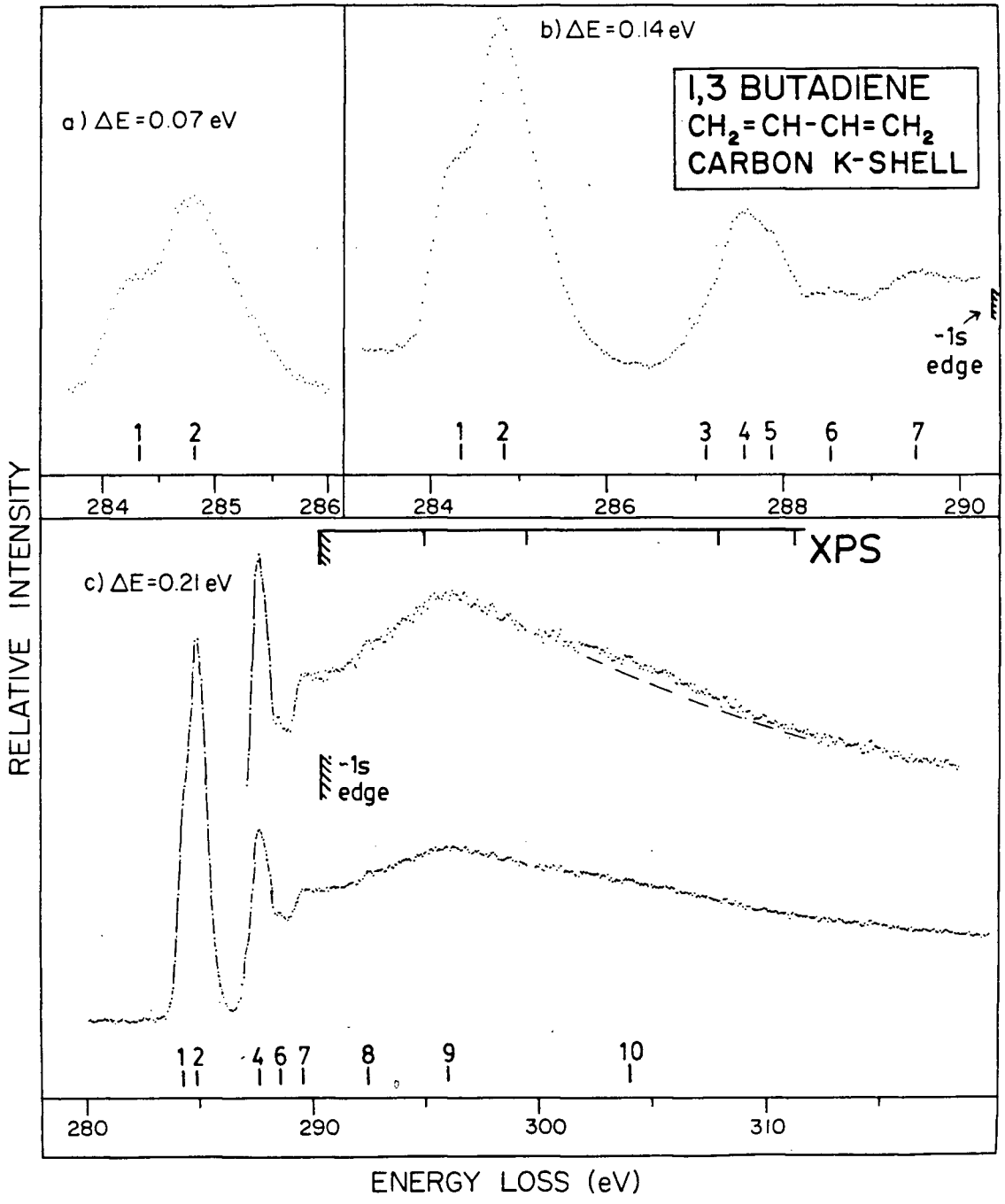

Fig. 9.1: Inner shell electron energy loss spectra of butadiene at (a) 0.07 eV, (b) 0.14 eV and (c) 0.21 eV spectral resolution. The 1s edge is the estimate of Hitchcock et al. [100]. The positions of the XPS satellite structure from the edge is from Carlson et al. [227].

energies, estimated term values and proposed assignments of the features are summarised in Table 9.1. There has been no reported value for the C 1s IP's of butadiene and so the value (290.4(3) eV) estimated by Hitchcock et al. [100] from a consideration of the IP's of related hydrocarbons has been used to predict the term values. Hitchcock et al. [100] assumed that the IP's of the two different C 1s environments would be very similar and indistinguishable. This is supported by the (uncalibrated) XPS spectrum of butadiene [227] which shows a single peak in the C 1s region.

Butadiene is of C_{2h} symmetry and its two unoccupied π^* levels are of a_u and b_g symmetries. Transitions from the C 1s levels (which have a_g and b_u symmetries) to both of these π^* levels might be expected to be seen at the high resolution of the present ISEELS experiment.

Features 1 and 2 (Fig. 9.1a) are clearly attributable to transitions to the π^* levels because of their very high term values (6.1 eV and 5.6 eV respectively) and thus they are assigned as the C $1s(a_g)\rightarrow\pi^*(a_u)$ and C $1s(b_u)\rightarrow\pi^*(b_g)$ transitions accordingly. The term value for the $\pi^*(a_u)$ level (6.1 eV with respect to the estimated [100] IP) is 3 eV greater than the corresponding term value obtained from the $\pi(b_g)(HOMO)\rightarrow\pi^*(a_u)$ transition observed in the valence shell spectrum [207-211]. The transition to the second π^* level from the HOMO level (i.e. $\pi(b_g)\rightarrow\pi^*(b_g)$) is dipole forbidden and has been the subject of much

Table 9.1

Energies, term values and possible assignments for the C 1s energy loss Spectrum of Butadiene

Feature	Energy (eV)	Term Value† (eV)	Possible Assignment
1	284.32	6.1	C $1s(a_g) \rightarrow \pi^*(a_u)$
2	284.83††	5.6	C $1s(b_u) \rightarrow \pi^*(b_g)$
3	287.1	3.2	3s
4	287.56	2.8	$3p_1$
5	287.87	2.5	$3p_2$
6	288.5	1.9	3d
7	289.52	0.9	4p etc
8	292.4		Double excitation
9	295.9		σ^* (C-C) shape resonance
10	~304		σ^* (C=C) shape resonance

† calculated using an estimated IP of 290.4(3)eV [100].

†† calibrated feature. Estimated uncertainty ±0.08eV.

search [207-210,212,213]. It has been recently identified using variable angle low energy EELS [209,210] and has been observed as a diffuse band underlying sharp Rydberg structure at ~7.4 eV in the valence shell spectrum. The separation of the π^* states in the ISEELS spectra (Fig. 9.1a) is 0.5 eV, whereas it is 1.5 eV in the valence shell spectrum [209,210]. This can be attributed to several factors including the fact that a frozen orbital picture cannot be assumed, as has been noted by Hitchcock et al. [100]. Adams [228] has estimated the relaxation energies for some hydrocarbons including butadiene using CNDO/2 calculations which indicate a different relaxation effect depending on which C atom the core hole resides. A further small difference may arise in that the a_g and b_u C 1s levels might be separated by as much as a few tenths of an eV, a separation which would not be seen in most XPS work.

The rest of the pre-edge features can be assigned to the various Rydberg transitions. The shoulder (feature 3), on the leading edge of peak 4, has a term value of ~3.2 eV and is assigned to the C $1s(b_u) \rightarrow 3s(a_g)$ Rydberg transition. Features 4 and 5 have approximate term values of 2.8 eV and 2.5 eV respectively and are assigned to $1s(a_g) \rightarrow 3p_1$ and $1s(a_g) \rightarrow 3p_2$ transitions (note: the designations $3p_1$ and $3p_2$ are used [210] because the p Rydberg orbitals are of a_u and b_u symmetries. Transitions to these levels are therefore dipole forbidden from the $1s(b_u)$ level). Term values for features ascribed to the 3s, $3p_1$ and $3p_2$ levels in valence shell spectra are 2.88 eV, 2.45 eV and 2.02 eV from EELS studies [210] and 2.88 eV, 2.43 eV and 2.06 eV from

multiphoton ionisation [213]. Thus it is seen that the ISEELS term values (3.2 eV, 2.8 eV and 2.5 eV respectively) are approximately 0.4-0.5 eV larger than those for the corresponding valence shell transitions. As discussed earlier, this is not unusual for Rydberg levels [Chapter 8 and ref. [72]) and is certainly much less than the difference for the π^* levels. Feature 6 is ascribed to C 1s → 3d transitions. The term value of ~1.9 eV is 0.2 eV larger than that for the 3d level obtained from multiphoton ionisation of the valence shell [213]. Feature 7 is assigned to transitions to the 4p and higher Rydberg levels leading up to the edge.

The spectrum shows considerable intensity beyond the C 1s ionisation edge. Features in the continuum can arise by several different means including (a) double excitations [50] (b) onsets of "shake-up continua" and (c) transitions to quasi-stationary states (shape-resonances). Hitchcock et al. [100] attributed the broad continuum feature centred at 295.9 eV and the structure at ~304 eV to σ^*(C-C) and σ^*(C=C) shape-resonances respectively. There has been much discussionon the possibility of some correlation between shape-resonance position and the distance between the ionised atom and its neighbour(s) (see Chapter 1, section F.III).

The linear correlation obtained by Hitchcock et al. [100] between features assigned to σ^* shape-resonances and bond length in a series of hydrocarbons, including butadiene, lend support to their assignment. However while features 9 and 10 can be assigned to σ^* shape-resonances, contributions from double excitation and "shake-up"

continua cannot be discounted (see subsequent section on allene). Considerable "shake-up (i.e. simultaneous excitation of a valence electron upon core ionisation) features can often be observed in XPS spectra. The production of these states would be manifested in ISEELS by onsets (adiabatic energies) of new continua. For example much of continuum structures in the N 1s ISEELS spectrum of NF_3 was assigned to "shake-up" continua by comparison with the corresponding XPS "shake-up" spectra. Carlson et al. [227] have reported the "shake-up" spectrum of butadiene. The (vertical) energies of the satellite peaks relative to the ionisation edge are indicated on the long range spectrum in Fig. 9.1. The first two (XPS) features are ascribed to $\pi \rightarrow \pi^*$ excitations. They are close to the features assigned to the shape resonances in the ISEELS spectrum [100]. However, the broad maximum (feature 9) in the ISEELS spectrum is similar (though broader) to the continuum feature observed in ethane [68], which is attributed to the σ^*(C-C) resonance [100]. This feature in ethane is closer to the ionisation edge, as would be expected from bond length considerations. Furthermore it cannot be ascribed to "shake-up" since the first feature in the XPS spectrum of ethane is observed 14.7 eV away from the C 1s peak [229]. Feature 8 (Fig. 9.1) is attributed to a double excitation process.

(b) Allene (CH_2=C=CH_2)

The ISEELS spectra of allene are shown in Fig. 9.2. The features as well as the possible assignments are summarised in Table 9.2. The value for the C 1s ionisation edge has been taken from X-ray

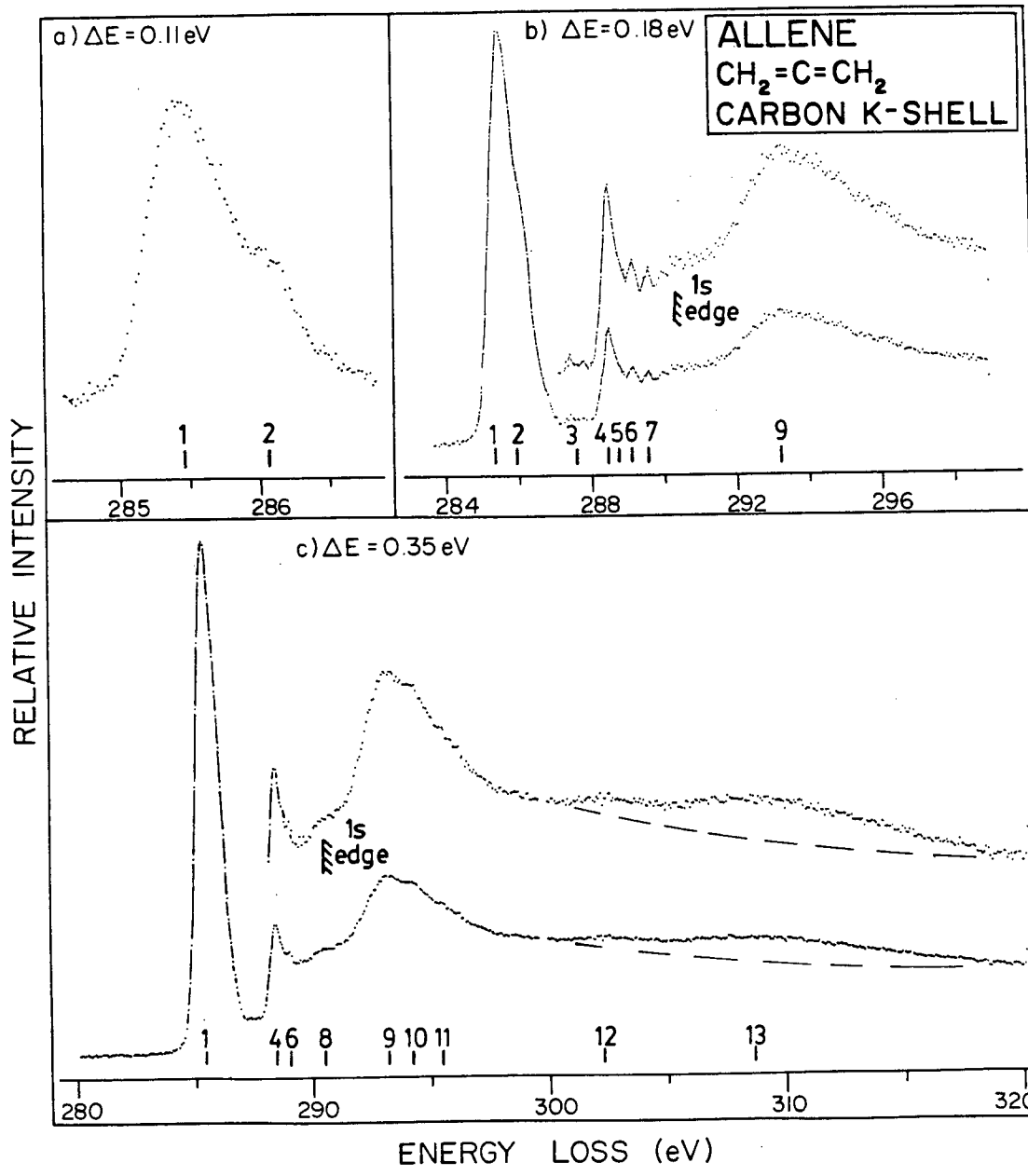

Fig. 9.2 Inner shell electron energy loss spectra of allene at (a) 0.11 eV, (b) 0.18 eV and (c) 0.35 eV spectral resolution. The 1s edge is taken from XPS [230].

Table 9.2

Energies, term values and possible assignments for the C 1s energy loss spectrum of allene

Feature	Energy (eV)	Term Value† (eV)	Possible Assignment††
1	285.40†††	5.05	C'1s → π^* (a)
2	286.01	4.44	C"1s → π^*
3	287.6	2.9	C 1s(b_2) → 3s
4	288.45	2.00	C'1s → $3p_1$ (b)
5	288.8	1.7	C'1s → $3p_2$
6	289.11	1.34	C"1s → 3p
7	289.57	0.88	C'1s → 4p
C 1s edge†	290.45		
8	290.5		ionisation edge
9	293.2		
10	294.2		double excitation/ "shake-up"
11	295.5		
12	~302.3		double excitation/ "shake-up"
13	~308.7		σ(C=C) shape-resonance

† Estimated from Experimental XPS C 1s IP [230].

†† C 1s orbitals are of a_1 symmetry for the central C atom and b_2 and a_1 combinations for the outermost C atomc C' and C".

††† Calibrated feature, estimated uncertaianty ±0.08eV.

(a) π^* orbitals are accidentally degenerate and of e symmetry

(b) p orbitals are split in this symmetry as b_2 and e. Difference is designated by p_1 and p_2.

photoelectron spectroscopy [230]. In spite of having two types of carbon environment, the allene XPS spectrum only shows one unstructured peak centred at 290.45 eV. However, this feature in the XPS spectrum has a FWHM of 1.47 eV [230] suggesting the presence of more than one closely spaced level.

The high resolution ISEELS spectrum, (Fig. 9.2a) shows two features (features 1 and 2) which can be assigned to the two expected C 1s $\rightarrow \pi^*$ transitions. Allene is of D_{2d} symmetry and its two π^* levels are degenerate [223] with e symmetry. Transitions from the C 1s orbitals, which have symmetries of a_1 for the central carbon and a_1, b_2 combinations for the outer carbons [225,231], are all allowed. The separation of features 1 and 2 may be indicative of the splitting of the 1s levels due to the two different types of carbon environment and the different relaxation effects upon the creation of a core hole on the outer carbons as opposed to the central carbon.

The rest of the pre-edge spectrum shows prominent Rydberg structure. The only dipole allowed transition to the s Rydberg levels is from the C 1s(b_2) level. The weak structure at 287.6 eV (feature 3) with a term value of ~2.9 eV is assigned to the C 1s(b_2) $\rightarrow$ 3s transition. The rest of the Rydberg structure is complex. As well as a possible separation between the C 1s orbitals, the p Rydberg levels are split in this symmetry, having b_2 and e symmetries. Transitions to these levels are allowed from the C 1s levels with the exception of the C 1s(b_2) $\rightarrow$ p(b_2) transition. Feature 4 is assigned to a transition

to one of the p Rydberg series ($3p_1$) with the shoulder on the high energy side (feature 5) assigned as a transition to the other p series ($3p_2$). The implied separation of the two series (0.3 eV) is in keeping with the separation of the 3p levels (0.12 eV) in the valence shell spectrum as assigned by Betts and McKoy [215]. However, as will be seen in the next section, the valence spectrum of allene is complex and unlike butadiene is subject to several very different interpretations. Application of the Rydberg formula to feature 4 gives a quantum effect of 0.4, which implies a 4p term value of 1.0 eV. Feature 7 is accordingly assigned to transitions to the 4p Rydberg level. From the term value of feature 3 and application of the formula a term value of 1.4 eV would be expected for the 4s Rydberg level. This would coincide with feature 6; however, the feature (3) assigned to the 3s level is very weak and the higher s Rydberg levels, having even less intensity, should not be seen. Feature 6 is therefore assigned to the transition to the 3p Rydberg levels from the other C 1s level. It should be noted that the separation of feature 6 from feature 4 is close to the separations of features 1 and 2. The term value of 1.34 eV is very low for a 3p level, however, it must be remembered that this is estimated from the mean C 1s edge and the true term value is probably higher. While the term values cannot be established with absolute certainty to their respective edges it can be concluded that the 3p term values for the inner shell spectrum of allene are low and certainly not more than 2 eV. Structure leading up to feature 8 can be assigned to transitions to the higher Rydberg levels converging onto the edge.

Considerable structure can be seen in the post-edge region. As in the case of butadiene these can be assigned to double excitations, "shake-up" or σ^* shape-resonances. The strong band encompassing features 9 - 11 is assigned to double excitation/"shake-up" continua. Strong $\pi \rightarrow \pi^*$ transitions can be expected in allene but unfortunately no XPS "shake-up" spectrum has so far been reported. It is tempting to assign this structure (9 - 11) as partly due to a shape-resonance. However, in light of the discussion given in the previous section and the proposed bond length/shape resonance relationships [99,100] a shape-resonance only ~3 eV from the edge would imply a bond length typical of a carbon-carbon single bond. Obviously this is not the case in allene. Further continuum structures are seen at higher energies. These are attributed to double excitation/"shake-up" and the σ^*(C=C) shape resonance features.

From a least squares fit on the resonance position above the edge (δ) against bond length (R) for a variety of molecules with carbon-carbon bonds, Hitchcock et al. [100] have obtained the following (empirical) relationship:

$$\delta = -54.8R + 84.8$$

Fourteen different carbon-carbon bonds were used and a correlation coefficient of -0.977 was obtained. Substituting the approximate positions of features 12 and 13 above the edge (11.8 eV and 18.2 eV) into this equation results in a prediction of ~1.33 Å and 1.21 Å for the

carbon-carbon bond length. The actual carbon-carbon bond length of allene found by other spectroscopic means is 1.3084(3) Å [162]. Thus on this basis feature 12 rather than feature 13 should be assigned to the σ^*(C=C) shape resonance. However, Sette et al. [99] have noted that the structurally related (valence isoelectronic) linear molecules CO_2, N_2O and COS give bond lengths predicted from the resonance positions that are systematically shorter than the actual bond length. Thus feature 13 is assigned to the σ^*(C=C) shape-resonance.

2. Valence Shell Spectra

(a) Butadiene

The long range valence electron energy loss spectrum of butadiene is shown in Fig. 9.3 as well as a more detailed spectrum of the 5-10 eV region. The energies of the spectral features are summarised in Table 9.3. There has been considerable work done on the region leading up to the first ionisation edge at 9.09 eV [205-218]. The detailed (dipole) spectrum (Fig. 9.3c) presented here agrees well with the higher resolution UV absorption spectrum [205] and is consistent with the earlier low energy EELS work [206-210]. There is general agreement in the assignment of the first members of the s and the two p Rydberg series originating from the HOMO ($1b_g$) orbital between the electron impact [209,210] and multiphoton ionisation [212,213] work. The positions of the (forbidden) 3s transition and (allowed) $3p_1$ and $3p_2$ transitions from the $1\ b_g$ orbital are indicated in the spectrum (Fig. 9.3c). The origin of a

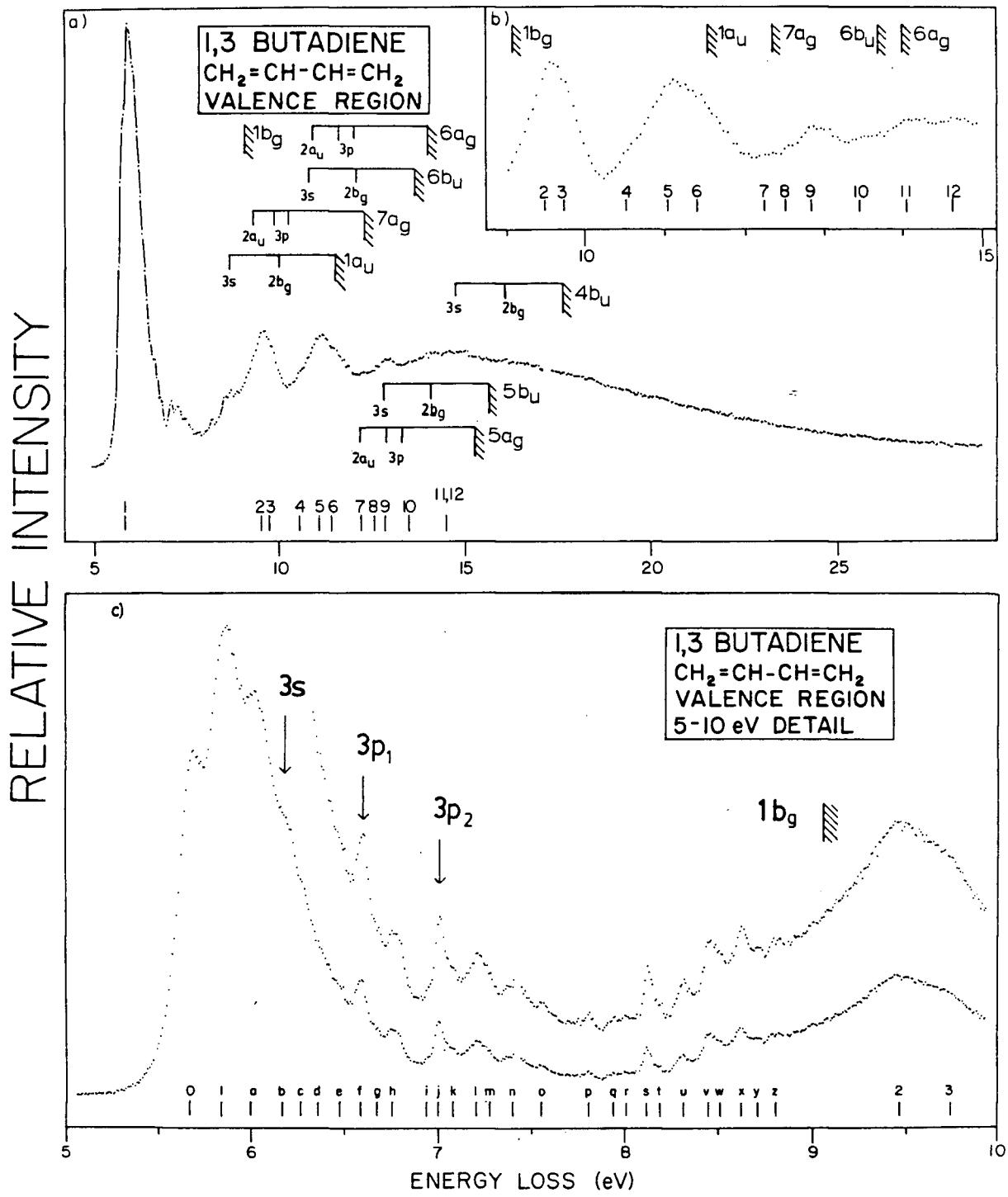

Fig. 9.3 Valence shell electron energy loss spectra of butadiene. The ionisation edges are taken from PES [232]. Position of the transitions shown in 3(a) are estimated from the term values (see Table 9.4). The features associated with the 3p $1b_g \rightarrow$ 3s and transitions are indicated in 3(b).

Table 9.3

Energies of the features in the valence shell electron energy loss spectrum of butadiene.

Feature	Energy (eV)	Feature	Energy (eV)	Feature	Energy (eV)	Feature	Energy (eV)
0	5.73	i	7.01	s	8.18	4	10.60
1	5.90†	j	7.06	t	8.25	5	11.11
a	6.06	k	7.14	u	8.38	6	11.48
b	6.23	l	7.27	v	8.51	7	12.33
c	6.33	m	7.34	w	8.58	8	12.59
d	6.42	n	7.47	x	8.69	9	12.93
e	6.54	o	7.62	y	8.78	10	13.52
f	6.65	p	7.87	z	8.87	11	14.12
g	6.74	q	8.00	2	9.54	12	14.71
h	6.82	r	8.06	3	9.81		

† calibrated feature, estimated uncertainty ±0.05eV.

d Rydberg series has also been located by multiphoton ionisation [213]. All the sharp structure has been assigned to the various Rydberg series and their vibrations. There has been some disagreement, however, with earlier UV work [208] on the exact nature of the series. These have been summarised by Mallard et al. [214].

As stated earlier the two π^* levels have a_u and b_g symmetry. Only the $\pi^*(a_u)$ level is accessible by dipole selection rules from the $1b_g$ level. This transition is identified with the strong feature and vibrational structure centred at 5.90 eV in agreement with earlier works [206-210]. The transition to the $\pi^*(b_g)$ level is dipole forbidden but has recently been identified by variable angle EELS spectroscopy [209, 210] to a broad structure under the sharp Rydberg transitions centred at 7.4 eV.

It is again of importance to note that the assignment of the presently obtained ISEELS spectrum is consistent with the valence shell spectral assignments given earlier for the π^* and Rydberg levels. Transitions to all these levels are allowed and observed from the C 1s levels (see Fig. 9.1 and Table 9.1). In spite of the separation of 0.5 eV observed between the π^* levels in the ISEELS spectrum (Table 9.1) the assignment, as discussed earlier, is still consistent with the valence shell assignment as given in the variable angle EELS work [209, 210].

Turning now to the long range spectrum shown in Fig. 9.3, transitions from the more tightly bound valence orbitals can be seen. The

features at 9.54 eV and 11.11 eV have been noted previously [206,207] If the term values obtained for the transitions arising from the $1b_g$ level are assumed to be transferrable to the more tightly bound valence orbital, the transition energies from these levels can be estimated. Table 9.4 summarises the expected positions of these transitions. The estimate positions of the allowed transitions are also indicated in Fig. 9.3. As noted by Flicker et al. [207], this method should be more reliable for the Rydberg transitions, although it should be possible to tentatively assign intravalence transitions in a similar fashion. This procedure has been used to help assign the valence shell excitation spectra of the phosphorus compounds in Chapter 7 as well as for NF_3 (Chapter 3) and $Si(CH_3)_4$ (Chapter 4). From this procedure it is clearly seen that the features v-z (Fig. 3a,c) can also contain contributions from the $1a_u \rightarrow 3s$ transition, a possibility not considered in the earlier interpretations. Similarly feature 4 can be assigned to the $6b_u \rightarrow 3s$ transition. The band encompassing features 2 and 3 can be assigned to $7a_g \rightarrow \pi^*(a_u)$ and $1a_u \rightarrow \pi^*(b_g)$ intravalence transitions. Likewise the band encompassing features 5 and 6 can be assigned to the $6a_g \rightarrow \pi^*(a_u)$ and $6b_u \rightarrow \pi^*(b_g)$ transitions. However, transitions to the various Rydberg series would also contribute intensity.

(b) Allene

The 2.5 keV valence shell electron energy loss spectrum of allene shown in Fig. 9.4 is similar to the EELS spectrum reported earlier by Mosher

Table 9.4

Estimated transition energies form the valence orbitals of butadiene assuming constant term values[a] for the valence shell

Originating orbital and (IP (eV))[232]	Transition energies[b]				
	$\pi^*(2a_u)$	$\pi^*(2b_g)$	3s	$3p_1$	$3p_2$
$1b_g$ (9.09)	5.9	(7.4)	(6.21)	6.64	7.07
$1a_u$ (11.55)	(8.5)	10.0	8.67	(9.11)	(9.53)
$7a_g$ (12.35)	9.3	(10.8)	(9.47)	9.91	10.33
$6b_u$ (13.7)	(10.6)	12.1	10.8	(11.3)	(11.7)
$6a_g$ (14.0)	10.9	(12.4)	(11.1)	11.6	12.0
$5a_g$ (15.3)	12.2	(13.7)	(12.4)	12.9	13.3
$5b_u$ (15.7)	(12.6)	14.1	12.8	(13.3)	(13.7)
$4b_u$ (17.7)	(14.6)	16.1	14.8	(15.3)	(15.7)

[a] Term Values: π_1^* - 3.1 eV, π_2^* - 1.6eV, s - 2.88 eV

[b] Final orbital symmetries $\pi_1^* - a_u$; $\pi_2^* - b_g$
s $- a_g$; p $- a_u, b_u$

Number in parentheses signify transitions which are dipole forbidden.

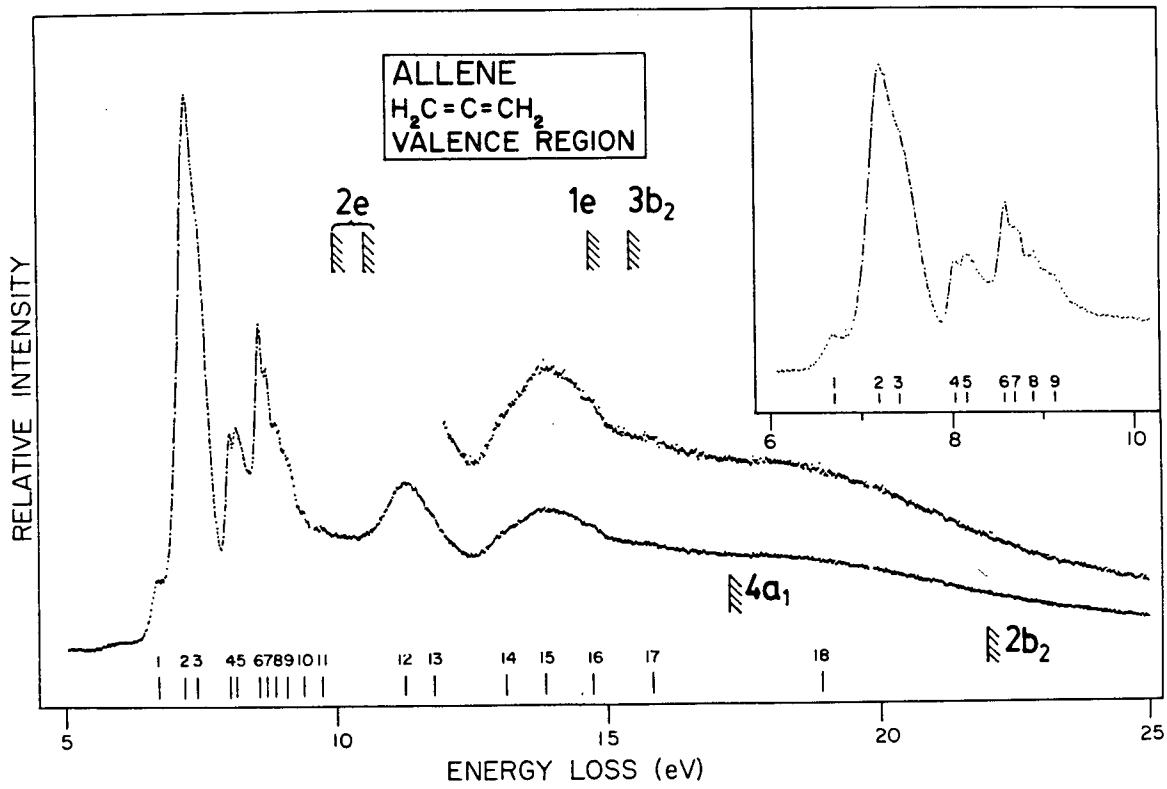

Fig. 9.4 Valence shell electron energy loss spectrum of allene. The ionisation edges are taken from PES [232].

et al. [223] using 40 eV electron impact energy at zero degree scattering angle and confirms the earlier work up to its limit at 12 eV energy loss. Mosher et al. [223] report that no features were observed between 12 eV and 16 eV; however, a broad structure centred at 13.85 eV can be clearly seen in the presently reported spectrum (Fig. 9.4). Higher resolution UV absorption spectra have been reported by Rabelais et al. [220] and Iverson et al. [221], but only up to ~10.2 eV.

As in the case of butadiene there has been much work on assigning the spectrum up to the first ionisation edge but for allene there is considerable disagreement among the various interpretations. The situation in allene is further complicated by the existence of degenerate states and hence the possibility of Jahn-Teller splitting. The first photoionisation band observed in the photoelectron spectrum shows two components at 10.02 eV and 10.58 eV which have been assigned to Jahn-Teller splitting of the HOMO 2e orbital [233,234]. In view of the clear assignment which can be made in the ISEELS spectrum between the π^* and Rydberg levels, and given the fact that the term values of Rydberg levels remain almost constant irrespective of the location of the hole, it is thought that the presently reported ISEELS spectrum of allene can be used to clarify the valence shell spectral assignment. The most recent interpretation of the valence shell electron excitation spectrum is that presented by Diamond and Segal [226] who have performed a large scale ab initio CI calculation of the excited singlet states of allene. They have compared their results [226] with previous interpretations of the optical spectrum as well as that obtained using magnetic circular

dichroism [222]. The spectral features below 10 eV in the valence shell spectrum of allene arise from transitions from the π(2e) orbital to the π^*(3e) orbital and to the various Rydberg levels. No low lying σ^* levels are predicted in keeping with the proposed assignments of the ISEELS spectrum (Table 9.2). Since allene is of D_{2d} symmetry only final states of $^1B_2$ and ^1E are accessible from the $^1A_1$ ground state. Table 9.5 summarises the energies and term values of the features, seen below the first IP in Fig. 9.4. Also summarised are some of the dramatically different assignments given in previous papers [215,220-224.226,235].

The most noteworthy disagreement comes with the recent high quality (ab initio) calculation of Diamond and Segal [226]. These authors assign [226] the intense band encompassing features 2 and 3 solely to transitions to the 3p Rydberg levels whereas most other earlier assignments attribute this intense band as mainly due to the $\pi \rightarrow \pi^*(^1A_1 \rightarrow {}^1B_2)$ transition with either a 3s Rydberg [220,224] or 3s and 3p Rydberg [222,235] transition(s) also present. Diamond and Segal [226] then attribute the $\pi \rightarrow \pi^*$ ($^1A_1 \rightarrow {}^1B_2$) transition to feature 6. Based upon their assignment, this would imply a term value of 1.45 eV for the π^* level and term values of 2.82 eV and 2.60 eV for the 3p(e) and 3p(b_2) Rydberg levels. Comparing these with the term values obtained from the ISEELS spectrum implies that the term value for the π^* state decreases by at least 3.3 eV (an average value has been used for the π^* ISEELS values) while the 3p term value <u>increases</u> by 0.8 eV. While the reduction in term value for the π^* orbital is large (based upon this assignment), it is nevertheless not unreasonable and nothing definite can be

Table 9.5

Energies, Term Values and various assignments for the valence electron excitation spectrum of allene [a] below the 1st I.P.

Feature	Energy (eV)	Term Value† (eV)	Assignments [b]								
			Rabelais et al. ref[220]	Iverson et al. ref[221] [c]	Betts et al. ref[215]	Robin ref[235]	Mosher et al. ref[223]	Fuke et al. ref[222]	Rauk et al. ref[224]	Diamond et al. ref[226]	This work [d]
1	6.70	3.32	^1E	diffuse		3s	$\pi^*(^1A_1)$ or ^1E	3s	$\pi^*(^1B_1)$,3s	$\pi^*(^1B_1)$,3s	
2	7.20	2.82	3s	diffuse	3s	$\pi^*(^1B_2)$	$\pi^*(^1B_2)$	$\pi^*(^1B_2)$	$\pi^*(^1B_2)$	3p(e)	$\pi^*(^1B_2)$
3	7.42	2.60(3.16)	$\pi^*(^1B_2)$			3p(e), (3s)‡		3p,(3s)‡	(3s)‡2	3p(b_2)	3s
4	8.04	1.98	3p	3p	3p(b_2)	3p(b_2)	3p		3p(b_2)	3d, 4s	3p
5	8.16	1.86	+ vib	diffuse	3p(e)				3p(e)($^1A_2$)		
6	8.57	1.45(2.01)	4s + vib	4s	4s	3p(b_2)‡	4s		4s,3p(e)($^1B_2$)	$\pi^*(^1B_2)$	
7	8.69	1.33	3d		etc				3d(e)		
8	8.88	1.14	4p	etc						etc	
9	9.13	0.89	etc								
10	9.39	0.63									
11	9.72	0.30									

† Calculated from the IP of the HOMO orbital (π(e)) at 10.02 eV except for the values in parentheses which are calculated from the higher Jahn-Teller component at 10.58 eV [233,234].

‡ Upper Jahn-Teller component.

[a] Allene is of D_2 symmetry. Only the $^1B_2$, ^1E states are dipole accessible from the $^1A_1$ ground state. π^* orbital is of e

[b] All transitions original from π(e) HOMO level. Only final orbital and state (if needed) is given.

[c] They assigned two Rydberg series with quantum defect of 0.92 and 0.372. These have been assumed to imply s and p Rydberg series respectively.

[d] These interpretations involve conclusions based upon consideration of both valence and inner shell spectra.

See text for further discussion.

inferred from this alone. However, the apparent increase in 3p term value contradicts what would be expected and implies that these features cannot be assigned to the 3p transition. On this basis the present work is in agreement with the earlier assignments [220,222-224,235] and the major component of feature 2 is attributed to the $\pi \rightarrow \pi^*$ ($^1A_1 \rightarrow {}^1B_2$) transition. It should be noted that Diamond and Segal [226] acknowledge the difficulty in describing this ($^1B_2$) state and cite the conclusions of Nascimento and Goddard [217,218] with regard to similar problems in the calculation of the ^1B_u state of butadiene. They [226] suggest that more extensive basis functions and calculations at non-vertical geometries might be required to describe these excited states adequately. It should also be noted that both the calculations of Diamond and Segal [226] and also those by Rauk et al. [224] indicate a strong mixing between the 3p(e) and π^* $^1B_2$ states. With features 2 and 3 assigned to the π^* transition features 4 and 5 are assigned to transitions to the 3p levels, in agreement with the assignments given in the earlier works (see Table 9.5), as opposed to the 3d/4s assignment suggested by Diamond and Segal [226].

Briefly reviewing some of the other assignments, feature 1 has been attributed to either a forbidden state of the $\pi \rightarrow \pi^*$ transition, the 3s Rydberg orbital or both [222-224,226,235]. Both of these assignments are reasonable. The term value (3.3 eV) is larger than that for the weak feature assigned to the 3s Rydberg level in the ISEELS spectrum (2.9 eV). However, in the latter the feature, being very weak, is hard to locate accurately, thus the term value may be in error. Rabelais et

al. [220] have assigned feature 1 as a transition to a ^1E final state. This was based upon its analogous relation to the forbidden $^1\Sigma^* \rightarrow {}^1\Pi_g$ transition in $D_{\infty h}$ systems. The lack of a low lying σ^* orbital rules out this possibility of a valence-valence transition though it should be remembered that the $\pi \rightarrow 3s$ transition leaves the molecule in a ^1E final state. The assignment of a contribution from the $\pi \rightarrow 3s$ transition (whether Jahn-Teller splitting occurs or not) to features 2 and 3 is also reasonable. However, the assignment of a $\pi \rightarrow 3p$ contribution [222,235] as well is unreasonable for the reasons stated above (i.e. the term values for the 3p would not be expected to be larger for the valence shell spectrum).

Moving onto the spectrum above the first IP, Table 9.6 summarises the energies of the features and their term values form the various valence orbitals. These features, as in butadiene, probably have a major contribution from intravalence-valence transitions. As Rydberg level term values are expected to remain constant, the term value of 3.48 eV for feature 12 implies a transition to the π^* level and supports the above suggested assignments of the π^* level being below the 3p level. An increase in term value for a valence level is not unlikely and is consistent with a relaxation effect upon valence orbitals which may occur upon removing an inner electron. The lack of structure for the features rules out any further assignments. Contributions from valence-Rydberg transitions can also be expected.

Table 9.6

Energies and Term Values for the features above the 1st ionisation potential in the valence shell electron energy loss spectrum of allene

Feature	Energy (eV)	Term Value (eV)†			
		1e (14.75eV)	$3b_2$ (15.5eV)	$4a_1$ (17.3eV)	$2b_2$ (22.0eV)
12	11.27	3.48			
13	11.79	2.96	3.7		
14	13.14	1.61	2.4		
15	13.85	0.90	1.7	3.5	
16	14.71		0.8	2.6	
17	15.85			1.5	
18	18.9				3.1

† Estimated from the various ionisation potential obtained from photoelectron spectroscopy [232].

Conclusions

The ISEELS spectra of butadiene and allene have been presented and assigned. In both molecules, transitions to the π^* levels were observed and seem to be well below the Rydberg structure. Transitions to both π^* levels were clearly identified in butadiene. The π^* levels in allene are degenerate, and therefore the two transitions which are seen reflect the different environments of the C 1s orbitals. Both molecules show extensive structure above the ionisation edge. Some of this is identified with σ^* shape-resonances, but features attributable to double excitations and "shake-up" are also seen and are especiallay strong in the case of allene.

The valence shell excitation spectra have also been presented and are in good agreement with previous UV and electron impact work. However, the spectral range has been considerably extended in the present work. Previous assignments of the valence spectrum of butadiene are consistent with the findings of the ISEELS spectrum. As expected, the π^* term values are observed to decrease substantially, while the Rydberg term values decrease by only a small amount (<0.5 eV) on going from inner shell excitation to valence shell excitation. The observation of the transitions to both of the π^* levels (separated by 0.5 eV) in the ISEELS spectrum of butadiene supports the assignment of Doering and McDiarmid [209,210] of a forbidden π^* transition in the low-energy, non-zero angle electron impact spectrum of the valence shell of butadiene. Application of the 3s term value to the $1a_u$ valence orbital of butadiene indicates that some of the structure below the first IP

($1b_g$) in the valence shell spectrum might arise form the $1a_u \rightarrow 3s$ transition.

With the differences observed between the inner shell and valence spectra of butadiene in mind, the ISEELS spectrum of allene supports the assignment of the 7.20 eV feature in the valence shell spectrum as primarily due to a $\pi \rightarrow \pi^*$ transition as predicted in numerous earlier works and not as the $\pi \rightarrow 3p$ transition suggested by the recent calculation of Diamond and Segal [226].

It is seen that as well as providing new spectral information, ISEELS can aid in the interpretation of more complex valence shell spectra.

CHAPTER 10

CONCLUDING REMARKS

In this work, the inner shell electron energy loss spectra of several different series of compounds have been obtained. In almost all cases these spectra have not been previously reported. The spectral assignments were aided by a consideration of the features in all of the series. It was seen that particular ligands had similar effects on the inner shell spectra of the central atom in the different series. This was seen to be especially so for the P and Si L-shell spectra, however, similar effects were also noted in the N K-shell spectra. In addition to the inner shell spectra, the valence shell spectra of many of the compounds have been obtained and analysed with the aid of the corresponding ISEELS spectra. Knowledge of the inner shell spectra have been shown to be very useful in interpreting the valence shell spectra. This arises from the relative ease in the assignment of the inner shell spectra in conjunction with the differing relaxation effects of the Rydberg and virtual valence orbitals when an inner shell vacancy is created as opposed to a valence shell vacancy. The Rydberg levels were seen to be less influenced than the virtual valence levels by the location of the hole and hence have the same, or only slightly higher ($\lesssim$0.5 eV) term values in the inner shell spectra as compared to the valence shell spectra. Conversely, the term values of the features in the discrete region of the spectra assigned to transitions to virtual

valence orbitals were seen to increase markedly in the inner shell spectra. In particular these factors allowed clarification of the complex and controversial valence shell spectrum of allene.

All of the inner shell spectra presented in this work showed continuum structures which in many cases could be reasonably ascribed to σ^* shape-resonances. These can be thought of, in a molecular orbital sense, in terms of transitions to high lying σ^* virtual orbitals in the continuum and hence can be assigned with a knowledge of the MO scheme. Continuum features arising from many-electron processes such as "shake-up" can also occur. This was seen most clearly in the ISEELS spectra of NF_3 where the transitions to the σ^* levels appear in the discrete region of the spectra implying that the continuum structure arises from other factors. Comparison of the N 1s and F 1s XPS satellite spectra clearly indicated the presence of onsets of "shake-up" continua in the ISEELS spectra. The proposed relationship of shape-resonance position and bond length was also examined in the systems studied in the present work. It was seen that some form of correlation does exist though care is needed in assigning the features. This factor provides a further possible means of identifying features associated with σ^* shape-resonances in a series of related molecules.

REFERENCES

1. S. Trajmar, J.K. Rice and A. Kupperman, Adv. Chem. Phys. 18 (Ed. I. Prigogine and S.A. Rice), Wiley Interscience, New York (1970) 15.

2. E.N. Lassettre and A. Skerbele, "Methods of Experimental Physics" 3B (Ed. D. Williams), Academic Press (1974) 868.

3. M.A. Dillon, "Creation and Detection of the Excited State", 1B (Ed. A.A. Lamola), Marcel Dekker, New York (1971) 375.

4. G.R. Wight, C.E. Brion and M.J. van der Wiel, J. Electron Spectrosc. Relat. Phenom 1 (1972/73) 457.

5. G.R. Wight, Ph.D. Thesis, University of British Columbia (1974).

6. A.P. Hitchcock, Ph.D. Thesis, University of British Columbia (1978).

7. F.H. Read, J. Physique Coll. C1 Supp 5, 39 (1978) 1.

8. C.E. Brion, S. Daviel, R. Sodhi and A.P. Hitchcock, AIP Conference Proceedings No. 94 "X-ray and Atomic Inner Shell Physics (Ed. B. Crasemann), American Institute of Physics (1982) 429.

9. C.E. Brion, "Physics of Electronic and Atomic Collisions" (Ed. S. Datz) North Holland (1982) 579.

10. A.P. Hitchcock, J. Electron Spectrosc. Relat. Phenom. 25 (1982) 245.

11. J. Berkowitz, "Photoabsorption, Photoionisation and Photoelectron Spectroscopy", Academic Press, New York (1979).

12. M.B. Robin, "Higher Excited States of Polyatomic Molecules", Vol. 1, Academic Press, New York (1974).

13. K. Wittel and S.P. McGlynn, Chemical Reviews 77 (1977) 745.

14. Ref. 15, p. 50.

15. J. Wayne Rabalais, "Principles of Ultraviolet Spectroscopy", Wiley Interscience, New York (1977).

16. K. Siegbahn, C. Nordling, A. Fahlman, R. Nordberg, K. Hamrin, J. Hedman, G. Johansson, T. Bergmark, S.E. Karlson, I. Lindgren and B. Lindberg, "ESCA, Atomic, Molecular and Solid State Structure studied by Means of Electron Spectroscopy", Nova Acta Regiae Soc. Sci., Upsaliensis, Ser. 4, vol. 20, Uppsala (1967).

17. K. Siegbahn, C. Nordling, G. Johansson, J. Hedman, P.F. Heden, K. Hamrin, U. Gelius, T. Bergmark, L.O. Werme, R. Manne and Y. Baer, "ESCA Applied to Free Molecules", North Holland, Amsterdam (1969).

18. K. Siegbahn, Science 217 (1982) 111.

19. U. Gelius, L. Asplund, E. Basilier, S. Hedman, K. Helenelund and K. Siegbahn, Nucl. Instr. Meth. Phys. Res. B1 (1984) 85.

20. R.J. Buenker and S.D. Peyerimhoff, Chem. Phys. Letters 36 (1975) 415.

21. R.L. Martin and D.A. Shirley, J. Chem. Phys. 64 (1976) 3685.

22. R.L. Martin, B.E. Mills and D.A. Shirley, J. Chem. Phys. 64 (1976) 3690.

23. L.S. Cederbaum and W. Domcke, Adv. Chem. Phys. 36 (Ed. I. Prigogine and S.A. Rice), Wiley Interscience, New York (1977) 205.

24. W. Domcke, L.S. Cederbaum, J. Schirmer, W. von Niessen, C.E. Brion and K.H. Tan, Chem. Phys. 40 (1979) 171.

25. M.O. Krause, J. Phys. Chem. Ref. Data 8 (1979) 307.

26. J. Nordgren, L. Selander, L. Pettersson, R. Bramner, M. Bäckström, C. Nordling and H. Ågren, Chem. Phys. 84 (1984) 333.

27. J. Nordgren, L. Pettersson, L. Selander, C. Nordling, K. Siegbahn and H. Ågren, J. Phys. B 15 (1982) L153.

28. L. Pettersson, J. Nordgren, L. Selander, C. Nordling and K. Siegbahn, J. Electron Spectrosc. Relat. Phenom. 27 (1982) 29.

29. K.D. Sevier, "Low Energy Electron Spectroscopy", Wiley Interscience, New York (1972).

30. P. Kelfve, B. Blomster, H. Siegbahn, K. Siegbahn, E. Sanhueza and O. Goscinski, Phys. Scr. 21 (1980) 75.

31. R. Sodhi and R.G. Cavell, J. Electron Spectrosc. Relat. Phenom. 32 (1983) 283.

32. R. Sodhi, M.Sc. Thesis, University of Alberta (1980).

33. E.J. Aitken, M.K. Bahl, K.D. Bomben, J.K. Gimzewski, G.S. Nolan and T.D. Thomas, J. Am. Chem. Soc. 102 (1980) 4873.

34. W.E. Moddeman, Ph.D. Thesis, Oak Ridge Nat. Lab., ORNL-TM-3012 (1970).

35. D.P. Chong, Chem. Phys. Letters 82 (1981) 511 and references within.

36. R.R. Rye, D.R. Jennison and J.E. Houston, J. Chem. Phys. 73 (1980) 4867 and references within.

37. M.O. Krause and J.H. Oliver, J. Phys. Chem. Ref. Data 8 (1979) 329.

38. H. Bethe, Ann. Phys. (Leipzig) 5 (1930) 325.

39. M. Inokuti, Rev. Mod. Phys. 43 (1971) 297.

40. E.N. Lasettre, Rad. Research (Supp) 1 (1959) 530.

41. E. McDaniel, "Collision Processes in Ionised Gases", John Wiley, New York (1964).

42. M. Born, Z. Physik 38 (1926) 803, or consult any standard physics quantum mechanics text, e.g. A. Messiah "Quantum Mechanics", J. Wiley and Son, New York.

43. E.N. Lassettre, A. Skerbele and M.A. Dillon, J. Chem. Phys. 50 (1969) 1829.

44. M.J. van der Wiel and G. Wiebes, Physica 53 (1971) 225.

45. C.E. Brion and A. Hamnett. Adv. Chem. Phys. 45 (Ed. J. Wm. McGowan), Wiley Interscience, New York (1981) 1.

46. I.V. Hertel and K.J. Ross, J. Phys. B 1 (1968) 697.

47. I.V. Hertel and K.J. Ross, J. Phys. B 2 (1969) 285.

48. J.A.R. Samson, "Techniques of Vacuum Ultraviolet Spectroscopy", John Wiley, New York (1967).

49. F.C. Brown, "Synchrotron Radiation Research" (Ed. H. Winick and S. Doniach), Plenum Press (1980) 61.

50. D.A. Shaw, G.C. King, D. Cvejanovic and F.H. Read, J. Phys. B 17 (1984) 2091.

51. G.C. King, F.H. Read and M. Tronc, Chem. Phys, Letters. 52 (1977) 50.

52. A.P. Hitchcock and C.E. Brion, J. Electron Spectrosc. Relat. Phenom 18 (1980) 1.

53. S. Daviel, C.E. Brion and A.P. Hitchcock, Rev. Sci. Instrum. 55 (1984) 182.

54. F.C. Brown, R.Z. Bachrach and A. Bianconi, Chem. Phys. Letters 54 (1978) 425.

55. P. Gürtler, V. Saile and E.E. Koch, Chem. Phys. Letters 48 (1977) 245.

56. W. Eberhardt, R.-P. Haelbich, M. Iwan, E.E. Koch and C. Kunz, Chem. Phys. Letters 40 (1976) 180.

57. M.J. van der Wiel, Th. M. El-Sherbini and C.E. Brion, Chem. Phys. Letters 7 (1970) 161.

58. M.J. van der Wiel and Th. El-Sherbini, Physica 59 (1972) 453.

59. R.B. Kay, Ph.E. van der Leeuw and M.J. van der Wiel, J. Phys. B 10 (1977) 2521.

60. W.H.E. Schwarz, Chem. Phys. 9 (1975) 157.

61. W.H.E. Schwarz, Chem. Phys. 11 (1975) 217.

62. D.A. Shaw, G.C. King and F.H. Read, J. Phys. B 13 (1980) L723.

63. A.P. Hitchcock and C.E. Brion, J. Electron Spectrosc. Relat. Phenom. 13 (1978) 193.

64. A.P. Hitchcock and C.E. Brion, J. Electron Spectrosc. Relat. Phenom. 17 (1979) 139.

65. H. Friedrich, B. Sonntag, P. Rabe, W. Butscher and W.H.E. Schwarz, Chem. Phys. Letters 64 (1979) 360.

66. M. Tronc, G.C. King and F.H. Read, J. Phys. B 12 (1979) 137.

67. A.P. Hitchcock, M. Pocock and C.E. Brion, Chem. Phys. Letters 49 (1977) 125.

68. A.P. Hitchcock and C.E. Brion, J. Electron Spectrosc. Relat. Phenom. 10 (1977) 317.

69. A.P. Hitchcock and C.E. Brion, Chem. Phys. 33 (1978) 55.

70. D. Blechschmidt, R. Haensel, E.E. Koch, U. Nielsen and T. Sagawa, Chem. Phys. Lett. 14 (1972) 33.

71. R.B. Kay, Ph.E. van der Leeuw and M.J. van der Wiel, J. Phys. B10 (1977) 2513.

72. G.R. Wight and C.E. Brion, J. Electron Spectrosc. Relat. Phenom. 4 (1974) 25.

73. J.L. Dehmer, J. Chem. Phys. 56 (1972) 4496.

74. J.L. Dehmer and D. Dill, Phys. Rev. Letters 35 (1975) 213.

75. J.L. Dehmer and D. Dill, J. Chem. Phys. 65 (1976) 5327.

76. J.L. Dehmer and D. Dill, "Electron-Molecule and Photon-Molecule Collisions" (Eds. T.N. Rescigno, V. McKoy and B. Schneider), Plenum, New York (1979) 225.

77. J.L. Dehmer, D. Dill and A.C. Parr, "Photophysics and Photochemistry in the Vacuum Ultraviolet" (Eds. S. McGlynn, G. Findley and R. Huebner).

78. T. Gustafsson, Atomic Physics 8, Proceedings of the 8th International Conference, Goteburg, Sweden, Aug. 1982, 355.

79. G.J. Schulz, Rev. Mod. Phys. 45 (1973) 422.

80. M. Krauss and F.H. Mies, Phys. Rev. A 1 (1970) 1592.

81. J.L. Dehmer and D. Dill, "Symposium on Electron-Molecule Collisions (Eds. I. Shimamura and M. Matsuzawa), Univ. Tokyo Press, Tokyo (1979) 95.

82. D. Loomba, S. Wallace, D. Dill and J.L. Dehmer, J. Chem. Phys. 75 (1981) 4546.

83. P.W. Langhoff, "Electron-Molecule and Photon-Molecule Collisions" (Eds. T.N. Rescigno, V. McKoy and B. Schneider), Plenum, New York (1979) 183.

84. T.N. Rescigno and P.W. Langhoff, Chem. Phys. Letter, 51 (1977) 65.

85. T.N. Resigno, C.F. Bender, B.V. McKoy and P.W. Langhoff, J. Chem. Phys. 68 (1978) 970.

86. N. Padial, G. Csanak, B.V. McKoy and P.W. Langhoff, J. Chem. Phys. 69 (1978) 2992.

87. A.E. Orel, T.N. Resigno, B.V. McKoy and P.W. Langhoff, J. Chem. Phys. 72 (1980) 1265.

88. L.E. Machado, E.P. Leal, G. Csanak, B.V. McKoy and P.W. Langhoff, J. Electron Spectrosc. Relat. Phenom. 25 (1982) 1.

89. W.J. Hunt and W.A. Goddard, Chem. Phys. Letters 3 (1969) 414.

90. F.A. Gianturco, C. Guidotti and U. Lamanna, J. Chem. Phys. 57 (1972) 840.

91. E. Ishiguro, S. Iwata, Y. Suzuki, A. Mikuri and T. Sasaki, J. Phys. B 15 (1982) 1841.

92. W.H.E. Schwarz, L. Mensching, K. Hallmeier and R. Szargan, Chem. Phys. 82 (1983) 57.

93. J.R. Swanson, D. Dill and J.L. Dehmer, J. Chem. Phys. 75 (1981) 619.

94. J.L. Dehmer, J. Siegel and D. Dill, J. Chem. Phys. 69 (1978) 5205.

95. C.R. Natoli, D.K. Misemer, S. Doniach and F.W. Kutzler, Phys. Rev. A 22 (1980) 1104.

96. T. Gustafsson and H.J. Levinson, Chem. Phys. Letters 78 (1981) 28.

97. C.R. Natoli, "EXAFS and Near Edge Structure" (Eds. A. Bianconi, L. Incoccia and S. Stipcich), Springer-Verlag, Berlin (1983) 43.

98. A. Bianconi, M. Dell'Ariccia, A. Gargano and C.R. Natoli, "EXAFS and Near Edge Structure" (Eds. A. Bianconi, L. Incoccia and S. Stipcich), Springer-Verlag, Berlin (1983) 57.

99. F. Sette, J. Stöhr and A.P. Hitchcock, J. Chem. Phys. (1984) submitted.

100. A.P. Hitchcock, S. Beaulieu, T. Steel, J. Stöhr and F. Sette, J. Chem. Phys. 80 (1984) 3927.

101. Datron Instruments Limited, Norwich, U.K.

102. A.P. Hitchcock and C.E. Brion, J. Electron Spectrosc. Relat. Phenom. 22 (1981) 283.

103. a) E.N. Lassettre, A. Skerbele, M.A. Dillon and K. Ross, J. Chem. Phys. 48 (1968) 5066.
b) J. Geiger and B. Schröder, J. Chem. Phys. 50 (1969) 7.

104. C.E. Moore, Atomic Energy Levelss 1 U.S. Nat. Bureau Standards, Circular L67 (1949).

105. C.E. Brion and S. Daviel, to be published.

106. D.A. Shaw, D. Cvajanović, G.C. King and F.H. Read, J. Phys. B,

17 (1984) 1173.

107. R.N. Lee, J. Electron Spectrosc. 28 (1982) 195.

108. G.C. King, M. Tronc, F.H. Read and R.C. Bradford, J. Phys. B, 10 (1977) 2479.

109. A.P. Hitchcock and C.E. Brion, J. Phys. B, 13 (1980) 3269.

110. T.M. Zimkina and V.A. Fomichev, Soviet Phys. Doklady 11 (1967) 726.

111. D.M. Barrus, R.L. Blake, A.J. Burek, K. Chambers and A.L. Pregenzer, Phys. Rev. A, 20 (1979) 1045.

112. R.E. La Villa, J. Chem. Phys. 57 (1972) 899.

113. A.S. Vinogradov, T.M. Zimkina and V.A. Fomichev, J. Struct. Chem. 12 (1971) 823.

114. F. Wuilleumier, C.R. Acad. Sci., Paris B270 (1970) 825.

115. E.N. Lassettre, F.M. Glaser, V.D. Meyer and A. Skerbele, J. Chem. Phys. 42 (1965) 3429.

116. G.M. Lawrence, D.L. Mickey and K. Dressler, J. Chem. Phys. 48 (1968) 1989.

117. A.W. Potts, H.J. Lempka, D.C. Streets and W.C. Price, Phil. Trans. Roy. Soc. London, A 268 (1970) 59.

118. P.J. Bassett and D.R. Lloyd, Chem. Phys. Lett., 6 (1970) 16; J.C.S. Dalton Trans., (1972) 248.

119. R.G. Cavell and R.N.S. Sodhi, to be published.

120. T.M. Zimkina and A.S. Vinogradov, Bull. Acad. Sci. USSR Phys. Ser., 36 1972) 229 (Izv. Akad. Nauk. SSSR, Ser. Fiz., 36 (1972) 248).

121. R.L. Barinskii and I.M. Kulikova, Bull. Acad. Sci. USSR Phys. Ser., 38 (1974) 16 (Izv. Akad. Nauk SSSR Ser. Fiz., 38 (3) (1974) 444).

122. B. Cadioli, U. Pincelli, E. Tosalti, U. Fano and J.L. Dehmer, Chem. Phys. Lett., 17 (1972) 15.

123. G.R. Wight and C.E. Brion, J. Electron Spectrosc. Relat. Phenom., 4 (1974) 327.

124. F.C. Brown, R.Z. Bachrach and A. Bianconi, Chem. Phys. Letters, 54 (1978) 425.

125. A.S. Vinogradov, T.M. Zimkina, V.N. Akimov and B. Schlarbaum, Bullk. Acad. Sci. USSR Phys. Ser., 38 (3) (1974) 69 (Izv. Akad. Nauk. SSSR Fiz. Ser., 38 (1974) 508).

126. S.R. La Paglia and A.B.F. Duncan, J. Chem. Phys., 34 (1961) 1003.

127. P. Finn, R.K. Pearson, J.M. Hollander and W.L. Jolly, Inorg. Chem., 10 (1971) 378.

128. D.W. Davis, Ph.D. Thesis, University of California, Berkeley, Lawrence Berkeley Laboratory Report LBL-9900, May 1973.

129. M.L. Unland, J.M. Letcher and J.R. Van Wazer, J. Chem. Phys., 50 (1969) 3214.

130. B. Kellerer, L.S. Cederbaum and G. Hohlneicher, J. Electron Spectrosc. Relat. Phenom. 3 (1974) 107.

131. C. Chen, Int. J. Quant. Chem., 18 (1980) 199.

132. P.I. Mansell, C.J. Danby and I. Powis, J. Chem. Soc. Far. Trans. 2, 77 (1981) 1449.

133. G. Ciullo, A. Sgamellotti, F. Tarantelli, C. Famiglietti, G. De Alti and P. Decleva, Z. für Phys. Chem. Neue Folge, 127 (1981) 1.

134. G. Ciullo, A. Sgamellotti, F. Tarantelli, G. De Alti and P. Decleva, Gazz. Chim. Italiano, 110 (1980) 305.

135. T.D. Thomas and R.W. Shaw, J. Electron Spectrosc. Relat. Phenom. 5 (1974) 1081.

136. W.C. Tam and C.E. Brion, J. Electron Spectrosc. & Relat. Phenom., 2 (1973) 111.

137. M. Kobukovskii, private communication.

138. C.S. Fadley, Thesis, (Univ. of California, 1970) UCRL 19535.

139. L. Åsbrink, C. Fridh and E. Lindholm, Chem. Phys. Lett. 52 (1977) 63.

140. P. Langhoff, private communication.

141. L. Åsbrink, C. Fridh and E. Lindholm, Chem. Phys. Lett. 52 (1977) 72.

142. D.K. Creber, J.S. Tse and G.M. Bancroft, J. Chem. Phys., 72 (1980)

4291.

143. R. Roberge, C. Sandorfy, J.I. Matthews and O.P. Strausz, J. Chem. Phys. 69 (2978) 5105.

144. H. Friedrich, B. Pittel, P. Rabe, W.H.E. Schwartz and B. Sonntag, J. Phys. B: Atom Molec. Phys. 13 (1980) 25.

145. T.M. Zimkina and A.C. Vinogradov, J. Phys. (Paris) (Suppl. 10) 32 (1971) C4-3.

146. W. Hayes and F.C. Brown, Phys. REv. A 6 (1972) 21.

147. V.A. Fomichev, T.M. Zimkina, A.S. Vinogradov and A.M. Evdokimov, Zhurnal Strukturnoi Khimii 11 (1970) 676.

148. S. Evans, J.C. Green, P.J. Joachim, A.F. Orchard, D.W. Turner and J.P. Maier, J. Chem. Soc. Faraday Trans. 2, 68 (1972) 905.

149. A.E. Jonas, G.K. Schweitzer, F.A. Grimm and T.A. Carlson; JH. Electron Spectrosc. 1 (1972/73) 29.

150. R. Boschi, M.F. Lappert, J.B. Pedley, W. Schmidt and B.T. Wilkins, J. Organometall. Chem. 50 (1973) 69.

151. W.B. Perry and W.L. Jolly, Chem. Phys. Letters 17 (1972) 611.

152. J.E. Drake, C. Riddle and L. Coatsworth, Can. J. Chem. 53 (1975) 3602.

153. J.E. Drake, C. Riddle, B. Glavincevski, K. Gorzelska and H.E. Henderson, Inorg. Chem. 17 (1978) 2333.

154. R.C. Gray, J.C. Carver and D.M. Hercules, J. Electron Spectrosc. 8 (1976) 343.

155. R.G. Cavell and R.N.S. Sodhi, J. Electron Spectrosc. 15 (1979) 145.

156. F.C. Brown in Solid State Physics (Ed. H. Ehrenreich et al) Volume 29 (1974), Academic Press, pages 1-73.

157. A. Venezia-Floriano and R.G. Cavell, private communication.

158. P.R. Keller, J.W. Taylor, F.A. Grimm, P. Senn, T.A. Carlson and M.O. Krause, Chem. Physics, 74 (1983) 247.

159. A.A. Pavlychev, A.S. Vinogradov, T.M. Zimkina, D.E. Onopko and S.A. Titov, Opt. Spectrosc. (USSR) 47 (1979) 40.

160. V.I. Nefedov, Ya. V. Salyn, G. Leonhardt and R. Schreibe, J.

Electron. Spectrosc. Relat. Phenom. 10 (1977) 121.

161. F. Bechstedt, Phys. Stat. Sol. (b) 91 (1979) 167.

162. Landholdd-Börnstein (New Series) II/7, "Structure Data of Free Polyatomic Molecules", Springer-Verlag, Berlin 1976.

163. Tables of Interatomic Distances, Chemical Society Special Publications (Ed. L.E. Sutton) 11 (1958).

164. W.B. Pery and W.L. Jolly, J. Electron Spectros. Relat. Phenom., 4 (1974) 219.

165. J.J. Toman, A.A. Frost, S. Topiol, S. Jacobson and M.A. Ratner, Theoret. Chim. Acta. 58 (1981) 285.

166. Z. Berkovitch-Yellin, D.E. Ellis and M.A. Ratner, Chem. Phys. 62 (1981) 21.

167. A.G. Alexander, O.P. Strausz, R. Pottier and G.P. Semeluk, Chem. Phys. Lett. 13 (1972) 608.

168. Y. Harada, J.N. Murrell and H.H. Skeena, Chem. Phys. Lett., 1 (968) 595.

169. R.N.S. Sodhi, C.E. Brion and R.G. Cavell, to be published.

170. M.B. Robin, Chem. Phys. Lett., 31 (1975) 140.

171. L.N. Mazalov and A.V. Kondratenko, Proc. c6th Int. Conf. on VAc. UV Rad. Phys. II-71 (Charlottesville, 1980).

172. I.A. Topol, A.V. Kondratenko, and L.N. Mazolov, Opt. Spectrosk. 50 (1981) 494 [Engl. trans. Opt. Spectrosc. (USSR) 50 (1981) 267].

173. I.A. Topol, A.V. Kondratenko, and L.N. Mazalov, Izv. Akad. Nauk (SSSR) Ser. Fiz. 46 (1982) 776 [Engl. Trans: Bull. Acad,. Sci (USSR) Phys. Ser. 46(4) (1982) 143].

174. E.S. Ghuskin, L.N. Mazalov, A.A. Krasnoperova, V.A. Kochubei, S.I. Mishnev, A.N. Shrinskii, E.M. Trahbtenberg, and G.M. Tumaikin, Izv. Akad. Nauk. SSSR Ser. Fiz. 40 (1976) 226 [Engl. Trans: Bull. Acad. Sci. USSR Phys. Ser. 40(2) (1976) 1].

175. R.N.S. Sodhi and R.G. Cavell, unpublished results.

176. S.-X. Xiao, W.C. Trogler, D.E. Ellis and Z. Berkovitch-Yellin, J. Am. Chem. Soc. 105 (1983) 7033.

177. J. Norman, Jr., J. Chem. Phys. 61 (1974) 4630.

178. A.D. Walsh and P.A. Warsop, "Advances in Molecular Spectroscopy" (ed. A. Mangini) 2 (1962) 582.

179. R.G. Cavell, Inorg. Chem. 14 (1975) 2828.

180. W.B. Perry, T.F. Schaaf, and W.L. Jolly, J. Am. Chem. Soc. 97 (1975) 4899 (corrected value from A.A. Bakke, H-W. Chen and W.L. Jolly, J. Electron Spectrosc. Relat. Phenom. 20 (1980) 333.

181. A. Barrier, I.W. Drummond, and Q.C. Herd, J. Electron Spectrosc. Relat. Phenom. 5 (1974) 217.

182. A.P. Hitchcock and C.E. Brion, J. Electron Spectrosc. Relat. Phenom. 14 (1978) 417.

183. R.W. Shaw, Jr., T.X. Carroll and T.D. Thomas, J. Am. Chem. Soc. 95 (1973) 5870.

184. C.M. Humphries, A.D. Walsh and P.A. Warsop, Discuss. Faraday Soc., 35 (1963) 148.

185. M. Halmann, J. Chem. Soc. (1963) 2853.

186. M.J. McAdams and B.R. Russell, Chem. Phys. Letters 18 (1973) 402.

187. I.H. Hillier and V.R. Saunders, Trans. Faraday Soc., 66 (1970) 2401.

188. M. Xin, L-Y.C. Chiu, D. Li and Y-K. Pan, J. Electron Spectrosc. Relat. Phenom. 33 (1984) 93.

189. I.H. Hillier and V.R. Saunders, J.C.S., Dalton Trans. (1972) 21.

190. T.H. Gan, J.B. Peel and G.D. Willett, Chem. Phys. Letters, 48 (1977) 483.

191. A. Strich and A. Veillard, J. Am. Chem. Soc. 95 (1973) 5574.

192. J.P. Maier and D.W. Turner, J.C.S. Far. Trans. 2, 68 (1972) 711.

193. P.A. Cox, S. Evans, A.F. Orchard, N.V. Richardson and P.J. Roberts, Discuss. Faraday Soc. 54 (1972) 26.

194. D.W. Goodman, M.J.S. Dewar, J.R. Schweiger and A.H. Cowley, Chem. Phys. Letters 21 (1973) 474.

195. M.F. Lappert, J.B. Pedley, B.T. Wilkins, O. Stelzer and E. Unger, J.C.S. Dalton Trans. (1975) 1207.

196. V.N. Akimov, A.S. Vinogradov and T.M. Zimkina, Opt. Spectrosk. 53 (1982) 476 [Engl. Trans. Opt. Spectrosc. (USSR) 53 (3) (1982)

280].

197. E. Tannenbaum, E.M. Coffin and A.J. Harrison, J. Chem. Phys. 21 (1953) 311.

198. Ref. 12 + references within.

199. D.R. Salahub, Theor. Chim. Acta 22 (1971) 325.

200. R. Rianda, R.P. Frueholz and W.A. Goddard III, Chem. Phys. 19 (1977) 131.

201. P. Avouris and A.R. Rossi, J. Phys. Chem. 85 (1981) 2340.

202. J.S. Jen and T.D. Thomas, J. Electron Spectrosc. Relat. Phenom. 4 (1974) 43.

203. B.E. Mills, R.L. Martin and D.A. Shirley, J. Am. Chem. Soc., 98 (1976) 2380.

204. W.R. Harshbarger, J. Chem. Phys. 54 (1971) 2504.

205. R. McDiarmid, J. Chem. Phys. 64 (1976) 514.

206. O.A. Mosher, W.M. Flicker and A Kuppermann, J. Chem. Phys., 59 (1973) 6502.

207. W.M. Flicker, O.A. Mosher and A. Kuppermann, Chem. Phys. 30 (1978) 307.

208. J.P. Doering, J. Chem. Phys. 70 (1979) 3902.

209. J.P. Doering and R. McDiarmid, J. Chem. Phys. 73 (1980) 3617.

210. J.P. Doering and R. McDiarmid, J. Chem. Phys. 75 (1981) 2477.

211. R. McDiarmid and J.P. Doering, Chem. Phys. Lett. 88 (1982) 602.

212. P.M. Johnson, J. Chem. Phys. 64 (1976) 4638.

213. L.J. Rothberg, D.P. Gerrity and V. Vaida, J. Chem. Phys. 73 (1980) 5508.

214. W.G. Mallard, J.H. Miller and K.C. Smyth, J. Chem. Phys. 79 (1983) 5900.

215. T.C. Betts and V. McKoy, J. Chem. Phys. 60 (1974) 2947.

216. R.J. Buenker, S. Shih and S.D. Peyerimhoff, Chem. Phys. Lett. 44 (1976) 385.

217. M.A.C. Nascimento and W.A. Goddard III, Chem. Phys. 36 (1979) 147.

218. M.A.C. Nascimento and W.A. Goddard III, Chem. Phys. 53 (1980) 251.

219. L.H. Sutcliffe and A.D. Walsh, J. Chem. Soc. (1952) 899.

220. J.W. Rabelais, J.M. McDonald, V. Scherr and S.P. McGlynn, Chem. Rev. 71 (1971) 73.

221. A.A. Iverson and B.R. Russell, Spectrochim. Acta 28A (1972) 447.

222. K. Fuke and O. Schnepp, Chem. Phys. 38 (1979) 211.

223. O.A. Mosher, W.M. Flicker and A. Kupperman, J. Chem. Physs. 62 (1975) 2600.

224. A. Rauk, A.F. Drake and S.F. Mason, J. Am. Chem. Soc. 101 (1979) 2284.

225. L.J. Schaad, L.A. Burnelle and K.P. Kressler, Theor. Chim. Acta. 15 (1969) 91.

226. J. Diamond and G.A. Segal, J. Am. Chem. Soc. 106 (1984) 952.

227. T.A. Carlson, W.B. Dress, F.A. Grimm and J.S. Haggerty, J. Electron Spectrosc. Relat. Phenom. 10 (1977) 147.

228. D.B. Adams, J. Electron Spectrosc. Relat. Phenom. 13 (1978) 123.

229. J.J. Pireaux. S. Svensson, E. Basilier, P.-Å Malmquist, U. Gelius, R. Candano and K. Siegbahn, Phys. Rev. A 14 (1976) 2133.

230. R.G. Cavell, private communication.

231. Yu A. Kruglyak, H. Preuss and R. Janoschek, Teor.: Eksp. Khim. 7 (1971) 291.

232. K. Kimura, S. Katsumata, Y. Achiba, T. Yamazaki and S. Iwata, "Handbook of HeI Photoelectron spectra of fundamental organic molecules", Japanese Scientific Societies Press, Tokyo, Halsted Press, New York (1981).

233. C. Baker and D.W. Turner, Chem. Commun. (1969) 480.

234. R.K. Thomas and H.T. Thompson, Proc. R. Soc. Lond. A 339 (1974) 29.

235. M.B. Robin, "Higher excited states of polyatomic molecules" (Vol. 2), Academic Press, New York (1975).